Katedra Optiky
Přírodovědecká fakulta
Univerzita Palackého v Olomouci

Thesis submitted for the degree

Doctor of Philosophy

Stochastic Non-Linear Dynamics of Optically Trapped Particles

by

M.Sc. Luca Ornigotti

Supervisor: **Prof. Mgr. Radim Filip, Ph.D.**
Co-Supervisor: **RNDr. Artem Ryabov, Ph.D.**

May 2021

Declaration of Original and Sole Authorship

I, M.Sc. Luca Ornigotti, declare that this thesis entitled *Stochastic Non-Linear Dynamics of Optically Trapped Particles* and the data presented in it are original and my own work, carried out under the guidance of my supervisor prof. Mgr. Radim Filip, Ph.D., and my co-supervisor RNDr. Artem Ryabov, Ph.D.

I confirm that:

- No part of this work has previously been submitted for a degree at this or any other university.
- References to the work of others have been clearly acknowledged. Quotations from the work of others have been clearly indicated, and attributed to them.
- In cases where others have contributed to part of this work, such contribution has been clearly acknowledged and distinguished from my own work.

I agree with the further usage of this thesis in accordance with the requirements of Palacky University and the Department of Optics.

Date: May 2021

Signature:

Abstract

The fast pace that optically levitated platforms have experienced over the past decade has opened new ways to investigate a plethora of nonlinear stochastic mechanical effects. Amongst them, noise-to-signal transitions, peculiar and interesting processes in physics, are the focus of this thesis. They allow to transform the environmental noise to useful mechanical effects.

This thesis investigates the paradigm of stochastic highly nonlinear dynamics of a levitated nanosphere in the classical, overdamped and underdamped regime. With main focus on the dynamical noise-to-signal transitions in the optical cubic potential $V(x) = kx^3/3$, where its inherent instabilities were positively exploited as a thermally driven source to autonomously transform noise into useful coherent mechanical displacement.

Such transformation can be performed because the nonlinearity, one of the essential ingredients together with instabilities, brings the mechanical system out of its thermal equilibrium, thus allowing energy from the fluctuating environment to be used as a source of coherent mechanical displacement and oscillations.

The first part of the thesis opens with a general overview of stochastic processes in linear oscillators, stable and unstable, in the high and low friction regime. General nomenclature and analytical methods are introduced.

The second part discusses stability and noise-to-signal transitions for a particle in cubic potential in the overdamped regime followed by the investigation of maximum of position distribution as a new methodology to characterise the dynamics of highly nonlinear systems. Moreover, the underdamped dynamics of a particle in cubic potential is discussed, introducing new unexplored nonlinear ballistic effects appearing in the in-

stantaneous speed and acceleration, obtained for parameters of current underdamped experiments.

Last, but not least, the numerical methodology to compute dynamics in highly unstable systems, subjected to rapid diverging trajectories, is discussed; with focus on accuracy of computation within and beyond the characteristic time of divergence.

Keywords— Nonlinear Dynamics, Optical Trapping and Manipulation, Brownian Motion, Transient Stochastic Effects, Non-equilibrium Statistical Mechanics

Acknowledgment

As my doctorate verges to the end, I can't but look back and take a moment to thank everyone who shared this journey, imparting me knowledge, and helped me reach this milestone.

A necessary mention goes to my mentor during my chemistry studies, Silvano Romano, who guided me through my transition to physics, helping me immensely in the process. His help inspired me to start my doctorate journey, where I had the pleasure to meet and work alongside Radim Filip. His guidance and supervision were pivotal for my studies, and I cannot thank him enough for the constant support he provided. His passion for science sparkled my thirst for knowledge, and challenged me to become a better version of myself every day. Despite his busy schedule, he always found time to dedicate solely to me, and our scientific discussions over coffee were the best moments of my doctorate. I hope we can continue these meetings in the future.

Another important guidance figure of my journey was Artem Ryabov, whom I met while collaborating on our first manuscript together. He influenced me substantially on my scientific work perspective, and he patiently listened to all my ramblings.

Throughout this journey I relied a lot on the help and support of my colleagues. Thank you Darren, Andrey, Michal, Ivan, Ivo and Giacomo for the memorable times together, from boardgames to conferences.

Furthermore, I would like to thank Nikolai Kiesel and all members of the thermo team, Mario, Maxime, Tobias, and Jakob, for all the fruitful discussions during my abroad stay. You made me feel part of the family right from the beginning, and I am excited to continue my journey with you.

My deepest gratitude goes to my family. They inspired me every step of the way, and helped me in every way imaginable. If I am who I am today, I owe it to them.

My parents, Paola and Roberto, always supported me lovingly and raised me to be inquisitive; and I am eternally thankful for that.

My brother Marco, was and always will be an inspiration to me. A role model to follow, who got me interested in science in the first place.

A special thank goes to my grandma Maró. With her stories and her wits she always cheered me up and made me smile. Grazie di cuore.

I owe a special debt of gratitude to my fiancée, Petra, who stood lovingly by my side through thick and thin. She always had the perfect thing to say regardless of my level of craziness. Thank you for always believing in me, and for being there.

I would also like to thank my friends from Brno: Lucas, Cristopher, Mona, Jirka, Jenny, Abdu, and Martina for keeping me sane with our D&D sessions. I hope this pandemic ends soon, so we can all sit around a table and continue our epic story with roleplay and d20s.

Thank you very much!

Děkuju moc!

Ďakujem vel'mi pekne!

Grazie Mille!

Luca Ornigotti

Olomouc, May 2021

We are nonlinear, thus we exist

Contents

List of Figures

List of Tables

Introduction

Since 1619, the knowledge of observable mechanical motion induced by radiation pressure from the light was known and reported in *De Cometis* by Kepler [3], who suggested that the deflection of comet tails is a result of radiation pressure from the Sun. It can be considered as foundation of modern optomechanics.

Centuries after, in 1901, the landmark experiments of Nichols and Lebedev have proved that light carries momentum, unambiguously demonstrating the radiation pressure predicted by Maxwell [4–6]. These studies have then paved the way to the development of optical trapping, and manipulation of neutral atoms with light, pioneered by Arthur Ashkin in 1970 [7, 8].

Since Ashkin's seminal work, optomechanics has witnessed a significant increase in interest and effort, showing great promise in the development of quantum technologies and force sensing [9]. However, optomechanical devices like cantilever [10–15], and membranes [16–18], are limited by unavoidable mechanical dissipation deriving from (i) clamping losses generated by radiation of elastic waves from the support of the oscillator to the substrate [19–22] (ii) thermo-elastic and -refractive noise generated by temperature dependent properties of the mechanics [23–27], and (iii) viscous damping generated by interactions with gas molecules [28–31]. Moreover, these tethered systems suffer the thermal loading, such as the case for nanoelectromechanical systems (NEMS) [32, 33]. As a result, these technologies are bounded to be working in cryogenic environments. Levitating the micro- or nano-sized mechanical object using optical, magnetic or electric field, allows for minimisation of such mechanical dissipation, leaving only (i) viscous damping given by interaction with the surrounding gas molecules, minimisable by working in vacuum [1], (ii) noises in the optical field [34–37], and (iii) photon recoil due to the discrete nature of the optical radiation [38] as the relevant heating sources of levitated systems.

To evaluate how well decoupled is a system from its surrounding, the mechanical quality factor has been used. Defined as the ratio of energy initially stored to the energy lost in one radian of oscillation cycle, $Q = \Omega_m/\gamma$ bears the information of how often a particle oscillates Ω_m before energy is dissipated γ [1]. The higher the quality factor, the more decoupled the system is from the environment, and hence more oscillations are visible. As can be seen in Fig.1, levitated systems are well above the cube root scaling (black line) typical of the optomechanical resonators, with a predicted Q of over 10^{11} for nanoparticles suspended in vacuum (red shaded area), showing how well decoupled the optically levitated systems are from the environment. The comparison with the state of the art tethered optomechanical exeriments is presented (black dots) [39–41].

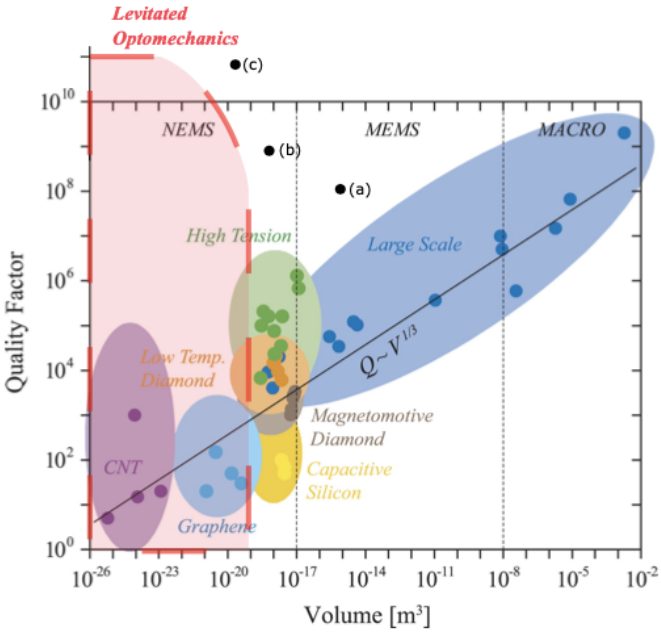

Figure 1: Scaling of mechanical quality factor with oscillator volume [1].
The red area, representing the range at which levitated optomechanical platform are predicted to operate, goes beyond the general scaling of optomechanical experiments (black line), allowing higher quality factor for smaller resonator's volume. Black points represent the state-of-the-art tethered optomechanics experiments: (a) [39], (b) [40], (c) [41]

The thriving young field of levitated optomechanics has then served as a versatile platform to test light matter interactions [42–45], probe the limits of force sensing [36, 37, 46–55], and test the fundamental theories in physics [56–59]. Furthermore, due to the advantages given by coupling the levitated system to an optical cavity, the regime of room-temperature quantum optomechanics has been investigated [60–62], and owing to the recent milestone of quantum ground state cooling [63], the exploration of macro-quantum physics [60, 61, 64], with application to quantum sensing [65, 66] and non-classical state engineering [64, 67, 68] has been opened. Moreover, the freedom from the mechanical vibration of the environment has pushed levitated optomechanics to investigate fundamental theorem of thermodynamics [69–72], nonlinear dynamics [73–94],

and synchronization [95–98].

At the core of the most widespread nonlinear stochastic phenomena in biology and chemistry, such as protein folding dynamics and chemical kinetics [99–104], lies the dynamics at the saddle node bifurcation. Examples include optical bistability in lasers [105–107], firing of neurons [108–110], Brownian ratchets [111–114], nonlinear maps [115], and decays from metastable states [116, 117]. The understanding of thermally activated escapes has been widely known since the 1940, when Kramers calculated escape rates both in the high and low damping regimes [118]. Other analytical techniques have since been developed, leading to a deeper understanding of such problems giving indirect information about particle position, or asymptotic approximations for different regimes. They can roughly be summarised in (i) first passage times [84, 106–109, 115, 118–127], (ii) nonlinear relaxation times (an extension of the previous taking multiple passages into account) [128, 129], and (iii) time evolution of PDF in a symmetric inverted parabolic potential [130–136]. These regimes have been experimentally observed for a particle trapped in optical tweezers [137], even in the low pressure regime [83, 138–141], where for high mechanical factor oscillators the nonlinearity generated by the laser beam, typically exhibiting a soft Duffing term, has been observed [48, 75].

Many platforms have been exploited to observe underdamped nonlinear equilibrium properties and anharmonic oscillations. Amongst them nano- and micro- electromechanical systems have shown phase stochastic resonance [96, 98], anomalous phase diffusion [142], and coherent energy transfer [82] generated by nonlinear dynamics. Moreover, a high cubic nonlinear response has been observed for macroscopic mechanical systems by exploring the anharmonicity in the chemical bonding interactions [81].

To venture in the realm of nonequilibrium physics, and harness the nonlinear features for application ranging from nanosensing to thermodynamical engines, a new approach based on a broader class of transient effects in nonlinear stochastic dynamics has been examined [93]. Nonlinearity brings the mechanical system out of its thermal equilibrium in a different way than coherent driving, hence allowing energy from the fluctuating environment to be used as a primary source of coherent mechanical displacement and oscillations [143]. It has been shown that instability and nonlinearity are the essential ingredients necessary to convert thermal noise to a directed motion, and their dynamics has been characterised by both passage times statistics [127, 144],

and short time statistics of particle position [143] allowing access to unexplored local dynamics [2, 87] that cleared the role of thermal noise in nonlinear stochastic systems.

This complementary direction, main topic of this thesis, is primarily focused on dynamical noise-to-signal transitions, in the cubic potential that has been feasibly prepared by two counter-propagating beams [84, 87], where its inherent instabilities were positively employed as a thermally driven source to autonomously transform noise into useful coherent mechanical displacement [143]. While a feedback control can be used to manipulate the optical potential to achieve models beyond the double-well potential, its main disadvantage lies in its idea to use the output of the dynamical system (measurement) to influence the interaction with the system itself. This operation results in a non autonomous process that hinders the control at the quantum level, as unitary quantum dynamics cannot be reached. A different, yet complementary, way of controlling the mechanical motion can be achieved by nonlinear transient stochastic effects, achievable by the recent progress in fast and accurate preparation, and potential control in levitated systems [69, 137, 145, 146], allowing to explore these dynamical noise-to-signal transitions. They are direct and conclusive evidences of nonlinearity in the system. In these cases, the measurement is used as a verification protocol of the dynamics rather than an active player throughout the protocol, and the nonlinearity comes directly as a modification of the optical trapping potential, that allows access to quantum control. The choice of the cubic nonlinearity, which features will be laid down in details in Chapter 3 of this thesis, is inspired by the highly nonlinear Hamiltonians that can implement analog quantum simulations with mechanical objects, essential in quantum information protocols [147–150].

In such way, when levitating optomechanics achieves the quantum level, the effects from stochastic nonlinear dynamics can be compared with unexplored area of quantum highly nonlinear effects [151–156]. Such systems are investigated in parallel in the superconducting circuits [157–159]

Chapter 1

Principles of Optical Tweezers and Levitation

In 1970, Arthur Ashkin pioneered the field of optical trapping by demonstrating that optical forces could be used to displace, accelerate, and levitate micron-sized dielectric objects both in water and air [7, 160]. What Ashkin et al. [8, 161] observed was a stable trapping of dielectric particles with the gradient force of a strongly focused laser beam. His seminal work led to the development of a single beam gradient force optical trap, the optical tweezer. This technique has since been widely used to manipulate viruses and bacteria [162], and subsequently in trapping and cooling of atoms [163, 164].

An optical trap consists of a tightly focused laser beam with high numerical aperture (NA). The optical forces exerted on a dielectric object are due to transfer of momentum from the scattering of the impinging photons. Such forces can be decomposed in two components *(i) the gradient force* pointing towards the region of highest laser intensity, allowing for stable trapping in the focus of a laser beam, and *(ii) scattering force* pointing towards beam propagation thus pushing the particle out of the trap. To achieve stable trapping it is imperative to eliminate the scattering force, or have the gradient force overcome the scattering [160, 165, 166].

1.1 Forces in an Optical Tweezer

The most general ansatz to compute forces of an electromagnetic field on a dielectric object is given by Maxwell's equations. By integrating the stress tensor over the surface of the dielectric particle one obtains the mechanical force acting on the object [6, 167]

$$\langle \vec{F} \rangle = \oint_{\partial V} \langle \mathbf{T} \rangle \, d\vec{n}, \tag{1.1}$$

where ∂V is the surface of the object, $\vec{n}$ is the unit vector perpendicular to the surface, and $\mathbf{T}$ is the Maxwell stress tensor containing the incident fields impinging on and scattered off the dielectric object. As a consequence of energy and momentum conservation of the incident and scattered fields, the forces acting on the dielectric particle arise, requiring to solve the scattering problem of the field and the object in order to compute the optical forces. The most general solution for a spherical particle illuminated by Gaussian beams is provided by the Lorentz-Mie theory as explained in detail by Gousbet and Gréhan [168]. The special case of a sub-wavelength particle $r \ll \lambda$ results in the application of the Rayleigh approximation which provides closed formulas to compute the optical forces.

1.2 Dipole Approximation

The dipole (or Rayleigh) approximation describes the particle as a point dipole interacting with an electromagnetic field. A dielectric particle illuminated by laser can absorb, scatter, or transmit the impinging photons. Consider a particle of radius r, with a refractive index n_p being illuminated by a Gaussian beam (TEM_{00}) of power P propagating along the z axis. The intensity distribution of the Gaussian beam is

$$I(x, y) = I_0 e^{-\frac{(x^2+y^2)}{\omega(z)^2}}, \tag{1.2}$$

with $I_0 = 2P/\pi\omega(z)^2$ the intensity, $\omega(z) = \omega_0\sqrt{1+(z/z_0)^2}$ the beam radius, and z_0 is the Rayleigh length. The optical forces $\mathbf{F}(\mathbf{r})$ comprise of two terms

$$\mathbf{F}(\mathbf{r}) = \mathbf{F}_{grad}(\mathbf{r}) + \mathbf{F}_{scatt}(\mathbf{r}). \tag{1.3}$$

The first term, $\mathbf{F}_{grad}(\mathbf{r}) = \frac{\alpha'}{4}\nabla I(r)$ is the gradient force, while the second term, $\mathbf{F}_{scatt}(\mathbf{r}) = \frac{\alpha''}{2}I(r)\nabla\phi(r)$ is the scattering force. The terms α', α'' are respectively the real and imaginary part of the polarisability α calculated with the Clausius-Mossotti relation [6, 167, 169]. The phase $\phi(\mathbf{r}) = \mathbf{k}\cdot\mathbf{r}$ shows that the scattering force results from momentum transfer from the radiation field to the particle.

Momentum transfer can occur via absorption ($p = h/\lambda$) or scattering ($p = 2h/\lambda$) of photons. As a result the scattering net force is along the beam propagation and pushes the particle away from the focus thus hindering the trapping.

Similarly, an impinging photon can be diffracted by the particle, and due to the momentum conservation, the particle gets pushed towards the focus of the laser, thus trapping it [170]. The mass of the object becomes then pivotal to achieve stable trapping. For smaller particles thermal excitations have higher probability to kick the particle out of the trap, while bigger particles undergo strong scattering force hence pushing them out of the trap.

1.3 Harmonic Approximation

Optically levitated particles are subjected to thermal noise via collisions with the surrounding gas molecules. When the particle gets displaced by a collision, the gradient force counteracts the momentum transfer by acting in the opposite direction. For small displacement, compared to the local intensity maximum, the scattering force can be approximated by

$$\vec{F}_{scatt} \approx \frac{\alpha''}{2} I_0 \vec{e}_z + \mathcal{O}(z^2). \tag{1.4}$$

The gradient force can be approximated by the linear Hooke's law

$$\vec{F}_{grad}(r) = \frac{\alpha'}{4}\nabla I(r) \approx \frac{\alpha' I_0}{2}\left(\frac{x}{\omega_x^2}\vec{e}_x + \frac{y}{\omega_y^2}\vec{e}_y\right). \tag{1.5}$$

The optical force along the radial directions (x, y) is conservative and can therefore be written as a gradient of the optical potential $\vec{F}_{grad} = -\nabla V_{opt}$. The resulting equations of motion unfold

$$m\ddot{x} + m\gamma\dot{x} + m\Omega_x^2 x = F_{th}, \tag{1.6}$$

$$m\ddot{y} + m\gamma\dot{y} + m\Omega_y^2 y = F_{th}, \tag{1.7}$$

$$m\ddot{z} + m\gamma\dot{z} + m\Omega_z^2 z = F_{th} + F_{scatt}, \tag{1.8}$$

as a thermally driven and damped harmonic oscillator with $m\gamma\dot{x}$ a Stokes friction force due to the interactions with the surrounding gas particles, F_{th} a Brownian force noise at room temperature, and F_{scatt} to be an offset introduced by the scattering force, constant for small displacement.

1.4 Nonlinear Potential

To obtain a cubic potential in Eq.(1.6), another pair of identical counter-propagating Gaussian beams, displaced in the x-axis, are added [171]. Assuming the waists and phases of the beams remain the same, the resulting optical intensity becomes [171]

$$I_3(x, y, z) = 4\frac{\omega_{03}^2}{\omega_3^2}e^{-2\frac{y^2}{\omega_3^2}}\left\{\sqrt{I_{31}}e^{-\frac{(x-x_{31})^2}{\omega_3^2}} + \sqrt{I_{32}}e^{-\frac{(x-x_{32})^2}{\omega_3^2}}\right\}^2 \cos(kz)^2, \tag{1.9}$$

where x_{ij} denotes the position of the Gaussian beam waist.

The above can be further simplified by assuming that the particle moves in the vicinity of the waist positions $y = z = 0$ and the beam is wide enough to preserve the width ($\omega_3 \equiv \omega_{03}$) in the region of the particle's dynamics. Moreover, $x_{32} = 0$ can be further assumed, leading to [171]

$$I_3(x, y, z) = 4\left\{\sqrt{I_{31}}e^{-\frac{(x-x_{31})^2}{\omega_3^2}} + \sqrt{I_{32}}e^{-\frac{x^2}{\omega_3^2}}\right\}^2. \tag{1.10}$$

From Eq.(1.3) and $\mathbf{F}_{grad}(\mathbf{r}) = \frac{\alpha'}{4}\nabla I(r)$ the optical potential $V_3(x) \propto I_3(x)$ exhibits a cubic profile around the point $x = x_c$ [171]

$$V_3(x) \approx V_3^{opt}(x_c) + \frac{1}{3}\mu_3^{opt}(x - x_c)^3, \tag{1.11}$$

with the depth of the potential $V_3^{opt}(x_c)$, and the coefficient of cubic nonlinearity μ_3^{opt} being function of the beam parameters. This method was employed in [84, 87] to observe the noise-to-signal transitions discussed in this thesis.

1.5 Optical measurement techniques

After having realised a stable trap, one must be able to measure and track the position of the particle. The following sections provides a general overview of optical techniques for measurement.

1.5.1 CCD and Quadrant Detectors

In [84, 87], to measure the particle position of a particle evolving in the optical cubic potential, a charge coupled device (CCD) was used, which provides a direct method to measure the position evolution in an optical trap.

Its basic structure comprises of a shift register, essentially an array of closely spaced potential well capacitors, and a thin layer of silicon dioxide grown on a silicon substrate with a transparent electrode (pixel gate) deposited on it [172]. Upon absorption of incident photons, a pair electron-hole is created through the photoelectric effect. By positively biasing discrete areas of the surface, the electrons thereby created are gathered and then counted [172].

The number of electrons (photons) per pixel, gives the intensity profile of the field, thus allowing to record the particle position directly, without measuring any time variation enabling direct particle velocity measurement [172].

When a higher time resolution is needed, for instance in force measurements, a quadrant detector (QD) is used [173]. The QD is a position sensitive device which is composed of four identical p-n junction photodiodes, separated by very small gaps [174]. Its main advantage lies in higher

resolutions with lower inherent noise, useful for micro- and nano- meter displacement [173, 174]. Venturing towards the quantum regime, where smaller changes in position need to be detected, both the CCD and QD fail to provide the necessary precision, and a different measurement technique, based on phase detection, has been developed.

1.5.2 Homodyne and Heterodyne Detection

The derivation of this section is inspired by [175, 176].

We consider an incident Gaussian beam E_{00} with intensity I as per Eq.(1.2), polarised along x. The dipole induced by the incident field, via $\mu(\mathbf{r}_{dp}) = \alpha E_{00}(\mathbf{r}_{dp})$, radiates an electric field via the dyadic Green's function $\mathbf{G}(\mathbf{r}, \mathbf{r}_{dp})$

$$\mathbf{E}_{dipole}(\mathbf{r}, \mathbf{r}_{dp}) = \omega^2 \mu \mu_0 \mathbf{G}(r, r_0), \tag{1.12}$$

where ω and μ_0 are the optical frequency and the vacuum permeability respectively.

In the paraxial approximation ($z \approx f$, with f distance from the focus) the far field of the dipole becomes a spherical wave

$$\mathbf{E}_{dipole}(\mathbf{r}, \mathbf{r}_{dp}) = E_{dipole} e^{i(kf + \phi_{dipole})} \mathbf{n}_x, \tag{1.13}$$

with amplitude E_{dipole} and phase ϕ_{dipole} position dependent. The scattered light that arrives at the detector is then transformed into a plane wave by a lens of focal length f, thus characterised by the following amplitude and phase

$$E_{dipole} = E_0 \frac{\alpha \omega^2 \mu_0}{4\pi f} e^{\rho^2_{dipole}/w_0^2}, \tag{1.14}$$

$$\phi_{dipole} = \mathbf{k} \cdot \mathbf{r}_{dipole} + \frac{k-1}{z_0} z_{dipole}, \tag{1.15}$$

with ρ and w_0 the radial position and beam waist respectively.

From Eq.(1.15) it can be seen that the particle motion is primarily imprinted into the phase of the scattered light and hence a phase sensitive measurement is required. Moreover, the total scattered light intensity and signal are rather weak, and require a reference beam field $\mathbf{E}_{ref}$ to

interfere with the scattered light to amplify the signal and read out the phase. The intensity distribution at the detector then become

$$I(\mathbf{r}, \mathbf{r}_{dp}) \propto |\mathbf{E}_{dipole} + \mathbf{E}_{ref}|^2 \tag{1.16}$$

$$= E_{dipole}^2 + 2E_{dipole}E_{ref}\cos(\phi_{dipole}(\mathbf{r}, \mathbf{r}_{dp}) + \phi_{ref}) + E_{ref}^2, \tag{1.17}$$

with ϕ_{ref} being the relative phase between the scattered light and the reference field.

If the scattered light interferes with the reference beam at the same optical frequency, a homodyne measurement can be performed. Assuming that the intensity of the scattered light is weaker compared to the intensity of the reference $E_{dipole}^2 \ll E_{ref}^2$, and that the intensity of the reference E_{ref}^2 can be eliminated by balanced detection, the first and last term of Eq.(1.16) can be dropped, leading to

$$2E_{dipole}E_{ref}\cos(\phi_{dipole}(\mathbf{r}, \mathbf{r}_{dp}) + \phi_{ref}). \tag{1.18}$$

Moreover, since to first approximation the particle motion is harmonic, i.e. $\phi_{dipole} \approx q_0\cos(\Omega_0)$, we obtain that the spectrum of the detected signal from Eq.(1.18) consists of harmonics of the particle oscillation frequency Ω_0.

For the homodyne signal of Eq.(1.18) to be linear in particle displacement, a relative phase $\phi_{ref} = -\pi/2$ is required.

Oppositely, when the reference beam and the scattering light have different optical frequency, a heterodyne measurement can be performed. The detector signal is given by

$$E_{dipole}E_{ref}\cos(\phi_{dipole}(\mathbf{r}, \mathbf{r}_{dp}) + \phi_{ref} + \Delta\omega t), \tag{1.19}$$

where $\Delta\omega$ is the difference in the optical frequencies, meaning that the spectrum of the detection signal is shifted to $\Delta\omega$ and has sidebands at $\Delta\omega \pm \Omega_0$.

Typically $\Delta\omega \ll \Omega_0$ is chosen to measure both quadratures and extract the phase $\phi_{dipole} + \phi_{ref}$, which then has to be high-pass filtered to obtain ϕ_{dipole}.

Chapter 2

Theory of Stochastic Linear Dynamics

Levitating spherical particles, moving in one-dimensional approximation, can be sufficiently described by the following Langevin equation

$$\ddot{x} = -\gamma\dot{x} - \frac{\partial_x V(x)}{m} + \sqrt{2D_{\mathrm{UD}}}\xi(t), \tag{2.1}$$

where $\gamma = \Gamma/m$ is the damping coefficient, $V(x)$ is a time independent potential in one spatial dimension, $D_{\mathrm{UD}} = k_B T\gamma/m$ represents the diffusion coefficient in the underdamped regime, with k_B is the Boltzmann constant and T the effective environment temperature, satisfying the fluctuation dissipation theorem [177, 178], and $\xi(t)$ is the standard Gaussian white Markovian noise. Historically, it was representing collisions of fluid molecules with the Brownian particle. However, for levitating particles this simplified description is effective as other noises, i.e. photon shot noise and recoil, are more relevant in deeply underdamped regime.

The integral $W(t) = \int_0^t \xi(t')dt'$ is the standard Wiener process with continuous trajectories. For the probability density function $p(x,t) = \frac{1}{\sqrt{2\pi t}}e^{-x^2/2t}$, we obtain zero mean $\langle W(t)\rangle = 0$ and a second moment evolving linear in time $\langle W^2(t)\rangle = t$ [178]. Moreover, the Wiener process has independent increments, and the two-time correlation function is given by $\langle W(t)W(t')\rangle = |t'-t|$. For simplicity we will always assume unitary mass $m = 1$, unless differently specified, or relevant for the discussed effect.

2.1 Free Particle Motion

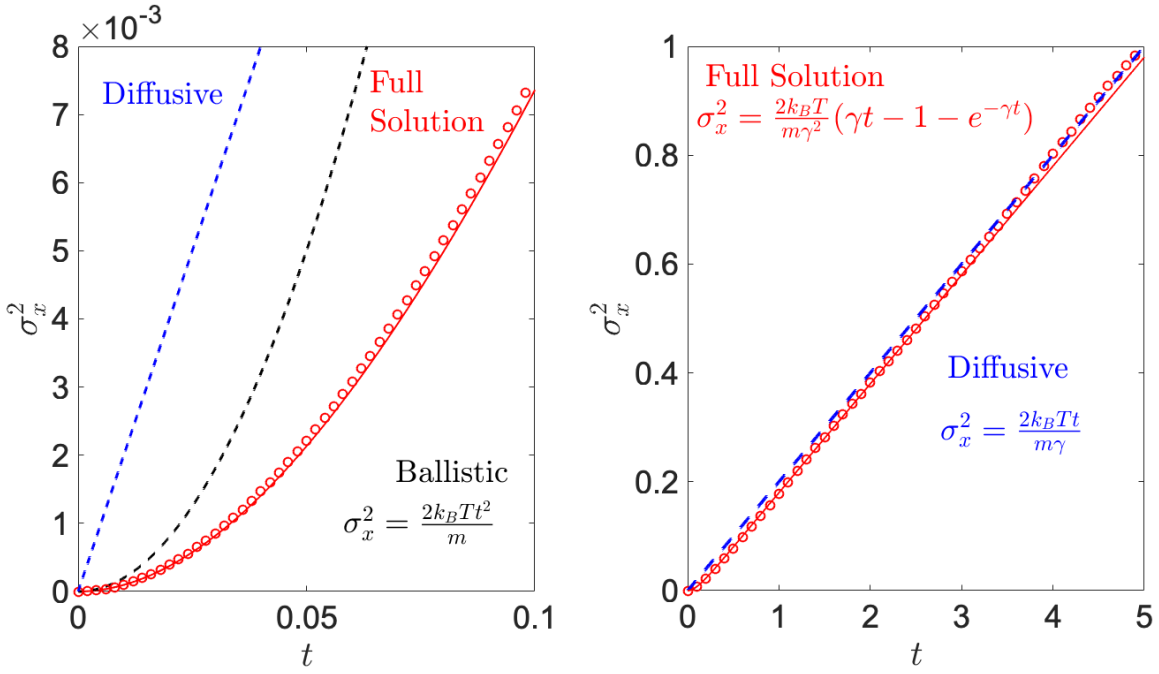

Figure 2.1: Time scales comparison of position variance σ_x^2, and nonexistence of instantaneous velocity for overdamped dynamics.
The figure shows the full evolution of position variance (red dots), corroborated by the analytical result of Eq.(2.8) (red line), for initial condition drawn from a Gaussian distribution with $\langle x_0\rangle = \langle \dot{x}_0\rangle = 0$, and standard deviations $\sigma_{x_0}^2 = 0$, $\sigma_{\dot{x}_0}^2 = k_BT$, where $k_B = 1$ has been taken to simplify visualisation. For times $t \ll 1/\gamma$ the dynamics is dominated only by inertia, resulting in an evolution of position variance $\sigma_x^2 \propto t^2$ (left panel, black dashed line). Contrarily, for $t \gg 1/\gamma$, the dynamics is diffusive, and the position variance evolves as $\sigma_x^2 \propto t$ (right panel, blue dashed line). The latter is the result for the overdamped dynamics, which cannot predict the evolution at ballistic timescales. For this reason, and because $\sigma_x^2 \propto t$ is not root mean squared differentiable, the instantaneous velocity for the overdamped dynamics (non inertia approximation) does not exist. The linear ballistic effect, $\sigma_x^2 \propto t^2$ evolution, was for the first time demonstrated and measured, for a particle optically trapped in liquid in a harmonic optical potential [179–181]. Environmental temperature $T = 1$ has been used to generate $nt = 10^4$ trajectories with a sample size $N = 5000$, and timestep $dt = 10^{-4}$.

When no potential is confining the particle free motion, such as the case for the short time scale of a particle trapped in both a liquid or gas, the dynamics can be described by the following Langevin equation

$$\ddot{x} = -\gamma\dot{x} + \sqrt{2D_{\mathrm{UD}}}\xi(t). \tag{2.2}$$

For a particle starting at a definite phase point (x_0, v_0), the position difference $\Delta x(t) = x(t) - x_0$

and velocity $\dot{x}(t) = v(t)$ dynamics of Eq.(2.2) unfolds [178]

$$\Delta x(t) = \frac{v_0}{\gamma}\left(1 - e^{-\gamma t}\right) + \frac{\sqrt{2D_{\mathrm{UD}}}}{\gamma}\int_0^t \left(1 - e^{-\gamma(t-t')}\right)\xi(t')dt' \tag{2.3}$$

$$v(t) = \dot{x}(t) = v_0 e^{-\gamma t} + \sqrt{2D_{\mathrm{UD}}}\int_0^t e^{-\gamma(t-t')}\xi(t')dt', \tag{2.4}$$

$$\ddot{x}(t) = -\gamma v_0 e^{-\gamma t} - \gamma\sqrt{2D_{\mathrm{UD}}}\int_0^t e^{-\gamma(t-t')}\xi(t')dt' + \sqrt{2D_{\mathrm{UD}}}\xi(t). \tag{2.5}$$

From Eq.(2.3) the mean square displacement $\langle(\Delta x(t))^2\rangle$ can be calculated as [178]

$$\langle(\Delta x(t))^2\rangle = \frac{\langle v_0^2\rangle}{\gamma^2}\left(1 - e^{-\gamma t}\right)^2 + \frac{2D_{\mathrm{UD}}}{\gamma^2}\iint_0^t (1 - e^{-\gamma(t-t')})(1 - e^{-\gamma(t-t'')})\langle\xi(t')\xi(t'')\rangle dt'dt'', \tag{2.6}$$

$$= \frac{\langle v_0^2\rangle}{\gamma^2}\left(1 - e^{-\gamma t}\right)^2 + 2\frac{D_{UD}t}{\gamma^2} + \frac{D_{UD}}{\gamma^3}\left(-3 + 4e^{-\gamma t} - e^{-2\gamma t}\right). \tag{2.7}$$

If one considers a Boltzmann distribution of initial velocities, i.e. $\langle v_0^2\rangle = k_B T/m$, and substitutes the value of $D_{\mathrm{UD}} = k_B T\gamma/m$, the resulting mean square displacement of Eq.(2.6) becomes [178, 181]

$$\langle(\Delta x(t))^2\rangle = \frac{2k_B T t}{\gamma m} + \frac{2k_B T}{\gamma^2 m}\left(e^{-\gamma t} - 1\right), \tag{2.8}$$

known as the Ornstein-Fürth formula [178].

For long times $t \gg 1/\gamma$ the first term of Eq.(2.8) is the relevant one, resulting in a mean square displacement $\langle(\Delta x(t))^2\rangle = 2K_B T t/m\gamma$ (diffusive) (Fig.2.1 blue line), result of Langevin and Einstein [178], that is not root mean square differentiable at $t = 0$. This means that in the non-intertial approximation the velocity $v(t) = \dot{x}(t)$ does not exist, but rather only $\bar{v} = \Delta x/\Delta t$ does. Contrarily, for the short time dynamics $t \ll 1/\gamma$ the exponential can be expanded in series, revealing the term $\langle(\Delta x(t))^2\rangle = 2K_B T t^2/m$ to be relevant in Eq.(2.8). Note that the ballistic Brownian motion is independent of γ, and the $1/m$ dependency suggests that massive objects make for harder observation of the ballistic regime. The latter, result of the ballistic dynamics as observed in Fig.2.1 (black line), is root mean square differentiable at $t = 0$, thus demonstrating the existence of velocity when inertia is taken into consideration.

Another way to obtain the result of Eq.(2.8) is by means of the velocity autocorrelation function

$\langle(\Delta x(t))^2\rangle = 2\int_0^t (t-u)\langle v(0)v(u)\rangle du$, where the correlation $\langle v(t_1)v(t_2)\rangle = k_B T e^{-\gamma|t_1-t_2|}/m$ can be calculated from Eq.(2.4) [178]. Simultaneously the variances for velocity $\dot{x}$ and acceleration $\ddot{x}$ approach [178]

$$\langle(\Delta\dot{x}(t))^2\rangle = \sigma_{v_0}^2 e^{-2\gamma t} + \frac{k_B T}{m}(1 - e^{-2\gamma t}), \tag{2.9}$$

$$\langle(\Delta\ddot{x}(t))^2\rangle = \gamma^2\sigma_{v_0}^2 e^{-2\gamma t} + \frac{\gamma^2 k_B T}{m}\left(1 - e^{-2\gamma t}\right) + \frac{2k_B T\gamma}{m}. \tag{2.10}$$

If one considers a Boltzmann distribution of initial velocities, i.e. $\langle v_0^2\rangle = k_B T/m$, both variance of velocity and acceleration remain constant to $\langle(\Delta\dot{x}(t))^2\rangle = k_B T/m$, and $\langle(\Delta\ddot{x}(t))^2\rangle = k_B T\gamma(2+\gamma)/m$ respectively. For the above reason, in the free particle motion there is no distinction between ballistics and diffusive regime for velocity and acceleration.

2.2 Particle in Quadratic Potential

When the parabolic potential $V(x) = kx^2/2$ is used as a trap for a particle, Eq.(2.1) describes the damped motion of a Brownian particle subjected to the action of a linear restoring force [178]:

$$\ddot{x} = -\gamma\dot{x} - \omega_0^2 x + \sqrt{2D_{\mathrm{UD}}}\xi(t), \tag{2.11}$$

where $\omega_0 = \sqrt{k/m}$ is the natural frequency of the oscillator. For low friction, namely $\omega_0 > \gamma/2$, the system described by Eq.(2.11) can exhibit oscillating solution in $\langle x(t)\rangle$ with exponentially damped amplitude [178]. By gradually increasing the damping in the system, the oscillation's period and frequency starts to be affected, as damping opposes by slowing periodic motion. Transiting in the large friction limit, namely $\omega_0 < \gamma/2$, the oscillations cease to exist and the system relaxes to equilibrium. The special case of critically damped motion, is defined by the condition ($\omega_0 = \gamma/2$) for which the damping of the oscillation results in a fast return to equilibrium positions, overshooting it only once [178].

2.2.1 Low Friction Limit

For $\omega_0 > \gamma/2$, solutions of Eq.(2.11) describe an oscillatory motion for stochastic displacement, $x(t)$, instantaneous stochastic velocity $\dot{x}(t)$, and instantaneous stochastic acceleration $\ddot{x}(t)$ [178, 182],which ensemble averages evolve as

$$\langle x(t)\rangle = e^{-\frac{\gamma t}{2}}\Big[\langle x_0\rangle\cos(\omega_d t) + S_{HO}\sin(\omega_d t)\Big], \tag{2.12}$$

$$\langle \dot{x}(t)\rangle = e^{-\frac{\gamma t}{2}}\Big[\langle \dot{x}_0\rangle\cos(\omega_d t) - S'_{HO}\sin(\omega_d t)\Big], \tag{2.13}$$

$$\langle \ddot{x}(t)\rangle = -e^{-\frac{\gamma t}{2}}\Big[C_{HO}\cos(\omega_d t) + S''_{HO}\sin(\omega_d t)\Big], \tag{2.14}$$

where $2\omega_d = \sqrt{|\gamma^2 - 4\omega_0^2|}$ is the damped angular frequency. Note how the central frequency of oscillation is modified by the damping γ. For clarity we used

$$S_{HO} = \frac{2\langle \dot{x}_0\rangle + \gamma\langle x_0\rangle}{\omega_d}, \tag{2.15}$$

$$S'_{HO} = \frac{\gamma(2\langle \dot{x}_0\rangle + \langle x_0\rangle\gamma) + \langle x_0\rangle\omega_d^2}{2\omega_d}, \tag{2.16}$$

$$C_{HO} = \gamma(4\langle \dot{x}_0\rangle + \langle x_0\rangle\gamma) + \langle x_0\rangle\omega_d^2, \tag{2.17}$$

$$S''_{HO} = \frac{\gamma^2(2\langle \dot{x}_0\rangle + \langle x_0\rangle\gamma) + (-2\langle \dot{x}_0\rangle + \langle x_0\rangle\gamma)\omega_d^2}{2\omega_d}. \tag{2.18}$$

The moments of Eqs.(2.12)-(2.14) can be rewritten to better visualise oscillation amplitude $A = e^{-\frac{\gamma t}{2}}\sqrt{\langle x_0\rangle^2 + 4\langle \dot{x}_0\rangle^2/\omega_d^2}$ and phase shift ϕ in the following form

$$\langle x(t)\rangle_{HO} = A(t)\cos(\omega_d t + \phi), \qquad \phi = \arctan\frac{S_{HO}}{\langle x_0\rangle}, \tag{2.19}$$

$$\langle \dot{x}(t)\rangle_{HO} = \frac{A(t)\sqrt{\gamma^2+\omega_d^2}}{2}\cos(\omega_d t + \phi'), \qquad \phi' = \arctan\frac{S'_{HO}}{\langle \dot{x}_0\rangle}, \tag{2.20}$$

$$\langle \ddot{x}(t)\rangle_{HO} = A(t)(\gamma^2+\omega_d^2)\cos(\omega_d t + \phi''), \qquad \phi'' = \arctan\frac{S''_{HO}}{C_{HO}}. \tag{2.21}$$

The maximum amplitude of the oscillations are therefore given by $x_{max,t=0} = A$, $\dot{x}_{max,t=0} = A\sqrt{\gamma^2+\omega_d^2}/2$, and $\ddot{x}_{max,t=0} = A(\gamma^2+\omega_d^2)$.

In the short time regime, the mean position of Eq.2.19 evolves linearly in time $\langle x(t)\rangle \approx \langle x_0\rangle + (4\langle \dot{x}_0\rangle + \gamma\langle x_0\rangle)t/2$. Note how its evolution does not depend on ω_d. Similarly, the mean velocity

of Eq.2.20, $\langle \dot{x} \rangle \approx \langle \dot{x}_0 \rangle - (3\langle \dot{x}_0 \rangle \gamma + \langle x_0 \rangle(\gamma^2 + \omega_d^2))t/2$, and mean acceleration of Eq.2.21, $\langle \ddot{x} \rangle \approx -\gamma\langle \dot{x}_0 \rangle - \langle x_0 \rangle(\gamma^2 + \omega_d^2) + (\langle \dot{x}_0 \rangle(\gamma^2 + \omega_d^2) + \gamma\langle x_0 \rangle(\gamma^2 + \omega_d^2))t$ evolve linearly in time with the slope determined by the initial conditions $\langle x_0 \rangle, \langle \dot{x}_0 \rangle$ and the damped angular frequency ω_d.

To witness the oscillations from the dynamics of a damped particle in a quadratic potential, it is sufficient to let the particle swing from nonzero initial position, or to give it a nonzero initial velocity.

To externally induce a sustainable coherent shift of the particles initially sitting at the potential minimum, $\langle x_0 \rangle = \langle \dot{x}_0 \rangle = 0$, a constant driving force is required to drive the system out of its equilibrium, resulting in a non-autonomous oscillatory motion. Such process can be described by the Langevin equation of the form

$$\ddot{x} = -\gamma\dot{x} - \omega_0^2 x + F_0\theta(t) + \sqrt{2D_{UD}}\xi(t), \tag{2.22}$$

where $F_0\theta(t)$ describes a step-function driving force of strength F_0 that pushes the system out of its equilibrium. The solutions to Eq.(2.22) are oscillating trajectories with expected values

$$\Delta\langle x(t) \rangle = \frac{F_0}{\omega_0^2} - 4F_0 A_{drive} e^{-\frac{\gamma t}{2}} \cos(\omega_d t + \phi_{drive}), \tag{2.23}$$

$$\Delta\langle \dot{x}(t) \rangle = e^{-\frac{\gamma t}{2}} 2F_0 A_{drive}^2 \omega_0^2 \omega_d \sin(\omega_d t), \tag{2.24}$$

$$\Delta\langle \ddot{x}(t) \rangle = e^{-\frac{-\gamma t}{2}} F_0 A_{drive}^2 \omega_0^2 \omega_d (\gamma^2 + \omega_d^2) \cos(\omega_d t - \phi_{drive}), \tag{2.25}$$

$$\phi_{drive} = \arctan\left(\frac{\gamma}{\omega_d}\right), \tag{2.26}$$

$$A_{drive} = \frac{\sqrt{\omega_d^2 + \gamma^2/\omega_0^4\omega_d^2}}{4}, \tag{2.27}$$

where $\Delta\langle ... \rangle = \langle ... \rangle - \langle ... \rangle_{HO}$, with $\langle ... \rangle_{HO}$ being the moments of the damped harmonic oscillator from Eqs.(2.19)-(2.21). Notice that the quantities in Eqs.(2.23)-(2.25) are independent of the initial conditions $\langle x_0 \rangle, \langle \dot{x}_0 \rangle$, and they display only the dynamics generated by the driving force $F_0\theta(t)$.

In the short time regime, the mean position $\Delta\langle x(t) \rangle \approx -F_0\gamma t/2\omega_0^2$ from Eq.(2.23), evolves linearly in time, decreasing with a slope proportional to the driving force F_0 and the natural frequency of the oscillator ω_0, oppositely to the short time dynamics of Eq.(2.19). Simultaneously, the

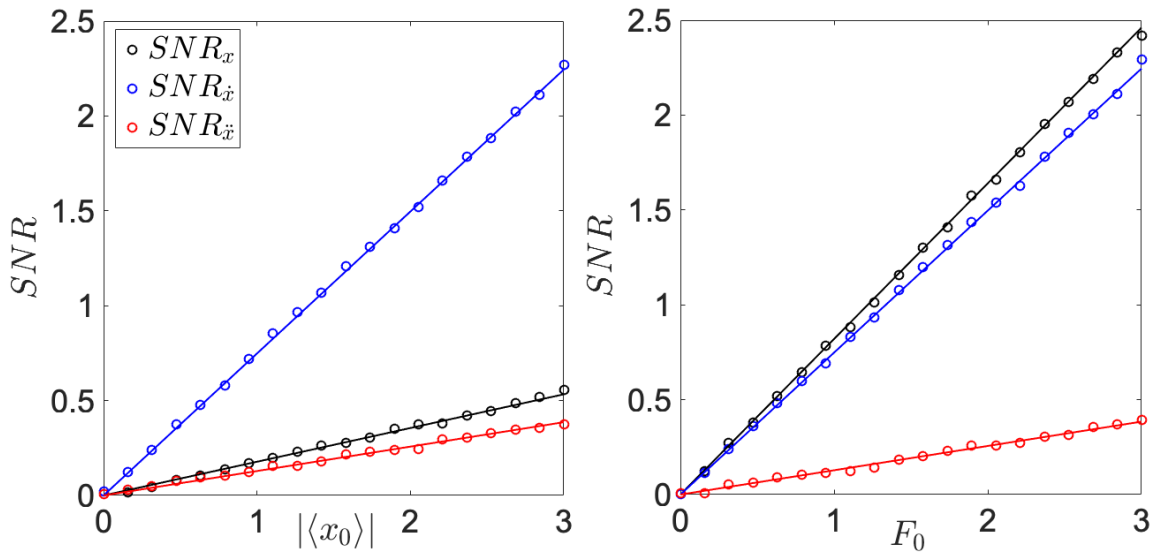

Figure 2.2: Comparison of SNR ***of particle position (black), velocity (blue) and acceleration (red) between the damped (left) and driven (right) oscillator, which dynamics is described by Eqs.***(2.11),(2.22) ***respectively.***
On the left panel, the evolution of the SNR *is displayed as a function of initial particle position* $|\langle x_0 \rangle|$*, with* $\langle \dot{x}_0 \rangle = 0$*, and initial standard deviations* $\sigma^2_{x_0} = 1$*, and* $\sigma^2_{\dot{x}_0} = T/k$*.*
The main effect of the dynamics is visible in velocity (blue) with a fastly increasing $\mathrm{SNR}_{\dot{x}}$ *compared to that of position (black) and acceleration (red).*
On the right panel, the evolution of the SNR *as a function of driving strength* F_0 *for initial conditions drawn from a Gaussian distribution with* $\langle x_0 \rangle = \langle \dot{x}_0 \rangle = 0$*, and* $\sigma^2_{x_0} = 1, \sigma^2_{\dot{x}_0} = T/k$*.*
The SNR_x *of position (black), quantity that is primarily driven by* $F(t) = F_0\theta(t)$*, increases much faster than its not driven counterpart (left), whereas the remaining quantities, i.e. velocity (blue) and acceleration (red), display the same* SNR *evolution.*
A quality factor $Q = \omega_0/\gamma$ *of* $Q = 10$ *has been used, indicating that the dynamics is in the low friction regime. The environmental temperature* $T = 1$*, together with a time step of* $dt = 10^{-5}$ *have been used to generate* $nt = 10^4$ *trajectories with a sample size of* $N = 5000$ *evolving for* $t = 5$*.*

mean velocity $\Delta\langle \dot{x}(t) \rangle \approx -F_0\gamma/2\omega_0^2 + F_0 f(\gamma, \omega_d)t$ increases linearly in time, with a negative value $-F_0\gamma/2\omega_0^2$ at $t = 0$, contrastingly to that of Eq.(2.20). Lastly, the mean acceleration $\Delta\langle \ddot{x}(t) \rangle \approx F_0 f(\gamma, \omega_d) + f(\gamma, \omega_d)t$ Eq.(2.25), increases linearly in time, with an initial value at $t = 0$ much larger $F_0(3\gamma^2 + 4\omega_d)/4\omega_0^2$. Amongst the three quantities, the velocity increases faster than the remaining two.

As the result is involving, for clarity we used $f(\gamma, \omega_d)$ indicating a general function of damping γ and damped angular frequency ω_d. Regardless of the driving, the noise term in position $x_\xi(t) = \sqrt{2D_{UD}}W(t)$, arising from Eq.(2.1) is the important term to be computed to further

understand the role of the noise in the dynamics [182]

$$x_\xi^2(t) = \frac{2D_{UD}}{\omega_d^2} \iint_0^t e^{-\gamma(t-t'-t'')} \sin(\omega_d(t-t')) \sin(\omega_d(t-t''))\xi(t')\xi(t'')dt'dt'', \tag{2.28}$$

from which the mean square displacement can be calculated as

$$\langle(\Delta x_\xi(t))^2\rangle = \frac{D_{UD}}{\gamma\omega_0^2} + e^{-2\gamma t}\frac{D_{UD}}{\gamma\omega_0^2\omega_d^2}\left[\frac{\gamma}{2}\cos(2\omega_d t) - \frac{\gamma\omega_d}{2}\sin(2\omega_d t) - \omega_0^2\right]. \tag{2.29}$$

The saturating second moment converges faster as the trap stiffness $k = \omega_0^2$ increases, leading to a stationary value $(\Delta x(t))^2\rangle = D_{UD}/(\gamma\omega_0^2)$ mass-independent (the mass only determines the relaxation time [182]).

In the short time limit, the variance of position generated by the noise Eq.(2.29), decreases in time, $\langle(\Delta x_\xi(t))^2\rangle \approx D_{UD}(f(\gamma,\omega_d) - \gamma f(\gamma,\omega_d)t - f(\gamma,\omega_d)t^2)$. Thus, the variance of position, at vanishing $\sigma_{x_0}^2$, for the damped and driven oscillator increases quadratically in time. The same scaling was introduced in Eq.(2.8) for a free particle motion. Differently than the aforementioned, the ballistic Brownian motion for a particle trapped in an optical quadratic potential depends on the damping γ and the damped angular frequency ω_d.

Note that as the dynamics is linear, the variance of position for the damped and driven oscillator is the same, as it does not depend on driving force F_0.

Similarly the mean square velocity deviation $\langle(\Delta\dot{x}_\xi(t))^2\rangle$ evolves as [182]

$$\langle(\Delta\dot{x}_\xi(t))^2\rangle = \frac{D_{UD}}{\gamma} + e^{-2\gamma t}\frac{D_{UD}}{\gamma\omega_d^2}\left[\frac{\gamma\omega_d}{2}\sin(2\omega_d t) - \frac{\gamma^2}{2}\sin^2(2\omega_d t) - \omega_d^2\right], \tag{2.30}$$

which value at the stationary state is given by $\langle(\Delta\dot{x}(t))^2\rangle = D_{UD}/\gamma$, independent of the potential stiffness k.

In the short time dynamics, the variance of velocity Eq.(2.30) evolves as $\langle(\Delta\dot{x}_\xi(t))^2\rangle \approx D_{UD}(2\gamma t - 7\gamma^2 t^2/2)$. As a result, the variance of velocity $\langle(\Delta\dot{x}(t))^2\rangle \approx D_{UD}(4 - 6\gamma t + (7\gamma^2 - 8\omega_d)t^2/2)$ increases quadratically in time, contrarily to the free motion of Eq.(2.9) which remains constant at kBT.

Lastly, the mean square acceleration $\langle(\Delta\ddot{x}_\xi(t))^2\rangle$ evolves as

$$\langle(\Delta\ddot{x}_\xi(t))^2\rangle = D_{UD}\left[2+\frac{1}{\gamma}+\gamma e^{-\gamma t}\left(-\frac{\gamma^2\omega_d^2+\omega_0^2}{\gamma\omega_d^2}+\frac{1}{2\omega_d^2}A-\frac{1}{2\omega_d}B\right)\right], \tag{2.31}$$

$$A = (\cos(2\omega_d t)-\gamma^3\sin(2\omega_d t)), \tag{2.32}$$

$$B = (\sin(2\omega_d t)-\gamma^2\sin(2\omega_d t)). \tag{2.33}$$

In the limit of $t\to\infty$ the variance of acceleration converges to $\langle(\Delta\ddot{x}(t))^2\rangle_{\to\infty} \approx k_BT(2\gamma+\gamma^2\omega_0^2)/m$. Notice how its stationary value depends on the damping γ, and in the limit of strong damping, the variance of acceleration reaches large values, while its mean vanishes. In the short time evolution, the variance of acceleration increases linearly in time, approaching $\langle(\Delta\ddot{x}(t))^2\rangle \approx kBT(f(\gamma,\omega_0)+f(\gamma,\omega_0)t)/m$.

A good quantifier of the quality of the oscillator undergoing noise disturbance is the SNR, defined as the ratio between the coherent and incoherent (noise) part of the quantities $\mathrm{SNR}_x = |\langle x\rangle|/\sigma_x$, and $\mathrm{SNR}_{\dot{x}} = |\langle\dot{x}\rangle|/\sigma_{\dot{x}}$ [183]. A comparison of the SNR between the damped (left) and driven (right) oscillator, as shown in Fig.2.2, exhibits a comparable evolution of the SNR of velocity (blue) and acceleration (red), while the position SNR (black) increases much faster in the driven oscillator (right) becoming comparable with the evolution of the velocity SNR.

2.2.2 High Friction Approximation

The regime of strong damping, i.e. when $\omega_0 < \gamma/2$ is satisfied, comprises of two main timescales of interest. For ballistic short time scales, i.e. $t \ll t_B$ ($t_B = k/\gamma$), the dynamics is only dominated by inertia where the particle is discretely kicked, even without any external forces, for instance by the surrounding fluid molecules, exhibiting a variance evolution $\sigma_x^2|_{t\to 0} \propto t^2$ [178] as shown in Fig.2.1 for the free particle evolution.

For longer times scales, $t \gg t_B$, the overdamped diffusive motion appears, displaying a linear increase of variance in time, $\sigma_x^2 \propto t$ [178]. For times larger than $\tau_{HT} = \gamma/k$ the harmonic potential sets in and confines the particle diffusion [178]. The strong damping regime of Eq.(2.11) can be

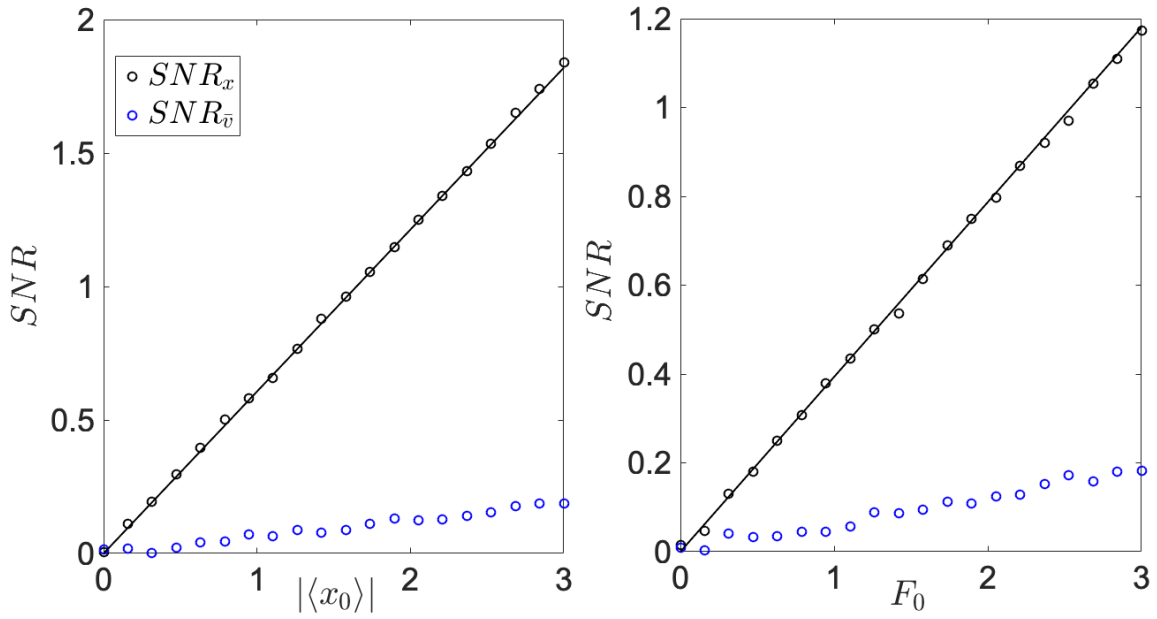

Figure 2.3: Comparison of SNR ***of particle position (black) and average velocity*** $\bar{v}$ ***(blue) between the damped (left) and driven (right) oscillator in the high friction limit, which dynamics is described by Eqs.***(2.11),(2.22) ***respectively.***
The lines represent the analytical results obtained from the overdamped approximation of that limit using Eqs.(2.34),(2.37).
On the left panel, the evolution of the SNR *is displayed as a function of initial particle position* $|\langle x_0 \rangle|$*, with* $\langle \dot{x}_0 \rangle = 0$*, and initial standard deviations* $\sigma^2_{x_0} = 1$*, and* $\sigma^2_{\dot{x}_0} = T/k$.
The main effect of the dynamics is visible in position (black) with a fastly increasing $\mathrm{SNR}_{\dot{x}}$ *compared to that of average velocity (blue).*
On the right panel, the evolution of the SNR *as a function of driving strength* F_0 *for initial conditions drawn from a Gaussian distribution with* $\langle x_0 \rangle = \langle \dot{x}_0 \rangle = 0$*, and* $\sigma^2_{x_0} = 1, \sigma^2_{\dot{x}_0} = T/k$.
The SNR_x *of position (black), is still more pronounced than the average velocity (blue) but, when compared to the damped oscillator (left), its position* SNR_x *is slower, while the average velocity* SNR_x *remains the same (blue).*
A quality factor $Q = \omega_0/\gamma$ *of* $Q = 0.1$ *has been used, indicating that the dynamics is in the high friction regime. The environmental temperature* $T = 1$*, together with a time step of* $dt = 10^{-5}$ *have been used to generate* $nt = 10^4$ *trajectories with a sample size of* $N = 5000$ *evolving for* $t = 5$.

approximated by the following overdamped equation of motion

$$\dot{x} = -\frac{k}{\gamma}x + \sqrt{2D}\xi(t), \tag{2.34}$$

where γ, k are respectively the friction constant, and the potential stiffness, whereas $D = k_B T/\gamma$ denotes the diffusion coefficient. For the optically trapped particles, in the over-damped approximation, only the mean velocity $\langle \bar{v} \rangle = \langle \Delta x/\Delta t \rangle = -(k/\gamma)\langle x \rangle$ survives. The resulting dynamics

of the over-damped motion is described by an exponentially vanishing mean displacement and saturating second moment

$$\langle x(t)\rangle = \langle x_0\rangle e^{-\frac{k}{\gamma}t} \tag{2.35}$$

$$\sigma_x^2 = \sigma_{x_0}^2 e^{-2\frac{k}{\gamma}t} + \frac{D\gamma}{k}(1 - e^{-2\frac{k}{\gamma}t}). \tag{2.36}$$

For the driven system, the overdamped equation of motion reads

$$\dot{x} = -\frac{k}{\gamma}x + \frac{F_0}{\gamma}\theta(t) + \sqrt{2D}\xi(t). \tag{2.37}$$

Its solution comprises of a saturating first $\langle x\rangle_{st} = F_0/k$, and second $\sigma_{x,st}^2 = k_BT/k$ moment evolving as follows

$$\langle x(t)\rangle = \langle x_0\rangle e^{-\frac{k}{\gamma}t} + \frac{F_0}{k}\left(1 - e^{-\frac{k}{\gamma}t}\right) \tag{2.38}$$

$$\sigma_x^2 = \sigma_{x_0}^2 e^{-2\frac{k}{\gamma}t} + \frac{D\gamma}{k}(1 - e^{-2\frac{k}{\gamma}t}). \tag{2.39}$$

For the long time evolution, the mean position $\langle x(t)\rangle$ of Eqs.(2.35),(2.19) vanish, while the mean position of Eqs.(2.38),(2.23) converge to F_0/k. In the short time, the mean position of Eq.(2.35) evolves as $\langle x(t)\rangle \approx \langle x_0\rangle(1-kt\gamma)$. Notice how in the overdamped regime, the short time dynamics exhibits a clear dependence on the potential stiffness k, whereas the full solution of Eq.(2.19) does not.

The mean position of Eq.(2.38), in the short time dynamics, increases linearly in time $\langle x(t)\rangle \approx \langle x_0\rangle + (F_0 - \langle x_0\rangle k/\gamma)t$. When compared to the short time evolution of Eq.(2.23), one notices how the latter decreases linearly in time, as opposed to the former. Moreover, the former does not depend on the potential stiffness k.

Simultaneously, the second moments equilibrate to T/k. In the short time, the variances of Eqs.(2.36),(2.39) evolve linearly in time $\sigma_x^2 \approx 2Tt/\gamma$, as opposed to the ballistic regime of the previous section.

A comparison of the SNR between the strongly damped oscillator (left) and the driven (right), shown in Fig.2.3, exhibits a negative effect of the driving force in the strong damping regime,

ultimately producing a slower SNR for position (black). The average velocity $\bar{v}$ is not modified by the driving force, similar to how the instantaneous velocity and acceleration were not influenced in the low friction limit Fig.2.2.

2.3 Inverted Quadratic Potential

2.3.1 High Friction Approximation

The dynamics of a particle in an inverted quadratic potential, appearing for instance at the centre of a symmetrical optical double well potential, is the simplest theoretical model to introduce instability. Being a linear model it allows for full analytical control while exploring the role of instabilities, i.e. low noise linear amplification [184, 185].

Such dynamics can be described by the following time-invariant dynamical system

$$\dot{x} = \frac{k}{\gamma} x, \tag{2.40}$$

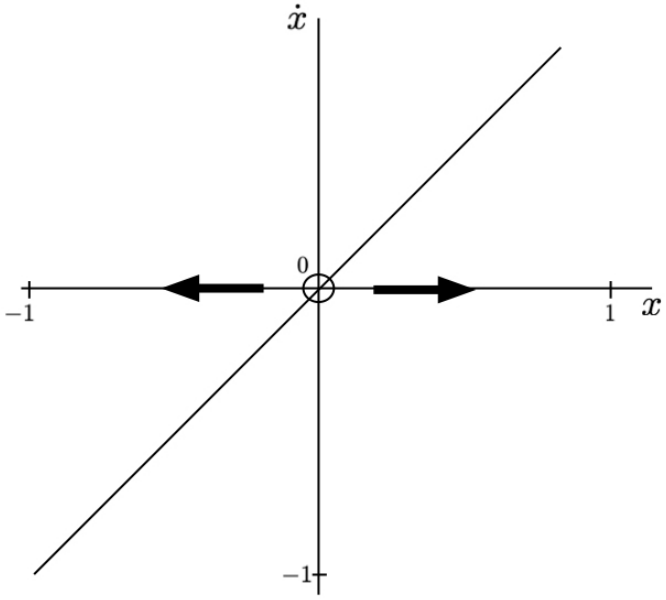

Figure 2.4: Sketch of the vector field of Eq. (2.40)**.** *The figure shows the unstable point at $x_e = 0$ (open circle), with the flow (arrows) diverging from it. The further away trajectories are from the the fixed point, the larger the flow is, indicating exponentially diverging trajectories as described by Eq.* (2.41)*.*

characterised by a fixed point at $x_e = 0$. The sketch of the vector field (see Fig.2.4) exhibits the flow (arrows) diverging from the unstable fixed point (open circle), growing larger the further away they are from it. This indicates that trajectories $x(t)$ are prone to divergence.

The solution of Eq.(2.40) displays exponentially diverging trajectories

$$x(t) = x_0 e^{\frac{k}{\gamma} t}. \tag{2.41}$$

If instead of sharp initial conditions we use a normal random variable with distribution centered at $\langle x_0 \rangle = x_e$, with non-zero variance $\sigma^2_{x_0}$, we can see if and how a change in the uncertainty of the initial state realises dynamics of the signal $\langle x \rangle$.

A glimpse to this can be observed in the illustration of Fig.2.5, where trajectories with initial conditions drawn from a Gaussian distribution are displayed, showing how an increase in the uncertainty of the initial state does not modify the dynamics of mean position, but only increases its variance.

The computation of the moments of position for a particle evolving in the inverted quadratic potential demonstrate that no dynamics is induced by the change of the uncertainty of the initial state $\sigma^2_{x_0}$

$$\langle x(t) \rangle = \langle x_0 \rangle e^{\frac{k}{\gamma}t}, \tag{2.42}$$

$$\sigma^2_x(t) = \sigma^2_{x_0} e^{2\frac{k}{\gamma}t}. \tag{2.43}$$

Its SNR $= \langle x_0 \rangle / \sigma_{x_0}$ does not change in time, as it only depends on the initial conditions.

When noise is included, the dynamics of Eq.(2.40) can be described by the following

$$\dot{x} = \frac{k}{\gamma} x + \sqrt{2D}\xi(t). \tag{2.44}$$

The above Brownian motion has a formal solution

$$x(t) = x_0 e^{\frac{k}{\gamma}t} + \sqrt{2D} e^{\frac{k}{\gamma}t} \int_0^t e^{-\frac{k}{\gamma}t'} \xi(t') dt', \tag{2.45}$$

leading to an exponentially growing first and second moment

$$\langle x(t) \rangle = \langle x_0 \rangle e^{\frac{k}{\gamma}t}, \tag{2.46}$$

$$\sigma^2_x(t) = \sigma^2_{x_0} e^{2\frac{k}{\gamma}t} + \frac{D\gamma}{k}\left[e^{2\frac{k}{\gamma}t} - 1\right]. \tag{2.47}$$

While it can be seen that noise does not modify the statistics of the first moment $\langle x(t) \rangle$, it does so for the variance of Eq.(2.47), ultimately leading to a decreasing SNR with increasing D, saturating at $\langle x_0 \rangle \left(\sqrt{D\gamma/k + \sigma^2_{x_0}}\right)^{-1}$. In the short time dynamics, the mean position evolves as

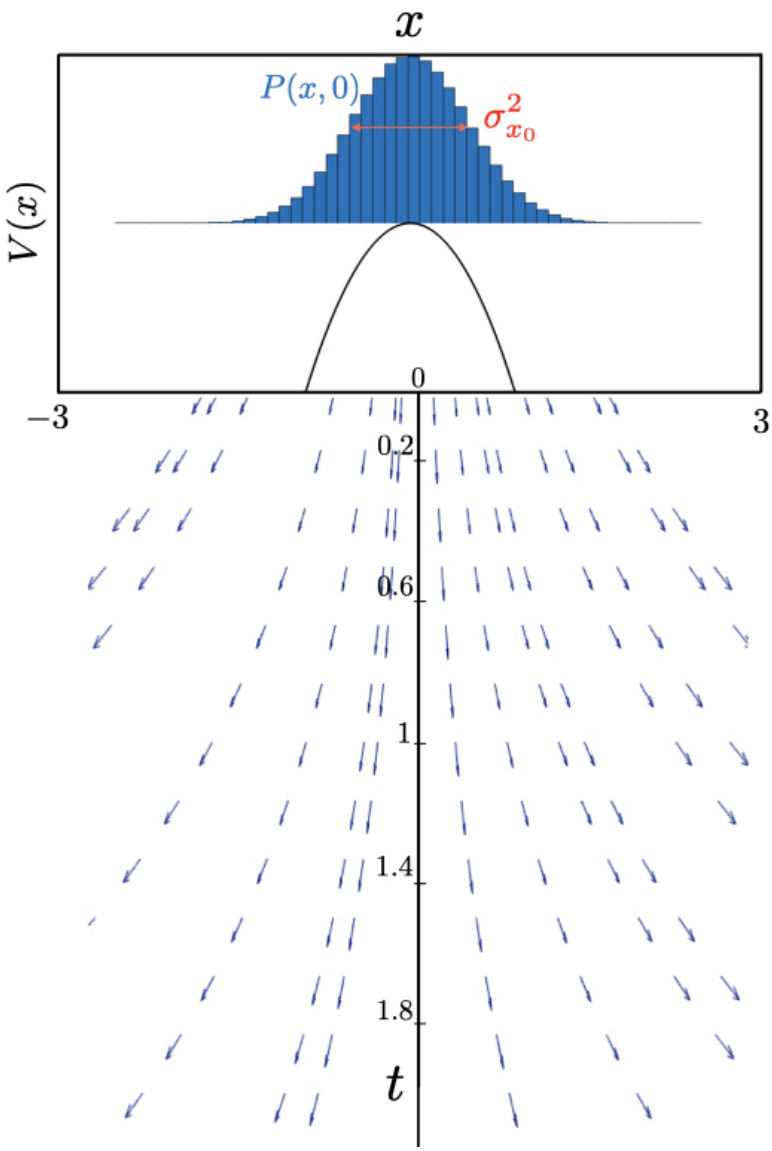

Figure 2.5: The uncertainty of the initial state in the unstable inverted quadratic potential in the deterministic dynamics.
It shows the exponentially diverging trajectories, as demonstrated in Eq.(2.41). The symmetrical shape of the potential, unbounded on both sides, results in no displacement of mean position $\langle x(t)\rangle$ induced by uncertainty of the initial state $\sigma^2_{x_0}$, as showed in Eq.(2.42).

$\langle x(t)\rangle \approx \langle x_0\rangle(1 + kt/\gamma$, where the potential stiffness k leads to faster diverging trajectories for larger values. Simultaneously, the second moment increases linearly in time $\sigma^2_x \approx \sigma^2_{x_0} + (2T/\gamma + 2k\sigma^2_{x_0}/\gamma)$, leading to a decreasing SNR from its initial value at $t = 0$ of $|\langle x_0\rangle|/\sigma_{x_0}$.

2.3.2 Low Friction Limit

In the limit of low friction, the equation of motion can be described by

$$\ddot{x} = -\gamma\dot{x} + \omega_0^2 x + \sqrt{2D_{UD}}\xi(t), \tag{2.48}$$

which deterministic solutions are exponentially diverging position x, velocity $\dot{x}$ and acceleration $\ddot{x}$

$$x(t) = a\Gamma^+ + b\Gamma^-, \tag{2.49}$$
$$\dot{x}(t) = a\frac{(-\gamma+\omega_d)}{2}\Gamma^+ - b\frac{(\gamma+\omega_d)}{2}\Gamma^-, \tag{2.50}$$
$$\ddot{x}(t) = a\frac{(-\gamma+\omega_d)^2}{4}\Gamma^+ + b\frac{(\gamma+\omega_d)^2}{4}\Gamma^-, . \tag{2.51}$$
$$a = \left[\frac{x_0}{2}\left(1+\frac{\gamma}{2\omega_d}\right) + \frac{\dot{x}_0}{\omega_d}\right], \tag{2.52}$$
$$b = \left[\frac{x_0}{2}\left(1-\frac{\gamma}{2\omega_d}\right) - \frac{\dot{x}_0}{\omega_d}\right]. \tag{2.53}$$

where $\Gamma^\pm = e^{(-\gamma\pm\omega_d)t/2}$ describes the amplification gain Γ^+, and attenuation loss Γ^- . For initial conditions drawn from a Gaussian distribution centered at $\langle x_0\rangle$, $\langle\dot{x}_0\rangle$ with non-zero variances $\sigma^2_{x_0}$,$\sigma^2_{\dot{x}_0}$ the correspondent first moments evolve as

$$\langle x(t)\rangle = \langle a\rangle\Gamma^+ + \langle b\rangle\Gamma^-, \tag{2.54}$$
$$\langle\dot{x}(t)\rangle = \langle a\rangle\frac{(-\gamma+\omega_d)}{2}\Gamma^+ - \langle b\rangle\frac{(\gamma+\omega_d)}{2}\Gamma^-, \tag{2.55}$$
$$\langle\ddot{x}(t)\rangle = \langle a\rangle\frac{(-\gamma+\omega_d)^2}{4}\Gamma^+ + \langle b\rangle\frac{(\gamma+\omega_d)^2}{4}\Gamma^-. \tag{2.56}$$
$$\langle a\rangle = \left[\frac{\langle x_0\rangle}{2}\left(1+\frac{\gamma}{\omega_d}\right) + \frac{\langle\dot{x}_0\rangle}{\omega_d}\right], \tag{2.57}$$
$$\langle b\rangle = \left[\frac{\langle x_0\rangle}{2}\left(1-\frac{\gamma}{\omega_d}\right) - \frac{\langle\dot{x}_0\rangle}{\omega_d}\right]. \tag{2.58}$$

In the short time dynamics, where Γ^+,Γ^- are comparable, the mean position of Eq.(2.54), evolves quadratically in time $\langle x(t)\rangle \approx \langle x_0\rangle + \langle\dot{x}_0\rangle t + (-4\langle\dot{x}_0\rangle\gamma + \langle x_0\rangle(-\gamma^2+\omega_d^2))t^2$. Contrastingly, velocity and acceleration Eqs.(2.55),(2.56), display a linear time-evolution, respectively $\langle\dot{x}(t)\rangle \approx \langle\dot{x}_0\rangle + (-4\langle\dot{x}_0\rangle\gamma + \langle x_0\rangle(-\gamma^2+\omega_d^2))t$, and $\langle\ddot{x}(t)\rangle \approx (-4\langle\dot{x}_0\rangle\gamma + \langle x_0\rangle(-\gamma^2+\omega_d^2)) +$

$(\langle \dot{x}_0 \rangle (3\gamma^2 + \omega_d^2) - \langle x_0 \rangle \gamma(-\gamma^2 + \omega_d^2))t$.

Comparing the short time evolution above with that of the overdamped approximation of Eq.(2.46), one notices that the former exhibits a dependency on the geometry of the potential at the second order in time.

In the long time evolution, $\Gamma^+ \gg \Gamma^-$, and the dynamics of Eqs.(2.54)-(2.56) can be further simplified by dropping the negative exponential Γ^-. Furthermore, the term $((\pm\gamma + \omega_d)/2)^n$ can be approximated to $\approx \omega_d^n$.

Simultaneously the variances approach

$$\sigma_x^2(t) = \mathrm{Var}[a]\Gamma^{+2} + \mathrm{Var}[b]\Gamma^{-2} - e^{-\gamma t}\mathrm{Var}[2ab] + \langle (\Delta x_\xi(t))^2 \rangle, \tag{2.59}$$

$$\sigma_{\dot{x}}^2(t) = \mathrm{Var}[a]\frac{(-\gamma + \omega_d)}{2}\Gamma^{+2} - \mathrm{Var}[b]\frac{(\gamma + \omega_d)}{2}\Gamma^{-2} - \gamma e^{-\gamma t}\mathrm{Var}[2ab] + \langle (\Delta \dot{x}_\xi(t))^2 \rangle, \tag{2.60}$$

$$\sigma_{\ddot{x}}^2(t) = \mathrm{Var}[a]\frac{(-\gamma + \omega_d)^2}{4}\Gamma^{+2} + \mathrm{Var}[b]\frac{(\gamma + \omega_d)^2}{4}\Gamma^{-2} + \gamma^2 e^{-\gamma t}\mathrm{Var}[2ab] + \langle (\Delta \ddot{x}_\xi(t))^2 \rangle, \tag{2.61}$$

$$\mathrm{Var}[a] = \left[\frac{\sigma_{x_0}^2}{4}\left(1 + \frac{2\gamma}{\omega_d} + \frac{\gamma^2}{\omega_d^2}\right) + \frac{\sigma_{\dot{x}_0}^2}{\omega_d^2}\right], \tag{2.62}$$

$$\mathrm{Var}[b] = \left[\frac{\sigma_{x_0}^2}{4}\left(1 - \frac{2\gamma}{\omega_d} + \frac{\gamma^2}{\omega_d^2}\right) + \frac{\sigma_{\dot{x}_0}^2}{\omega_d^2}\right], \tag{2.63}$$

$$\mathrm{Var}[2ab] = \frac{4\sigma_{\dot{x}_0}^2 + \sigma_{x_0}^2(\gamma^2 + \omega_d^4)}{2\omega_d^2}. \tag{2.64}$$

The noise terms $\langle (\Delta x_\xi(t))^2 \rangle$, $\langle (\Delta \dot{x}_\xi(t))^2 \rangle$, and $\langle (\Delta \ddot{x}_\xi(t))^2 \rangle$ are obtained from Eqs.(2.29)-(2.31) with hyperbolic sine and cosine functions [186].

In the short time evolution, the variances of position and velocity increase quadratically in time, respectively $\sigma_x^2 \approx Tt^2$ and $\sigma_{\dot{x}}^2 \approx T + (-9\gamma^2 + \omega_d^2)Tt^2/4$ (for vanishing $\sigma_{x_0}^2$). In the overdamped regime, the short time dynamics produces a linear time evolution of Eq.(2.47).

The variance of acceleration, contrarily, exhibits an initial decrease linear in time, followed by a quadratic increase in time $\sigma_{\ddot{x}}^2 \approx \gamma^2 T - (4\gamma^2 + \omega_d^2)\gamma Tt/2 + (17\gamma^4 + 14\gamma^2\omega_d^2 + \omega_d^4)Tt^2/16$.

The SNR for position, velocity and acceleration initially increase from $|\langle x_0 \rangle|/\sigma_{x_0}$ and subsequently saturates to asymptotic $\mathrm{SNR}_{t->\infty} = (2\langle \dot{x}_0 \rangle + \langle x_0 \rangle(\gamma + \omega_d))/\sqrt{4\sigma_{\dot{x}_0}^2 + \sigma_{x_0}^2(\gamma + \omega_d)^2}$. A comparison of SNR, see Fig.2.6, exhibits for the low friction regime (left panel) a larger SNR for all quantities compared to that of the damped oscillator of Fig.2.2 (left panel), where the

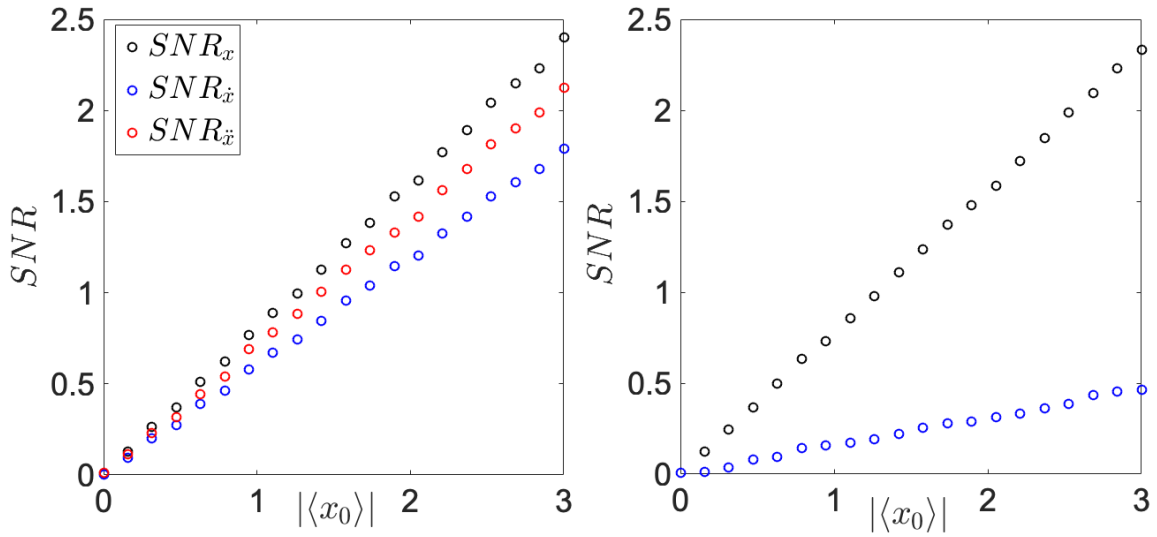

Figure 2.6: SNR ***as a function of initial position*** $|\langle x_0 \rangle|$ ***in the inverted quadratic potential.***
Left panel: evolution of SNR *in the low friction limit, as per Eq.*(2.48) *with a quality factor* $Q = \omega_0/\gamma$ *of* $Q = 10$*, for particle position (black), instantaneous velocity (blue) and acceleration (red). The main effect is not anymore primarily on velocity (as in Fig.2.2, left panel), but position and acceleration* SNR*s are enhanced by the instability of the inverted quadratic potential.*
Right panel: evolution of SNR *in the high friction limit, as per Eq.*(2.48) *with a quality factor* $Q = \omega_0/\gamma$ *of* $Q = 0.1$*, for particle position (black), and average velocity* $\bar{v}$ *(blue). The instability of the inverted quadratic potential enhanced the motion of position, leading to a larger* SNR *than that of Fig.2.3.*
The environmental temperature $T = 1$*, together with a time step of* $dt = 10^{-5}$ *have been used to generate* $nt = 10^4$ *trajectories with a sample size of* $N = 5000$ *evolving for* $t = 5$*. The initial conditions were drawn from a Gaussian distribution with* $\sigma^2_{x_0} = 1$*,* $\sigma^2_{\dot{x}_0} = k_B T$*, and* $\langle \dot{x}_0 \rangle = 0$*.*

position SNR_x (black) and acceleration $\text{SNR}_{\ddot{x}}$ (red) signal to noise ratios are less pronounced. Similarly, for the high friction limit (right panel), the position SNR (black) increases faster for larger displacement $|\langle x_0 \rangle|$ than that of Fig.2.3 (left panel).

2.4 Conclusions

Throughout this chapter, the quadratic optical potential has been considered, and its dynamics in the low and high friction regime has been unveiled.

The free particle motion showed, through Fig.2.1, the difference between the ballistic timescale ($t \ll \gamma$) in which variance of position evolves $\sigma_x^2 \propto t^2$, and the diffusive($t \gg \gamma$) in which $\sigma_x^2 \propto t$. For the reason above, the non-inertia approximation (overdamped regime), which lacks of the

term $\sigma_x^2 \propto t^2$ at short time scale, does not have instantaneous velocity $\dot{x}$ and acceleration $\ddot{x}$, but only the average quantities $\langle \bar{v} \rangle$ and $\langle \bar{a} \rangle$ survive.

Once the trap geometry has been taken into consideration, specifically $V(x) \propto x^2$, the focus shifted onto realising the regime under which the SNR could increase, comparing the damped harmonic potential Eq.(2.11) with the driven system Eq.(2.22). Both high and low friction regimes were discussed, exhibiting a primary effect on instantaneous velocity (faster SNR) for the low friction regime, which is then realised also in position for the driven oscillator Fig.2.2. In the strong damping regime, the main effect is displayed by mean position $\langle x \rangle$ (larger SNR), not ameliorated by the driving Fig.2.3 (black). Although instantaneous velocity $\dot{x}$ disappears in the regime of strong damping, the mean average velocity $\langle \bar{v} \rangle$ (blue) still exhibits a shift induced by initial position (left) and by driving force strength F_0 (right), although less pronounced.

Lastly, the dynamics in the inverted quadratic potential has been introduced and discussed with the focus on the role of instability, which generates exponentially diverging dynamics Fig.2.4. The instability, together with the symmetry of the potential (being unbound from both sides), proved to be pivotal in the increase of the particle's standard deviation for increased uncertainty of the initial state, without creating mean displacement, Fig.2.5.

To quantify the dynamics the SNR has been employed, showing the role of the instability which enhanced the dynamics of both position $\langle x \rangle$ and acceleration $\langle \ddot{x} \rangle$ in the low friction regime (Fig.2.6, left panel).

Still, the unstable dynamics of the inverted quadratic potential amplifying the position or speed is linear, and hence noise-induced displacement phenomena are not possible The natural question arises as to what new noise-induced effects can come from the unstable nonlinear potentials, and whether the performances of the noise-driven oscillator can be reached. A paradigmatic example is when the particle is initially placed at equilibrium in a quadratic potential without any external drive, and the potential is suddenly swapped to a cubic profile without any linear or quadratic terms. The particle becomes out-of-equilibrium at initial moment, similarly as the external force or inverted quadratic potential, but now the dynamics is highly nonlinear.

In the next chapter such questions are explored, by means of noise-driven features typical of nonlinear systems.

Chapter 3

Theory of Stochastic Dynamics in Cubic Potential

3.1 Overdamped Regime

3.1.1 Stability and Divergence

Nonlinear stochastic dynamics is qualitatively different with new opportunities.

To begin, let us consider a nonlinear time-invariant dynamical system, such as

$$\dot{x} = -\kappa x^2, \tag{3.1}$$

where $\kappa = k/\gamma$ is the normalised cubic potential stiffness. Without solving the equation of motion, one can retrieve information about the dynamics of the system by looking for stability of fixed points [187]. To do so, it is required to look at the vanishing conditions of the right hand side of the equation of motion, which for Eq.(3.1) results in an fixed point at $x_e = 0$. Its properties are assessed by investigating the behavior introduced by a small perturbation ϵ in the initial conditions around the fixed point $x_e = 0$ to the dynamics. When the perturbation keeps the system close to the fixed point $|x(t) - x_e| < \epsilon$, $\forall t > 0$, it can be labelled as a stable point [187], condition that is met only for positive positions in Eq.(3.1). Contrarily, for negative $x(t)$, the dynamics is quickly met by divergent trajectories, labelling the fixed point as unstable

from the left. This difference in stability is illustrated in Fig.3.1 by the half full (black)/ half empty (white) circle at $x_e = 0$.

Despite the unidirectional flow to the left, there exist trajectories which survive the strong divergence of the cubic potential. To further characterise this peculiar stability, a convergence condition i.e., $\lim_{t\to\infty} |x(t) - x_e| = x_e$ can be investigated showing that a deterministic trajectory of a particle in cubic potential, starting from the right of the fixed point $x_e = 0$, asymptotically converges to the fixed point $x_e = 0$ therefore avoiding the divergence. A complementary method, not always feasible in nonlinear systems, that leads to the same conclusion drawn in Fig.3.1 requires the analytical solution of the equation of motion, which for Eq.(3.1) leads to [143]

$$x(t) = \frac{x_0}{1 + \kappa x_0 (t - t_0)}. \qquad (3.2)$$

For positive initial conditions x_0, Eq.(3.2) is asymptotically stable, converging to x_e for longer time, as $\lim_{t\to\infty} x(t)|_{x_0>0} = x_e$, while for negative x_0, $\lim_{t\to\infty} x(t)|_{x_0<0} = -\infty$ it diverges.

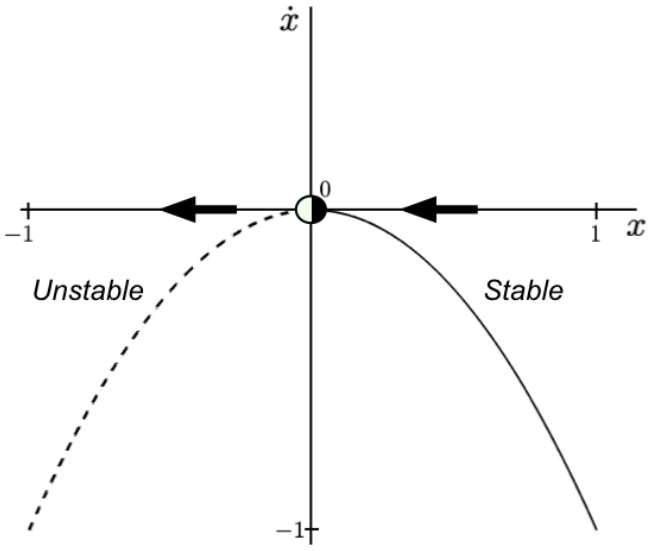

Figure 3.1: Sketch of the vector field of Eq.(3.1). *Used as an investigative tool of the stability of the fixed point $x_e = 0$, it shows how the dynamics is dominated by the fixed point, visible from the flow on a line illustrated by the arrows. The half white half black circle indicates that the fixed point is of the half-stable kind, allowing asymptotically stable solution on the $x > 0$ region, while diverging on the $x < 0$ one, rendering the point $x_e = 0^-$, unstable, and $x_e = 0^+$ stable.*

A new information that arises from Eq.(3.2) is the time scale at which the divergence appears. In fact, a characteristic time $\tau_d = 1/(\kappa|x(t_0)|)$, limiting the deterministic dynamics of a particle in cubic potential, exists [143]. In other words, the dynamics can run only for time shorter than τ_d [143, 187].

Imagine now that the initial condition to Eq.(3.1) is a normal random variable with distribution centered at $\langle x(t_0)\rangle = x_e$, with non-zero variance $\sigma^2_{x_0}$, hence $x(t_0)$ can be positive or negative. As

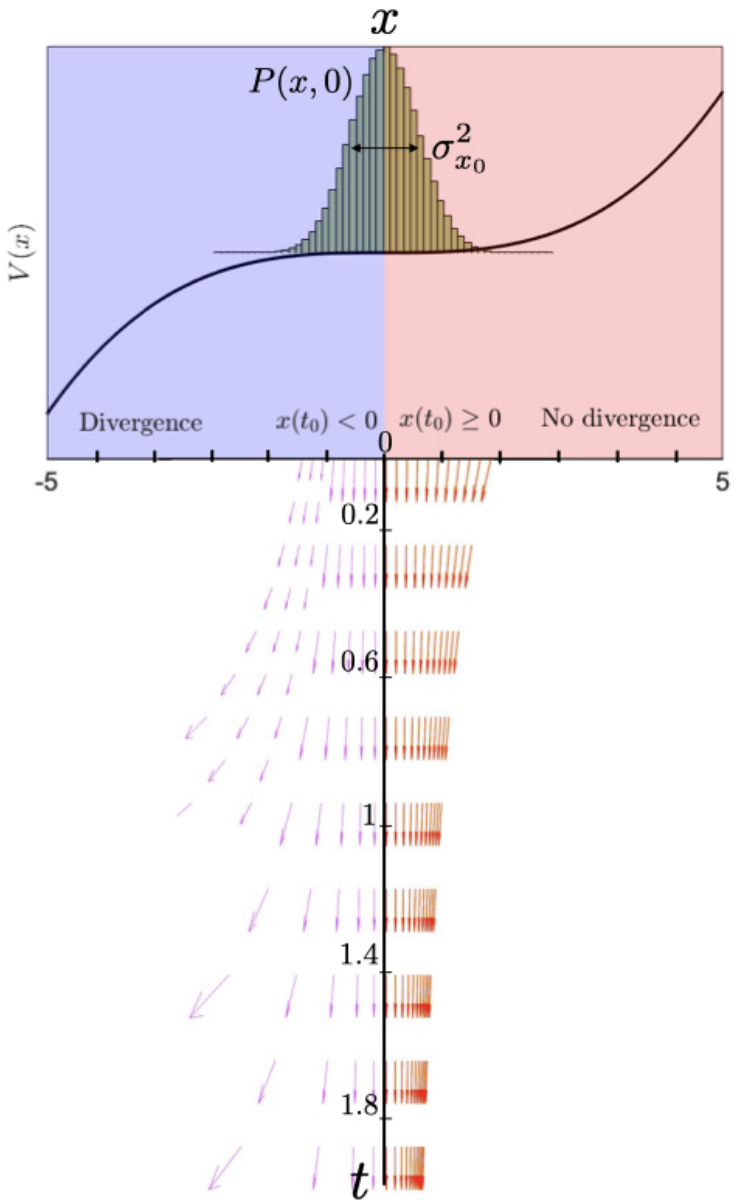

Figure 3.2: The uncertainty of the initial state in the unstable cubic potential. *It defines, in the deterministic dynamics, the important role of the instability, showing first hand the non-linear effect of the noise-induced displacement, due to the symmetrical shape of the potential being bounded on one side (purple region) and unbounded on the other (orange region). The effect is further described in Eq.(3.2), and subsequently in Eq.(3.11).*

illustrated in Fig.3.2, the uncertainty of the initial state enhances the role of the instability, introducing the noise-induced displacement effect (discussed thoroughly in Sec.3.1.2), and showing the fragile evolution against the instability resulting in fast divergence, requiring a short time approach to discuss its features. The divergence encountered in the cubic potential is so strong that, if any trajectory approaches it, the whole ensemble is influenced by it [144]. A better point

of view for the above statement can be viewed by accessing the PDF, solving the Fokker-Planck equation complementary to Eq.(3.1),

$$\partial_t P(x,t) = \kappa \partial_x [x^2 P(x,t)], \tag{3.3}$$

which solution is [143]

$$P(x,t) = \frac{e^{-\frac{\left[\frac{x}{1-\kappa x(t-t_0)} - \langle x(t_0)\rangle\right]^2}{2\sigma_{x_0}^2}}}{\sqrt{2\pi\sigma_{x_0}^2}(1-\kappa x(t-t_0))^2}. \tag{3.4}$$

The above PDF develops heavy tails as time increases, due to the divergent trajectories dragging the mean of particle position to infinity [143].

Ideally the PDF presented in Eq.(3.4) is only valid for times shorter than the divergence time τ_d, after which no moments of particle position can be defined [2, 144].

More precisely, to keep the divergence probability $P_\infty = 1 - \int_{-\infty}^{+\infty} \mathcal{H}(1+\kappa x t) P(x,t) dx$ sufficiently small, the maximal time interval can be bounded by $\tau_{x^3} \approx 1/(\kappa \sigma_{x_0})$ [143]. Introducing the noise term into Eq.(3.1), i.e.,

$$\dot{x} = -\kappa x^2 + \sqrt{2D}\xi(t), \tag{3.5}$$

changes the stability of the system. The noise acts as a forcing term, tilting the cubic potential depending on the sign of $\xi(t)$. In other words, the Langevin noise introduces bifurcations in the saddle node [187]. Rewriting Eq.(3.5) as $\dot{x} = -x^2 + r$, where $r = \sqrt{2D}\xi(t)$ denotes the Langevin force, shows how the sign of r can create or annihilate the fixed point $x_e = 0$. When $r < 0$, the inverted parabola shown in Fig.3.3 (bottom right) moves down, eliminating the fixed point and rendering the whole dynamics unstable. When $r > 0$, the inverted parabola of Fig.3.3 (bottom left) moves up splitting the fixed point into two; a stable one (black circle) for positive positions, and an unstable one (white circle) for negative ones.

3.1.2 Noise-Induced Displacement

Operating at short time scales, $t - t_0 < \tau_\infty^0$ the evolution of moments of the stochastic particle position can be calculated directly by numerical integration of the PDF in Eq.(3.4) by $\langle x^n \rangle = \int_{-\infty}^{+\infty} x^n P(x,t) dx$. Neglecting the diffusion, the short time evolution of moments of particle

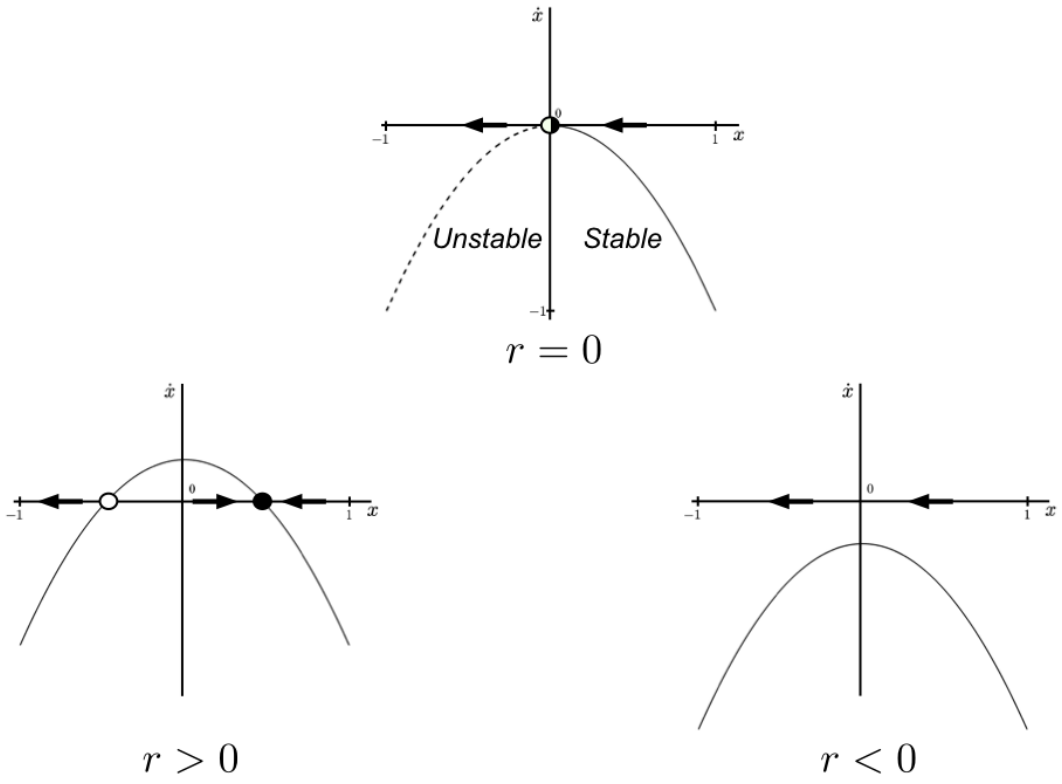

Figure 3.3: Sketch of the vector field for Eq.(3.5), illustrating the bifurcation induced by the Langevin noise.
For negative values of the Langevin force, $r < 0$ (right panel) the dynamics shows divergent inclinations $\forall x$ as the downward movement of the inverted parabola annihilates the fixed point. Simultaneously, for $r > 0$ (left panel) the inverted parabola moves upwards, creating new fixed points preserving instability (white circle) for negative positions, and generating a stable point (black circle) for positive positions, revealing non trivial dynamics around the plateau area, thoroughly discussed in Sect.3.1.4

position can be approximated by expanding Eq.(3.4) in time, obtaining [143]

$$\langle x(t)\rangle \approx \langle x_0\rangle - \kappa(t-t_0)(\sigma_{x_0}^2 + \langle x_0\rangle^2), \tag{3.6}$$

$$\sigma_x \approx \sqrt{\sigma_{x_0}^2 - 4\kappa(t-t_0)\langle x_0\rangle\sigma_{x_0}^2}, \tag{3.7}$$

From Eq.(3.6) it can be noticed that, even at $\langle x_0\rangle = 0$, the mean of particle position undergoes an initial noise-induced drift, while the standard deviation σ_x of Eq.(3.7) remains unchanged for the short time dynamics. The latter well demonstrates the noise-induced displacement effect in the dynamics of a particle in cubic potential [143].

The first witness of noise-to-signal transition embedded in Eq.(3.6) can be quantified by the signal to noise ratio [143, 171]. The SNR can be defined as a ratio between the useful average signal in the motion ($\langle x(t)\rangle$), and its uncertainty

$$\mathrm{SNR} = \frac{|\langle x(t)\rangle|}{\sigma_x}, \tag{3.8}$$

where the numerator represent the coherent part of the displacement, while the denominator consists of the incoherent part of the displacement, illustrating the noise disturbing the motion [143].

The SNR quantifies the quality of the noise-to-signal process and if it grows, the coherent displacement increases faster than the incoherent one, viceversa, when the dynamics is taken over by the noise, the SNR starts to decrease, irrespective of the increasing mean value $\langle x(t)\rangle$ [143]. The turning point of the SNR introduces a new upper-bound to the noise-to-signal transitions, limiting the maximum interval of time more strictly than $\tau_{x^3} = 1/(k\sigma_{x_0})$ [143], as shown in Fig.3.4 as a function of increasing initial thermal noise. Different initial positions, and their signs, induce a time-dependent evolution upon the variance of particle position, without introducing different dynamics on the mean displacement, as shown in Fig.3.5. For positive initial conditions, towards the increasing branch of the

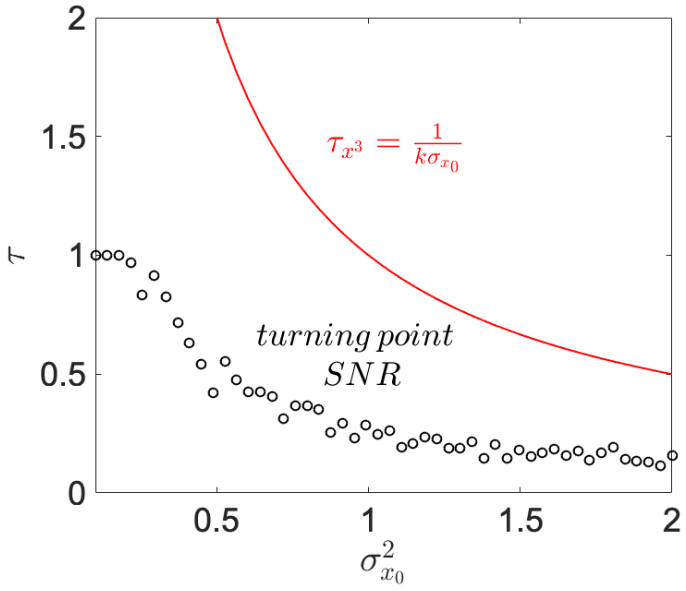

Figure 3.4: Upper bound to the characteristic time of divergence of a particle in cubic potential. *The figure shows how the turning point of the* SNR *introduces a stricter limitation to the characteristic time of divergence of a particle evolving in the cubic potential. When the* SNR *drops, the second moments increases faster the the signal $\langle x\rangle$, and no information is bared by the moments. The black curve is obtained fully numerically, and for zero initial variance $\sigma^2_{x_0} = 0$ the particle, placed at $\langle x_0\rangle = 0$ does not move from the saddle point and the divergence time should go to $\tau \to \infty$. $N = 5000$, $dt = 10^{-5}$ and $nt = 1000$ were used.*

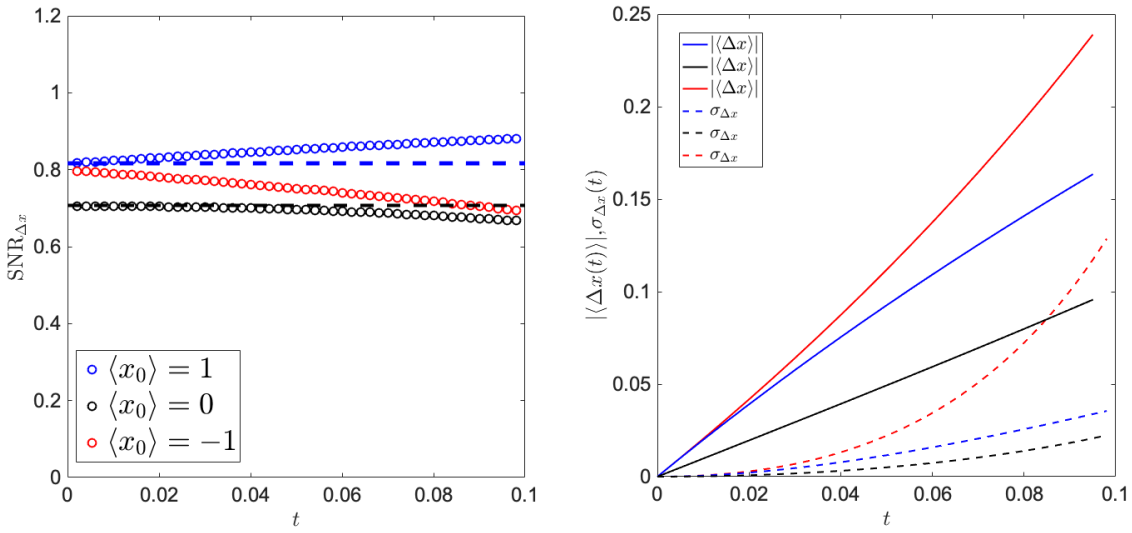

Figure 3.5: Evolution of SNR ***(left) and moments*** $\langle x\rangle, \sigma_x$ ***(right) for different initial positions.***
The figure illustrates the differences between the dynamics in different regions of the cubic potential expressed in terms of relative positions $\Delta x(t) = x(t) - x_0$. *The blue and black dashed line in the left panel are solutions obtained from Eqs.*(3.6),(3.7)
When the particle is initially positioned left of the plateau $\langle x_0\rangle = -1$ *(red), the absolute mean displacement* $|\langle\Delta x\rangle|$ *(red solid) increases much faster than when initially positioned at the plateau* $\langle x_0\rangle = 0$ *(black). Similarly its standard deviation (red dashed) increases much faster, leading to a decreasing* SNR *(red dots). Higher order nonlinear terms, beyond the approximation of Eqs.*(3.6),(3.7)*, dominate the dynamics left the inflection point.*
A particle initially positioned right of the plateau $\langle x_0\rangle = 1$ *(blue), however, exhibits a growing* SNR *(blue dots) for the short time dynamics (while trajectories are far away from the divergence). Its correspondent mean* $|\langle\Delta x\rangle|$ *(blue solid) and standard deviation* $\sigma_{\Delta x}$ *(blue dashed), although increasing faster than a particle initially positioned at the plateau (black), evolve quicker in the mean displacement, hence generating a growing* SNR. *At later times* $t > 0.2$, *when the divergence becomes relevant, it too starts to decrease, as the standard deviation grows faster than the mean. For this figure, Eq.*(3.5) *has been simulated, using* $\sigma^2_{x_0} = 1, D = 0, dt = 10^{-5}, k = 1,$ *and* $nt = 1000$ *trajectories were used*

cubic potential, the variance decreases in time as the particle moves towards the plateau (blue line), after which it starts to feel the divergence and the variance starts to increase, resulting in a drop of the SNR. Simultaneously, for negative initial conditions (black line), the particle is located at the slide of the cubic potential, where the divergence is strongly felt, and the variance increases in time, faster than the the mean displacement, resulting in a faster drop of the SNR.

To investigate the role of the environmental noise in the noise-to-signal process, one can consider $D \neq 0$ in Eq.(3.5). The stochastic dynamics generated, can still be discussed in the short time regime ($t - t_0 < \tau^0_\infty$), and compared to the previous case. We assume that the initial conditions

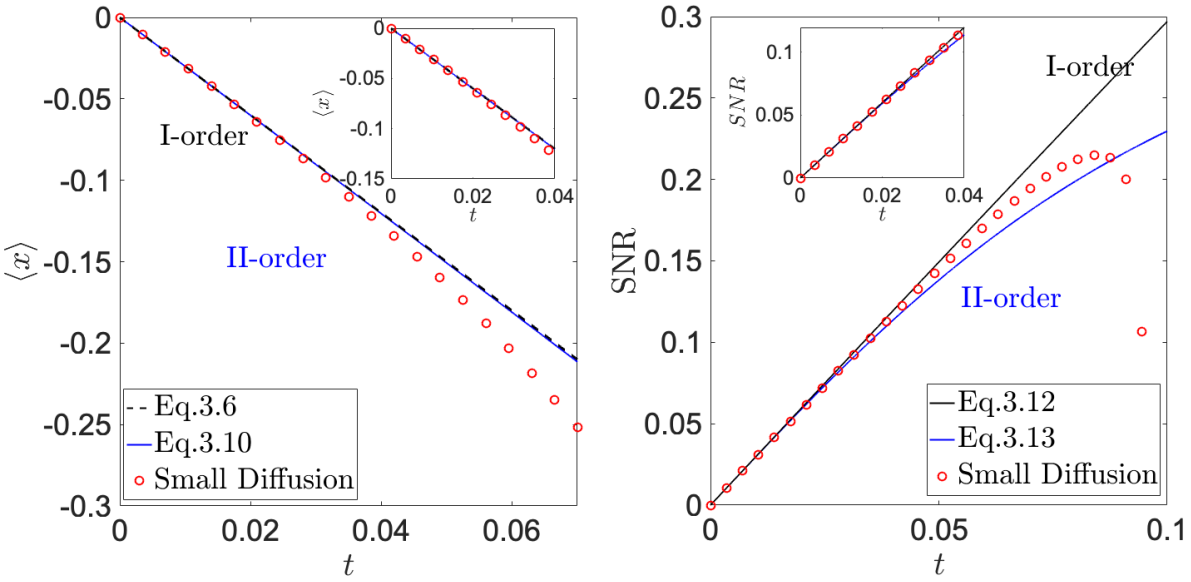

Figure 3.6: Comparison of first (black) and second (blue) order solution of mean position (Eq.(3.6),(3.10)) for short time dynamics (inset) and longer time dynamics simulation (red dots) of mean position (left panel) and SNR ***(Eqs.(3.12),(3.13)) (right panel) in the regime of small diffusion.***
On the left panel it is shown how for a regime of small diffusion, $D = 0.1$ the first (black) and second order (blue) match well together and fit nicely with the short time dynamics (red dots in inset). Simultaneously, on the right panel the SNR *for short time (inset) shows how impactless the Langevin force is upon the standard deviation σ_x, demarcating a* SNR *powered by the initial position noise, as described by Eq.(3.12).*
Note how the second order solution (blue), while it does not overestimate the SNR *for short time dynamics, it is still not able to predict its drop.*
For this figure, Eq.(3.5) has been simulated, using $k = 3, D = 0.1, \sigma_{x_0}^2 = 1, dt = 10^{-5}$, and 1000 trajectories were generated

will be drawn from a Gaussian distribution with mean and standard deviation defined, and we integrate Eq.(3.5), obtaining [143]

$$x(t_n) = x(t_0) - \kappa \int_{t_0}^{t_n} x(t_{n-1})^2 dt_{n-1} + \sqrt{2D} \int_{t_0}^{t_n} \xi(t_{n-1}) dt_{n-1}, \tag{3.9}$$

for the n^{th} order in time; and subsequently take the ensemble average, to obtain

$$\langle x(t) \rangle = \langle x(t_0) \rangle - \kappa(\sigma_{x_0}^2 + \langle x_0 \rangle^2)(t - t_0) - \kappa D(t - t_0)^2, \tag{3.10}$$

$$\sigma_x = \sqrt{\sigma_{x_0}^2 + 2D(t - t_0) + 8\kappa^2(t - t_0)^2 \sigma_{x_0}^4}, \tag{3.11}$$

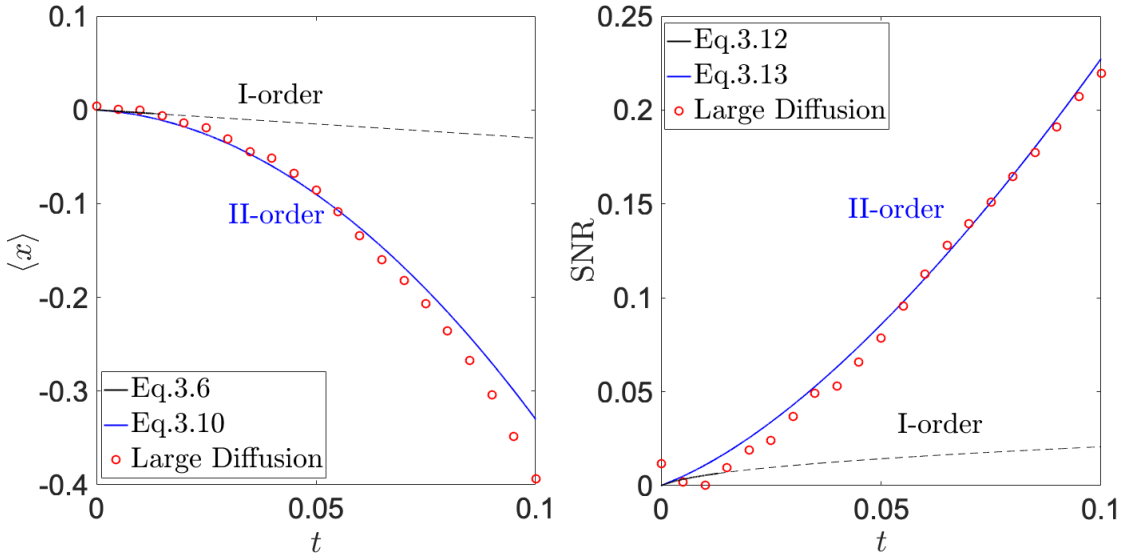

Figure 3.7: Comparison of first (black) and second (blue) order solution of mean position (Eqs.(3.6),(3.10)) (left panel) and SNR ***(Eqs.(3.12),(3.13)) (right panel) and numerical simulations (red), in the regime of dominant diffusion.***
On the left panel, it is shown the divergence between the two order solutions for the case of $D = 10$ *(large diffusion), showing on the right panel how impactful the role of the environmental noise is for the standard deviation* σ_x*, leading to a* SNR *increasing quadratically in time as discussed in Eq.(3.13), clearly demarcating a* SNR *powered by environmental noise.*
For this figure Eq.(3.5) has been simulated, using $k = 3, D = 10, \sigma_{x_0}^2 = 0.1, dt = 10^{-5}$*, and* $nt = 1000$ *trajectories were generated*

at the second order approximation in time [143].

At the first order approximation, Eq.(3.10) shows a first moment evolving linearly in time, where the initial second moment gets transformed to mean displacement, and the Langevin noise does not affect the motion. The latter describes the deterministic motion presented in Eq.(3.6). Simultaneously, the second moment of position does not feel the cubic nonlinearity, as it is independent of the stiffness k, and it evolves analogously to pure diffusion of a free particle. At the second order approximation, necessary for negligible initial thermal noise, the thermal noise introduces a quadratic term in time that transforms environmental noise into displacement. Simultaneously the variance evolves with free diffusion when the initial thermal noise is neglected, as the term linear in time is the only leading term. The environmental noise can dominate the dynamics if [143] $D(t - t_0) \gg \sigma_{x_0}^2$. The above inequality introduces a new characteristic time [143], $\tau_D = \sigma_{x_0}^2/D$, which can be used to define the regime where the dynamics becomes dominated by diffusion. To further justify the noise-to-signal transitions

observed from Eq.(3.10), it is instructive to examine the SNR in the regime of weak diffusion, presented in Fig.3.6, and for the strong diffusion regime, Fig.3.7.

For the weak diffusion regime, defined by $t - t_0 \ll \tau_D$, the environmental noise is negligible, and the SNR reaches [143]

$$\mathrm{SNR}(t) \propto \kappa\sigma_{x_0}(t - t_0), \tag{3.12}$$

where it can be seen that it evolves linearly in time, and it is powered by the initial thermal noise, as shown in Fig.3.8(left), quantifying the noise supplying the transitions. Simultaneously, for the strong diffusion regime, $t - t_0 \gg t_D$, the SNR reaches [143]

$$\mathrm{SNR}(t) \propto \frac{\sqrt{2}}{2}\kappa\sqrt{D}(t - t_0)^{3/2}, \tag{3.13}$$

which increases faster in time, for large t, than the SNR in Eq.(3.12), as the system is continuously supplied with energy due by the Brownian noise, and it is as well powered by the environmental noise, as shown in Fig.3.8 (right). In a real experimental environment the SNR can be powered by both initial thermal noise, and Brownian environmental noise [143, 171].

3.1.3 Average Velocity

A further insight on the dynamics of a particle in the cubic potential can be obtained by exploring the noise-induced effect of the average velocity. From the equation of motion $\dot{x} = -\kappa x^2 + \sqrt{2D}\xi(t)$, one can calculate the average velocity as $\langle\bar{v}\rangle = \Delta x/\Delta t$. For the short time dynamics, i.e. while Eq.(3.6) is still valid, it comprises of constant evolution in time, and an initial position noise dependence as follows

$$\langle\bar{v}\rangle = \left\langle\frac{\Delta x}{\Delta t}\right\rangle \approx -\kappa\sigma_{x_0}^2, \tag{3.14}$$

$$\sigma_{\bar{v}} \approx \sqrt{2\kappa^2\sigma_{x_0}^4 + 2D}, \tag{3.15}$$

$$\mathrm{SNR}_{\bar{v}} = \frac{|\langle\bar{v}\rangle|}{\sigma_{\bar{v}}} \approx \frac{1}{\sqrt{2\left(1 + D\kappa^{-1}\sigma_{x_0}^{-2}\right)}}. \tag{3.16}$$

When the evolution time is beyond the short time approximation, the convergence of $\bar{v}$ is lost and the above result is not valid any longer (see Fig.3.9, blue dots).

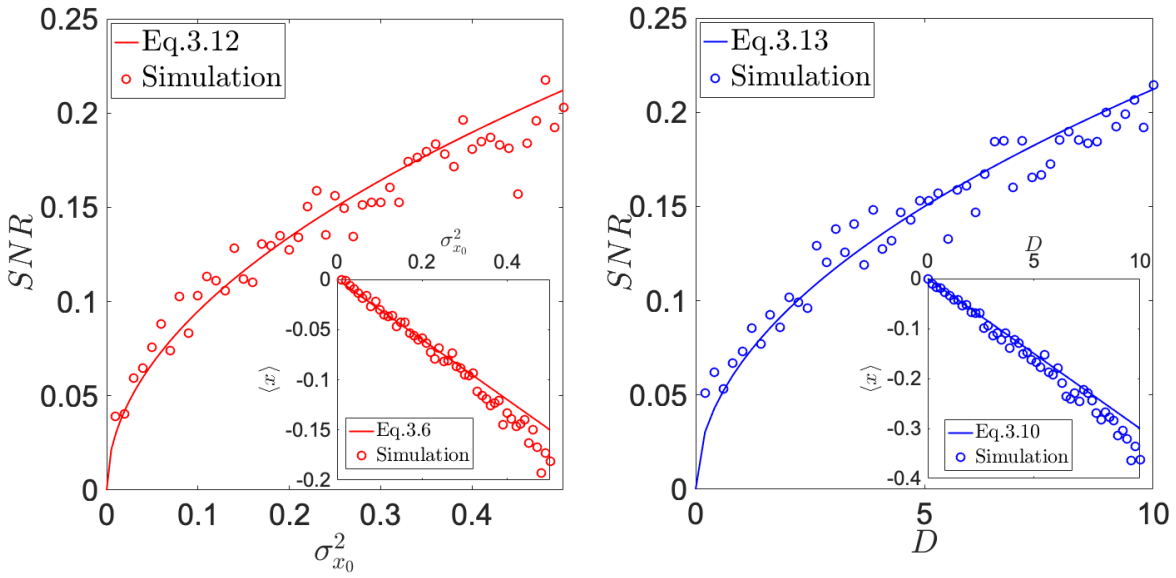

Figure 3.8: Noise-to-signal transitions powered by initial noise (left), and environmental noise (right) of a particle in cubic potential, and mean displacement evolution in both regimes (inset).
Comparing the evolution of SNR *from the left and right panel demonstrates that the latter can be powered by both quantities, and being the environmental noise-driven* SNR *continuously supplied with energy (right panel) for short time dynamics it increases slower than the* SNR *powered by initial position noise (left panel). For this figure, Eq.*(3.5) *has been simulated, using, for the left picture,* $t = 0.1, D = 0, dt = 10^{-5}, k = 3$, *and for the right one,* $\sigma^2_{x_0} = 0, t = 0.1, dt = 10^{-5}, k = 3$. 5000 *trajectories were generated*

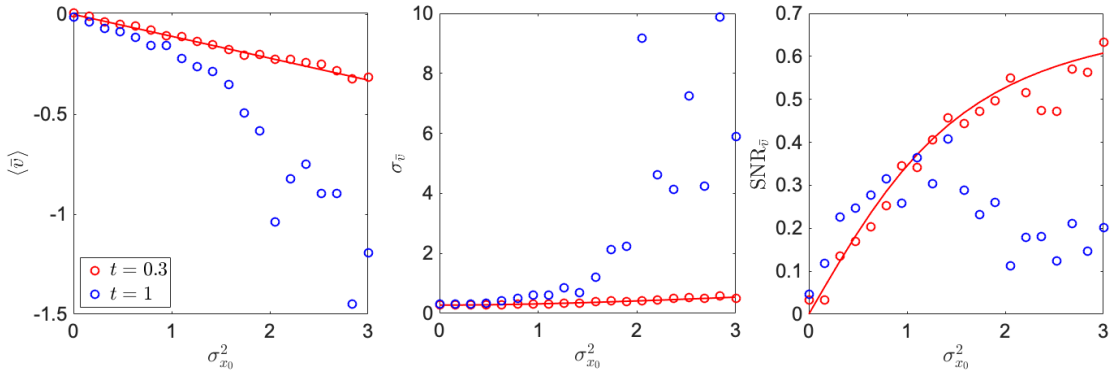

***Figure 3.9: Noise-induced average velocity statistics for short time (red), and long time (blue) evolution. The red line corresponds to the analytical result of Eqs.*(3.14)-(3.16).**
It is shown that even at short time dynamics (red), the average velocity is driven by initial position noise. For this figure, Eq.(3.5) *has been simulated, using* $D = 10^{-3}$, $dt = 10^{-5}$, $k = 0.1$. $nt = 10^4$ *trajectories were generated. The* Δt *chosen to compute the average velocity* $\bar{v}$ *is* $\Delta t = 200dt$.

However, for the short time dynamics (Fig.3.9, red dots), the simulation fits well with the approximation of Eqs.(3.14)-(3.16) (red). From the above equation for $\mathrm{SNR}_{\bar{v}}$ it can be seen that

for $D \ll \kappa^2\sigma_{x_0}^4$ the environmental temperature plays a negligible role, resulting in a constant signal-to-noise ratio of $1/\sqrt{2}$. Although the main noise-induced effect lies in the statistics of particle position, the knowledge of average velocity paves the way towards the underdamped regime, where instantaneous velocity becomes the principal quantity, together with instantaneous acceleration, to feel the noise-induced effect, and the instability. We will then show how in the high friction regime of the underdamped evolution one retrieves the same results as of Eqs.(3.14)-(3.16) (see Fig.3.16, green dots).

3.1.4 Dynamics of Most Probable Trajectory

From the previous discussion and results, there are two take home messages. In the cubic potential, there is a noise-induced displacement effects that uses environmental fluctuations to generate useful mechanical work [2, 143]. Moreover, another essential ingredient to witness the effect is hidden in the instability, a resource that can be positively exploited but that can be dangerous for the system as it leads to divergences and renders description of dynamics by global statistical moments useless [2, 144]. Fig.3.10 summarises the main features investigated in the cubic potential, showing not only the generation of heavy tails towards the divergence, dominating the flow of $\langle x \rangle$, and σ_x dynamics, culprit of the drop of SNR, but also the experimentally not observable light tails generated by the cubic wall. To go beyond the divergence limitation of particle dynamics, one has to find a different, yet measurable, quantity, as shown in the illustration 3.10 by the atypical dynamics in the plateau region (green lines). The experimentally motivated choice [87], falls on the characterisation of the most probable particle position described by the maximum of $P(x,t)$, to substitute the mean value, exploiting the dynamics of the particle around the plateau region, subjected to an uncertainty characterised by the curvature around [188].

The method grants a coherent picture near the instability for particle positions that have little or no information about the diverging trajectory in the system [2]. The quantification of the dynamics is still done by the signal to noise ratio, written now for the maximum of the distribution x_{max}, and the curvature around it σ^2_{max},

$$\mathrm{SNR}(t) = \frac{x^2_{max}(t)}{\sigma^2_{max}(t)}, \tag{3.17}$$

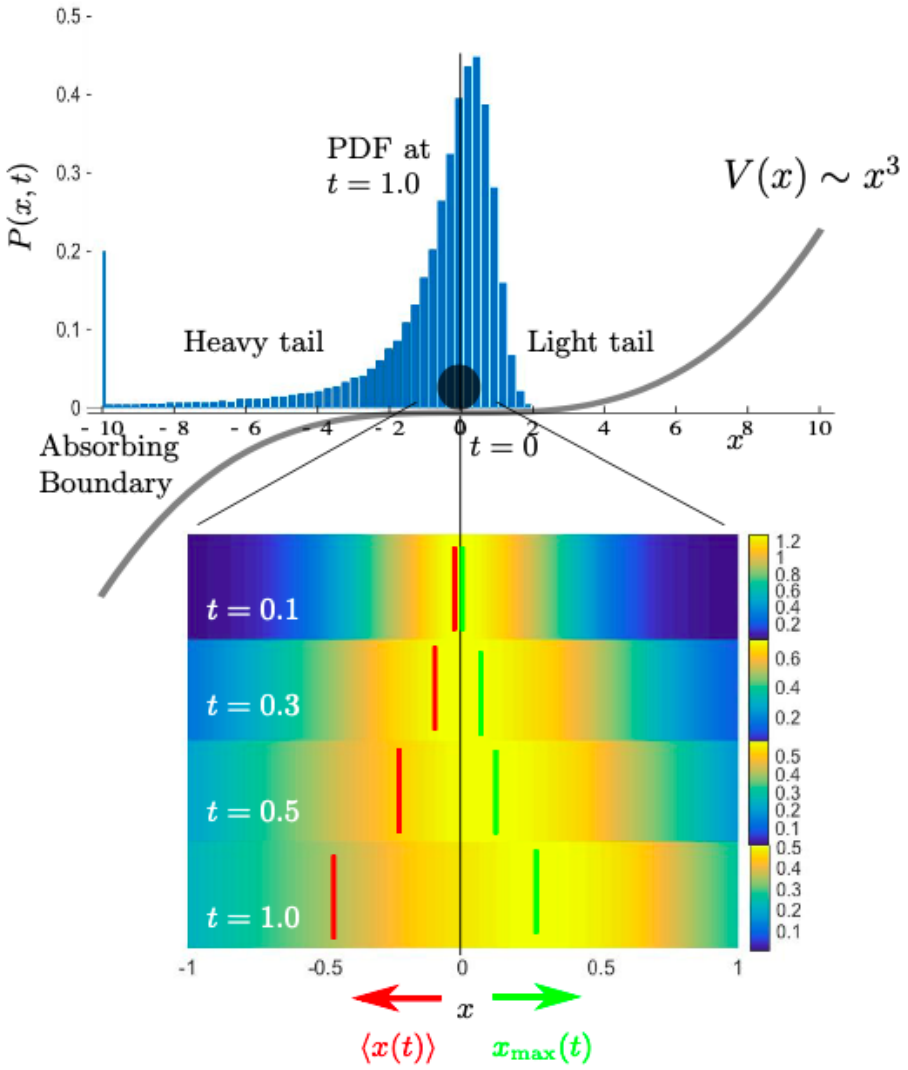

Figure 3.10: Characteristics of the unstable dynamics of a Brownian particle in cubic potential [2].
The most prominent feature of such dynamics lies in the heavy tail (for negative positions) generated by diverging trajectories. Such characteristic has rendered impossible to fully define the dynamics past the point of divergence, and hence the maximum x_{max} and curvature $\sigma^2_{x_{max}}$ of the PDF is introduced ((3.18), (3.19)). Their dynamics consists of a unique property of atypical motion against the potential force (green) that survives the divergence, opposite to the mean position (red).

where x_{max} is calculated by looking at the zero point of the derivative of the PDF, $\partial_x P(x,t) = 0$, leading for deterministic dynamics, to [2]

$$x_{max}(t) = \frac{1}{\kappa t} + \frac{1 + \langle x_0 \rangle \kappa t - \sqrt{(1 + \langle x_0 \rangle \kappa t)^2 + 8\sigma^2_{x_0}(\kappa t)^2}}{4\sigma^2_{x_0}(\kappa t)^3}, \tag{3.18}$$

and the local curvature at the maximum is defined as [2]

$$\sigma^2_{max}(t) = \frac{P(x_{max}(t), t)}{|\partial^2_x P(x_{max}(t), t)|}. \tag{3.19}$$

To better understand the origin of the most probable particle position, one can imagine a trajectory starting from x_0 that follows the deterministic dynamics $x(t) = x_0/(1 + x_0\kappa t)$. A trajectory initially starting on the right of the inflection point, converges to the origin as $x(t) \approx 1/\kappa t$ [2], while a trajectory starting on the left diverges. The trade-off between the two evolution leads to a plethora of behaviors of local characteristics that strongly depend on the initial distribution [2]. For non-vanishing x_0, at short times, the evolution of maximum and curvature of position distribution can be approximated by [2]

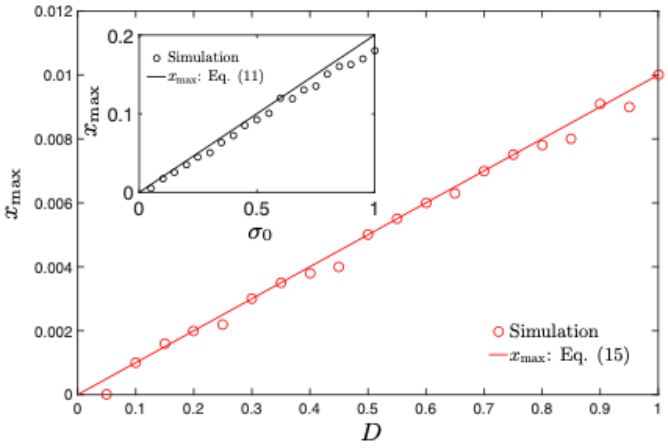

Figure 3.11: Atypical shift of maximum powered by initial thermal noise (inset, black) and environmental noise (red) [2].
The solid lines are analytical results from Eq.(3.22) (red) and Eq.(3.18) (black, inset).
The figure demonstrates the noise-to-signal transition for the most likely trajectory, with the atypical shift against the potential force. Eq.(3.5) has been simulated using $\gamma = 1, \langle x_0 \rangle = 0, dt = 2 \times 10^{-}3$, $\sigma^2_{x_0} = 0$ *(*$D = 0$ *for the inset), and* $nt = 3 \times 10^5$ *trajectories where generated.*

$$x_{max}(t) \approx \langle x_0 \rangle + (2\sigma^2_{x_0} - \langle x_0 \rangle^2)\kappa t, \tag{3.20}$$

$$\sigma^2_{max}(t) \approx \sigma^2_{x_0} - 4\sigma^2_{x_0}\langle x_0 \rangle \kappa t - 10\kappa^2\sigma^4_{x_0} t^2. \tag{3.21}$$

Notice how the maximum $x_{max}(t)$ in Eq.(3.20) evolves opposite to the mean position of Eq.(3.6) (namely $\langle x(t) \rangle \approx \langle x(t_0) \rangle - \kappa t(\sigma^2_{x_0} + \langle x_0 \rangle^2)$), and hence its motion against the potential force can be regarded as atypical. The sufficient condition to observe such atypical shift in Eq.(3.20), against the potential force $-\partial_x V(x)$ is given by the inequality $0 < \langle x_0 \rangle/\sqrt{2} < \sigma_{x_0}$, while the narrowing of the curvature in Eq.(3.21) requires only $\langle x_0 \rangle > 0$ [2]. For $x_0 = 0$ the maximum

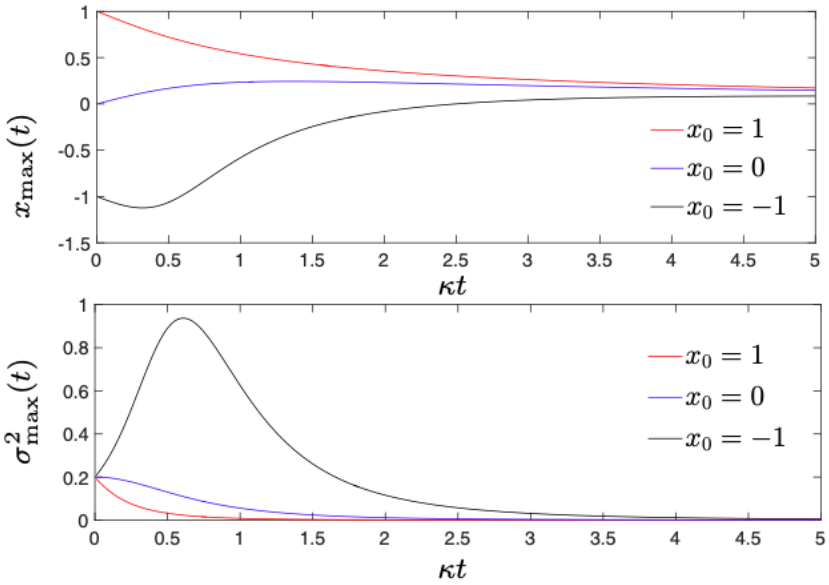

Figure 3.12: Time evolution of maximum $x_{max}(t)$ ***(top) and curvature*** σ^2_{max} ***(bottom) of position distribution, evolving deterministically in a cubic potential at different initial positions.***
For $\langle x_0 \rangle = 1$ *(red), the maximum shifts alongside the potential force, converging to the saddle point but never crossing it, while the curvature becomes narrower and narrower as the maximum approaches zero. For* $\langle x_0 \rangle = 0$ *(blue), the maximum moves atypically against the potential force only to converge, in longer time, back to zero and never crossing it. Simultaneously the curvature slowly decreases as the maximum becomes more localised to the inflection point. At* $\langle x_0 \rangle = -1$ *(black), the maximum initially feels the divergence by moving alongside the potential force, but at* $t \approx 0.4$ *the maximum begins to move atypically climbing the potential towards the inflection point (never passing to the positive values). Simultaneously the curvature feels an initial broadening, followed by a sharp narrowing when the maximum climbs the potential.*
$\dot{x} = -(k/\gamma)x^2$ *has been simulated using* $\gamma = 1, \sigma^2_{x_0} = 0.2, dt = 10^-5$*, and* $nt = 10^4$ *trajectories where generated.*

always evolves atypically, and the curvature always decreases, albeit for $\langle x_0 \rangle = \pm 1$ the maximum decreases for short time, and the curvature increases for negative initial position as shown in Fig.3.12. In the case of weak diffusion, imposing $\sigma^2_{x_0} = 0$, the only source of randomness is the weak thermal noise. Initiating the trajectory at $\langle x_0 \rangle$, the noise at short time is negligible compared to the deterministic drift. To calculate the local characteristics one must substitute the initial conditions $\langle x_0 \rangle \to \langle x(t) \rangle$, $\sigma^2_{x_0} \to \sigma^2_x$ with global moments from short time dynamics Eq.(3.10)(3.11), obtaining [2]

$$x_{max}(t) \approx \frac{1 + 7D\kappa^2 t^3 - \sqrt{1 + 14D\kappa^2 t^3 + D^2\kappa^4 t^6}}{8D\kappa^3 t^4}. \tag{3.22}$$

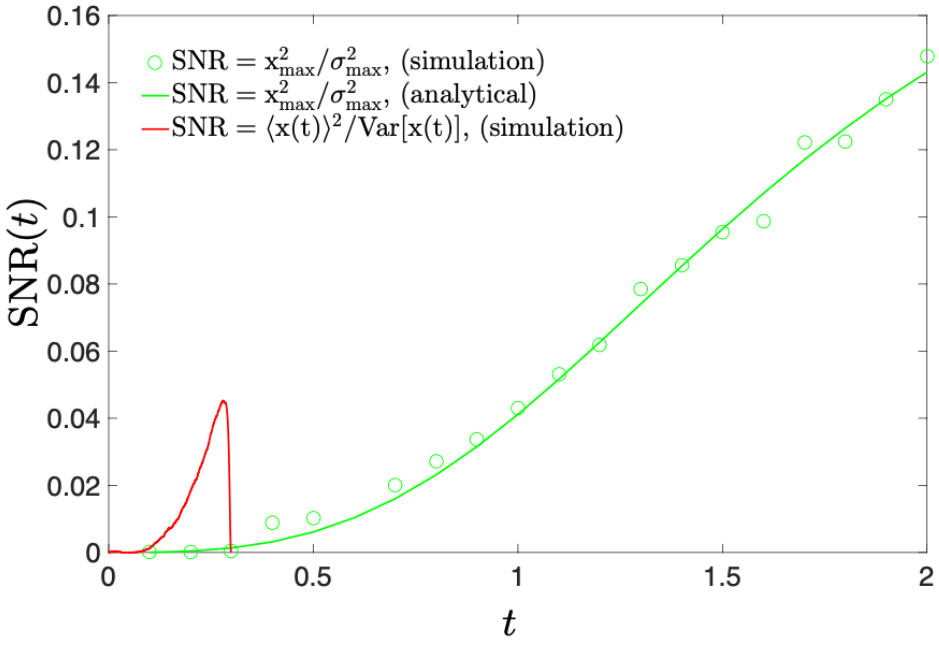

Figure 3.13: Fast divergence of the global description using averages is demonstrated by a swift drop of the SNR ***(red line).***
The local description using the maximum of the PDF, and the curvature around it, maintains its information value for all times (green line). $D = 0.1$, $k = 1$, $dt = 2 \cdot 10^{-3}$, $x_0 = 0$, *and* $4 \cdot 10^5$ *trajectories where used.*

The noise to signal transition for the maximum of particle position is shown in Fig.3.11 showing the atypical shift powered by noise in the limit of negligible environmental noise, and weak diffusion. The SNR for local characteristics, is a parameter that determines how well the most likely position can be observed experimentally [2]. In turn it is required to have a non-negligible SNR to be able to detect the shift of the maximum of particle position. In contrast to the SNR for global characteristics, it does not show a drop as time grows, remaining nonzero for any t, as both maximum and curvature converge to a positive value [2]. As shown in Fig.3.13, while the drop of the ratio for averages shows that the signal in the position is negligible compared to the noise, the SNR for the most likely trajectory exhibits the maximum of particle position maintaining its information values for all times.

3.2 Underdamped Regime

3.2.1 Stability and Divergence

Let us now consider a two dimensional nonlinear dynamical system, such as

$$\ddot{x} = -\kappa x^2, \tag{3.23}$$

where $\kappa = k/m$ is the normalised cubic potential stiffness. The motion in the phase space plane is determined via a vector field obtained from Eq.(3.23). The state of the system is characterised now by its current position x, and its velocity $\dot{x}$. Knowing both values uniquely determines the future states of the system. We therefore write Eq.(3.23) in terms of the two quantities x, v

$$\dot{x} = v, \tag{3.24}$$

$$\dot{v} = -\kappa x^2. \tag{3.25}$$

In Eq.(3.24) the definition of velocity is simply applied, and Eq.(3.25) contains the differential equation under study. The above system assigns a vector $(\dot{x}, \dot{v}) = (v, -\kappa x^2)$ at each pair (x, v) and thus represents a vector field in the phase space plane [187].

The phase portraits shown in Fig.3.14 offer a plethora of dynamical behaviors that were not possible in the overdamped regime Fig.3.3. For the deterministic motion of Eq.(3.23) (middle panel, $r = 0$ in Fig.3.14) the dynamics possesses an unstable fixed point at $x_e = 0$. As shown by the streamlines, any pair (x, v) is subjected to a leftward flow that ultimately brings the trajectories to a divergence.

There are however a trajectories (red line) that divide the phase space in two regions, comprising of distinctly different behaviours. Such trajectories are called *separatrix* [187] and they allow, for instance in the middle panel of Fig.3.14, to cross the inflection point to the positive position $x > 0$ even for unstable initial conditions (i.e., particle initially placed to large negative values and with large initial velocity). Similarly in the right panel of Fig.3.14 the separatrix (red line) displays closed orbits around fixed stable point (black circle), and the cubic dynamics of the $r = 0$ case. On the left panel, the cubic potential is linearly tilted to destroy the plateau region,

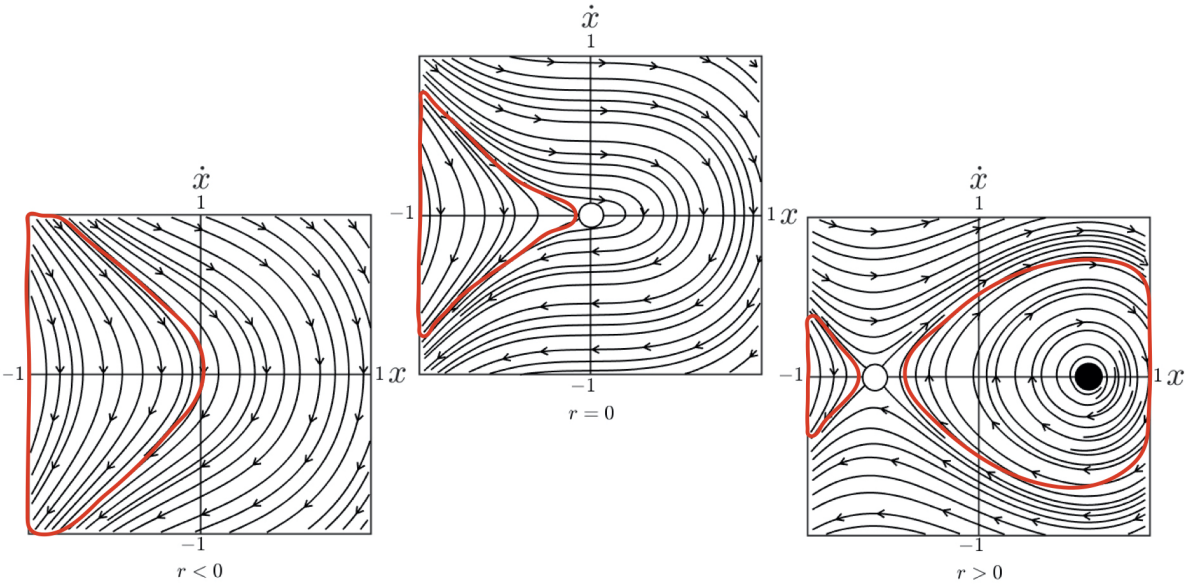

Figure 3.14: Sketch of the vector field for Eq. (3.26)***, illustrating the stability regions, and how the Langevin noise affects them.***
For $r < 0$ (left) every pair $(x, \dot{x})$ generates unstable and divergent dynamics, as the fixed point gets annihilated, while for $r > 0$ (right) a new stable point with closed orbits in proximity gets created (black circle). At $r = 0$ (middle) the dynamics comprises of a single fixed point at $(0, 0)$ of the unstable kind. It can be seen, from the streamlines becoming more negative in v than in x, how the instability has turned to velocity

and the separatrix (red line) shows how to overcome the instability, for instance at $x_0 = 0$, and large $\dot{x}_0$.

Differently from the phase portrait of Fig.3.3(middle panel $r = 0$) in the overdamped regime, the divergence is mostly but not uniquely felt by the velocity trajectory (as can be noticed by the streamlines becoming negative in velocity v quicker than in position x).

When introducing the noise term, Eq.(3.23) becomes

$$\ddot{x} = -\kappa x^2 - \gamma\dot{x} + \sqrt{\frac{2k_BT\gamma}{m}}\xi(t), \tag{3.26}$$

where $\gamma = \Gamma/m$ is the medium damping with drag coefficient Γ of the medium (i.e. air at low pressure), T is the absolute temperature, and k_B is the Boltzmann constant. The environmental noise acts like a forcing term, and at low pressure the second term $-\gamma\dot{x}$ remains negligible, allowing to write Eq.(3.26) as $\ddot{x} = -\kappa x^2 + r$ where $r = \sqrt{\frac{2k_BT\gamma}{m}}\xi(t)$. For $r < 0$, as shown in Fig.3.14 (left panel), the fixed point is annihilated, rending every pair (x, v) unstable and

subjected to divergence. Different is the case for $r > 0$ (Fig.3.14 right panel), where two new fixed point $x_e = \pm r$ are created for $v = 0$. It is instructive in this case to look particularly at the arrangements of trajectories near the fixed points, and their behavior, as for positive positions there exists closed orbits suggesting the possible existence of motion against the potential force (atypical) in position.

3.2.2 Noise-Induced Instantaneous Speed and Acceleration

In the limit of low friction, the dynamics is that of Eq.(3.26), where the characterisation of the statistics of instantaneous speed $\dot{x}$ and acceleration $\ddot{x}$ unfold without changing initial position x_0. While these quantities are well defined in the underdamped regime, they exist only on average in the high friction limit $\bar{v} = \Delta x/\Delta t$, and $\bar{a} = \Delta\bar{v}/\Delta t$.

To better explore the main feature of the nonlinear ballistic regime, we consider the dynamics to be deterministic $\gamma = 0$ and characterised by a Gaussian initial distribution with $\langle \dot{x}_0 \rangle = \sigma_{\dot{x}_0} = 0$. The nonlinear ballistic dynamics is therefore using only initial position uncertainty in the initial position as a thermal energy resource. The short time scale of the transient regime is defined by a particle, which on average does not move $\langle x(t) \rangle \approx 0$ and the nonlinear effect is explored by the instantaneous quantities $\dot{x}, \ddot{x}$. From Eq.(3.26) the quantitative description of the moments of instantaneous acceleration can be calculated as

$$\langle \ddot{x} \rangle \approx -\kappa \sigma_{x_0}^2, \tag{3.27}$$

$$\sigma_{\ddot{x}} \approx \sqrt{2}\kappa \sigma_{x_0}^2, \tag{3.28}$$

$$\mathrm{SNR}_{\ddot{x}} = \frac{|\langle \ddot{x} \rangle|}{\sigma_{\ddot{x}}} \approx \frac{1}{\sqrt{2}}. \tag{3.29}$$

A shift of instantaneous acceleration powered by initial position noise is the first experimental verification to distinguish the nonlinear ballistics, as shown by the comparison of the high (left, green arrow) and low (right, black arrow) friction limit in Fig.3.15 (bottom panel). Notice how the mean instantaneous acceleration $\langle \ddot{x} \rangle$ and its standard deviation are equally powered by $\sigma_{x_0}^2$ to produce a constant $\mathrm{SNR}_{\ddot{x}}$ as shown in Fig.3.16 (bottom panel). The second main feature of the nonlinear ballistic can be obtained by formally integrating Eq.(3.26), namely $\dot{x}(t) \approx$

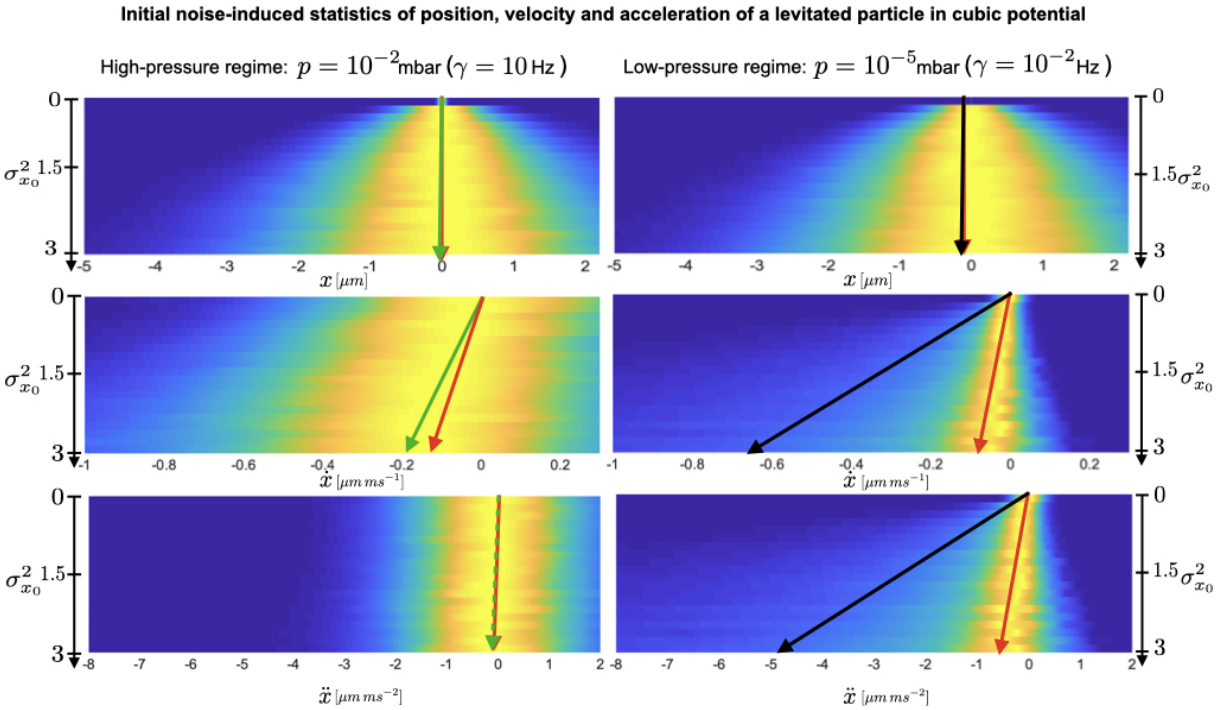

Figure 3.15: Noise-induced position, velocity and acceleration statistics of a levitated particle in cubic potential for the high pressure limit (left column) and for the low pressure limit (right column).
The initial Gaussian distribution for particle position comprises of $\langle x_0 \rangle = 0$*, while* $\sigma^2_{x_0}$ *triggers the nonlinear dynamics. In all cases, the Gaussian distribution of particle instantaneous speed has* $\langle \dot{x}_0 \rangle = 0$ *and* $\sigma^2_{\dot{x}_0} = 0$*. The initial position and speed are statistically independent. Top panel: the mean of particle position* $\langle x \rangle$ *(green, black) remains unchanged for the short time dynamics, while its standard deviation (green-blue halo) increases as initial noise increases. Similarly, the maximum of position distribution* x_{max} *(red) does not develop at such short time scale. Middle panel: the mean of average velocity* $\langle \bar{v} \rangle$ *(left column, green arrow) produces a smaller noise-induced shift compared to the mean of instantaneous velocity* $\langle \dot{x} \rangle$ *(right column, black arrow), while simultaneously their standard deviation are significantly reduced in the low pressure regime (right column, green-blue halo). The respective maxima of velocity distributions (red arrow) increases alongside the potential force, showing again a significant reduction in the curvature for the low pressure regime (right column, yellow halo). Bottom panel: the mean of average acceleration* $\langle \bar{a} \rangle$ *(left column, green arrow) does not display any indication of a noise-induced effect, while the mean instantaneous acceleration* $\langle \ddot{x} \rangle$ *(right column, black arrow) exhibits a substantial noise-induced shift as its standard deviation (green-blue halo) increases too with initial noise* $\sigma^2_{x_0}$*. The respective maxima of acceleration distributions (red) display for the high pressure regime (left column) a complete independence on initial noise, surrounded by a large curvature (yellow halo), while in the low pressure regime (right column) the noise-induced shift is visible and alongside the potential force, presenting a reduced curvature (yellow halo). To generate all the density plots, Eq. (3.26) has been simulated using* $\kappa = 6k_BT\mu m^{-3}Kg^{-1}$*,*$T = 300$ *K,* $t = 0.1$ *ms,* $dt = 2 \times 10^{-5}$ *ms.* $nt = 10^4$ *trajectories where generated with* 5000 *samples each. To calculate the instantaneous quantities,* $\dot{x} = dx/dt$*,* $\ddot{x} = d\dot{x}/dt$*, the time interval used is given by the time-step* $dt = 2 \times 10^{-5}$ *ms, whereas for the average quantities* $\bar{v} = \Delta x/\Delta t$*,* $\bar{a} = \Delta v/\Delta t$*, the time interval, multiple of the time-step, has been used* $\Delta t = 10 \times dt$*.*

$\dot{x}_0 - \kappa \int_0^{t_n} x^2(t'_{n-1})dt'_{n-1}$, unravelling the short time evolution of the moments of instantaneous velocity. At the lowest order, and with $\langle x_0 \rangle = 0$, the latter becomes

$$\langle \dot{x}(t) \rangle \approx -\kappa \sigma_{x_0}^2 t, \tag{3.30}$$

$$\sigma_{\dot{x}}(t) \approx \sqrt{2}\kappa \sigma_{x_0}^2 t, \tag{3.31}$$

$$\mathrm{SNR}_{\dot{x}}(t) = \frac{|\langle \dot{x}(t) \rangle|}{\sigma_{\dot{x}}(t)} \approx \frac{1}{\sqrt{2}}. \tag{3.32}$$

The mean of instantaneous velocity $\langle \dot{x} \rangle$ evolves qualitatively similar to the mean instantaneous acceleration $\langle \ddot{x} \rangle$ of Eq.(3.27), growing linearly with initial position uncertainty $\sigma_{x_0}^2$ and ultimately producing a constant $\mathrm{SNR}_{\dot{x}} \approx 1/\sqrt{2}$ as observable in Fig.3.16 (middle panel). A comparison with the high friction counterpart $\langle \bar{v} \rangle$ (left, green arrow) in Fig.3.15(middle panel), prominently dominated by noise (green-azure halo), reveals the second verification to distinguish the nonlinear ballistic effect characterised by a prominent noise-induced shift of mean instantaneous velocity $\langle \dot{x} \rangle$ (right, black arrow) accompanied by a reduced uncertainty (green-azure halo).

Further integration of Eq.(3.26), $x(t) \approx x_0 + \int_0^{t_n} \dot{x}(t'_{n-1})dt'_{n-1} - \int_0^{t_n} \int_0^{t'_n} \kappa x^2(t''_{n-1})dt''_{n-1}dt'_{n-1}$, allows access to the position evolution, which first two moments, and corresponding SNR are given by

$$\langle x(t) \rangle \approx -\frac{1}{2}\kappa \sigma_{x_0}^2 t^2, \tag{3.33}$$

$$\sigma_x(t) \approx \sqrt{\sigma_{x_0}^2 + \frac{1}{2}\kappa^2 t^4 \sigma_{x_0}^4}, \tag{3.34}$$

$$\mathrm{SNR}_x(t) = \frac{|\langle x \rangle|}{\sigma_x} \approx \frac{1}{\sqrt{2\left(1 + 2k^{-2}\sigma_{x_0}^{-2}t^{-4}\right)}}. \tag{3.35}$$

For the long time transient dynamics, but before the divergence, the mean position of Eq.(3.33) evolves quadratically in time. Its instantaneous values can be enriched by increasing the initial position uncertainty $\sigma_{x_0}^2$. Simultaneously, the standard deviation depends on two terms, the first of which becomes negligible at long time scales, $t > 0.9$ ms (for the parameters used to produce Fig.3.16), leaving a standard deviation that grows comparably to mean position and realising a constant $\mathrm{SNR}_x \approx 1/\sqrt{2}$. For short time scale ($t \leq 0.1$ for the parameters used to produce Fig.3.16) the position does not move on average, while the standard deviation of Eq.(3.34) is

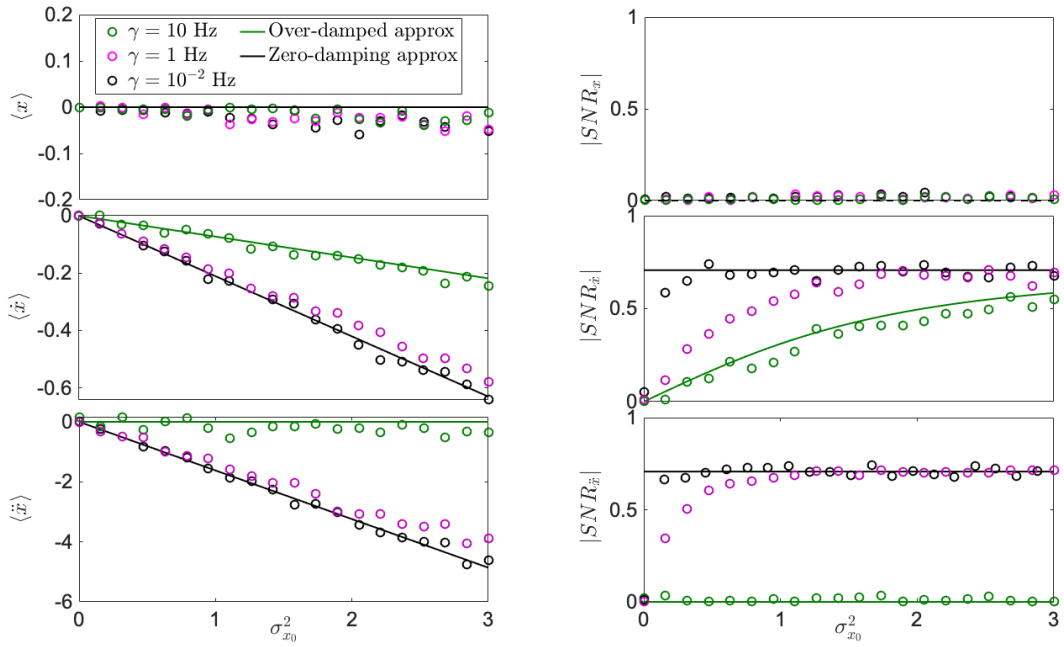

Figure 3.16: Noise-induced effect for initially steady particle in position x (top), instantaneous velocity $\dot{x}$ (middle), and acceleration $\ddot{x}$ (bottom), driven by variance $\sigma^2_{x_0}$ of initial position.
All simulations (dots) have been performed based on Eq. (3.26). Top panel: the mean position $\langle x \rangle$ (left) does not develop with increasing initial noise $\sigma^2_{x_0}$ at the short time scale in neither of the damping values explored, spacing from low pressure regime (black) to high pressure regime (green). Because of the vanishing mean position, and the large noise spread dominating the position dynamics, the SNR_x (right) vanishes too. Middle panel: the mean instantaneous velocity $\langle \dot{x} \rangle$ (left) displays a noise-induced shift that reaches the deterministic limit (black line) for both $\Gamma = 10^{-2}$ (black dots), and $\Gamma = 1$ (purple dots), while it retrieves the overdamped approximation of Eq.(3.14) for $\Gamma = 10$ (purple dots). The respective $SNR_{\dot{x}}$ (right) shows how sensitive is the standard deviation of velocity to environmental temperature T, at different pressures, keeping the low pressure closer to deterministic approximation (black), while leading to a converging $SNR_{\dot{x}}$ for the higher pressure regime (green), retrieving once again the results from the overdamped regime, namely Eq.(3.16). Bottom panel: the mean of instantaneous acceleration $\langle \ddot{x} \rangle$ (left) clearly shows the main difference between the two limits (low pressure, black line, and high pressure green line), demonstrating the noise-induced feature for instantaneous acceleration close to the deterministic approximation (black) for $\Gamma = 10^{-2}$ (black) and $\Gamma = 1$ (purple), while vanishing for larger damping (green). The role of environmental temperature can be observed for $SNR_{\ddot{x}}$ (left) where an increase in pressure (purple) leads to a larger standard deviation and to a converging $SNR_{\ddot{x}}$. Eq. (3.26) has been simulated using $\kappa = 6k_B T \mu m^{-3} K g^{-1}$,$T = 300$ K (ambient temperature), $\langle x_0 \rangle = 0$, $\langle \dot{x}_0 \rangle = 0$, $\sigma_{\dot{x}_0} = 0$, $t = 0.1$ ms, $dt = 2 \times 10^{-5}$ ms. 10^4 trajectories where generated with 5000 samples each. To compute the average quantities, $\bar{v}$, $\bar{a}$, the multiple time-step has been used, $\delta t = 10 \times dt$.

dominated by the first term $\sigma^2_x(t) \approx \sigma^2_{x_0}$. The resulting dynamics produces a vanishing SNR_x.

This quick overview of the deterministic motion proves that the noise-induced effect is prominently visible in the moments of instantaneous quantities $\ddot{x}, \dot{x}$ Eqs.(3.27),(3.30) respectively,

and vanishes for position x as can be seen in Fig.3.16 for the short time dynamics. The curves in Fig.3.16, have been simulated using real experimental parameters of the current setups [93], showing that at values of $\Gamma = 10^{-2}$Hz (black dots) the zero-damping approximation of Eqs.(3.27)to(3.35) (black line) is reached. Moreover, it shows that at larger damping values $\Gamma = 10$Hz (green dots), the results from the high friction limit (green line) are obtained for position (top panel) and average velocity (middle panel), and the vanishing of acceleration is observed (bottom panel).

Nonvanishing initial velocity and position

Thus far we have considered only an initially steady particle with $\langle \dot{x}_0 \rangle = 0$, but as the vector field in Fig.3.14 (middle panel, $r = 0$) shows we have a plethora of particles evolving at the plateau $\langle x_0 \rangle = 0$ with nonzero initial velocity. Let us now discuss the noise-induced dynamics for particles with nonvanishing mean initial velocity. To fully visualise how moving particles affect the moments of instantaneous acceleration $\ddot{x}$, we refer to Eqs.(3.24),(3.25) and substitute the short time solution of position $x \approx x_0 + \dot{x}_0 t$, to the dynamical equation for $\dot{v}$, obtaining $\ddot{x}(t) \approx -\kappa(x_0^2 + 2x_0\dot{x}_0 t + \dot{x}_0^2 t^2)$. Furthermore, we introduce the quantity $\Delta\ddot{x} = \ddot{x}(t) + \kappa\dot{x}_0^2 t^2$ to describe the effect of $\sigma_{x_0}^2$ on the instantaneous acceleration for particles with nonzero initial velocity $\langle \dot{x}_0 \rangle \neq 0, \sigma_{\dot{x}_0}^2 = 0$, initially positioned at the plateau $\langle x_0 \rangle = 0$

$$\langle \Delta\ddot{x} \rangle \approx -\kappa\sigma_{x_0}^2, \tag{3.36}$$

$$\sigma_{\Delta\ddot{x}} \approx \sqrt{2}\kappa\sigma_{x_0}^2, \tag{3.37}$$

$$\mathrm{SNR}_{\Delta\ddot{x}} = \frac{|\langle \Delta\ddot{x} \rangle|}{\sigma_{\Delta\ddot{x}}} \approx \frac{1}{\sqrt{2}}. \tag{3.38}$$

As can be seen in Fig.3.17(bottom panel), the results of Eqs.(3.36),(3.38) hold true for slowly moving particles (blue dots), where the $\mathrm{SNR}_{\ddot{x}}$ (right panel) fastly approaches $1/\sqrt{2}$.

For particles with higher initial speed (red dots) the mean instantaneous acceleration $\langle \ddot{x} \rangle$ (left column) is dominated by higher terms that deviates from that of Eq.(3.36) obtaining less negative average acceleration for smaller $\sigma_{x_0}^2$, while the $\mathrm{SNR}_{\ddot{x}}$ (right column) initially decreases and slowly converges to $1/\sqrt{2}$ after the turning point. To retrieve the results of Eqs.(3.36)-(3.38) for such initially fast particles, and bring the red dots closer to the black line, the computed timescale

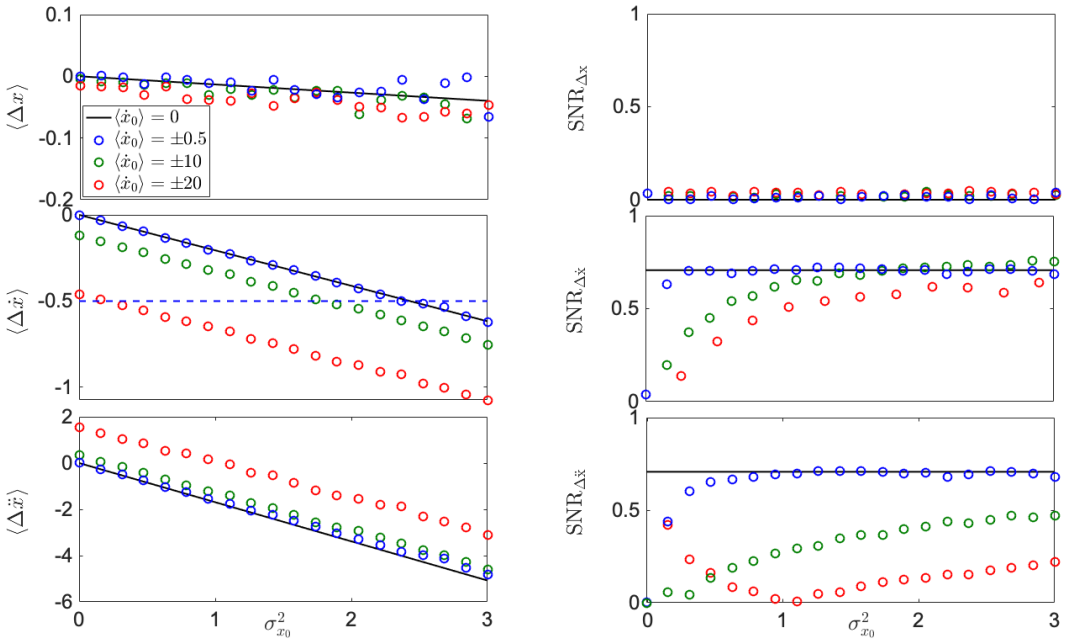

Figure 3.17: Noise-induced effects for initially moving particle in position statistics (top), instantaneous velocity statistics (middle), and instantaneous acceleration statistics (bottom).
All simulations (dots) have been performed based on Eq. (3.26) using $\sigma^2_{\dot{x}_0} = 0$. *Top panel: the mean particle position difference* $\langle\Delta x\rangle$ *(left) displays no deviation from that of Eq.(3.42) (black line) independent of the chosen initial velocity* $\langle\dot{x}_0\rangle$, *leaving the* $SNR_{\Delta x}$ *(right) small. Middle panel: the mean instantaneous velocity difference* $\langle\Delta\dot{x}\rangle$ *(left) shows deviation from the approximation of Eq.(3.39) (black line) for initially fastly moving particles (green and red), as higher order nonlinear term dominates the evolution. For initially slowly moving particles (blue), stochastic speeding (for* $\langle\dot{x}_0\rangle > 0$*) and stochastic breaking (for* $\langle\dot{x}_0\rangle < 0$*) is witnessed at* $\langle\Delta\dot{x}\rangle = -0.5$ *(blue dashed line) The resulting* $SNR_{\Delta\dot{x}}$ *(right) display a slower convergence to the black line as the initial velocity becomes larger in magnitude. Bottom panel: the mean instantaneous acceleration* $\langle\Delta\ddot{x}\rangle$ *(left) displays a higher robustness against initial moving particles, compared to the instantaneous velocity, as only very fast initial moving particles (red) deviate substantially from the approximation of Eq.(3.36) (black line) The* $SNR_{\Delta\ddot{x}}$ *on the other hand tell a different story, as a slowly moving particle (blue) remains consistent with the approximation (black line), but faster moving particles (green, red) are slowly converging, even displaying an initial decrease for extremely fast (red) particles. Eq. (3.26) has been simulated using* $\kappa = 6k_BT\mu m^{-3}Kg^{-1}$, $T = 300\ K$, $\Gamma = 10^{-2}\ Hz$, $t = 0.1\ ms$, $dt = 2 \times 10^{-5}\ ms$. 10^4 *trajectories where generated with* 5000 *samples each.*

has to be decreased tenfold $t = 0.01$ms (for the parameters used to produce Fig.3.17).

Similarly, for instantaneous velocity $\dot{x}$ Eq.(3.30) can be manipulated to introduce the velocity

difference $\Delta\dot{x} = \dot{x}(t) - \dot{x}_0$, leading to the following statistical evaluation

$$\langle \Delta\dot{x} \rangle \approx -\kappa\sigma_{x_0}^2 t, \tag{3.39}$$

$$\sigma_{\Delta\dot{x}} \approx \sqrt{2}\kappa\sigma_{x_0}^2 t, \tag{3.40}$$

$$\mathrm{SNR}_{\Delta\dot{x}} = \frac{|\langle \Delta\dot{x} \rangle|}{\sigma_{\Delta\dot{x}}} \approx \frac{1}{\sqrt{2}}. \tag{3.41}$$

Looking at Fig.3.17(middle panel), the mean velocity difference $\Delta\dot{x}$ (left column) holds true even for slowly moving particles (blue dots), however for higher initial speed (green and red dots) the above approximation of Eqs.(3.39)-(3.41) fails to describe the motion which is dominated fully by higher nonlinear terms that produce more negative average velocity for smaller $\sigma_{x_0}^2$. The correspondent $\mathrm{SNR}_{\dot{x}}$ (right column) converges more slowly the higher initial speed the particle possesses.

Lastly, for particle position, Eq.(3.33) can be used to introduce the position difference $\Delta x = x(t) - \dot{x}_0 t$ which moments evolve as follows

$$\langle \Delta x \rangle \approx -\frac{\kappa\sigma_{x_0}^2 t^2}{2}, \tag{3.42}$$

$$\sigma_{\Delta x} \approx \sqrt{\sigma_{x_0}^2 + \frac{k^2 t^4 \sigma_{x_0}^4}{2}}, \tag{3.43}$$

$$\mathrm{SNR}_{\Delta x} = \frac{|\Delta x|}{\sigma_{\Delta x}} \approx \frac{1}{\sqrt{2\left(1 + 2k^{-2}\sigma_{x_0}^{-2} t^{-4}\right)}}. \tag{3.44}$$

From Fig.3.17 (top panel), the position difference (left column) does not change on average even for initially quickly moving particles. The correspondent SNR_x (right column) remains small, and the approximation of Eqs.(3.42)-(3.44) holds true for all the considered initial velocities. Not only Fig.3.17 demonstrates that the noise-induced effect of instantaneous velocity and acceleration, enhanced by initial position noise $\sigma_{x_0}^2$, can be observed for both deterministic and slowly moving particles (black, blue and green dots), but even more stochastic breaking and speeding can be argued.

For positive initial speed, $\langle \dot{x}_0 \rangle > 0$ the particle can break at average $\langle \dot{x} \rangle = 0$ for large initial position noise $\sigma_{x_0}^2$, whereas for negative initial speed, $\langle \dot{x}_0 \rangle < 0$ the particle gains velocity by increasing the initial position noise. To better observe such events, in Fig.3.17 (middle panel left

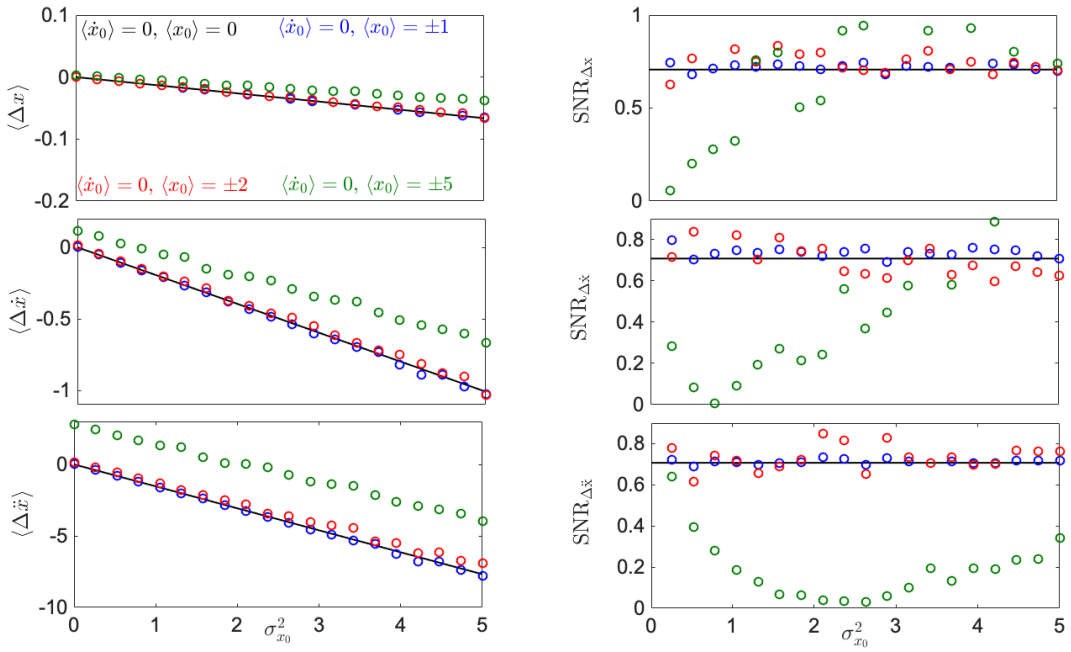

Figure 3.18: Noise-induced effects for non vanishing initial position $\langle x_0 \rangle$ for position statistics (top), instantaneous velocity statistics (middle), and instantaneous acceleration statistics (bottom).
All simulations (dots) have been performed based on Eq. (3.26) using $\sigma^2_{\dot{x}_0} = 0$, and $\langle \dot{x}_0 \rangle = 0$. Positioning the particle in different parts of the plateau region (blue dots), and on the potential slope (red), reveals no introduction of higher order term of the time series for neither position, velocity, nor acceleration. Their dynamics is well described by Eqs. (3.47). A different case is when the particle is positioned in a highly nonlinear region of the potential (green), i.e., down the slope of the cubic potential (negative values), or on the cubic wall (positive values). Such positions highly affect the dynamics, introducing new terms of the time series, where the approximate equations are no longer valid. Common to these initial highly nonlinear positions (green) is a smaller noise-induced effect accompanied by a larger standard deviation that results in a slowly converging signal to noise ratio. Eq. (3.26) has been simulated using $\kappa = 6k_BT\mu m^{-3}Kg^{-1}, T = 300K, \sigma^2_{\dot{x}_0} = 0, \langle \dot{x}_0 \rangle = 0, dt = 2 \times 10^{-5}$ ms. 10^4 trajectories where generated with 5000 samples each.

column) the blue dashed line has been plotted, indicating the above effect for $\langle \dot{x}_0 \rangle = \pm 0.5$. To generalise the detection of stochastic breaking or speeding, the mean velocity difference displays a sign flip $\langle \Delta \dot{x}_0 \rangle = -|\dot{x}_0|$.

The complementary case of non vanishing initial position $\langle x_0 \rangle \neq 0$ is explored, for $\langle \dot{x}_0 \rangle = \sigma^2_{\dot{x}_0} = 0$, to realise how it affects the noise induced effects so far described. To further understand the behavior of different initial positions, one has to refer to the equation of motion for position x,

speed $\dot{x}$, and acceleration $\ddot{x}$ and rewrite their moments as follows

$$\langle \Delta\ddot{x}(t)\rangle = -\kappa\sigma_{x_0}^2, \tag{3.45}$$

$$\langle \Delta\dot{x}(t)\rangle = -\kappa\sigma_{x_0}^2 t, \tag{3.46}$$

$$\langle \Delta x(t)\rangle = -\frac{\kappa\sigma_{x_0}^2 t^2}{2}, \tag{3.47}$$

where the differences for acceleration $\langle \Delta\ddot{x}(t)\rangle = \langle \ddot{x}(t)\rangle + \kappa\langle x_0\rangle^2$, velocity $\langle \Delta\dot{x}(t)\rangle = \langle \dot{x}(t)\rangle + \kappa\langle x_0\rangle^2 t$, and position $\langle \Delta x(t)\rangle = \langle x(t)\rangle + \kappa\langle x_0\rangle^2 t^2/2 - \langle x_0\rangle$, have been introduced.

As can be seen in Fig.3.18(left column) the mean position difference (top panel), velocity difference (middle panel), and acceleration difference (bottom panel) are still performing within the approximation of Eqs.(3.45) to (3.47), where their respective SNR (right column) show no appreciable deviation from the constant $1/\sqrt{2}$. For large initial position $\langle x_0\rangle = \pm 5$ (green dots), the above equations do not anymore describe the dynamics, and their evolution is modified by higher order nonlinear terms. It can be noticed in Fig.3.18 (right column) that the SNR_x (top panel) converges slowly to its constant value, whereas for both velocity (middle panel) and acceleration (bottom panel) their respective SNR undergo an initial decrease for small $\sigma_{x_0}^2$, followed by a subsequent convergence (slower for the case of acceleration).

Role of environmental temperature T and initial velocity noise $\sigma_{\dot{x}_0}^2$

The initial noise-induced effects can be affected by the temperature T of the environment. To allow for such effect to be taken into consideration, we rewrite the deterministic equation of motion of Eq.(3.23) as

$$\ddot{x} = -\gamma\dot{x} - kx^2 + \sqrt{\frac{2k_B T\gamma}{m}}\xi(t), \qquad \langle\xi(t)\rangle = 0, \langle\xi(t)\xi(t')\rangle = \delta(t-t'). \tag{3.48}$$

For zero initial position $\langle x_0\rangle = 0$, and $\langle \dot{x}\rangle = \sigma^2_{\dot{x}_0} = 0$ the role of environmental noise unfolds as an extension of the approximate formulae obtained in the previous section

$$\langle x(t)\rangle \approx -\frac{1}{2}\kappa\sigma^2_{x_0}t^2, \quad \sigma_x(t) \approx \sqrt{\sigma^2_{x_0} + \frac{2k_BT\gamma}{3m}t^3 + \frac{1}{2}\kappa^2\sigma^4_{x_0}t^4}, \tag{3.49}$$

$$\langle \dot{x}(t)\rangle \approx -\kappa\sigma^2_{x_0}t, \qquad \sigma_{\dot{x}}(t) \approx \sqrt{2\kappa^2\sigma^4_{x_0}t^2 + 2\frac{k_BT\gamma}{m}t}, \tag{3.50}$$

$$\langle \ddot{x}(t)\rangle \approx -\kappa\sigma^2_{x_0}, \qquad \sigma_{\ddot{x}}(t) \approx \sqrt{2\kappa^2\sigma^4_{x_0} + 2\frac{k_BT\gamma}{m}}, \tag{3.51}$$

with their respective SNR evolving as

$$\mathrm{SNR}_x(t) = \frac{|\langle x\rangle|}{\sigma_x} \approx \frac{1}{\sqrt{2\left(1 + \frac{2k_BT\gamma}{3m\kappa^2\sigma^4_{x_0}t} + \frac{2}{\kappa^2\sigma^2_{x_0}t^4}\right)}}, \tag{3.52}$$

$$\mathrm{SNR}_{\dot{x}}(t) = \frac{|\langle \dot{x}\rangle|}{\sigma_{\dot{x}}} \approx \frac{1}{\sqrt{2\left(1 + \frac{k_BT\gamma}{m\kappa^2\sigma^4_{x_0}t}\right)}}, \tag{3.53}$$

$$\mathrm{SNR}_{\ddot{x}}(t) = \frac{|\langle \ddot{x}\rangle|}{\sigma_{\ddot{x}}} \approx \frac{1}{\sqrt{2\left(1 + \frac{k_BT\gamma}{m\kappa^2\sigma^4_{x_0}}\right)}}. \tag{3.54}$$

It is clear from the above equations Eqs.(3.49) to (3.51), that the environmental noise does not modify the means, but rather the standard deviations. For position statistics, Eq.(3.49), the standard deviation is affected at slower time scales (t^3 dependance), resulting in a vanishing SNR_x as shown in Fig.3.16 (top panel, right column) for the range of Γ used for the short time scale. Longer time scales allows the environmental noise to compete against the noise-induced effect for $T \geq 3m\kappa^2 t\sigma^4_{x_0}/(4k_B\gamma)$ ($T \approx 800\sigma^4_{x_0}$ K, for $\Gamma = 10^{-2}$ Hz), realising a slowly converging $\mathrm{SNR}_x \to 1/\sqrt{2}$, as described by Eq.(3.52) (see Fig.3.16).

For particle velocity, Eq.(3.50) the standard deviation shows a stronger and more visible environmental effect at the short time scales. The temperature T affects the standard deviation, and $\mathrm{SNR}_{\dot{x}}$ (3.53) when $T \geq m\kappa^2\sigma^4_{x_0}t/k_B\gamma$ ($T \approx 125 \times 10^2\sigma^4_{x_0}$ for $\Gamma = 10^{-2}$Hz, and $T \approx 140\sigma^4_{x_0}$, for $\Gamma = 1$Hz). As shown in Fig.3.16 (middle panel), even at low damping $\Gamma = 10^{-2}$Hz the room temperature is enough to modify the statistics of the $\mathrm{SNR}_{\dot{x}}$, for small $\sigma^2_{x_0}$ where the convergence to $1/\sqrt{2}$ is fast (black dots). An increase in damping (purple dots) shows the relevant modification the environmental temperature T applies to the convergence of the $\mathrm{SNR}_{\dot{x}}$. For particle

acceleration, Eq.(3.51), the condition on environmental temperature T are much stricter, as no time dependence appears in the moments of instantaneous acceleration Eq.(3.51), and $\mathrm{SNR}_{\ddot{x}}$ Eq.(3.54). As a result, at small damping $\Gamma = 10^{-2}$Hz (black dots in Fig.3.16 bottom panel) the environmental noise is negligible at the short time scale, whereas for larger damping (purple dots) the condition softens $T \approx 144 \times 10^2 \sigma_{x_0}^4$K, allowing a reduction of $\mathrm{SNR}_{\ddot{x}}$ for small $\sigma_{x_0}^2$.

Another source of noise that competes with the initial position noise-induced effect resides with

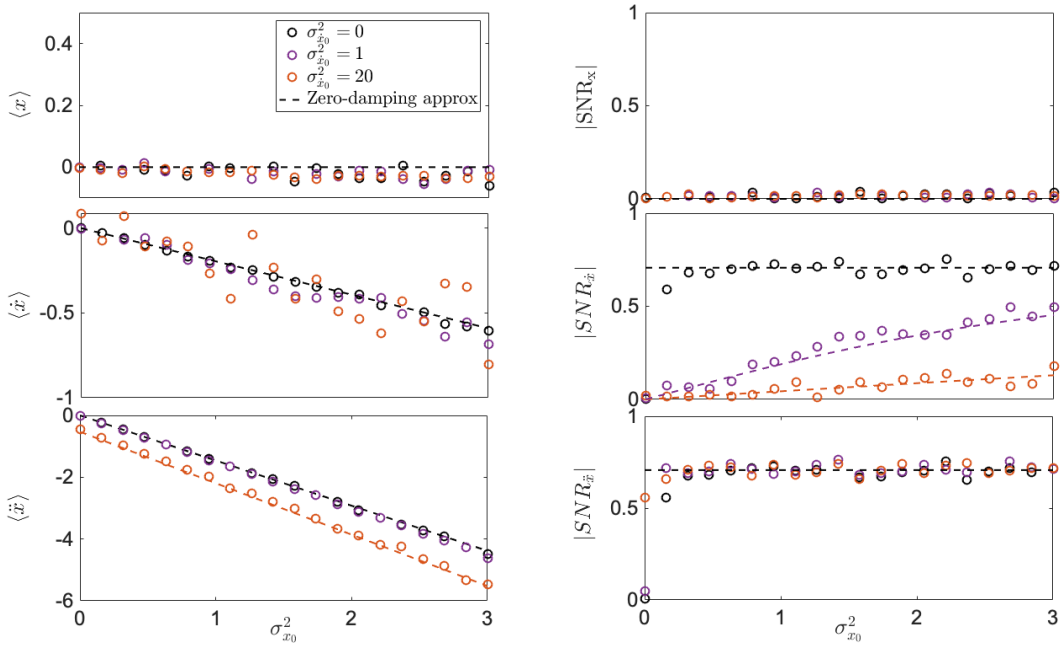

Figure 3.19: Robustness of initial noise-induced effect to initial velocity noise $\sigma_{\dot{x}_0}^2$ for position statistics (top), instantaneous velocity statistics (middle), and instantaneous acceleration (bottom). All simulations (dots) have been performed based on Eq. (3.26) using $\langle x_0 \rangle = \langle \dot{x}_0 \rangle = 0$.
Top panel: mean position (left), together with its SNR_x (right), are unaffected by increasing initial velocity noise $\sigma_{\dot{x}_0}^2$.
Middle panel: the mean instantaneous velocity (left) maintains its noise-induced shift visible even at large initial velocity noise (orange dots). Its $\mathrm{SNR}_{\dot{x}}$ (right) still displays the noise-induced effects, although increasing initial velocity noise shows a disruptive tendency (purple and orange dots).
Bottom panel: Mean instantaneous acceleration (left) shows only positive effects for increasing $\sigma_{\dot{x}_0}^2$ (orange) enhancing its shift beyond the zero-damping approximation (black dashed line). Its $\mathrm{SNR}_{\ddot{x}}$ (right) remains unaffected even at large $\sigma_{\dot{x}_0}^2$. Eq. (3.26) has been simulated using $\kappa = 6k_BT\mu m^{-3}Kg^{-1}$, $T = 300$ K, $\Gamma = 10^{-2}$ Hz, $t = 0.1$ ms, $dt = 2 \times 10^{-5}$ ms. $nt = 10^4$ trajectories where generated with $N = 5000$ samples each.

the initial velocity noise $\sigma_{\dot{x}_0}^2$. Assuming deterministic dynamics $\gamma = 0$ in Eq.(3.23), the effect of initial velocity fluctuations can be observed in the following moments for strictly zero initial

velocity $\langle \dot{x}_0 \rangle = 0$, and $\langle x_0 \rangle = 0$

$$\langle x(t) \rangle \approx -\frac{\kappa \sigma_{x_0}^2 t^2}{2}, \qquad \sigma_x \approx \sqrt{\sigma_{x_0}^2 + \sigma_{\dot{x}_0}^2 + \frac{1}{2}\kappa^2 \sigma_{x_0}^4 t^4}, \tag{3.55}$$

$$\langle \dot{x}(t) \rangle \approx -\kappa \sigma_{x_0}^2 t, \qquad \sigma_{\dot{x}} \approx \sqrt{\sigma_{\dot{x}_0}^2 + 2\kappa^2 t^2 \sigma_{x_0}^4}, \tag{3.56}$$

$$\langle \ddot{x}(t) \rangle \approx -\kappa(\sigma_{x_0}^2 + \sigma_{\dot{x}_0}^2 t^2), \qquad \sigma_{\ddot{x}} \approx \sqrt{2\kappa^2(\sigma_{x_0}^4 + \sigma_{\dot{x}_0}^4 t^4)}, \tag{3.57}$$

with their respective SNR evolving as

$$\mathrm{SNR}_x \approx \frac{1}{\sqrt{2}\sqrt{\frac{2\sigma_{x_0}^2 + 2\sigma_{\dot{x}_0}^2 t^2}{\kappa^2 \sigma_{x_0}^4 t^4} + 1}}, \tag{3.58}$$

$$\mathrm{SNR}_{\dot{x}} \approx \frac{1}{\sqrt{2}\sqrt{\frac{\sigma_{\dot{x}_0}^2}{2\kappa^2 \sigma_{x_0}^4 t^2} + 1}}, \tag{3.59}$$

$$\mathrm{SNR}_{\ddot{x}} \approx \frac{\left(\frac{\sigma_{x_0}^2}{\sigma_{\dot{x}_0}^2} + t^2\right)}{\sqrt{2}\sqrt{\frac{\sigma_{x_0}^4}{\sigma_{\dot{x}_0}^4} + t^4}}. \tag{3.60}$$

At short time scales, the mean position of Eq.(3.55) remains unaffected by increasing initial velocity noise $\sigma_{\dot{x}_0}^2$ (Fig.3.19 left column, top panel), resulting in a vanishing SNR_x also independent of $\sigma_{\dot{x}_0}^2$ (right column, top panel). For larger times, when the nonlinear term (last term in σ_x Eq.(3.55)) becomes prominent, the initial velocity noise modifies the standard deviation, and hence the SNR, if $\sigma_{\dot{x}_0}^2 \gg \kappa \sigma_{x_0}^2 t^2/\sqrt{2}$ ($\sigma_{\dot{x}}^2 \approx 10^{-2}\sigma_{x_0}^2$, at $t = 0.3$ ms, $\Gamma = 10^{-2}$ Hz).

Similarly, the mean instantaneous velocity of Eq.(3.56) results unaffected by increasing velocity noise at short time scales. Standard deviation $\sigma_{\dot{x}}$ and $\mathrm{SNR}_{\dot{x}}$ are however subjected to it (right column, middle panel), and for values of $\sigma_{\dot{x}_0}^2 \gg 2\kappa^2 t^2 \sigma_{x_0}^2 \approx 4 \times 10^{-2}\sigma_{x_0}^2$ (at $t = 0.1$ ms, $\Gamma = 10^{-2}$ Hz), the statistics of $SNR_{\dot{x}}$ slowly converges the constant $1/\sqrt{2}$ (purple and orange dots) and it is described by Eq.(3.59).

Mean instantaneous acceleration, as shown directly in Eq.(3.57), bears the ability to be driven both by initial, velocity noise $\sigma_{\dot{x}_0^2}$, dominating in the long time scale, and initial position noise $\sigma_{x_0^2}$, dominating in the short time scale. However, as shown in Fig.3.19 (left column, bottom panel), at the short time scale ($t = 0.1$ ms) increasing values of initial velocity noise can enhance the shift of mean acceleration (orange dots) beyond the zero-damping approximation (black

dashed), still resulting in a constant $SNR_{\ddot{x}} = 1/\sqrt{2}$ (right column, bottom panel).

3.2.3 Dynamics of Most Probable Trajectories

To fully characterise the dynamics of a levitated particle in cubic potential, the maxima of position x_{max}, velocity $\dot{x}_{max}$, and acceleration $\ddot{x}_{max}$ distributions need to be analysed. A comprehensive analytical treatment of the problem at hand is not available, because the complexity of the equation of motion does not allow to derive an exact expression for the probability density function from which the maximum and curvature could be obtained. Therefore, the results presented in this section are obtained by numerical simulations of Eq.(3.48). In principle, both mean and maximum of the instantaneous quantities should increase coherently (motion in the same direction) with a constant signal-to-noise ratio, and as the noise-induced evolution is unveiled (Fig.3.20), we recall the result of the over-damped regime for maximum of position (Fig.3.11, inset, and Fig.3.20 top panel, left column) moving atypically against the potential force (Fig.3.20, top panel, right column).

The new feature of coherent motion of maximum velocity and acceleration appears at low frictions, where the latter shift alongside the potential force (qualitatively visible in Fig.3.15 middle and bottom panel, right column, red arrow). A quantitative analysis of the shift of the most-likely velocity and acceleration can be based on the results shown in Fig.3.20, where the sharp shape of the acceleration distribution (bottom panel, right column, inset) leaves room for a visible shift of its maximum, which is larger compared to the shift of the maximum of velocity distribution (bottom, panel, left column).

Similarly to the mean instantaneous velocity $\langle \dot{x} \rangle$ Fig.3.19 (left column, middle panel), the maximum $\dot{x}_{max}$ Fig.3.21 (left column, middle panel) is unaffected by increasing $\sigma^2_{\dot{x}_0}$. However, the local curvature is more sensitive to increasing initial velocity noise, resulting in a slowly converging SNR (right column, middle panel) even at small $\sigma^2_{\dot{x}_0}$ (red dots).

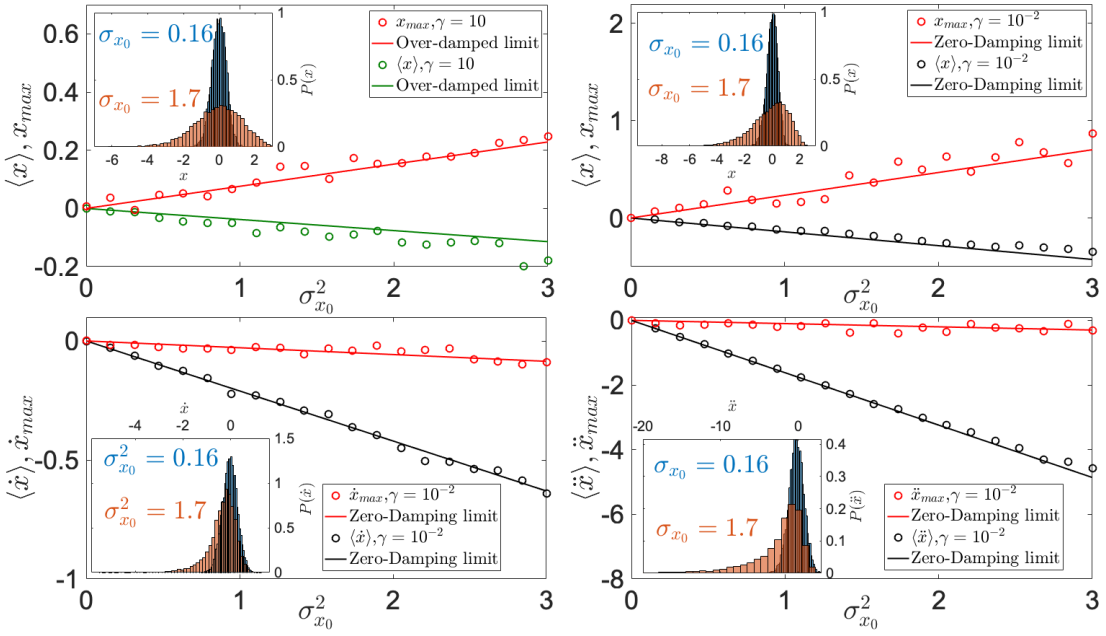

Figure 3.20: Initial noise-induced shift of maximum of position x_{max} ***(top), for high (left) and low (right) pressure limit, maximum of instantaneous velocity*** $\dot{x}_{max}$ ***(bottom left), and acceleration*** $\ddot{x}_{max}$ ***(bottom right).***
All simulations (dots) have been performed based on Eq. (3.26) using $\langle x_0 \rangle = \langle \dot{x}_0 \rangle = 0$, *and* $\sigma^2_{\dot{x}_0} = 1$. *Top panel: The atypical motion of maxima of position is highlighted (red), following in the high friction limit (left) the results obtained in the overdamped regime, namely Eq.(3.22) [2, 87]. The same atypical evolution is yet encountered at low pressures (right, red), where the red line indicates the zero damping limit evolution of the maxima. To make the shift in maximum more visible, Eq. (3.26) has been simulated with* $t = 0.3$ *ms. Bottom panel: The maximum of instantaneous velocity at the low pressure limit (left) comprises of a coherent shift (red) alongside the mean instantaneous velocity (black). A similar behavior is noticeable for statistics of acceleration (right) with its maxima (red) shifting faster at higher initial noise than that of velocity. All the insets show a snapshot of the probability distribution at different* $\sigma^2_{x_0}$ *highlighting the instability (heavy tails on the left), and showing once again a clear shift of the maximum alongside the potential force. To produce the figure on the bottom panel, Eq. (3.26) has been simulated with* $t = 0.1$ *ms. The other parameters used to produce this graph from Eq. (3.26) are* $\kappa = 6k_BT\mu m^{-3}Kg^{-1}, T = 300K, dt = 2 \times 10^{-5}$ *ms.* $nt = 10^4$ *trajectories where generated with* $N = 5000$ *samples each.*

3.3 Conclusion

We have analysed and predicted interesting noise-to-signal transitions for an overdamped Brownian particle evolving in the cubic potential. We showed that the mean position is linearly powered both by initial position noise $\sigma^2_{x_0}$ and environmental temperature T. We characterised the quality of the noise-to-signal transitions by means of the SNR, also linearly powered by initial position noise and environmental temperature.

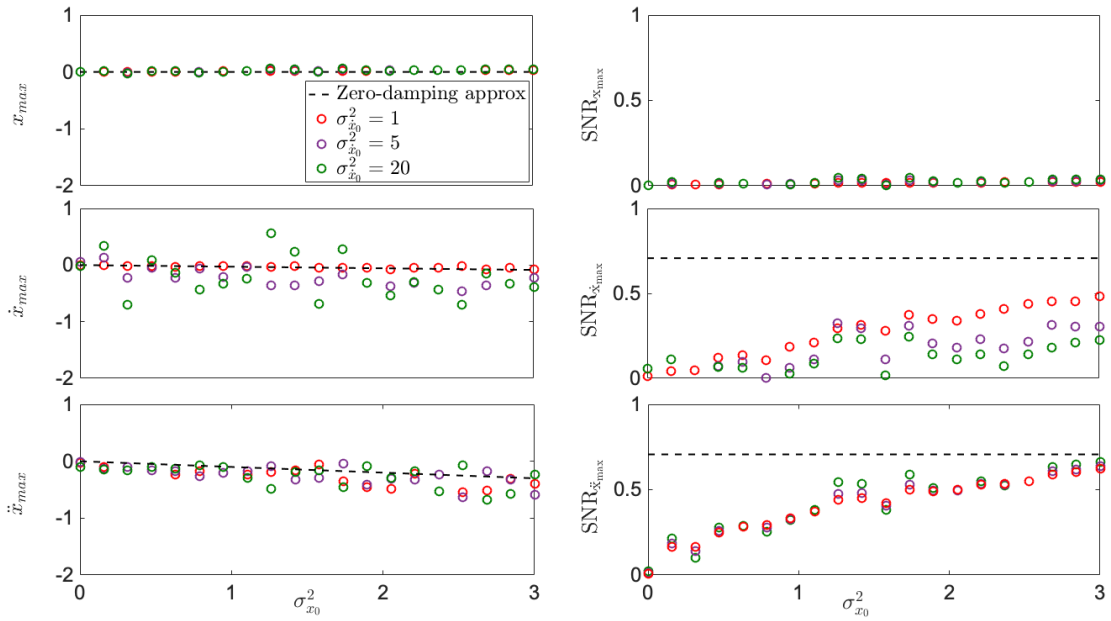

Figure 3.21: Noise-induced effect in the maxima of distribution for position (top), instantaneous velocity (middle) and acceleration (bottom) to the uncertainty of the initial velocity state, $\sigma^2_{\dot{x}_0}$.
Top panel: the evolution of the maximum of position distribution (left) is not modified by increasing initial uncertainty of the velocity state, $\sigma^2_{\dot{x}_0}$, resulting in a vanishing $SNR_{x_{max}}$ (right). Middle panel: the evolution of maximum of velocity distribution (left) displays no sensitivity to changes in initial velocity noise, whereas its $SNR_{\dot{x}_{max}}$ (right) slowly converges to $1/\sqrt{2}$ (black) with a reduced convergence for higher initial velocity noise. Bottom panel: The evolution of the maximum of instantaneous acceleration (left) is not modified by increasing initial velocity noise, and while its $SNR_{\ddot{x}}$ (right) requires a higher ensemble to calculate, it too is not affected by initial velocity noise throughout its convergence to the black line. Eq. (3.26) has been simulated using $\kappa = 6k_BT\mu m^{-3}Kg^{-1}, T = 300K, \langle x_0\rangle = 0, \langle \dot{x}_0\rangle = 0, t = 0.1ms, dt = 2\times10^{-6}$ ms. $nt = 10^6$ trajectories where generated with $N = 5000$ samples each.

These observations pave the way for nonlinear stochastic effects that can autonomously transform noise into useful mechanical effects, allowing to do autonomous mechanical work at the micro- and nano- meter scales.

Furthermore, the high instability and nonlinearity of our model, sources of fast divergent trajectories, proved to be a limiting factor for these transitions, which in turn required a different statistical description. Thus we proposed an experimentally accessible description which focuses on the maximum of position distribution, as opposed to mean position, and local curvature at the maximum, instead of the variance. Those quantities are well defined even at large time scales [2, 144]. We showed that such approach leads to atypical evolution (against the potential force) of the maximum, and a curvature that does not grow faster than the shift (increasing SNR).

Such results are general for unstable potentials comprising of an inflection point and proved to be easily observable through position detection, such as the case for these experiments [84, 87]. Instabilities are powerful resources naturally exploited by engines to perform useful work, or by amplifiers to magnify small mechanical signals for practical applications. Their characterisations are therefore an important building block towards the understanding of highly nonlinear quantum dynamics, required for quantum information processing with complex systems.

While the experimental platform of stochastic levitating optomechanics in vacuum is quickly expanding, with a unique potential to test and exploit strong nonlinear motional effects without any friction, their low pressures also allow for a direct observation of stochastic underdamped mechanical phenomena, i.e. instantaneous speed and acceleration. They therefore become new transient quantities to be first explored and later exploited for applications. Stimulated by this knowledge we focused on the development of the first transient nonlinear ballistic effects of noise-induced shift of instantaneous velocity and acceleration for parameters of the levitated nanoparticles optically trapped in high vacuum. Our results pave the way to explore quantum mechanical analysis deeply underdamped and highly cooled particles in unstable potentials, initially close to the mechanical ground state.

Methods 4

Numerical Simulation of Stochastic Dynamics in Cubic Potential

Only a few problems in statistical mechanics are exactly solvable. In non-linear dynamics this is typically not the case [187, 189]. While not being exactly solvable, these problems cease to analysis based on approximations schemes. Computer simulations, therefore, provide insights and results for problems that otherwise will not be fully tractable [189]. Moreover, computer simulations proved to be a useful tool for comparability with experimental results, and they can offer insights on new features of the problem at hand, due to their high versatility [189, 190]. One can say that computer simulations are nothing but a bridge between theoretical models and experimental results.

4.1 Overdamped Regime

In this section, we will focus on the tricks of the trade used in the computation of highly nonlinear systems in the overdamped regime, using the cubic potential as the toy model. We will focus on the computation of the maximum of the distribution, and how to compute it beyond the characteristic time.

4.1.1 Stochastic Simulation and Time-Steps

A stochastic differential equation (SDE) is an object of the form

$$\dot{x} = h(x,t) + g(x,t)\eta(t), \tag{4.1}$$

where $h(x,t), g(x,t)$ describe respectively, the drift and diffusion term. The solution of Eq.(4.1) is a stochastic process $x(t)$ that satisfies

$$x(t) = x_0 + \int_0^t h(x,t')dt' + \int_0^t g(x,t')dW, \tag{4.2}$$

where $dW = \eta(t')dt'$ is a Wiener process [178]. The first step to compute the Langevin equation (4.1) lies in the discretisation of time, by dividing it into N small finite steps of a length dt, such that

$$t_n = \tau n, \qquad n = 1, 2, ..., N. \tag{4.3}$$

The primary problem in stochastic processes is the computation of the stochastic integral

$$\int_0^t g(x,t)dW_t \approx \sum_{n=0}^{N} g(x,t_n)(W_{t_n+1} - W_{t_n}), \tag{4.4}$$

which can be approximated by the sum in the limit of $dt \to 0$ [190].

To simulate the stochastic integral in Eq.(4.4), there are different algorithms that one can use. The one used in this thesis, is the Euler-Maruyama scheme [190, 191]. The algorithm uses the Markov chain approximation to compute the true solution of Eq.(4.1) (ref). Moreover, one can explore the convergences of this scheme, by varying the step size, to define a strongly convergent scheme, when $\lim_{dt\to 0} E\big[|x_t - x_t^{dt}|\big] = 0$, and a weakly convergent scheme when $\lim_{dt\to 0} \big|E\big[x_t\big] - E\big[x_t^{dt}\big]\big| = 0$. where x_t is the exact solution, and x_t^{dt} is the result of the simulation with the step dt. The convergences are not unconditional, therefore the following conditions need to be valid [191]

1. The functions $h(x,t)$, and $g(x,t)$ are four time continuously differentiable and their first derivatives are bounded.

2. The functions do not grow too fast with parameters.

The above conditions are the basic building blocks to the concept of the convergence order

$$E\big[|x_t - x_t^{dt}|\big] \leq K_t^{\gamma}(dt) \tag{4.5}$$

$$\Big|E\big[x_t\big] - E\big[x_t^{dt}\big]\Big| \leq K_t^{\gamma}(dt), \tag{4.6}$$

where the constant $K_t^{\gamma}(dt)$ depends on the time, t, of the considered stochastic equation, with the order γ. The meaning behind this convergence order is simply that if the scheme is convergent with order γ, and we make a step k times smaller, the approximation error will decrease by a factor of k^{γ} [191]. This give us the idea of the time-step of the problem we are computing.
The Euler-Maruyama scheme is weakly convergent with order 1, and strongly convergent with order 1/2 [190, 191]. Of course there exists a limitation to the dimension of the time-step, because if it is too small then computational errors caused by the use of finite precision numbers might arise.

4.1.2 Simulating within the Characteristic Time

In the specific case of a Brownian particle in cubic potential

$$\dot{x} = -kx^2 + \sqrt{2\frac{k_B T}{\gamma}}\eta(t), \tag{4.7}$$

the dynamics is subjected to a divergence for finite time [2, 143]. The reason behind this is due to the fact that the particle dynamics is considerably different for $|x(t)| < (3k_BT/k)^{1/3}$, where the particle diffuses freely with a weak drag to the unbounded region, and $|x(t)| > (3k_BT/k)^{1/3}$, where the drag force rapidly increases as $x(t)$ leaves the plateau [2, 144]. For the above reasons, one needs to be extremely careful in exploring the convergent schemes for the Euler-Maruyama method. Specifically, referring to the convergence conditions, the cubic potential is four times continuously differentiable with bounded first derivative, but the divergence can violate the second point, given that in certain regions of parameters, the function grows quickly towards the divergence. Notwithstanding, for short time dynamics defined by the characteristic time, one can safely assume that both conditions 1, and 2 for the convergence are obeyed.

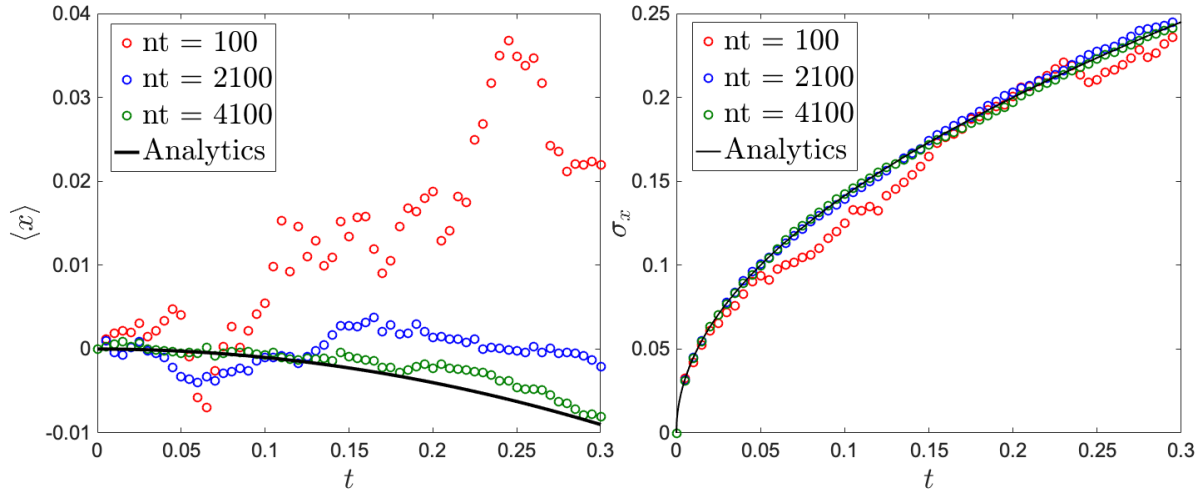

Figure 4.1: Evolution of mean position (left), and standard deviation (right) in time, for different ensemble size.
The convergence of position moments, for the short time dynamics, is reached for a fairly small number of trajectories , nt ≈ 4000 (green), allowing high accuracy at a small cost of computation time. For this figure, Eq.(3.5) has been simulated, using $\sigma_0 = 0, D = 0.1, dt = 10^{-5}, k = 1$

The diverging trajectories generate heavy tails in the PDF $P(x,t)$, which shows the increase of moments, first and second, that are responsible for the drop of the SNR in Fig.3.13. Although in simulation it is easy to witness the aforementioned heavy tails, and the drop of the SNR, the dynamics is bounded by a divergence time (see Sec. 3.1.1) that requires a certain control over the time-step to be able to follow the fast divergent dynamics. Once the divergence dominates the dynamics, the convergence conditions cease to be valid, rendering moot the numerical method in use. For time smaller than the characteristic time, estimable from the divergence time introduce in chapter 3 (see Fig.3.4), the accuracy of the simulation is conditioned by the ensemble size (number of trajectories). For the global moments calculation, the ensemble requirement are rather frivolous, as can be seen in Fig.4.1, where good accuracy can be obtained even for 4000 trajectories, translatable in small time computation. For local moments computation, the simulation requires a larger ensemble size, as shown in Fig.4.2, where convergence is slow and with small accuracy.

Both Fig.4.1, and Fig.4.2 depict a scenario in which a time evolution is plotted, with arbitrarily small environmental noise and no initial thermal noise. Although Figs.4.1,4.2 show qualitative ensemble size requirements, it is important to keep in mind that the more noise acts on the system, the higher the ensemble size is.

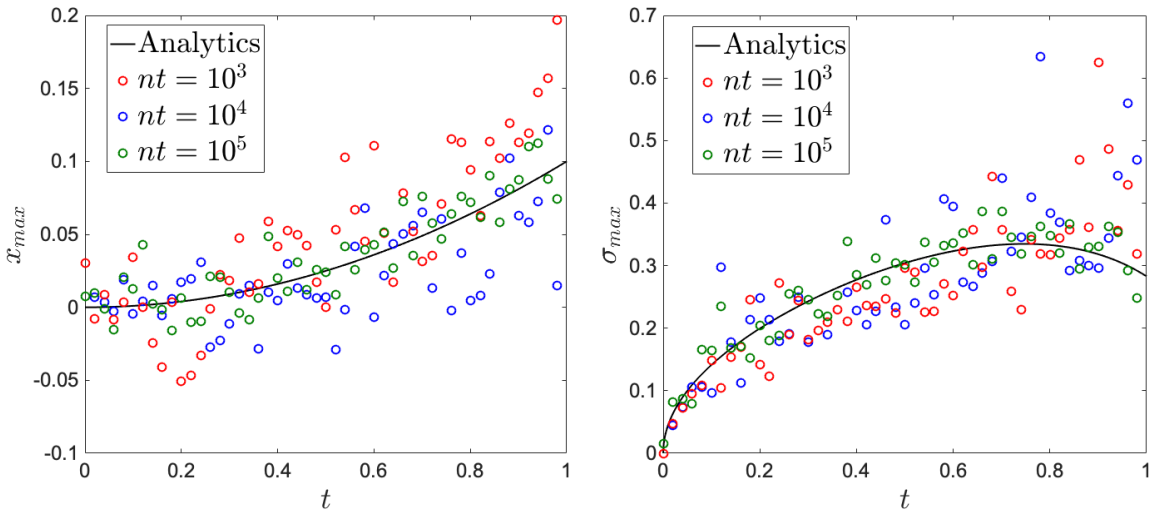

Figure 4.2: Time evolution of maximum of distribution (left), and curvature (right) for different ensemble size.
The convergence of moments for the most likely trajectory, for the short time dynamics, is slow, requiring at least $nt \approx 10^5$ *(green). The accuracy of the simulation therefore requires a higher computation time, of the order of* 30 *minutes. For this figure, Eq.*(3.5) *has been simulated, using* $\sigma_0 = 0, D = 0.1, dt = 10^{-5}, k = 1$

4.1.3 Simulating beyond the Characteristic Time

Passed the point of characteristic time, dictated by the bounds discussed in Sec. 3.1.1, the global moments of particle position bare no information. For this reason the computation of local moments has been introduced in Section 3.1.4. Beyond this point, the convergence rule is no longer valid, as the drift force in the Langevin equation grows fast with the growing distance from the origin of coordinates. Diverging trajectories are dominating the dynamics, and heavy tails are hiding the maximum of the distributions. An alternative method to reach higher accuracy, rather than brute forcing with increasing ensemble size, is required. To better explain the problem, and understand the root of the solution, it is good to introduce the concept used as "accuracy". Accuracy can be defined as a measure of closeness between the simulated value and the real value [191, 192]. A good measure of accuracy, numerically, is the mean absolute error (MAE), which is calculated as

$$MAE = \sum_{i=1}^{n} \frac{|y_i - x_i|}{n}, \tag{4.8}$$

where y_i is the prediction, and x_i is the true value. Looking at Fig.4.3, one can see the accuracy for mean and maximum as a function of the ensemble size (number of trajectories)

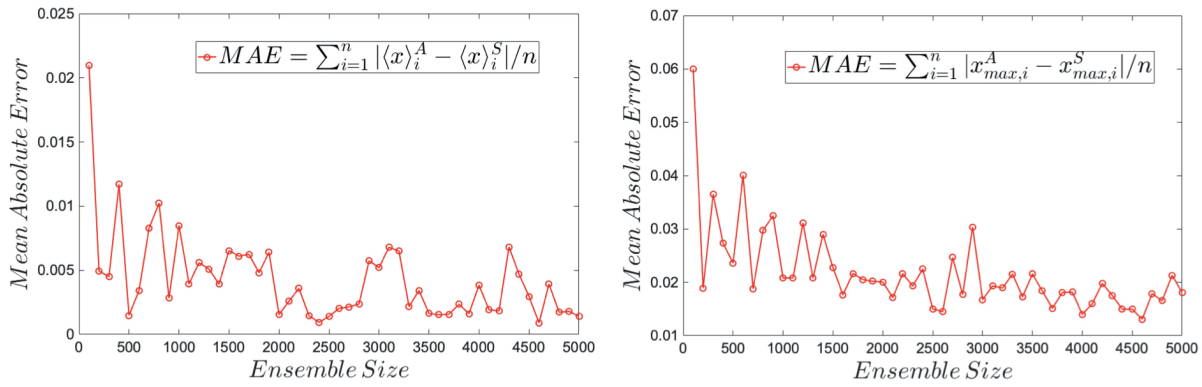

Figure 4.3: Mean Absolute Error for mean position (left) and maximum of the distribution (right), as a function of ensemble size.
The computed MAE is obtained by comparing the analytical results (subscript A), Eq.(3.10) (left), and Eq.(3.22) (right), with the simulated one (subscript S). The MAE of mean position, for small ensemble size $nt \approx 4000$ *converges to a small error* $MAE \approx 5 \times 10^{-3}$*, whereas for the maximum of the distribution, at the same ensemble size, the MAE reaches a value an order of magnitude higher* $MAE \approx 2 \times 10^{-}2$*, which as depicted in Fig.4.2, is of the order of the value of* x_{max}*. For this figure Eq.(3.5) has been simulated, using* $k = 1, D = 0.1, \sigma_0 = 0.0, t = 0.2, dt = 10^{-5}$

in the unstable cubic potential (4.7), with diverging trajectories. It can be seen that all of the MAE curves saturate, showing, not surprisingly, that the ensemble size makes for great accuracy. Comparing the top and bottom panels of Fig.4.3, it can be seen that while the global moments can be calculated with high accuracy, limited by the precision given by the standard deviation, the maximum of the distribution is computed with a smaller accuracy, 1 order of magnitude compared to the global moments. Moreover, the convergence of MAE is slower in the maximum, than the first moment of particle position. It has been shown in the previous section that for times shorter than the characteristic times, a mere increasing of the ensemble size could be enough to obtain accurate numerical results. The natural arising question is whether the latter is true if we are simulating for times larger than the characteristic times, while looking at local moments only.

To answer the question, it could be interesting to compare the SNR, that shows time scales of the problem, to the evolution of the maximum of PDF of particle position. As shown in Fig.4.4, for time smaller than the characteristic time, the accuracy obtained on the x_{max} can be increased by increasing the ensemble size; more importantly whilst approaching the characteristic time, after which the divergence dominates the dynamics, the accuracy obtained in the computation of x_{max} decreases vertiginous. To push the simulation further, and ultimately being able to

compute features of the cubic potential beyond the characteristic time, a deeper investigation on the system is required. As presented more in detail in [2, 144], the PDF vanishes at $|x| \to \infty$, whereas the probability current does not. As a result, one can approximate the singular point $x = -\infty$ by an absorbing boundary [127, 193] at a finite position, a.

The way the absorbing boundary works is simply catching the particles when the point $x = a$ gets hit for the first time. The condition limiting the absorbing boundary is given by $a < -(3k_BT/k)^{\frac{1}{3}}$, where no properties on the plateau, for the slow stochastic motion, will be affected [2].

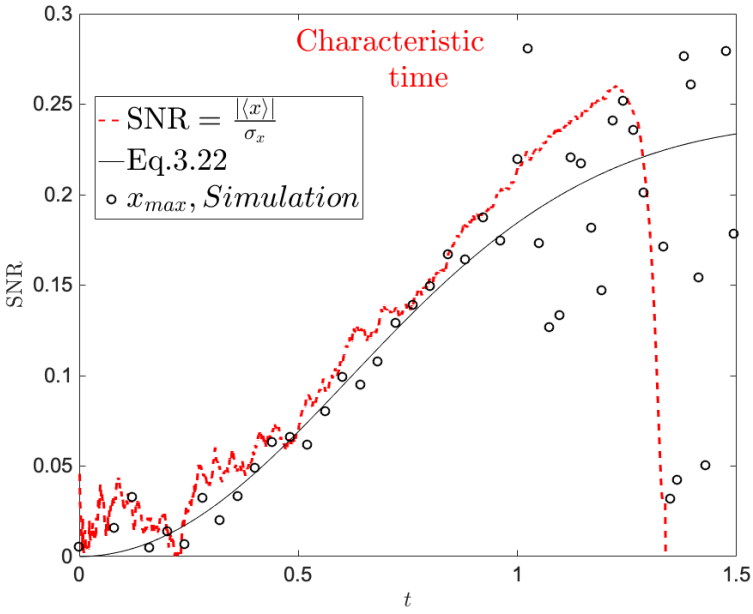

Figure 4.4: Computation of x_{max} compared to characteristic time.
The graph can be split into two main parts; the first is for time smaller than the characteristic time, defined in this graph as the maximum of the SNR *calculated from global dynamics, where the x_{max} can be computed accurately by mere increase of ensemble size. Secondly approaching the characteristic time, the error performed on the computation of x_{max} increases, resulting in a poor accurate computation for time larger than the the turning point of* SNR*. For this figure Eq.(3.5) has been simulated, using $k = 1, D = 0.1, \sigma_0 = 0.0, dt = 10^{-5}$. An ensemble size of 3×10^5 has been used to generate this graph.*

The absorbing boundary method, is aimed to analyse those trajectories that survive at the plateau. To achieve such scenario, one has to implement a rejection scheme upon the evolving trajectory, following the rule: "*Whenever the trajectory hits the absorbing boundary for the first time, reject the entire trajectory*" [144]. Visually, what happens to the trajectory is shown in Fig.4.5, where on the left it is shown how an ensemble of trajectories evolves in the cubic potential, dictated by a dominating divergence for time larger than the characteristic time defined by the parameter of the problem, and it can be seen that while trajectories are rapidly diverging, there are few that survives the plateau.

Those trajectories are the ones that characterise the dynamics of the maximum of the PDF. Imagining now to draw an imaginary line on the trajectory of Fig.4.5 (left) following the rules

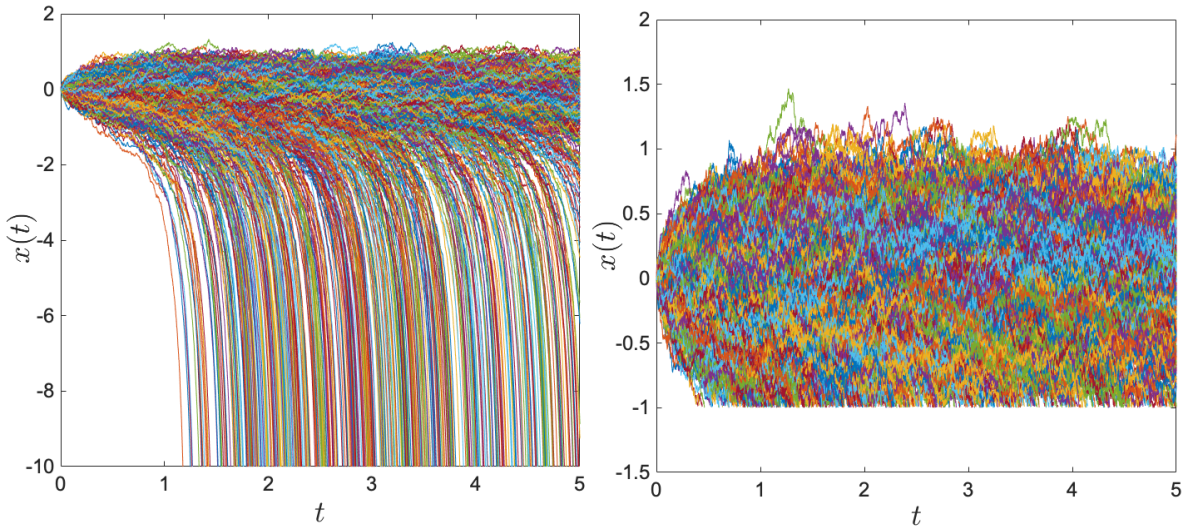

Figure 4.5: Comparison of the trajectory evolution, and the role of absorbing boundary.
On the left, the evolution without absorbing boundary is presented, where diverging trajectories are driving the dynamics. On the right, the evolution of trajectories when the absorbing boundary is used. To produce this graphs, Eq.(3.5) has been simulated, using the following parameters: $x_0 = 0$, $\sigma_0 = 0$, $T = 0.1$, $k = 1$, $dt = 10^{-3}$, *and* 10^3 *trajectories were generated. The number of absorbed trajectories, for the above parameters, is* $\approx 60\%$.

dictated by a previously defined, and continuously monitoring during the simulation if a trajectory hits the point on the line. If it does, we just eliminate the trajectory and only keep the ones which survive for the time interval of the simulation. The survived trajectories will contain the information of the local moments even beyond the characteristic time of divergence, Fig.4.5 (right). After having applied the absorbing boundary, even for short times, the global moments are strongly influenced by the position of the boundary, as they are biased by the presence of the absorbing boundary, as soon as even a trajectory gets rejected by the scheme. Having eliminated all the diverging trajectories, the resulting PDF will have a narrower width than the full cubic evolution if the boundary is placed inside the plateau region.

As a result, the precision upon the numerical estimation of the maximum of particle position, increases as the uncertainty is smaller, Fig.4.6 (right) (blue line), when diverging trajectories are rejected. The resulting estimation is presented in Fig.4.7, showing an improvement upon the computation of x_{max} compared to Fig.4.4, approaching and surpassing the characteristic time of divergence for a particle in cubic potential. Moreover, in Fig.4.7 (right), the MAE about the new rejection scheme is shown as a function of ensemble size, illustrating the improvement on

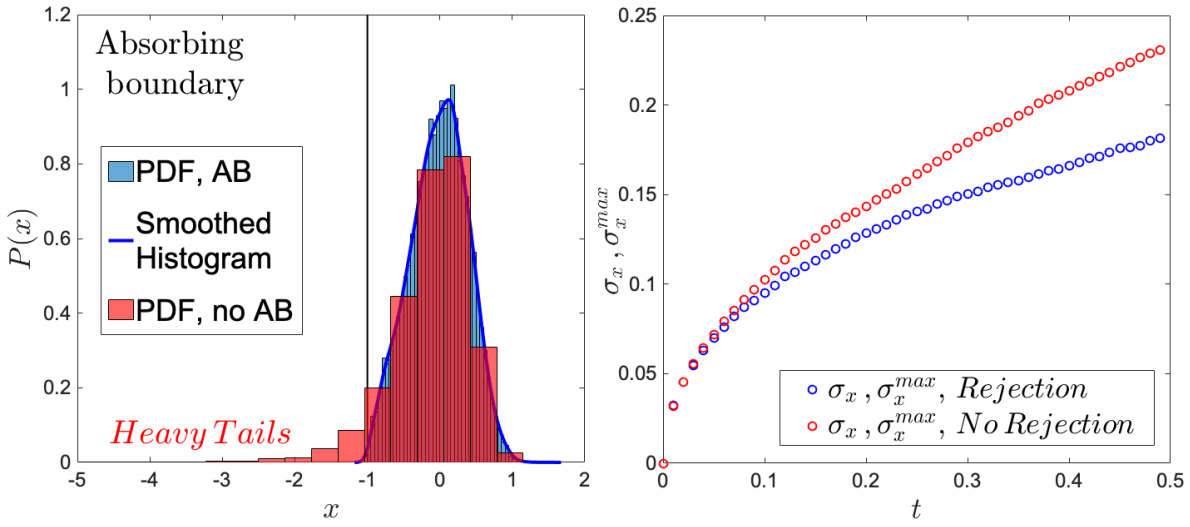

Figure 4.6: Comparison of the rejection (blue) and no rejection (red) methods of computing the maximum of position distribution.
On the left, a comparison of PDFs generated via the two methods is presented, showing not only how can one increase the accuracy of the estimation, but also how to reduce the error, and consequentially increase the precision. On the right, the suppression of the error for the estimation of x_{max} is presented. To produce this graphs, the following parameters were used: $x_0 = 0$, $\sigma_0 = 0$, $T = 0.1$, $k = 1$, $dt = 10^{-4}$, $t = 1.0$, and 210^4 trajectories were generated.

the accuracy computation of the local moments of particle position.

4.2 Underdamped Regime

In this section we will focus on discussing the strategies and precautions used to compute averaged $\bar{v}, \bar{a}$ and instantaneous $\dot{x}, \ddot{x}$ quantities for highly nonlinear systems, such as the case of a particle in the cubic potential. In the underdamped regime, the SDE assumes the following general form

$$\dot{x}(t) = \frac{v(t)}{m}, \tag{4.9}$$

$$\dot{v}(t) = -\gamma v(t) - kx^2 + \sqrt{\frac{2k_B T\gamma}{m}}\eta(t). \tag{4.10}$$

The above equation allows the computation of instantaneous velocity $\dot{x}$, and acceleration $\ddot{x}$, quantities that vanish in the high friction limit (Eq.(4.1)), leaving space to average quantities $\bar{v} = \Delta x/\Delta t$, and $\bar{a} = \Delta\bar{v}/\Delta t$. It is of the utmost importance to understand how to properly compute the two quantities numerically.

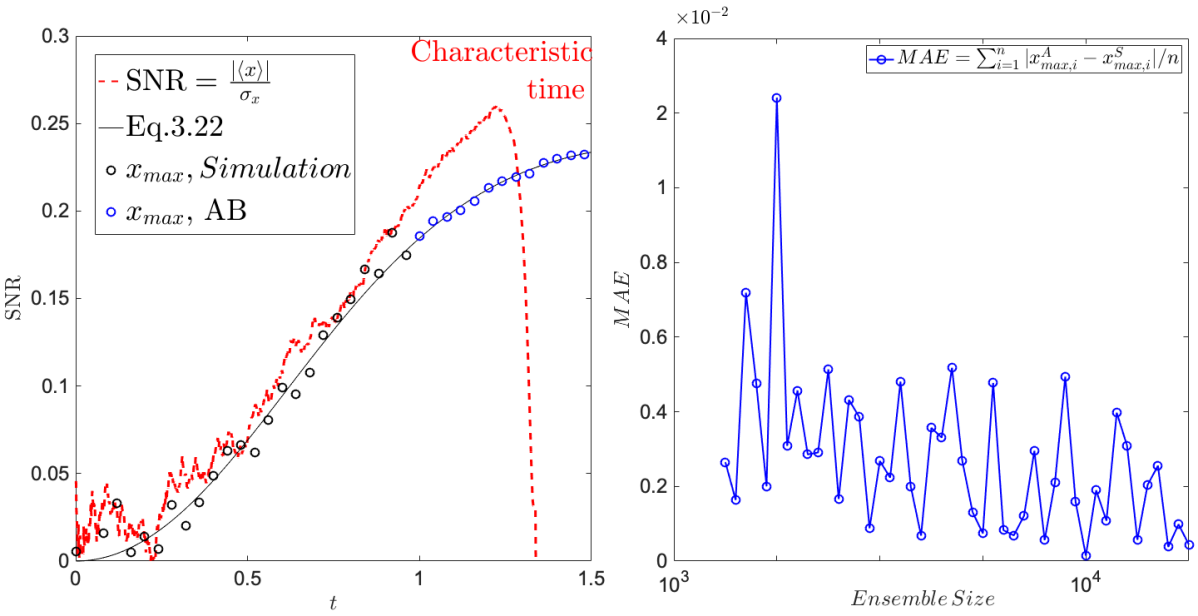

Figure 4.7: Computation of x_{max} compared to characteristic time, extension with rejection scheme.
Left: The black dots for time $t < 1$ remains unchanged with respect to Fig.4.4, whereas the blue dots show the improvement upon the calculation of x_{max} for time approaching the characteristic time defined by the max of the SNR *for global dynamics, and beyond. The accuracy obtained by applying the rejection scheme is much higher than in the computation of x_{max} in Fig.4.4, for the same ensemble size.*
Right: The Mean Absolute Error referring to the blue circles of the left plot, where it can be seen the improvement upon the MAE compared to Fig.4.3. For this figure Eq.(3.5) has been simulated, using $k = 1, D = 0.1, \sigma_0 = 0.0, dt = 10^{-5}$. An ensemble size of 3×10^5 has been used to generate this graph.

4.2.1 Average vs Instantaneous Quantities

Given a position trajectory evolving in time $x(t)$, one can compute the average velocity simply as the ratio between the distance travelled and the elapsed time $\bar{v} = \Delta x/\Delta t$. By taking its limit as the elapsed time Δt approaches zero $\dot{x} = \lim_{\Delta t \to 0} \Delta x/\Delta t = dx/dt$ allows to calculate the instantaneous velocity, telling us how fast the particle is moving anywhere along its path. In the underdamped regime, the instantaneous velocity $\dot{x}$ is naturally introduced in the equation of motion (4.9) and in the low friction limit, where the damping time is long, the computation always outputs the instantaneous quantity with accuracy varying with the sample size (see Fig. 4.8 top panel). As the friction becomes larger, the damping time shortens resulting in a time evolution of velocity comprising both ballistic ($t \ll \Gamma$) and diffusive dynamics ($t \gg \Gamma$). The behavior can be observed in Fig. 4.8 (bottom panel, red dots), where for short time the velocity fits with the

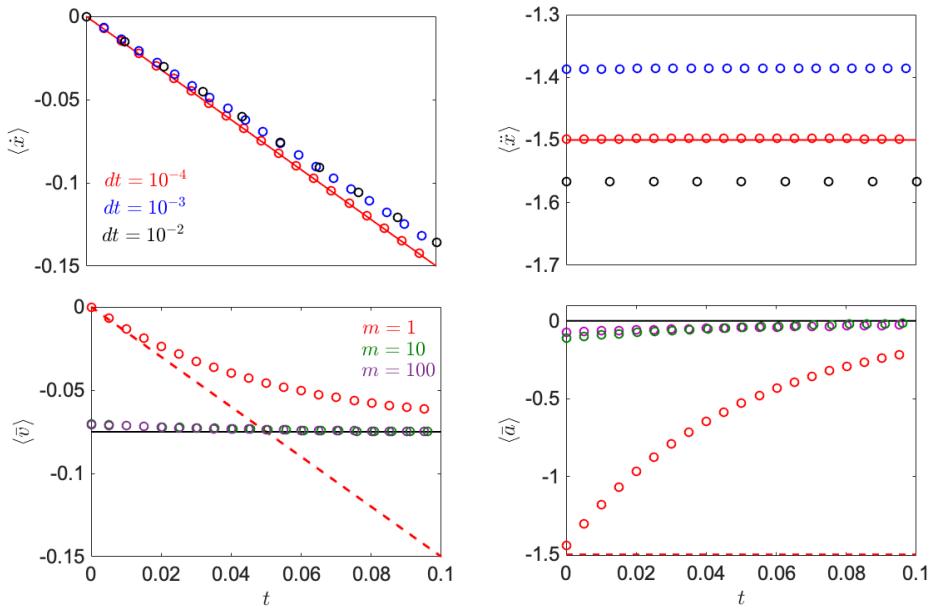

Figure 4.8: Computation of average and instantaneous velocity (left column) and acceleration (right column) for different timesteps dt***, for low pressure regime (top) and high pressure regime (bottom).***
To obtain the dots, Eq.(4.9) has been simulated. Top panel: The instantaneous velocity $\dot{x}$ *(left) is naturally introduced in the equation of motion Eq.(4.9), and its mean* $\langle \dot{x} \rangle$ *can be easily computed even at larger timesteps (black). Instantaneous acceleration* $\ddot{x}$ *(right) requires the numerical differentiation algorithm to be calculated, and hence its mean* $\langle \ddot{x} \rangle$ *is more prone to error for increasing timesteps (blue, black). Bottom panel: in the high friction limit, by accessing the velocity output from eq.(4.9), one registers both ballistics and diffusive timescales (red dots). By making use of the differentiation algorithm* $x(n+m)-x(n)/mdt$ *one can see a quick convergence of the average velocity (left) and acceleration (right) for small values of m (green) to the analytical results for overdamped dynamics (black). The Red lines correspond to analytical predictions at low pressure, whereas black lines correspond to analytical prediction at high pressure.*

theoretical approximation of Eq.(3.30) (red dashed line), whereas for larger time the simulated curve converges to the result of average velocity of Eq.(3.14))(solid black line). Tweaking the spacing between the position difference $\Delta x = x(n+m) - x(n)$ and time $\Delta t = mdt$, or simply running simulations for larger timesteps dt, allows to calculate more efficiently the average velocity $\bar{v} = \Delta x/\Delta t$. The above results is computationally inexpensive and quickly converges (green and purple dots) to the theoretical results of Eq.(3.14) for the overdamped dynamics. A similar logic applies for the computation of both instantaneous $\ddot{x} = d\dot{x}/dt$ and average $\bar{a} = \Delta\bar{v}/\Delta t$ acceleration. In the low friction regime, within the short time approximation, there exist a second way of computing acceleration statistics without using differentiation techniques. For this, one needs to rewrite Eq.(4.9) as $\ddot{x} = -kx^2$, describing the deterministic dynamics of a damped

particle in cubic potential, and realise that any statistics of acceleration can be obtained directly by the statistics of position determined by the geometry of the potential. This method does not decrease the ensemble size requirements, nor improve the accuracy of the result, but it allows for a faster computation of the statistical quantities of instantaneous acceleration $\langle\ddot{x}\rangle, \sigma_{\ddot{x}}, \mathrm{SNR}_{\ddot{\mathrm{x}}}$ (red dots).

4.2.2 Correlations and Crosschecks of the Dynamics

To double check the results of the simulations, we employ a correlation-based method, which consists of a normalised measurement of the covariance $\rho_{xy} = cov(xy)/\sigma_x\sigma_y$, where $cov(xy) = \langle xy\rangle - \langle x\rangle\langle y\rangle$ is the covariance matrix of the pair, with values bounded between -1 and 1. This quantity gives information about the absolute value and the direction of the correlation. Such method is often referred in literature as Pearson's correlation method [192], and for a particle in cubic potential the simulated pairs present for short time dynamics $t = 0.1$, and negligible γ, the following correlation

$$\rho_{\dot{x}\ddot{x}} = \frac{1}{\sqrt{\frac{\sigma_{\dot{x}_0}^2}{2\kappa^2\sigma_{x_0}^4 t^2} + 1}}, \tag{4.11}$$

$$\rho_{\dot{x}\Delta x} = \frac{\sigma_{\dot{x}_0}^2 t + \kappa^2\sigma_{x_0}^4 t^3}{\sqrt{\sigma_{\dot{x}_0}^4 t^2 + \frac{5}{2}\kappa^2\sigma_{\dot{x}_0}^2\sigma_{x_0}^4 t^3 + \kappa^4\sigma_{x_0}^8 t^6}} \tag{4.12}$$

$$\rho_{\Delta x\ddot{x}} = \frac{\kappa^2\sigma_{x_0}^4 t^2}{\sqrt{2}\kappa(\sigma_{x_0}^2 + \sigma_{\dot{x}_0}^2 t^2)\sqrt{\sigma_{\dot{x}_0}^2 t^2 + \frac{1}{2}\kappa^2\sigma_{x_0}^4 t^4}}. \tag{4.13}$$

The above equation, together with Fig.4.9, demonstrate that low damping, $\Gamma = 10^{-2}$ Hz (middle column), does non modify the correlations neither in time (top panel), nor in initial noise (bottom panel) allowing for a first initial check of the dynamics as for $\sigma_{\dot{x}_0}^2 = 0$ the correlations in Eq.(4.11) all output unity. Moreover, when external inputs are applied, such as nonvanishing initial velocity noise $\sigma_{\dot{x}_0}^2$ (rightmost column), the correlations containing velocity (red and blue dots) are affected the most, showing their convergence to unity as initial position noise increases.

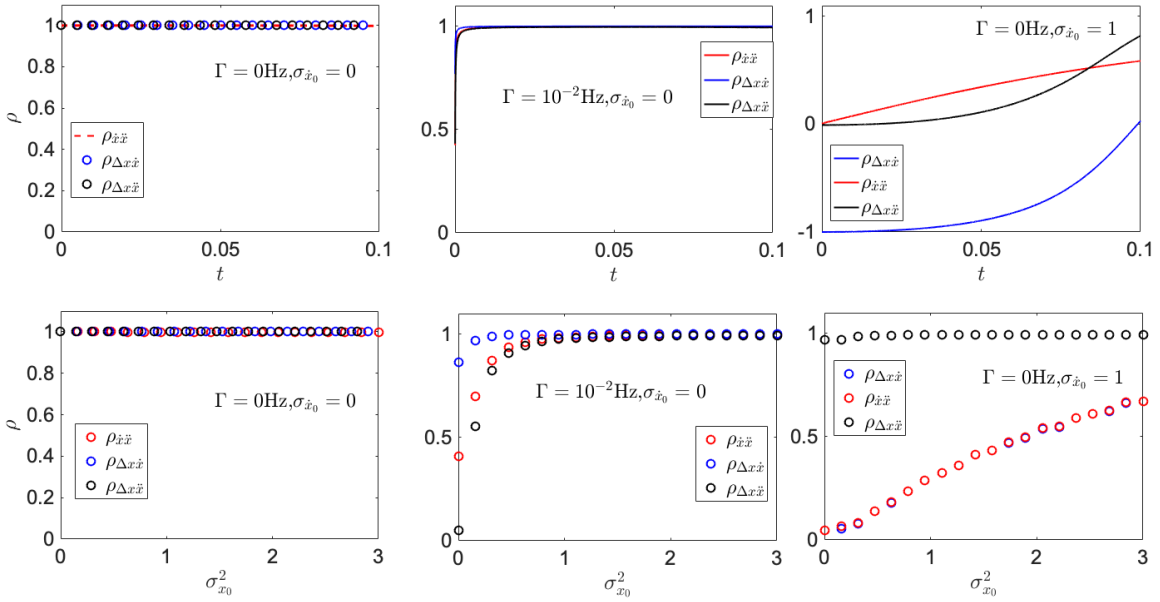

Figure 4.9: Pearson correlation coefficients, in time (top), and initial position noise (bottom) for the pairs $\rho_{\dot{x}\ddot{x}}, \rho_{\dot{x}\Delta x}, \rho_{\Delta x\ddot{x}}$.
From left to right the pure deterministic dynamics for $\langle \dot{x}_0 \rangle = \langle x_0 \rangle = 0$, *and noiseless initial velocity (left), followed by the small pressure regime (middle), and finally the noisy initial velocity (right). Left column: in the pure deterministic scenario,* $\Gamma = 0$ $\sigma^2_{\dot{x}_0} = 0$, *all the pairs are fully correlated with each other Middle column: A slight change in damping* $\Gamma = 10^{-2}$, $\sigma^2_{\dot{x}_0} = 0$, *shows little to no modifications as the pairs quickly converge to full correlation. Right column: a change in initial velocity noise* $\Gamma = 0$, $\sigma^2_{\dot{x}_0} = 1$ *disrupts the correlation, leaving all the pairs slowly converging to full correlation* $\rho = 1$, *aside for* $\rho_{\Delta x\ddot{x}}$ *(black), which remains fully correlated as the initial position noise increases. Eq. (3.26) has been simulated using* $\kappa = 6k_BT\mu m^{-3}Kg^{-1}, T = 300K, \langle x_0 \rangle = 0, \langle \dot{x}_0 \rangle = 0, dt = 2 \times 10^{-5}$ *ms.* 10^4 *trajectories were generated with* 5000 *samples each.*

4.3 Conclusion

We have shown the numerical approach to compute the transient features analysed and discussed in Chapter 3. We began by analysing the computation of the stochastic integral of Eq.(4.4), which introduced the Euler-Maruyama algorithm used throughout this thesis, followed by the analysis of its convergent scheme allowing to understand the importance of the choice of the timestep used in the computation.

We then proceeded by analysing the convergence scheme upon the computation of a particle in the cubic potential within the characteristic time, i.e., before the divergence kills the trajectories, where the scheme is still applicable for the short time dynamics. We showed, by virtue of Figs. 4.1- 4.2, that the accuracy of the simulation is conditioned only by the ensemble size,

proving to be frivolous for the computation of the global moments $\langle x \rangle, \sigma_x^2$, while demanding for the local ones x_{max}, σ_{max}.

Furthermore, we showed that the convergence scheme cease to be valid when computing beyond the characteristic time, where the drift force of Eq.(4.7) grows fast with the growing distance from the origin, generating diverging trajectories.

Such scenario required an alternative method of computation, based on a rejection scheme, which has been introduced and analysed by means of of the *mean absolute error*.

This rejection scheme allowed us to characterise and compute the properties of the surviving trajectories, even in the long time limit, with an increase accuracy of the computation, as showed by Figs. 4.4- 4.7.

When simulating the underdamped motion of a particle in cubic potential it is of the utmost importance to realise how to compute average $\bar{v}, \bar{a}$ and instantaneous $\dot{x}, \ddot{x}$ quantities. The last section of this chapter analyses the methods and techniques used to compute such quantities, see Fig. 4.8.

Lastly, we introduced a method, based on the Pearson correlation coefficient, as a crosscheck of the computed dynamics, see Fig. 4.9.

Such methodologies, broadly applicable to any highly unstable potential, allow for versatile simulations. In addition to that, they simultaneously unveil the increasing computational demands in terms of time of simulation and hardware requirements, because of the increasing complexity of the system.

Conclusion and Outlooks

In this work, we investigated noise-to-signal transitions for a Brownian particle evolving in the unstable cubic potential. We studied two essential regimes with high experimental relevance in the actual scientific scope, comprising of overdamped and underdamped regime.

Chapter 2 was devoted to an overview of linear potentials and the evolution of their moments. Specifically, the absence of a potential (free particle) was introduced to demonstrate ballistic dynamics at short time scale in the limit of strong damping, not predicted by Einstein theory of diffusion. The linear ballistic effects for a particle trapped in an optical harmonic potential in liquid has been observed in 2010 [179–181].

Furthermore, the damped and driven dynamics of a particle in a linear quadratic potential was presented to explore how the coherent motion can be induced by both initial conditions (thermal equilibrium at initial time without a driving force, or out of equilibrium at initial time), or by external forces. The signal to noise ratio SNR was then introduced, showing the relevant important dynamical quantities for the respective regime (i.e. position x in high friction limit, and instantaneous velocity $\dot{x}$ in the low friction regime). It dictates the upperbound of the linear potentials, to later be compared with the nonlinear system.

The inverted quadratic potential, which naturally appears at the centre of a symmetrical double well potential, is a very interesting system because although it is still linear, it allows to introduce and discuss the role of instability, which can be used to realise low noise linear amplification. Although there is a plethora of experimental realisations of stochastic dynamics in the optical double well potential [194–197], no analysis of fast transient effects, at the heart of low noise linear amplification, starting from unstable positions are available.

The fast pace at which the stochastic levitated optomechanics field is evolving, manipulation

of optical potentials and fast optical measurements, allowed to test and exploit nonlinear mechanical effects. Chapter 3 delves into the description of the mechanical dynamics of a particle trapped in the optical cubic potential. The main result, at the heart of the unstable nonlinear systems, lies in the noise induced mechanical mean displacement $\langle x \rangle$ (in the high friction limit) Fig.3.13 (red line) [143]. A consequence of the unstable dynamics sees the PDF of the particle position developing heavy tail, while its moments cease to exist. Motivated by the limitation imposed by the rapid diverging trajectories, resulting in variance of position growing faster than its mean, we proposed and analyzed local directly measurable characteristics $x_{max}, \sigma_{x,max}$, overcoming such limitation [2]. A key result in this framework shows the peculiar behavior of the most probable position, which moves opposite to the acting force; both in time and temperature. Those results have been experimentally observed [84, 87], showing the time evolution of both mean and maximum of position distribution in short and long times dynamics.

Motivated by the already reached underdamped regime for levitated experiments [38, 48, 140, 180], which allow to probe the fundamentals of nonlinear stochastic dynamics in the limit of weak friction, we proposed and demonstrated the first nonlinear ballistic effect for levitated nanoparticles optically trapped in high vacuum, consisting of the noise-induced instantaneous speed and acceleration of in the highly unstable cubic potential. The key result, shown in Fig.3.15, demonstrates that the noise-induced effect turns to instantaneous velocity and acceleration. Moreover, we observed the coherent motion, alongside the potential force, of the mean and maxima of instantaneous speed and acceleration distributions, Fig.3.20.

Such results, obtained for parameters of the current underdamped experiments, motivate an experimental verification with further investigation on the robustness of the effect against particle with initial nonzero velocity 3.17. While cryogenic cooling is not necessary to observe the transient effect, a reduction of initial velocity noise seems required for a reliable experimental observation (Fig.3.19), either via cooling or post-selection.

In the last chapter, 4, we discuss the numerical methodologies to simulate the dynamics of a particle in unstable potentials. Although we focus on a particle in cubic potential, our methodologies are broadly applicable to any highly unstable potential.

The key result of this chapter is contained within the rejection scheme that not only allowed to compute the maximum of the distribution beyond the characteristic time, but it also proved

useful to minimise the demanding ensemble size requirement for its computation.

Although out of the scope of this work, it has been emphasised the increasing computational demands in terms of time of simulation and hardware requirements. Such demands are due to the increasing complexity of the systems, unavoidable when analysing nonlinear systems.

To better visualise the experimental path that followed the theoretical results presented in this thesis work, and to understand the corners of interesting effects yet to observe, we present the following table

Table 4.1: Experimental Tests

Effect	**Measured**	**Not measured**
Eqs.(3.10),(3.11), Fig3.7. Short time evolution of position moments	[84]	
Eqs.(3.14),(3.16), Fig.3.9. Short time evolution of average velocity moments driven by initial noise		**X**
Fig.3.10 (light tail of position PDF)		**X** (demanding*)
Fig.3.12 (time evolution of local characteristics for different initial conditions)	[87]	
Fig.3.13 (SNR of mean maximum of position PDF	[84, 87]	
Figs.3.15,3.16, obtained via Eqs.(3.27)-(3.35) (noise-induced shift turning to instantaneous velocity and acceleration)		**X**
Fig.3.17, obtained via Eqs.(3.36)-(3.44) (stochastic breaking and speeding)		**X**
Fig.3.19 (initial velocity noise-induced shift of mean instantaneous acceleration as described in Eq.(3.57)		**X**
Fig.3.20 (shift of maxima of instantaneous velocity and acceleration PDFs alongisde the potential force)		**X**

$*$: The light tail are observable for $x \gg (3k_BT/k)^{1/3}$ and are generated by the hardness of the cubic potential wall. Larger T makes for harder detection of this effect. Cooling is required.

Outlook

Following from this work, we envision these three natural future steps to be of relevance.

Classical Nonlinear Squeezing: With classical nanomechanical systems being the centerpiece of sensing and manipulation in modern technologies, their application rely on reduced noise for efficient functioning. In linear systems, thermal squeezing helps to arbitrarily reduce noise in a linear combination of position and momentum [198], but they cannot do so with nonlinear variables. To further reduce such noise, nonlinear squeezing provided by nonlinear dynamics is required as a pre-step to its quantum version [151, 152].

Microscopic machines: The naturally arising quasistationary state obtained by overdamped dynamics in the cubic potential, has higher energetic content than the equilibrium one [87]. This stimulates the development of new designs of thermal machines based on unstable dynamics. In this direction, one could think of a thermal source transducing energy harnessed from a hot bath, which is then used to drive the working medium and generate motion on it.

Such systems require the engineering of the interaction between the thermal source and the working medium. Their applications range from understanding the heat transfer and effective fluctuation-induced forces in small mesoscopic systems strongly coupled to their surroundings, to quantum-to-classical transitions between quantum modes of light and mechanical nonlinear oscillator [199, 200]

Towards the quantum domain: In recent years, the progress in cooling of nanoparticles in optical traps has brought us to the quantum regime [63, 151, 154]. Being our approach directly translatable to unitary dynamics in the quantum regime, we envision a quantum mechanical analysis of deeply underdamped and highly cooled particles in the unstable cubic potential, initially close to the mechanical ground state, as a necessary step to further delve into the quantum realm [153, 156].

Bibliography

[1] J. Millen, T. S. Monteiro, R. Pettit, and A. N. Vamivakas, "Optomechanics with levitated particles," vol. 83, no. 2, p. 026401, 2020.

[2] L. Ornigotti, A. Ryabov, V. Holubec, and R. Filip, "Brownian motion surviving in the unstable cubic potential and the role of maxwell's demon," *Physical Review E*, vol. 97, no. 3, p. 032127, 2018.

[3] J. Kepler, *De Cometis*. 1619.

[4] P. Lebedew *Ann. Phys.*, vol. 311, no. 433, 1901.

[5] E. F. Nichols and G. F. Hull *Phys. Rev.*, vol. 13, no. 307, 1901.

[6] J. Jackson, *Classical Electrodynamics*. Wiley, 1986.

[7] A. Ashkin and J. M. Dziedzic, "Optical levitation by radiation pressure," *Applied Physics Letters*, vol. 19, no. 8, pp. 283–285, 1971.

[8] A. Ashkin and J. M. Dziedzic, "Feedback stabilization of optically levitated particles," *Applied Physics Letters*, vol. 30, pp. 202–204, 2020/05/14 1977.

[9] M. Aspelmeyer, T. J. Kippenberg, and F. Marquardt, "Cavity optomechanics," *Reviews of Modern Physics*, vol. 86, pp. 1391–1452, 12 2014.

[10] O. Arcizet, P. F. Cohadon, T. Briant, M. Pinard, and A. Heidmann, "Radiation-pressure cooling and optomechanical instability of a micromirror," *Nature*, vol. 444, no. 7115, pp. 71–74, 2006.

[11] T. Corbitt, Y. Chen, E. Innerhofer, H. Müller-Ebhardt, D. Ottaway, H. Rehbein, D. Sigg, S. Whitcomb, C. Wipf, and N. Mavalvala, "An all-optical trap for a gram-scale mirror," *Physical Review Letters*, vol. 98, pp. 150802–, 04 2007.

[12] S. Gigan, H. R. Böhm, M. Paternostro, F. Blaser, G. Langer, J. B. Hertzberg, K. C. Schwab, D. Bäuerle, M. Aspelmeyer, and A. Zeilinger, "Self-cooling of a micromirror by radiation pressure," *Nature*, vol. 444, no. 7115, pp. 67–70, 2006.

[13] C. H. Metzger and K. Karrai, "Cavity cooling of a microlever," *Nature*, vol. 432, no. 7020, pp. 1002–1005, 2004.

[14] M. Poggio, C. L. Degen, H. J. Mamin, and D. Rugar, "Feedback cooling of a cantilever's fundamental mode below 5 mk," *Physical Review Letters*, vol. 99, pp. 017201–, 07 2007.

[15] M. J. Weaver, B. Pepper, F. Luna, F. M. Buters, H. J. Eerkens, G. Welker, B. Perock, K. Heeck, S. de Man, and D. Bouwmeester, "Nested trampoline resonators for optomechanics," *Applied Physics Letters*, vol. 108, p. 033501, 2021/05/20 2016.

[16] R. Diehl, E. Hebestreit, R. Reimann, F. Tebbenjohanns, M. Frimmer, and L. Novotny, "Optical levitation and feedback cooling of a nanoparticle at subwavelength distances from a membrane," *Physical Review A*, vol. 98, pp. 013851–, 07 2018.

[17] J. C. Sankey, C. Yang, B. M. Zwickl, A. M. Jayich, and J. G. E. Harris, "Strong and tunable nonlinear optomechanical coupling in a low-loss system," *Nature Physics*, vol. 6, no. 9, pp. 707–712, 2010.

[18] J. D. Thompson, B. M. Zwickl, A. M. Jayich, F. Marquardt, S. M. Girvin, and J. G. E. Harris, "Strong dispersive coupling of a high-finesse cavity to a micromechanical membrane," *Nature*, vol. 452, no. 7183, pp. 72–75, 2008.

[19] G. Anetsberger, R. Rivière, A. Schliesser, O. Arcizet, and T. J. Kippenberg, "Ultralow-dissipation optomechanical resonators on a chip," *Nature Photonics*, vol. 2, no. 10, pp. 627–633, 2008.

[20] M. Eichenfield, J. Chan, R. M. Camacho, K. J. Vahala, and O. Painter, "Optomechanical crystals.," *Nature*, vol. 462, pp. 78–82, Nov 2009.

[21] G. D. Cole, I. Wilson-Rae, K. Werbach, M. R. Vanner, and M. Aspelmeyer, "Phonon-tunnelling dissipation in mechanical resonators," *Nature Communications*, vol. 2, no. 1, p. 231, 2011.

[22] A. Jöckel, M. T. Rakher, M. Korppi, S. Camerer, D. Hunger, M. Mader, and P. Treutlein, "Spectroscopy of mechanical dissipation in micro-mechanical membranes," *Applied Physics Letters*, vol. 99, p. 143109, 2021/05/20 2011.

[23] V. B. Braginsky, M. L. Gorodetsky, and S. P. Vyatchanin, "Thermodynamical fluctuations and photo-thermal shot noise in gravitational wave antennae," *Physics Letters A*, vol. 264, no. 1, pp. 1–10, 1999.

[24] V. B. Braginsky, M. L. Gorodetsky, and S. P. Vyatchanin, "Thermo-refractive noise in gravitational wave antennae," *Physics Letters A*, vol. 271, no. 5, pp. 303–307, 2000.

[25] Y. T. Liu and K. S. Thorne, "Thermoelastic noise and homogeneous thermal noise in finite sized gravitational-wave test masses," *Physical Review D*, vol. 62, pp. 122002–, 11 2000.

[26] V. B. Braginsky and S. P. Vyatchanin, "Thermodynamical fluctuations in optical mirror coatings," *Physics Letters A*, vol. 312, no. 3, pp. 244–255, 2003.

[27] A. Farsi, M. Siciliani de Cumis, F. Marino, and F. Marin, "Photothermal and thermo-refractive effects in high reflectivity mirrors at room and cryogenic temperature," *Journal of Applied Physics*, vol. 111, p. 043101, 2021/05/20 2012.

[28] J. F. Vignola, J. A. Judge, J. Jarzynski, M. Zalalutdinov, B. H. Houston, and J. W. Baldwin, "Effect of viscous loss on mechanical resonators designed for mass detection," *Applied Physics Letters*, vol. 88, p. 041921, 2021/05/20 2006.

[29] D. M. Karabacak, V. Yakhot, and K. L. Ekinci, "High-frequency nanofluidics: An experimental study using nanomechanical resonators," *Physical Review Letters*, vol. 98, pp. 254505–, 06 2007.

[30] J. A. Judge, J. F. Vignola, and J. Jarzynski, "Dissipation from microscale and nanoscale beam resonators into a surrounding fluid," *Applied Physics Letters*, vol. 92, p. 124102, 2021/05/20 2008.

[31] S. S. Verbridge, H. G. Craighead, and J. M. Parpia, "A megahertz nanomechanical resonator with room temperature quality factor over a million," *Applied Physics Letters*, vol. 92, p. 013112, 2021/05/20 2008.

[32] K. L. Ekinci and M. L. Roukes, "Nanoelectromechanical systems," *Review of Scientific Instruments*, vol. 76, no. 6, p. 061101, 2005.

[33] M. Imboden and P. Mohanty, "Dissipation in nanoelectromechanical systems," *Physics Reports*, vol. 534, no. 3, pp. 89–146, 2014.

[34] K. W. Murch, K. L. Moore, S. Gupta, and D. M. Stamper-Kurn, "Observation of quantum-measurement backaction with an ultracold atomic gas," *Nature Physics*, vol. 4, no. 7, pp. 561–564, 2008.

[35] V. Sudhir, D. J. Wilson, R. Schilling, H. Schütz, S. A. Fedorov, A. H. Ghadimi, A. Nunnenkamp, and T. J. Kippenberg, "Appearance and disappearance of quantum correlations in measurement-based feedback control of a mechanical oscillator," *Physical Review X*, vol. 7, pp. 011001–, 01 2017.

[36] U. Delić, M. Reisenbauer, D. Grass, N. Kiesel, V. Vuletić, and M. Aspelmeyer, "Cavity cooling of a levitated nanosphere by coherent scattering," *Physical Review Letters*, vol. 122, pp. 123602–, 03 2019.

[37] D. Windey, C. Gonzalez-Ballestero, P. Maurer, L. Novotny, O. Romero-Isart, and R. Reimann, "Cavity-based 3d cooling of a levitated nanoparticle via coherent scattering," *Physical Review Letters*, vol. 122, pp. 123601–, 03 2019.

[38] V. Jain, J. Gieseler, C. Moritz, C. Dellago, R. Quidant, and L. Novotny, "Direct measurement of photon recoil from a levitated nanoparticle," *Phys. Rev. Lett.*, vol. 116, p. 243601, Jun 2016.

[39] Y. Tsaturyan, A. Barg, E. S. Polzik, and A. Schliesser, "Ultracoherent nanomechanical resonators via soft clamping and dissipation dilution," *Nature Nanotechnology*, vol. 12, no. 8, pp. 776–783, 2017.

[40] A. H. Ghadimi, S. A. Fedorov, N. J. Engelsen, M. J. Bereyhi, R. Schilling, D. J. Wilson, and T. J. Kippenberg, "Elastic strain engineering for ultralow mechanical dissipation," *Science*, vol. 360, no. 6390, pp. 764–768, 2018.

[41] G. S. MacCabe, H. Ren, J. Luo, J. D. Cohen, H. Zhou, A. Sipahigil, M. Mirhosseini, and O. Painter, "Phononic bandgap nano-acoustic cavity with ultralong phonon lifetime," 2019.

[42] J. Gieseler, B. Deutsch, R. Quidant, and L. Novotny, "Subkelvin parametric feedback cooling of a laser-trapped nanoparticle," *Phys. Rev. Lett.*, vol. 109, p. 103603, Sep 2012.

[43] Z.-Q. YIN, A. A. GERACI, and T. LI, "Optomechanics of levitated dielectric particles," *International Journal of Modern Physics B*, vol. 27, no. 26, p. 1330018, 2013.

[44] N. Kiesel, F. Blaser, U. Delić, D. Grass, R. Kaltenbaek, and M. Aspelmeyer, "Cavity cooling of an optically levitated submicron particle," *Proceedings of the National Academy of Sciences*, vol. 110, no. 35, pp. 14180–14185, 2013.

[45] J. Millen, P. Z. G. Fonseca, T. Mavrogordatos, T. S. Monteiro, and P. F. Barker, "Cavity cooling a single charged levitated nanosphere," *Phys. Rev. Lett.*, vol. 114, p. 123602, Mar 2015.

[46] A. A. Geraci, S. B. Papp, and J. Kitching, "Short-range force detection using optically cooled levitated microspheres," *Phys. Rev. Lett.*, vol. 105, p. 101101, Aug 2010.

[47] J. Chaste, A. Eichler, J. Moser, G. Ceballos, R. Rurali, and A. Bachtold, "A nanomechanical mass sensor with yoctogram resolution," *Nature Nanotechnology*, vol. 7, no. 5, pp. 301–304, 2012.

[48] J. Gieseler, L. Novotny, and R. Quidant, "Thermal nonlinearities in a nanomechanical oscillator," *Nature Physics*, vol. 9, no. 12, pp. 806–810, 2013.

[49] G. Ranjit, D. P. Atherton, J. H. Stutz, M. Cunningham, and A. A. Geraci, "Attonewton force detection using microspheres in a dual-beam optical trap in high vacuum," *Phys. Rev. A*, vol. 91, p. 051805, May 2015.

[50] B. Rodenburg, L. P. Neukirch, A. N. Vamivakas, and M. Bhattacharya, "Quantum model of cooling and force sensing with an optically trapped nanoparticle," *Optica*, vol. 3, p. 318, Mar. 2016.

[51] G. Ranjit, M. Cunningham, K. Casey, and A. A. Geraci, "Zeptonewton force sensing with nanospheres in an optical lattice," *Phys. Rev. A*, vol. 93, p. 053801, May 2016.

[52] F. Monteiro, S. Ghosh, A. G. Fine, and D. C. Moore, "Optical levitation of 10-ng spheres with nano-g acceleration sensitivity," *Physical Review A*, vol. 96, pp. 063841–, 12 2017.

[53] L. Magrini, R. A. Norte, R. Riedinger, I. Marinković, D. Grass, U. Delić, S. Gröblacher, S. Hong, and M. Aspelmeyer, "Near-field coupling of a levitated nanoparticle to a photonic crystal cavity," *Optica*, vol. 5, no. 12, pp. 1597–1602, 2018.

[54] C. Timberlake, G. Gasbarri, A. Vinante, A. Setter, and H. Ulbricht, "Acceleration sensing with magnetically levitated oscillators above a superconductor," *Applied Physics Letters*, vol. 115, p. 224101, 2021/05/21 2019.

[55] R. Lecamwasam, A. Graham, J. Ma, K. Sripathy, G. Guccione, J. Qin, G. Campbell, B. Buchler, J. J. Hope, and P. K. Lam, "Dynamics and stability of an optically levitated mirror," *Physical Review A*, vol. 101, pp. 053857–, 05 2020.

[56] O. Romero-Isart, A. C. Pflanzer, F. Blaser, R. Kaltenbaek, N. Kiesel, M. Aspelmeyer, and J. I. Cirac, "Large quantum superpositions and interference of massive nanometer-sized objects," *Phys. Rev. Lett.*, vol. 107, p. 020405, Jul 2011.

[57] A. Arvanitaki and A. A. Geraci, "Detecting high-frequency gravitational waves with optically levitated sensors," *Phys. Rev. Lett.*, vol. 110, p. 071105, Feb 2013.

[58] R. Kaltenbaek, M. Aspelmeyer, P. F. Barker, A. Bassi, J. Bateman, K. Bongs, S. Bose,

C. Braxmaier, Č. Brukner, B. Christophe, and et al., "Macroscopic quantum resonators (maqro): 2015 update," *EPJ Quantum Technology*, vol. 3, Mar 2016.

[59] S. Kuhn, G. Wachter, F.-F. Wieser, J. Millen, M. Schneider, J. Schalko, U. Schmid, M. Trupke, and M. Arndt, "Nanoparticle detection in an open-access silicon microcavity," *Applied Physics Letters*, vol. 111, no. 25, p. 253107, 2017.

[60] P. F. Barker and M. N. Shneider, "Cavity cooling of an optically trapped nanoparticle," *Phys. Rev. A*, vol. 81, p. 023826, Feb 2010.

[61] D. E. Chang, C. A. Regal, S. B. Papp, D. J. Wilson, J. Ye, O. Painter, H. J. Kimble, and P. Zoller, "Cavity opto-mechanics using an optically levitated nanosphere," *Proceedings of the National Academy of Sciences*, vol. 107, no. 3, pp. 1005–1010, 2010.

[62] O. Romero-Isart, M. L. Juan, R. Quidant, and J. I. Cirac, "Toward quantum superposition of living organisms," *New Journal of Physics*, vol. 12, p. 033015, mar 2010.

[63] U. Delić, M. Reisenbauer, K. Dare, D. Grass, V. Vuletić, N. Kiesel, and M. Aspelmeyer, "Cooling of a levitated nanoparticle to the motional quantum ground state," *Science*, vol. 367, p. 892, 02 2020.

[64] O. Romero-Isart, A. C. Pflanzer, M. L. Juan, R. Quidant, N. Kiesel, M. Aspelmeyer, and J. I. Cirac, "Optically levitating dielectrics in the quantum regime: Theory and protocols," *Phys. Rev. A*, vol. 83, p. 013803, Jan 2011.

[65] S. Qvarfort, A. Serafini, P. F. Barker, and S. Bose, "Gravimetry through non-linear optomechanics," *Nature Communications*, vol. 9, no. 1, p. 3690, 2018.

[66] M. Rademacher, J. Millen, and Y. L. Li, "Quantum sensing with nanoparticles for gravimetry: when bigger is better," vol. 9, no. 5, pp. 227–239, 2020.

[67] D. Leibfried, R. Blatt, C. Monroe, and D. Wineland, "Quantum dynamics of single trapped ions," *Reviews of Modern Physics*, vol. 75, pp. 281–324, 03 2003.

[68] K. C. Lee, M. R. Sprague, B. J. Sussman, J. Nunn, N. K. Langford, X.-M. Jin, T. Champion, P. Michelberger, K. F. Reim, D. England, D. Jaksch, and I. A. Walmsley, "Entangling macroscopic diamonds at room temperature.," *Science*, vol. 334, pp. 1253–1256, Dec 2011.

[69] J. Gieseler, R. Quidant, C. Dellago, and L. Novotny, "Dynamic relaxation of a levitated nanoparticle from a non-equilibrium steady state," *Nature Nanotechnology*, vol. 9, no. 5, pp. 358–364, 2014.

[70] J. Gieseler and J. Millen, "Levitated nanoparticles for microscopic thermodynamics—a review," *Entropy*, vol. 20, p. 326, Apr 2018.

[71] J. Millen and J. Gieseler, *Single Particle Thermodynamics with Levitated Nanoparticles*, vol. 195, p. 853. 2018.

[72] M. Debiossac, D. Grass, J. J. Alonso, E. Lutz, and N. Kiesel, "Thermodynamics of continuous non-markovian feedback control," *Nature Communications*, vol. 11, no. 1, p. 1360, 2020.

[73] A. Eichler, J. Moser, J. Chaste, M. Zdrojek, I. Wilson-Rae, and A. Bachtold, "Nonlinear damping in mechanical resonators made from carbon nanotubes and graphene," *Nature Nanotechnology*, vol. 6, no. 6, pp. 339–342, 2011.

[74] X. Zhou, F. Hocke, A. Schliesser, A. Marx, H. Huebl, R. Gross, and T. J. Kippenberg, "Slowing, advancing and switching of microwave signals using circuit nanoelectromechanics," *Nature Physics*, vol. 9, no. 3, pp. 179–184, 2013.

[75] J. Gieseler, M. Spasenović, L. Novotny, and R. Quidant, "Nonlinear mode coupling and synchronization of a vacuum-trapped nanoparticle," *Phys. Rev. Lett.*, vol. 112, p. 103603, Mar 2014.

[76] X.-Y. Lü, J.-Q. Liao, L. Tian, and F. Nori, "Steady-state mechanical squeezing in an optomechanical system via duffing nonlinearity," *Physical Review A*, vol. 91, pp. 013834–, 01 2015.

[77] M. Grimm, C. Bruder, and N. Lörch, "Optomechanical self-oscillations in an anharmonic potential: engineering a nonclassical steady state," vol. 18, no. 9, p. 094004, 2016.

[78] L. Latmiral, F. Armata, M. G. Genoni, I. Pikovski, and M. S. Kim, "Probing anharmonicity of a quantum oscillator in an optomechanical cavity," *Physical Review A*, vol. 93, pp. 052306–, 05 2016.

[79] R. Meucci, S. Euzzor, E. Pugliese, S. Zambrano, M. R. Gallas, and J. A. C. Gallas, "Optimal phase-control strategy for damped-driven duffing oscillators," *Physical Review Letters*, vol. 116, pp. 044101–, 01 2016.

[80] A. Leuch, L. Papariello, O. Zilberberg, C. L. Degen, R. Chitra, and A. Eichler, "Parametric symmetry breaking in a nonlinear resonator," *Physical Review Letters*, vol. 117, pp. 214101–, 11 2016.

[81] P. Huang, J. Zhou, L. Zhang, D. Hou, S. Lin, W. Deng, C. Meng, C. Duan, C. Ju, X. Zheng, F. Xue, and J. Du, "Generating giant and tunable nonlinearity in a macroscopic mechanical resonator from a single chemical bond," *Nature Communications*, vol. 7, no. 1, p. 11517, 2016.

[82] C. Chen, D. H. Zanette, D. A. Czaplewski, S. Shaw, and D. López, "Direct observation of coherent energy transfer in nonlinear micromechanical oscillators," *Nature Communications*, vol. 8, no. 1, p. 15523, 2017.

[83] L. Rondin, J. Gieseler, F. Ricci, R. Quidant, C. Dellago, and L. Novotny, "Direct measurement of kramers turnover with a levitated nanoparticle," *Nature Nanotechnology*, vol. 12, no. 12, pp. 1130–1133, 2017.

[84] M. Šiler, P. Jákl, O. Brzobohatý, A. Ryabov, R. Filip, and P. Zemánek, "Thermally induced micro-motion by inflection in optical potential," *Scientific Reports*, vol. 7, no. 1, p. 1697, 2017.

[85] J. Ahn, Z. Xu, J. Bang, Y.-H. Deng, T. M. Hoang, Q. Han, R.-M. Ma, and T. Li, "Optically levitated nanodumbbell torsion balance and ghz nanomechanical rotor," *Physical Review Letters*, vol. 121, pp. 033603–, 07 2018.

[86] G. Winstone, R. Bennett, M. Rademacher, M. Rashid, S. Buhmann, and H. Ulbricht, "Direct measurement of the electrostatic image force of a levitated charged nanoparticle close to a surface," *Physical Review A*, vol. 98, pp. 053831–, 11 2018.

[87] M. Šiler, L. Ornigotti, O. Brzobohatỳ, P. Jákl, A. Ryabov, V. Holubec, P. Zemánek, and R. Filip, "Diffusing up the hill: Dynamics and equipartition in highly unstable systems," *Physical review letters*, vol. 121, no. 23, p. 230601, 2018.

[88] J. F. Ralph, M. Toroš, S. Maskell, K. Jacobs, M. Rashid, A. J. Setter, and H. Ulbricht, "Dynamical model selection near the quantum-classical boundary," *Physical Review A*, vol. 98, pp. 010102–, 07 2018.

[89] A. Setter, J. Vovrosh, and H. Ulbricht, "Characterization of non-linearities through mechanical squeezing in levitated optomechanics," *Applied Physics Letters*, vol. 115, p. 153106, 2021/05/21 2019.

[90] Y. Amarouchene, M. Mangeat, B. V. Montes, L. Ondic, T. Guérin, D. S. Dean, and Y. Louyer, "Nonequilibrium dynamics induced by scattering forces for optically trapped nanoparticles in strongly inertial regimes," *Physical Review Letters*, vol. 122, pp. 183901–, 05 2019.

[91] F. Tebbenjohanns, M. Frimmer, A. Militaru, V. Jain, and L. Novotny, "Cold damping of an optically levitated nanoparticle to microkelvin temperatures," *Physical Review Letters*, vol. 122, pp. 223601–, 06 2019.

[92] U. Delić, D. Grass, M. Reisenbauer, T. Damm, M. Weitz, N. Kiesel, and M. Aspelmeyer, "Levitated cavity optomechanics in high vacuum," *Quantum Science and Technology*, vol. 5, p. 025006, Mar 2020.

[93] J. Flajšmanová, M. Šiler, P. Jedlička, F. Hrubý, O. Brzobohatý, R. Filip, and P. Zemánek, "Using the transient trajectories of an optically levitated nanoparticle to characterize a stochastic duffing oscillator," *Scientific Reports*, vol. 10, no. 1, p. 14436, 2020.

[94] J. Ma, J. Qin, G. T. Campbell, G. Guccione, R. Lecamwasam, B. C. Buchler, and P. K. Lam, "Observation of nonlinear dynamics in an optical levitation system," *Communications Physics*, vol. 3, no. 1, p. 197, 2020.

[95] Y. Arita, M. Mazilu, T. Vettenburg, E. M. Wright, and K. Dholakia, "Rotation of two trapped microparticles in vacuum: observation of optically mediated parametric resonances," *Opt. Lett.*, vol. 40, pp. 4751–4754, Oct 2015.

[96] A. Chowdhury, S. Barbay, M. G. Clerc, I. Robert-Philip, and R. Braive, "Phase stochastic resonance in a forced nanoelectromechanical membrane," *Physical Review Letters*, vol. 119, pp. 234101–, 12 2017.

[97] L. Huang, S. M. Soskin, I. A. Khovanov, R. Mannella, K. Ninios, and H. B. Chan, "Frequency stabilization and noise-induced spectral narrowing in resonators with zero dispersion," *Nature Communications*, vol. 10, no. 1, p. 3930, 2019.

[98] A. Chowdhury, M. G. Clerc, S. Barbay, I. Robert-Philip, and R. Braive, "Weak signal enhancement by nonlinear resonance control in a forced nano-electromechanical resonator," *Nature Communications*, vol. 11, no. 1, p. 2400, 2020.

[99] A. B. Kolomeisky, "Motor proteins and molecular motors: how to operate machines at the nanoscale," vol. 25, no. 46, p. 463101, 2013.

[100] R. D. Vale and R. A. Milligan, "The way things move: Looking under the hood of molecular motor proteins," *Science*, vol. 288, p. 88, 04 2000.

[101] L. S. B. Goldstein, "Kinesin molecular motors: Transport pathways, receptors, and human disease," *Proceedings of the National Academy of Sciences*, vol. 98, p. 6999, 06 2001.

[102] M. Schliwa and G. Woehlke, "Molecular motors," *Nature*, vol. 422, no. 6933, pp. 759–765, 2003.

[103] S. Erbas-Cakmak, D. A. Leigh, C. T. McTernan, and A. L. Nussbaumer, "Artificial molecular machines," *Chemical Reviews*, vol. 115, pp. 10081–10206, 09 2015.

[104] R. D. Astumian, "Optical vs. chemical driving for molecular machines," *Faraday Discussions*, vol. 195, no. 0, pp. 583–597, 2016.

[105] F. T. Arecchi and V. Degiorgio, "Statistical properties of laser radiation during a transient buildup," *Physical Review A*, vol. 3, pp. 1108–1124, 03 1971.

[106] P. Colet, M. San Miguel, J. Casademunt, and J. M. Sancho, "Relaxation from a marginal state in optical bistability," *Physical Review A*, vol. 39, pp. 149–156, 01 1989.

[107] L. Ramrez-Piscina and J. M. Sancho, "First-passage times for a marginal state driven by colored noise," *Physical Review A*, vol. 43, pp. 663–668, 01 1991.

[108] B. Lindner, A. Longtin, and A. Bulsara, "Analytic expressions for rate and cv of a type i neuron driven by white gaussian noise," *Neural Computation*, vol. 15, pp. 1761–1788, 5/21/2021 2003.

[109] N. Brunel and P. E. Latham, "Firing rate of the noisy quadratic integrate-and-fire neuron," *Neural Computation*, vol. 15, pp. 2281–2306, 5/21/2021 2003.

[110] D. Mishra, A. Yadav, S. Ray, and P. K. Kalra, "Effects of noise on the dynamics of biological neuron models," in *Soft Computing as Transdisciplinary Science and Technology* (A. Abraham, Y. Dote, T. Furuhashi, M. Köppen, A. Ohuchi, and Y. Ohsawa, eds.), (Berlin, Heidelberg), pp. 61–69, Springer Berlin Heidelberg, 2005.

[111] T. Guérin and D. S. Dean, "Universal time-dependent dispersion properties for diffusion in a one-dimensional critically tilted potential," *Physical Review E*, vol. 95, pp. 012109–, 01 2017.

[112] A. V. Arzola, M. Villasante-Barahona, K. Volke-Sepúlveda, P. Jákl, and P. Zemánek, "Omnidirectional transport in fully reconfigurable two dimensional optical ratchets," *Physical Review Letters*, vol. 118, pp. 138002–, 03 2017.

[113] P. Reimann, C. Van den Broeck, H. Linke, P. Hänggi, J. M. Rubi, and A. Pérez-Madrid, "Giant acceleration of free diffusion by use of tilted periodic potentials," *Physical Review Letters*, vol. 87, pp. 010602–, 06 2001.

[114] P. Reimann, C. Van den Broeck, H. Linke, P. Hänggi, J. M. Rubi, and A. Pérez-Madrid, "Diffusion in tilted periodic potentials: Enhancement, universality, and scaling," *Physical Review E*, vol. 65, pp. 031104–, 02 2002.

[115] J. E. Hirsch, B. A. Huberman, and D. J. Scalapino, "Theory of intermittency," *Physical Review A*, vol. 25, pp. 519–532, 01 1982.

[116] O. A. Tretiakov, T. Gramespacher, and K. A. Matveev, "Lifetime of metastable states in resonant tunneling structures," *Physical Review B*, vol. 67, pp. 073303–, 02 2003.

[117] C. M. L. C. A. P. A. D. V. D. Spagnolo, B.; Guarcello, "Nonlinear relaxation phenomena in metastable condensed matter systems," *Entropy*, vol. 19, no. 20, 2017.

[118] P. Hänggi, P. Talkner, and M. Borkovec, "Reaction-rate theory: fifty years after kramers," *Rev. Mod. Phys.*, vol. 62, pp. 251–341, Apr 1990.

[119] F. T. Arecchi, A. Politi, and L. Ulivi, "Stochastic-time description of transitions in unstable and multistable systems," *Il Nuovo Cimento B (1971-1996)*, vol. 71, no. 1, pp. 119–154, 1982.

[120] M. Young and S. Singh, "Decay of an unstable state.," *Phys Rev A Gen Phys*, vol. 31, pp. 888–891, Feb 1985.

[121] D. Sigeti and W. Horsthemke, "Pseudo-regular oscillations induced by external noise," *Journal of Statistical Physics*, vol. 54, no. 5, pp. 1217–1222, 1989.

[122] M. O. Caceres, C. E. Budde, and G. J. Sibona, "Stochastic escape processes from a non-symmetric potential normal form," vol. 28, no. 14, pp. 3877–3886, 1995.

[123] R. N. Mantegna and B. Spagnolo, "Noise enhanced stability in an unstable system," *Physical Review Letters*, vol. 76, pp. 563–566, 01 1996.

[124] N. V. Agudov, "Noise delayed decay of unstable states," *Physical Review E*, vol. 57, pp. 2618–2625, 03 1998.

[125] A. Fiasconaro, B. Spagnolo, and S. Boccaletti, "Signatures of noise-enhanced stability in metastable states," *Physical Review E*, vol. 72, pp. 061110–, 12 2005.

[126] M. O. Cáceres, "Passage time statistics in a stochastic verhulst model," *Journal of Statistical Physics*, vol. 132, no. 3, pp. 487–500, 2008.

[127] A. Ryabov, P. Zemánek, and R. Filip, "Thermally induced passage and current of particles in a highly unstable optical potential," *Physical Review E*, vol. 94, pp. 042108–, 10 2016.

[128] N. V. Agudov and A. N. Malakhov, "Decay of unstable equilibrium and nonequilibrium states with inverse probability current taken into account," *Physical Review E*, vol. 60, pp. 6333–6342, 12 1999.

[129] A. A. Dubkov, N. V. Agudov, and B. Spagnolo, "Noise-enhanced stability in fluctuating metastable states," *Physical Review E*, vol. 69, pp. 061103–, 06 2004.

[130] M. Suzuki, "Scaling theory of non-equilibrium systems near the instability point. ii: Anomalous fluctuation theorems in the extensive region," *Progress of Theoretical Physics*, vol. 56, pp. 477–493, 5/21/2021 1976.

[131] T. Maskawa and K. Yamawaki, "The problem of p+ = 0 mode in the null-plane field theory and dirac's method of quantization," *Progress of Theoretical Physics*, vol. 56, pp. 270–283, 5/21/2021 1976.

[132] M. Suzuki, "Scaling theory of non-equilibrium systems near the instability point. iii: Continuation to final region and systematic scaling expansion," *Progress of Theoretical Physics*, vol. 57, pp. 380–392, 5/21/2021 1977.

[133] F. Haake, "Decay of unstable states," *Physical Review Letters*, vol. 41, pp. 1685–1688, 12 1978.

[134] F. de Pasquale and P. Tombesi, "The decay of an unstable equilibrium state near a "critical point"," *Physics Letters A*, vol. 72, no. 1, pp. 7–9, 1979.

[135] F. de Pasquale, P. Tartaglia, and P. Tombesi, "New expansion technique for the decay of an unstable state," *Physical Review A*, vol. 25, pp. 466–471, 01 1982.

[136] H. Dekker, "Unstable state dynamics: A systematic evaluation of the master equation," *Physics Letters A*, vol. 88, no. 6, pp. 279–281, 1982.

[137] S. Kheifets, A. Simha, K. Melin, T. Li, and M. G. Raizen, "Observation of brownian motion in liquids at short times: Instantaneous velocity and memory loss," *Science*, vol. 343, no. 6178, pp. 1493–1496, 2014.

[138] K. Dholakia and T. Čižmár, "Shaping the future of manipulation," *Nature Photonics*, vol. 5, no. 6, pp. 335–342, 2011.

[139] P. Z. G. Fonseca, E. B. Aranas, J. Millen, T. S. Monteiro, and P. F. Barker, "Nonlinear dynamics and strong cavity cooling of levitated nanoparticles," *Phys. Rev. Lett.*, vol. 117, p. 173602, Oct 2016.

[140] F. Ricci, R. A. Rica, M. Spasenović, J. Gieseler, L. Rondin, L. Novotny, and R. Quidant, "Optically levitated nanoparticle as a model system for stochastic bistable dynamics," *Nature Communications*, vol. 8, no. 1, p. 15141, 2017.

[141] M. Konopik, A. Friedenberger, N. Kiesel, and E. Lutz, "Nonequilibrium information erasure below ktln2," 2018.

[142] F. Sun, X. Dong, J. Zou, M. I. Dykman, and H. B. Chan, "Correlated anomalous phase diffusion of coupled phononic modes in a sideband-driven resonator," *Nature Communications*, vol. 7, no. 1, p. 12694, 2016.

[143] R. Filip and P. Zemánek, "Noise-to-signal transition of a brownian particle in the cubic potential: I. general theory," *Journal of Optics*, vol. 18, p. 065401, apr 2016.

[144] A. Ryabov, V. Holubec, and E. Berestneva, "Living on the edge of instability," vol. 2019, no. 8, p. 084014, 2019.

[145] I. A. Martínez, É. Roldán, L. Dinis, D. Petrov, J. M. R. Parrondo, and R. A. Rica, "Brownian carnot engine," *Nature Physics*, vol. 12, no. 1, pp. 67–70, 2016.

[146] M. N. Romodina, M. D. Khokhlova, E. V. Lyubin, and A. A. Fedyanin, "Direct measurements of magnetic interaction-induced cross-correlations of two microparticles in brownian motion," *Scientific Reports*, vol. 5, no. 1, p. 10491, 2015.

[147] S. D. Bartlett and B. C. Sanders, "Universal continuous-variable quantum computation: Requirement of optical nonlinearity for photon counting," *Phys. Rev. A*, vol. 65, p. 042304, Mar 2002.

[148] D. Gottesman, A. Kitaev, and J. Preskill, "Encoding a qubit in an oscillator," *Phys. Rev. A*, vol. 64, p. 012310, Jun 2001.

[149] S. Lloyd and S. L. Braunstein, "Quantum computation over continuous variables," *Phys. Rev. Lett.*, vol. 82, pp. 1784–1787, Feb 1999.

[150] K. Miyata, H. Ogawa, P. Marek, R. Filip, H. Yonezawa, J.-i. Yoshikawa, and A. Furusawa, "Implementation of a quantum cubic gate by an adaptive non-gaussian measurement," *Phys. Rev. A*, vol. 93, p. 022301, Feb 2016.

[151] A. A. Rakhubovsky, D. W. Moore, and R. Filip, "Nonclassical states of levitated macroscopic objects beyond the ground state," vol. 4, no. 2, p. 024006, 2019.

[152] D. W. Moore, A. A. Rakhubovsky, and R. Filip, "Estimation of squeezing in a nonlinear quadrature of a mechanical oscillator," vol. 21, no. 11, p. 113050, 2019.

[153] A. A. Rakhubovsky and R. Filip, "Nonlinear stroboscopic quantum optomechanics," in *Quantum Information and Measurement (QIM) V: Quantum Technologies*, (Rome), p. F5A.68, Optical Society of America, 2019.

[154] A. A. Rakhubovsky, D. W. Moore, U. Delić, N. Kiesel, M. Aspelmeyer, and R. Filip, "Detecting nonclassical correlations in levitated cavity optomechanics," *Physical Review Applied*, vol. 14, pp. 054052–, 11 2020.

[155] A. Pitchford, A. A. Rakhubovsky, R. Mukherjee, D. W. Moore, F. Sauvage, D. Burgarth, R. Filip, and F. Mintert, "Optimal non-classical correlations of light with a levitated nanosphere," *arXiv*, vol. 2006.15050, 2020.

[156] A. A. Rakhubovsky and R. Filip, "Stroboscopic high-order nonlinearity for quantum optomechanics," *arXiv*, 2021.

[157] N. E. Frattini, V. V. Sivak, A. Lingenfelter, S. Shankar, and M. H. Devoret, "Optimizing the nonlinearity and dissipation of a snail parametric amplifier for dynamic range," *Physical Review Applied*, vol. 10, pp. 054020–, 11 2018.

[158] V. V. Sivak, N. E. Frattini, V. R. Joshi, A. Lingenfelter, S. Shankar, and M. H. Devoret, "Kerr-free three-wave mixing in superconducting quantum circuits," *Physical Review Applied*, vol. 11, pp. 054060–, 05 2019.

[159] V. Sivak, A. Lingenfelter, N. Frattini, V. Joshi, W. Dai, S. Shankar, and M. Devoret, "Exploiting the kerr-free point of a snail for improvement of dynamic range in parametric amplifiers," vol. 2019, (AA(Yale Univ), AB(Yale Univ), AC(Yale Univ), AD(Yale Univ), AE(Yale Univ), AF(Yale Univ), AG(Yale Univ)), p. C26.005, 01 2019.

[160] A. Ashkin, "Acceleration and trapping of particles by radiation pressure," *Physical Review Letters*, vol. 24, pp. 156–159, 01 1970.

[161] A. Ashkin and J. M. Dziedzic, "Optical levitation in high vacuum," *Applied Physics Letters*, vol. 28, pp. 333–335, 2021/05/21 1976.

[162] A. Ashkin and J. Dziedzic, "Optical trapping and manipulation of viruses and bacteria," *Science*, vol. 235, p. 1517, 03 1987.

[163] S. Chu, J. E. Bjorkholm, A. Ashkin, and A. Cable, "Experimental observation of optically trapped atoms," *Physical Review Letters*, vol. 57, pp. 314–317, 07 1986.

[164] W. D. Phillips, "Nobel lecture: Laser cooling and trapping of neutral atoms," *Reviews of Modern Physics*, vol. 70, pp. 721–741, 07 1998.

[165] P. Zemánek, A. Jonáš, L. Šrámek, and M. Liška, "Optical trapping of rayleigh particles using a gaussian standing wave," *Optics Communications*, vol. 151, no. 4, pp. 273–285, 1998.

[166] P. Zemánek, A. Jonáš, L. Šrámek, and M. Liška, "Optical trapping of nanoparticles and microparticles by a gaussian standing wave," *Optics Letters*, vol. 24, no. 21, pp. 1448–1450, 1999.

[167] L. Novotny and B. Hecht, *Principles of Nano-Optics*. Cambridge: Cambridge University Press, 2006.

[168] G. Gouesbet and G. Gréhan, *Generalized Lorenz-Mie Theories*. Springer International Publishing AG, second edition ed., 2017.

[169] A. Rohrbach and E. H. K. Stelzer, "Optical trapping of dielectric particles in arbitrary fields," *Journal of the Optical Society of America A*, vol. 18, no. 4, pp. 839–853, 2001.

[170] Y. Harada and T. Asakura, "Radiation forces on a dielectric sphere in the rayleigh scattering regime," *Optics Communications*, vol. 124, no. 5, pp. 529–541, 1996.

[171] P. Zemánek, M. Šiler, O. Brzobohatý, P. Jákl, and R. Filip, "Noise-to-signal transition of a brownian particle in the cubic potential: Ii. optical trapping geometry," vol. 18, no. 6, p. 065402, 2016.

[172] F. C. R.S. Sirohi, *Optical Methods of Measurement*. 2011.

[173] S. Keen, J. Leach, G. Gibson, and M. J. Padgett, "Comparison of a high-speed camera and a quadrant detector for measuring displacements in optical tweezers," vol. 9, no. 8, pp. S264–S266, 2007.

[174] H. J. Woltring, "Single- and dual-axis lateral photodetectors of rectangular shape," *IEEE Transactions on Electron Devices*, vol. 22, no. 8, pp. 581–590, 1975.

[175] J. Gieseler, *Dynamics of optically levitated nanoparticles in high vacuum*. PhD thesis, Universitat Politècnica de Catalunya, 2014.

[176] V. Jain, *Levitated optomechanics at the recoil limit*. PhD thesis, ETH Zurich, 2017.

[177] R. Kubo, "The fluctuation-dissipation theorem," vol. 29, no. 1, pp. 255–284, 1966.

[178] J. T. W. William Coffey, Yu P Kalmykov, *Langevin Equation, The: With Applications to Stochastic Problems in Physics, Chemistry and Electrical Engineering*. Singapore, River Edge NJ World Scientific, 2004.

[179] T. Li, S. Kheifets, D. Medellin, and M. G. Raizen, "Measurement of the instantaneous velocity of a brownian particle," *Science*, vol. 328, no. 5986, pp. 1673–1675, 2010.

[180] R. Huang, I. Chavez, K. M. Taute, B. Lukić, S. Jeney, M. G. Raizen, and E.-L. Florin, "Direct observation of the full transition from ballistic to diffusive brownian motion in a liquid," *Nature Physics*, vol. 7, no. 7, pp. 576–580, 2011.

[181] T. Li and M. G. Raizen, "Brownian motion at short time scales," *Annalen der Physik*, vol. 525, no. 4, pp. 281–295, 2013.

[182] M. Yaghoubi, M. E. Foulaadvand, A. Bérut, and J. Łuczka, "Energetics of a driven brownian harmonic oscillator," vol. 2017, no. 11, p. 113206, 2017.

[183] A. B. Carlson, *Communication Systems: An introductio to Signals and Noise in eletrical communication*. McGraw-Hill, 1937.

[184] J. A. Levenson, I. Abram, T. Rivera, and P. Grangier, "Reduction of quantum noise in optical parametric amplification," *Journal of the Optical Society of America B*, vol. 10, no. 11, pp. 2233–2238, 1993.

[185] H. A. Haus, *Electromagnetic Noise and Quantum Optical Measurements*. Springer, 2000.

[186] K. S. Lam, *Fundamental Principles of Classical Mechanics*. WORLD SCIENTIFIC, 2021/05/23 2013.

[187] S. H. Strogatz, *Nonlinear Dynamics and Chaos*. Westview Press, 2015.

[188] R. Filip, "Distillation of quantum squeezing," *Physical Review A*, vol. 88, pp. 063837–, 12 2013.

[189] M.P.Allen, *Computer Simulation of Liquids*. Oxford Science, 1989.

[190] B. S. Daan Frenkel, *Understanding Molecular Simulation*. Academic Press, 2002.

[191] D. C. Rapaport, *The Art of Molecular Dynamics Simulation*. Cambridge University Press, 2004.

[192] D. A. McQuarrie, *Statistical Mechanics*. Viva Books, 2008.

[193] S. Redner, *A guide to first-passage processes*. Cambridge University Press, 2007.

[194] A. Bérut, A. Arakelyan, A. Petrosyan, S. Ciliberto, R. Dillenschneider, and E. Lutz, "Experimental verification of landauer's principle linking information and thermodynamics.," *Nature*, vol. 483, pp. 187–189, Mar 2012.

[195] G. Volpe and G. Volpe, "Simulation of a brownian particle in an optical trap," *American Journal of Physics*, vol. 81, pp. 224–230, 2021/05/23 2013.

[196] Y. Jun, M. Gavrilov, and J. Bechhoefer, "High-precision test of landauer's principle in a feedback trap," *Physical Review Letters*, vol. 113, pp. 190601–, 11 2014.

[197] S. Dago, J. Pereda, N. Barros, S. Ciliberto, and L. Bellon, "Information and thermodynamics: Fast and precise approach to landauer's bound in an underdamped micromechanical oscillator," *Physical Review Letters*, vol. 126, pp. 170601–, 04 2021.

[198] M. Rashid, T. Tufarelli, J. Bateman, J. Vovrosh, D. Hempston, M. S. Kim, and H. Ulbricht, "Experimental realization of a thermal squeezed state of levitated optomechanics," *Physical Review Letters*, vol. 117, pp. 273601–, 12 2016.

[199] M. Kolář, A. Ryabov, and R. Filip, "Extracting work from quantum states of radiation," *Physical Review A*, vol. 93, pp. 063822–, 06 2016.

[200] R. Román-Ancheyta, M. Kolář, G. Guarnieri, and R. Filip, "Enhanced steady-state coherences via repeated system-bath interactions," *arXiv*, 2020.

Published articles

Brownian motion surviving in the unstable cubic potential and the role of Maxwell's demon

Luca Ornigotti,[1,*] Artem Ryabov,[2,†] Viktor Holubec,[2,3,‡] and Radim Filip[1,§]

[1]*Department of Optics, Palacký University, 17. listopadu 1192/12, CZ-771 46 Olomouc, Czech Republic*

[2]*Charles University, Faculty of Mathematics and Physics, Department of Macromolecular Physics, V Holešovičkách 2, CZ-180 00 Praha 8, Czech Republic*

[3]*Institut für Theoretische Physik, Universität Leipzig, Postfach 100 920, D-04009 Leipzig, Germany*

(Received 22 August 2017; published 23 March 2018)

The trajectories of an overdamped particle in a highly unstable potential diverge so rapidly, that the variance of position grows much faster than its mean. A description of the dynamics by moments is therefore not informative. Instead, we propose and analyze local directly measurable characteristics, which overcome this limitation. We discuss the most probable particle position (position of the maximum of the probability density) and the local uncertainty in an unstable cubic potential, $V(x) \sim x^3$, both in the transient regime and in the long-time limit. The maximum shifts against the acting force as a function of time and temperature. Simultaneously, the local uncertainty does not increase faster than the observable shift. In the long-time limit, the probability density naturally attains a quasistationary form. We interpret this process as a stabilization via the measurement-feedback mechanism, the Maxwell demon, which works as an entropy pump. The rules for measurement and feedback naturally arise from the basic properties of the unstable dynamics. All reported effects are inherent in any unstable system. Their detailed understanding will stimulate the development of stochastic engines and amplifiers and, later, their quantum counterparts.

DOI: 10.1103/PhysRevE.97.032127

I. INTRODUCTION

Various engines and amplifiers exploit a natural instability in their parts to perform useful work or required manipulations. Instability is therefore a resource, although it is simultaneously dangerous for the system. It can, in fact, prevent the machine from working or, in a drastic case, it can completely damage it. Unstable systems, when left to evolve freely, have a strong tendency to diverge during quite a short period of time. Their variables can reach unwanted extremely large values for finite time intervals. Statistically speaking, not only do all their statistical moments diverge, but, even more destructively, standard deviations can diverge faster than mean values. At this moment, the moments cannot inform about the unstable stochastic dynamics, and a different approach is required. An illustrative example of such instability is the unbounded cubic potential,

$$V(x) = \tfrac{1}{3}kx^3, \tag{1}$$

which exhibits all these aspects even in an overdamped regime.

Recently, the investigation of unstable systems got a large stimulus from experimental developments. Beyond the overdamped regime, the cubic nonlinear potential is experimentally accessible in the developing field of optomechanics with both nanoparticles [1–4] and solid-state objects [5,6]. In quantum optomechanics, cubic nonlinearity is principally required to construct highly nonlinear Hamiltonians and potentially implement analog quantum simulations with mechanical objects [7–9]. The investigation of unstable systems is also important for the development of quantum mechanical engines beyond simple double-well models [10,11], which is necessary for the further development of quantum thermodynamics. All these investigations also require both comparisons with and an understanding of the overdamped case.

In the present paper, we thus discuss the dynamics of an overdamped Brownian particle diffusing in an unstable cubic potential (1). Even though we focus on the particular case of a cubic potential, our approach can be easily generalized to other unstable potentials with an inflection point. We assume that the position of the particle $x(t)$ evolves in time according to the Langevin equation

$$\frac{dx}{dt} = -\frac{k}{\gamma}x^2(t) + \sqrt{2D}\xi(t), \tag{2}$$

where $\xi(t)$ is the standard Gaussian white noise [$\langle\xi(t)\rangle = 0$, $\langle\xi(t)\xi(t')\rangle = \delta(t-t')$], γ stands for the friction, and the diffusion coefficient satisfies the fluctuation-dissipation theorem, $D = k_B T/\gamma$. Although all derivations are carried out for arbitrary γ, in the illustrations we will always assume $\gamma = 1$.

Brownian dynamics as described by Eq. (2) occurs as a basic element of several nonlinear stochastic models in chemistry, physics, and biology. Examples include the firing of noisy neurons [12,13], optical bistability in lasers [14–16], or, more generally, passage through a saddle-node bifurcation [17–19], where the simplicity of Eq. (2) allows one to describe a phenomenon of intermittency. Another broad class of systems where Eq. (2) occurs naturally is one-dimensional Brownian ratchets modeled as the diffusion in tilted-periodic potentials.

*luca.ornigotti@gmail.com
†rjabov.a@gmail.com
‡Viktor.holubec@mff.cuni.cz
§filip@optics.upol.cz

The transport properties of the latter at a critical tilt were derived in Refs. [20–22]. Other examples of transitions from metastable states in condensed matter models can be found in Refs. [23,24].

The analytical techniques developed to describe such problems (the decay of unstable states) can be roughly subdivided into three groups. The first deals with first-passage times [12–15,17,18,25–35]. The second, a rather related one, focuses on a so-called nonlinear relaxation time (or a mean time spent by a particle in a given region) [36,37]. This approach differs from the first-passage approach by accounting for multiple passages (returns) of the particle and not only for the first one. Third, significant effort was made to analyze the time evolution of the probability density function (PDF) in a symmetric inverted parabolic potential (bounded by a quartic potential for large x) [38–46]. Whereas the first two approaches provide only indirect information about the particle position, the third aims directly at the position PDF. It exploits the symmetry of the problem and/or properties of the inverted parabolic potential near $x = 0$ to derive asymptotic approximations in different regimes.

In the present paper, we go beyond the aforementioned studies in the following ways. First, we argue that highly unstable dynamics (2) leads, already after a short time, to PDFs with heavy tails, which makes the description of $x(t)$ in terms of statistical moments useless. Instead, we propose to characterize the particle position by a directly measurable maximum of the PDF and use a curvature of the PDF at the maximum to characterize uncertainty. Second, we derive and discuss the generic properties of the PDF including short-time dynamics, the development of the heavy tail, and long-time properties, which turn out to be universal and described by the theory of *quasistationary distributions* [47,48]. Quasistationary distributions emerge in stochastic processes conditioned on "nonabsorption." Their study began with Yaglom's seminal paper on the Galton-Watson branching process [49]. Since then, the conditioned processes were successfully applied in mathematical biology [50], epidemiology [51], and demographic studies [52], where the absorption corresponds to the extinction of a modeled population. The conditioning on nonabsorption shifts focus on an ensemble of surviving individuals. In our context, nonabsorption roughly means that the particle remains on the potential plateau. The conditioning restricts our attention to trajectories which do not diverge up to a certain time. In addition, we relate the evolution of the PDF towards the quasistationary distribution to a mysterious creature known as Maxwell's demon [53,54].

All these main ideas are motivated and explained on physical grounds in Sec. II, which outlines the main results of our approach. Sections III–V comprise all technical details concerning derivations and thorough discussions of particular points.

II. PERTINENT DESCRIPTION OF RAPIDLY DIVERGING TRAJECTORIES

In the cubic potential (1), the particle dynamics is considerably different for $|x(t)| < (3k_BT/k)^{1/3}$ and $|x(t)| > (3k_BT/k)^{1/3}$ [34]. Near the inflection point ($x = 0$) on the potential plateau, the cubic potential is negligible compared

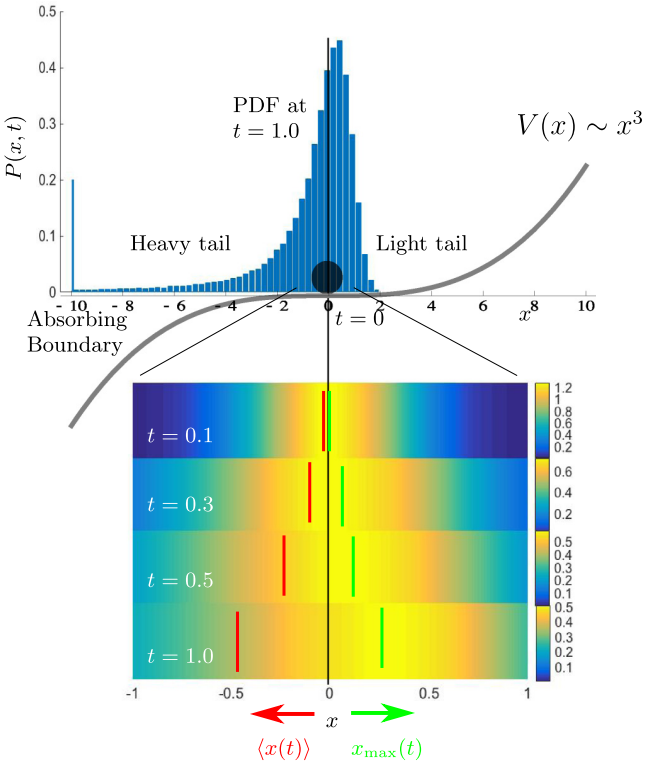

FIG. 1. Difference between the regular local and the divergent global statistical descriptions of Brownian motion in an unstable cubic potential. A particle is initially placed at the inflection point (black circle). In the global description (mean position), depicted by the red lines in the density plots, the mean is quickly dragged towards $-\infty$ due to the instability and hence it can be used for a very short time only. That behavior is also reflected in the presence of the heavy tail of $P(x,t)$ (upper panel). On the other hand, the maximum of $P(x,t)$ (green lines, the local description) moves atypically in the direction opposite to the acting force. The instability at negative x does not invalidate the latter quantity even for long times. This gives one the possibility to go beyond statistical moments in the local description of unstable motion. The higher moments vs their local counterparts are discussed in Fig. 2.

to the thermal noise. Hence, when $|x(t)| < (3k_BT/k)^{1/3}$, the particle diffuses almost freely with only a weak drag to the left. On the other hand, the drag force rapidly increases in strength as $x(t)$ departs from the plateau. Actually, for $|x(t)| > (3k_BT/k)^{1/3}$, the potential is so strong that the particle appearing at $x(t) < (3k_BT/k)^{1/3}$ reaches minus infinity *in a finite time* [34,55]. On the other hand, the particle at $x(t) > (3k_BT/k)^{1/3}$ is dragged extremely quickly to the plateau.

The rapid divergence of trajectories implies the unique features of the PDF $P(x,t)$. First of all, $P(x,t)$ develops a heavy tail for negative x (as derived in Sec. III). This renders worthless the usual description of $x(t)$ in terms of moments $\langle x(t) \rangle, \langle x^2(t) \rangle, \ldots$, even at relatively short times. The higher the moment, in fact, the faster is the divergence, which we illustrate in Fig. 2, where the ratio $\langle x(t) \rangle^2 / \mathrm{Var}[x(t)]$, $\mathrm{Var}[x(t)] = \langle x^2(t) \rangle - \langle x(t) \rangle^2$, is plotted by the blue line. Because of the divergence, the ratio quickly drops to zero [55]. Assuming $\langle x(t) \rangle$ as an average useful signal from the unstable dynamics,

this ratio can be interpreted as a signal-to-noise ratio (SNR). A drop in the SNR means that the signal in the position is negligible compared to the noise.

It is therefore necessary to adopt a description of the present unstable system, which goes beyond the statistical moments. The main idea is to focus on the most probable particle position, i.e., on the position of the maximum of $P(x,t)$, $x_{\max}(t)$ (instead of the mean value), and on the local curvature of $P(x,t)$ (instead of the variance). This approach has already been used to define the local uncertainty for non-Gaussian distributions in quantum optics [56]. In the present model, this choice is experimentally motivated. It corresponds to a picture obtained from a detector linearly sensitive to the larger density of particles (or trajectories) above some minimum threshold, as depicted in Fig. 1.

This measurement bears little information about diverging trajectories and provides a coherent picture of the most probable particle position near the instability. To quantify the relative fluctuations near the most probable position, we define the "signal-to-noise" ratio as

$$\mathrm{SNR}(t) = \frac{x^2_{\max}(t)}{\sigma^2_{\max}(t)}, \tag{3}$$

where we have introduced the normalized inverse curvature at the maximum [56],

$$\sigma^2_{\max}(t) = \frac{P(x_{\max}(t),t)}{\left|\partial^2_{xx} P(x_{\max}(t),t)\right|}. \tag{4}$$

Note that for a Gaussian distribution, the inverse curvature (4) is equal to the variance $\sigma^2_{\max}(t) = \mathrm{Var}[x(t)]$. The inverse curvature can be experimentally reached [56] following a conditional version of the central limit theorem [57]. We also note that an alternative regularized description based on quantiles (the median and quartiles) of the position distribution is possible. We leave a discussion of the advantages and disadvantages of this possibility to a further study.

SNR (3) specifies how well the most likely position can be observed in an experiment. It is a crucial parameter for a possible experimental test of our results. As we discuss below, $x_{\max}$ is shifted to the right from $x = 0$. This shift will be experimentally detectable only if the SNR is not negligible. SNR (3) is shown in Fig. 2. In contrast to the ratio of averages $\langle x(t)\rangle^2/\langle x^2(t)\rangle$, it shows no drop as time grows. In fact, the SNR (3) remains nonzero for any t, because both the maximum and the local curvature converges to a positive value. In contrast to this, the average particle position always moves in the direction of the force (cf. Fig. 1).

The second key feature of the PDF $P(x,t)$, induced by the high instability of the potential (1), is that $P(x,t)$ is not normalized to one on the real line $x \in (-\infty, +\infty)$. The normalization

$$S(t) = \int_{-\infty}^{\infty} dx\, P(x,t), \tag{5}$$

known as the survival probability [25], gives the weight of trajectories that have not reached $x = -\infty$ by time t. The survival probability decays with time exponentially when $D > 0$ (Sec. V). Thus, in an ensemble of trajectories, the total weight of those wandering on the potential plateau decreases as individual trajectories are quickly dragged towards minus infinity. This phenomenon can be well understood in the analytically tractable case of $D = 0$ discussed in Sec. III. Simultaneously, for $D = 0$, the instability causes $P(x,t)$ to vanish for $x > 1/\kappa t$.

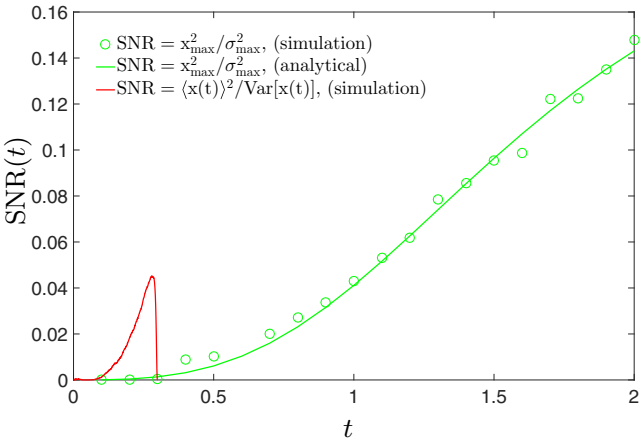

FIG. 2. Fast divergence of the global description using averages is demonstrated by a swift drop of the SNR (red line). The local description using the maximum of the PDF and the curvature at the maximum maintains its information value for all times (green line and ○). In Monte Carlo simulations we have generated 4×10^5 trajectories with the time step $\Delta t = 0.002$ starting at the origin, $x(0) = 0$, and diffusing with $D = 0.1$ in the cubic potential with stiffness $k = 1$. The analytical result for the SNR (3) (green line) is derived in Sec. IV. The figure clearly demonstrates that with the local description of the system we can go beyond the statistical moments description which is reflected in the growth of the SNR (3) (green line and ○).

The third intriguing feature of the present unstable system is that $P(x,t)$ quickly attains a universal spatial shape, $P(x,t) \sim Q_{\mathrm{st}}(x)e^{-\lambda_0 t}$, where $\lambda_0 > 0$ determines the decay rate of the unstable state. The normalized PDF $Q_{\mathrm{st}}(x)$ is the long-time limit of the ratio

$$Q(x,t) = \frac{P(x,t)}{S(t)}. \tag{6}$$

For any given x, the PDF $P(x,t)$ decays exponentially with time. Consequently, the survival probability $S(t)$, Eq. (5), which is just the normalization of $P(x,t)$, also decays to zero. However, their ratio (6) converges to the time-independent normalized distribution $Q_{\mathrm{st}}(x)$, which is known as the *quasistationary distribution* [47,48]. The PDF $Q(x,t)$ is the conditional distribution of particles which do not reach $x = -\infty$ before time t. Its long-time limit $Q_{\mathrm{st}}(x)$ thus describes the statistics of long-living (living = not diverging) trajectories. Note that $Q(x,t)$ and $P(x,t)$ are proportional and thus the maximum and the curvature of both PDFs are the same.

Hence, in the long-time limit, the quasistationary distribution $Q_{\mathrm{st}}(x)$ provides an analytical estimate of the local curvature of the generic PDF $P(x,t)$ around its maximum. Its position $x_{\max}$ nontrivially depends on both the potential $V(x)$ and the temperature T. Interestingly, the curvature at the maximum of $Q_{\mathrm{st}}(x)$ ($1/\sigma^2_{\max}$, derived in Sec. V) is determined by two qualitatively different factors,

$$\frac{1}{\sigma^2_{\max}} = \frac{V''(x_{\max})}{k_B T} + \frac{\lambda_0}{D}. \tag{7}$$

The first term on the right-hand side, $V''(x_{\max})/k_BT$, is the (scaled) curvature of the potential. In our case it equals $V''(x_{\max})/k_BT = 2kx_{\max}/k_BT$. This first term alone determines the curvature of any PDF of the functional form $p(V/k_BT)$ (such as the Gibbs equilibrium distribution). The second term, λ_0/D, is always positive. Its magnitude is related to the degree of instability of the system quantified by the decay rate λ_0. Thus, the quasistationary distribution is always narrower near its maximum than any PDF $p(V/k_BT)$. The more unstable the system (large decay rate λ_0), the narrower the distribution $Q_{st}(x)$ becomes.

The analytical result (7) has also two practical consequences. First, Eq. (7) provides an independent scheme for measurement of the local curvature $1/\sigma^2_{\max}$. This is important since a direct inference of $1/\sigma^2_{\max}$ from the experimental data may depend on the fitting procedure used. Measuring curvature according to Eq. (7) avoids fitting of the PDF. Instead, it uses easily accessible first-passage properties, e.g., the survival probability, to determine the decay rate λ_0, which can be reliably measured even for small samples of trajectories (see Ref. [35]). Second, the result (7) allows one to extract the scaling of the curvature with the intensity of thermal noise, $x_{\max} \sim (k_BT)^{1/3}, \sigma^2_{\max} \sim (k_BT)^{2/3}$ [cf. Eqs. (30)], which allows us to immediately find the SNR (3) to be temperature independent.

Last, but not least, the quasistationary distribution can be interpreted as a steady-state PDF, which we will explain in Sec. V. Surprisingly, to accomplish this task we will need to introduce the feedback mechanism which we can interpret as the action of a Maxwell's demon.

III. INSTABILITY YIELDS HEAVY TAILS AND DECAY OF NORMALIZATION OF $P(x,t)$

The simplified situation with negligible thermal noise ($D = 0$) is particularly useful, because it illustrates (i) the development of the heavy tail of $P(x,t)$ for negative x, (ii) the vanishing of $P(x,t)$ for large x in a finite time, (iii) an atypical shift of the PDF maximum, and (iv) it elucidates properties of the survival probability (5). The PDF for the present deterministic dynamics becomes nontrivial if we require a suitable initial distribution. We choose $P(x,0)$ to be Gaussian with the mean x_0 and the variance σ_0^2,

$$P(x,0) = \frac{e^{-\frac{(x-x_0)^2}{2\sigma_0^2}}}{\sqrt{2\pi\sigma_0^2}}. \tag{8}$$

Then, at time t, $t > 0$, we get the PDF [55]

$$P(x,t) = \theta(1/\kappa t - x)\frac{\exp\left\{-\frac{1}{2\sigma_0^2}\left(\frac{x}{1-x\kappa t} - x_0\right)^2\right\}}{\sqrt{2\pi\sigma_0^2}(1-x\kappa t)^2}, \tag{9}$$

where $\kappa = k/\gamma$ and $\theta(\cdot)$ stands for the Heaviside theta function. The derivation of Eq. (9) can be found in Ref. [55], where the fast divergence of averages $\langle x(t)\rangle, \langle x^2(t)\rangle$ was thoroughly discussed. For large negative x, the distribution decreases as $1/x^2$ and hence its moments do not exist. Figure 3 illustrates the gradual increase of the left tail with time.

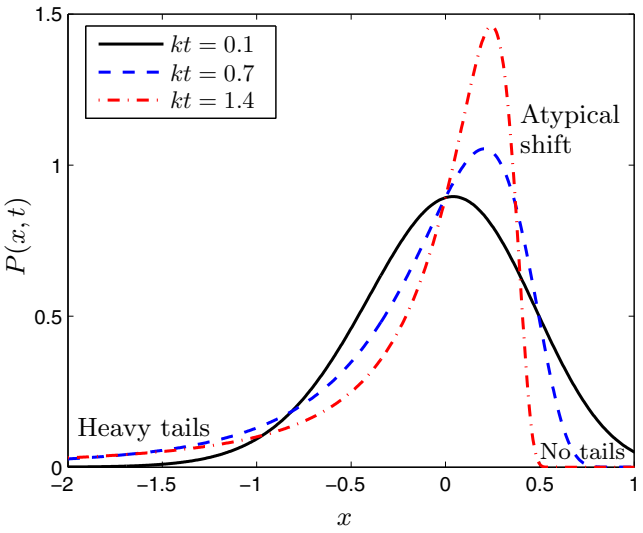

FIG. 3. PDF (9) in three different times for $D = 0$. The PDF (9) develops a heavy left tail starting from the initial Gaussian distribution with mean $x_0 = 0$ and variance $\sigma_0^2 = 0.2$. For $x > 1/\kappa t$, $P(x,t)$ is equal to zero ("no tails" for $x > 0$) due to the high speed of dynamics generated by the cubic potential. The maximum shifts in the opposite direction than the force acts and local uncertainty around the maximum decreases. Nonmonotonic behavior of the maximum, observed for longer times and different x_0, is further illustrated in Fig. 4.

A strong instability of the cubic potential manifests itself also in another feature of the PDF (9). The Heaviside theta function in Eq. (9) implies that $P(x,t)$ vanishes when $x > 1/\kappa t$ even though the initial Gaussian distribution (8) has infinite support $x \in (-\infty, +\infty)$. Thus, at time t, there are no trajectories on the right from $x = 1/\kappa t$. The cubic potential is so strong that all trajectories with $x(0) > 0$ quickly aggregate on the potential plateau on the right of $x = 0$. This happens in a finite time, regardless of the initial position of the trajectory. In Fig. 3, we denote the depopulated region as "no tails," in contrast to the heavy tail for $x \to -\infty$.

An analogous picture holds to the left of the inflection point. Any trajectory that starts on the negative half line is quickly dragged towards $x = -\infty$. This can be seen from a decrease of the survival survival probability (5) with time. The survival probability, which is the probability of finding the particle on $x \in (-\infty,\infty)$ [norm of the PDF $P(x,t)$ in Eq. (9)], is given by

$$S(t) = \frac{1}{2}\left[1 + \mathrm{erf}\left(\frac{1+x_0\kappa t}{\sqrt{2\sigma_0^2\kappa t}}\right)\right], \tag{10}$$

and its long-time limit reads

$$\lim_{t\to\infty} S(t) = \frac{1}{2}\left[1 + \mathrm{erf}\left(\frac{x_0}{\sqrt{2\sigma_0^2}}\right)\right]. \tag{11}$$

When the initial particle distribution is the delta function at x_0, i.e., for $\sigma_0 = 0$, the right-hand side of Eq. (11) depends solely on x_0 and reduces to a unit step function at $x_0 = 0$. A nonzero width of the initial Gaussian PDF, $\sigma_0 > 0$, broadens the step

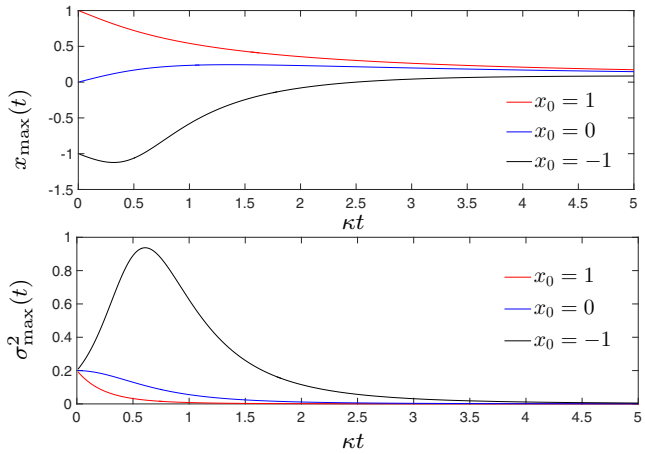

FIG. 4. Evolution of the maximum and the inverse curvature of the PDF (9) ($D = 0$) for three initial Gaussian distributions with different mean x_0 and the same variance $\sigma_0 = 0.2$. For $x_0 = 1$, the maximum decreases towards $x = 0$ and the inverse curvature quickly approaches zero. For $x_0 = 0$, the maximum will first shift against the acting force and, after that, it will decrease back to $x = 0$. The curvature behaves similarly as in the previous case. When $x_0 = -1$, the maximum climbs above $x = 0$ and converges back to $x = 0$ at later times. The inverse curvature possesses a maximum. In all three cases, the long-time limit of $P(x,t)$ is the delta function at the origin with the weight given by the long-time survival probability (11). The PDF for the case $x_0 = 0$ is shown in Fig. 3.

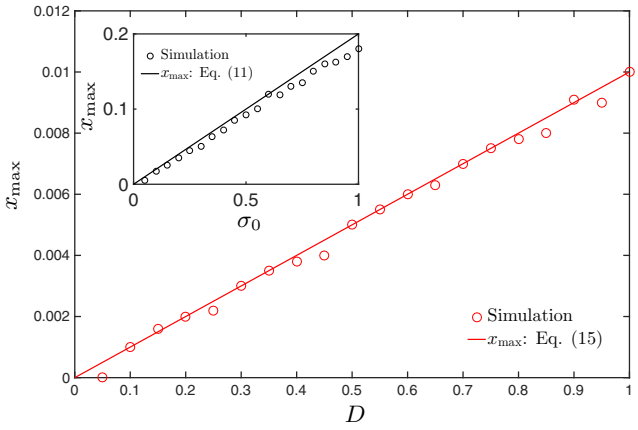

FIG. 5. Atypical shift of the maximum at a given time induced by increasing temperature (i.e., D) or the initial variance σ_0^2 (inset). In simulations, we used $k = 1$, $x_0 = 0$, the time step $\Delta t = 0.002$, $\sigma_0 = 0$ (and $D = 0$ for the inset), and $t = 0.1$; 3×10^5 trajectories were generated. The small D approximation used to plot the red line provides a satisfactory result also for $D \approx 1$. Both plotted dependencies are predicted by two approximate equations, Eq. (13) (black line, inset) and Eq. (16) (red line). Note that the SNR (3) grows linearly both with D and σ_0^2.

function because even for $x_0 < 0$, the nonzero σ_0 allows one to generate an initial position on the right of the origin.

Moreover, the decay of the survival probability $S(t)$ when $D > 0$ turns out to be exponential, as will be discussed in Sec. V. Differently from these asymptotic features, the local dynamics of the maximum and curvature of $P(x,t)$, discussed in the following section, does not depend on the normalization of $P(x,t)$.

IV. TRANSIENT DYNAMICS OF MAXIMUM AND CURVATURE

A. Diffusionless case ($D = 0$)

It is rather instructive to study the maximum and curvature of the PDF (9). In contrast to the statistical moments, the two quantities describing the most probable particle position are not limited to short times. The position of the maximum of $P(x,t)$ is given by

$$x_{\max}(t) = \frac{1}{\kappa t} + \frac{1 + x_0\kappa t - \sqrt{(1 + x_0\kappa t)^2 + 8\sigma_0^2(\kappa t)^2}}{4\sigma_0^2(\kappa t)^3}. \tag{12}$$

The inverse curvature $\sigma^2_{\max}(t)$ is derived according to its definition (4). The result is, however, rather involved and hence we do not report it explicitly.

The behavior of both quantities, illustrated in Fig. 4, should be understood based on the following consideration: A trajectory that starts from $x(0)$ follows the deterministic equation $x(t) = x(0)/[1 + x(0)\kappa t]$. If the particle is initially located on the left from the inflection point $x = 0$, it is quickly dragged towards $-\infty$. A particle located initially on the right of $x = 0$ converges towards the origin as $x(t) \approx 1/\kappa t$. The trade-off between the two kinds of trajectories in the statistical ensemble determines all properties of $P(x,t)$. Surprisingly, this trade-off leads to a rich behavior of $x_{\max}(t)$ and $\sigma^2_{\max}(t)$, which strongly depends on the parameters of the initial distribution.

Further analytical insight for the case of nonvanishing x_0 can be gained for small times. For $t \to 0$ we have

$$x_{\max}(t) \approx x_0 + \left(2\sigma_0^2 - x_0^2\right)\kappa t, \tag{13}$$

$$\sigma^2_{\max}(t) \approx \sigma_0^2 - 4\sigma_0^2 x_0 \kappa t - 10k^2\sigma_0^4 t^2. \tag{14}$$

The inequality $0 < x_0/\sqrt{2} < \sigma_0$ is a sufficient condition to observe the atypical shift of $x_{\max}$ against the acting force $-V'(x)$. To observe the narrowing of $\sigma^2_{\max}$, it is then sufficient to have $x_0 > 0$. The equations justify a qualitatively similar short-time decrease of $x_{\max}(t)$ for $x_0 = \pm 1$ shown in Fig. 4, and also the initial increase of $\sigma^2_{\max}(t)$ for $x_0 = -1$ and its decrease for $x_0 = 1$. For $x_0 = 0$, $x_{\max}$ always evolves atypically and the inverse curvature in Eq. (13) always decreases. These two characteristics also demonstrate an interesting nonlinear effect, namely, the transformation of the initial variance (noise) into directed motion [notice the appearance of σ_0^2 in Eq. (13)]; see Fig. 5 (inset). This effect is absent for the quadratic and the linear potential, where the corresponding Langevin equations are linear.

In the long-time limit, the peak of the PDF $P(x,t)$ slowly sharpens and moves towards the origin from the right because all trajectories, starting at $x(0) > 0$, are sliding towards $x = 0$. The tendency is clearly visible in Fig. 3. Thus, $x_{\max}(t) \approx 1/\kappa t$ converges to zero and also $\sigma^2_{\max}(t) \sim (1/\kappa t)^4$ as the peak becomes sharper. In contrast to this, the mean and variance are not defined for such a long period of time.

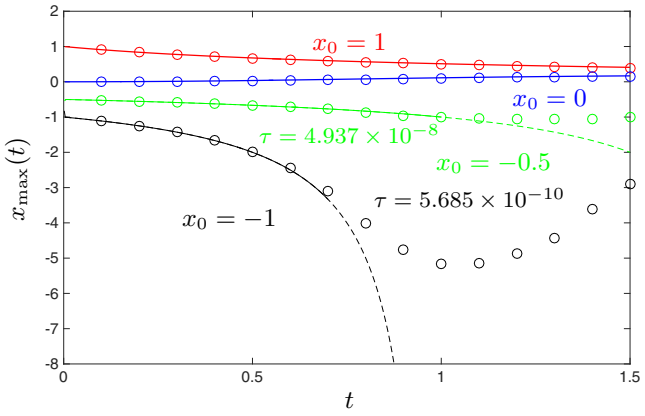

FIG. 6. Evolution of the maximum in the small noise regime for different values of the initial particle position x_0. The depicted dependencies are qualitatively similar to their zero-noise ($D = 0$) analogs from Fig. 4. When the initial position x_0 is zero or positive, $\tau = t$ (see main text). For negative x_0, values of τ are indicated in the graph by the corresponding color. In this graph we have used $k = 1$, $D = 0.05$, and simulated 3×10^5 trajectories with the time step $\Delta t = 0.002$.

Therefore the SNR (3) calculated for the PDF (9) depends linearly on σ_0^2 in the short-time approximation, and it behaves qualitatively similar to its $D \neq 0$ counterpart depicted in Fig. 2. In the long-time limit this SNR grows as t^2 (which guarantees the usefulness of the local description) as the span of the PDF on the positive half line $x > 0$ shrinks.

B. Small diffusion case ($D \ll 1$)

For nonlinear potentials, the small noise expansion is not uniform in time [58]. Below, we present a trick for how to extend the validity of the approximation, which is necessary when the particle starts on the left from the inflection point, $x_0 < 0$ (cf. Fig. 6). In the present section, we set the variance of the initial distribution to be equal to zero, $\sigma_0^2 = 0$. Hence the only source of randomness is the (small) diffusion term in the Langevin equation (2).

The particle starts from x_0 on the potential plateau and its motion is initiated by a small thermal noise. It is reasonable to assume that after a short initial period, the weak noise will play a negligible role as compared to the deterministic drift. The results from Ref. [55] for the short-time averages read $\langle x(\tau)\rangle \approx x_0 - \kappa x_0^2 \tau - \kappa D \tau^2$ and $\mathrm{Var}[x(\tau)] \approx 2D\tau$, where τ will be treated as a small fitting parameter. In order to obtain the equation for the maximum in terms of the initial position and the time scale τ, we substitute these moments into Eq. (9), $x_0 \to \langle x(\tau)\rangle$, $\sigma_0^2 \to \mathrm{Var}[x(\tau)]$. After that we find the position of maximum of the PDF,

$$x_{\max}(t) \approx \frac{1 + D\kappa^2 t\tau_1\tau - \sqrt{1 + 2D\kappa^2 t\tau_1\tau + D^2\kappa^4 t^2\tau^4}}{8D\kappa^3 t^3 \tau}, \tag{15}$$

for $x_0 = 0$, where $\tau_1 = 8t - \tau$ (for $x_0 \neq 0$ the result is rather lengthy).

The approximation is compared with simulations in Fig. 6. Two qualitatively different regimes arise. The first occurs for $x_0 \geqslant 0$, where we are able to predict the dynamics for longer times and we do not need the fitting parameter τ, i.e., τt in this case. The second type of dynamics with a different atypical effect occurs for $x_0 < 0$. Here, we fit τ to extend the validity of the small noise approximation. Even so, we are able to fit the data just before the turning point (the two lower curves in Fig. 6).

To gain further insight into the role of the diffusion term, one can expand Eq. (15) in a series and notice that the maximum grows linearly with D, as shown in Fig. 5, and quadratically with t,

$$x_{\max}(t) \approx \kappa D t^2. \tag{16}$$

Even more interestingly, Eq. (16) resembles the short-time limit of the first statistical moment, $\langle x(t)\rangle \approx -\kappa D t^2$ [55], but with the opposite sign. As can be seen directly from Eq. (16), the bigger the diffusion parameter, the larger shift of the maximum is obtained. This behavior is shown in Fig. 5 for both the weak diffusion and the diffusionless case. The latter presents the dependence on the initial variance, instead of D. Contrary to Eq. (16), the average would quickly diverge towards minus infinity, whereas the maximum, described by Eq. (15), shifts in an opposite direction and converges to a finite value described in the next section. Focusing on the maximum (the most probable particle position) instead of the average $\langle x(t)\rangle$ thus allows us to avoid the singular properties of unstable dynamics.

The curvature (4), calculated along similar lines as Eq. (15), reads

$$\sigma^2(t) \approx 2Dt - 12D^2\kappa^2 t^4, \tag{17}$$

where again a resemblance to the statistical moments can be seen in the first term, because we have $\mathrm{Var}[x(t)] \approx 2Dt$ [55].

Comparing Eqs. (15) and (17), one finds that the SNR (3) grows nonlinearly in time as depicted in Fig. 2 (green line) and for longer times it converges to a constant value. An experimental observation of this and other atypical transient effects may require a fast detection of particle position during the transient period.

V. QUASISTATIONARY DISTRIBUTION IN THE LONG-TIME LIMIT

The discussed zero- and small noise approximations are not capable of properly capturing the long-time nonlinear dynamics at the potential plateau (with non-negligible D). The reason is that even small noise significantly affects the long-time evolution, due to the high instability of the potential. A theoretical description, therefore, requires a different approach.

A. Definition and computation of $Q_{\mathrm{st}}(x)$

The cubic potential is highly unstable and hence one can hardly expect any nontrivial long-time behavior for the PDF $P(x,t)$. However, after a relatively short time, the PDF $P(x,t)$ attains a universal shape determined by the function $Q_{\mathrm{st}}(x)$, which is multiplied by a simple exponential decay in time, $P(x,t) \sim Q_{\mathrm{st}}(x)e^{-\lambda_0 t}$. The normalized function $Q_{\mathrm{st}}(x)$, known as a quasistationary distribution [47,48], is independent of time and initial conditions. It is determined solely by the form of the

potential. From a practical point of view, the quasistationary distribution can be used to characterize unstable systems when moments fail and transients are too fast.

In Monte Carlo simulations of individual trajectories, the quasistationary distribution is merely the normalized PDF of particles that are still on a finite x at time t, $t > \lambda_0$. Hence it should be understood as the long-time limit,

$$Q_{\rm st}(x) = \lim_{t\to\infty} Q(x,t), \tag{18}$$

of the PDF conditioned on survival [cf. (6)],

$$Q(x,t) = \frac{P(x,t)}{S(t)}, \tag{19}$$

where both the nominator and the denominator [the norm of $P(x,t)$; cf. Eq. (5)] tend to zero. The ratio, however, converges towards a finite value for any x. The function $Q(x,t)$ is the PDF of surviving trajectories (e.g., wandering on the potential plateau), which we described by the local measures in the previous sections.

To derive an equation for $Q_{\rm st}(x)$, we start from the Fokker-Planck equation corresponding to Eq. (2),

$$\frac{\partial}{\partial t}P(x,t) = \mathcal{L}P(x,t), \tag{20}$$

with the Fokker-Planck operator given by [58]

$$\mathcal{L} = D\frac{\partial^2}{\partial x^2} + \frac{1}{\gamma}\frac{\partial}{\partial x}V'(x), \tag{21}$$

where $V'(x)$ stands for a derivative of $V(x)$. We now introduce the ansatz $P(x,t) \sim Q_{\rm st}(x)e^{-\lambda_0 t}$ into Eq. (20), together with the exponentially decaying survival probability (5), and after some algebra we obtain that $Q_{\rm st}(x)$ is given by

$$Q_{\rm st}(x) = \frac{\psi_0(x)}{\int_{-\infty}^{\infty} dx\, \psi_0(x)}, \tag{22}$$

where $\psi_0(x)$, the normalized eigenvector of $\mathcal{L}$ corresponding to its largest eigenvalue $-\lambda_0$,

$$\mathcal{L}\psi_0(x) = -\lambda_0\psi_0(x). \tag{23}$$

For a rigorous proof, we refer to Ref. [48]. The quasistationary distribution $Q_{\rm st}(x)$ is shown in Fig. 7 for three different temperatures.

The eigenvalue problem (23) should be supplemented by boundary conditions. Interestingly enough, for the cubic potential, natural boundary conditions yield a PDF which vanishes for $|x| \to \infty$, but the probability current does not vanish in the limit $x \to -\infty$. Thus, we can approximate the singular point $x = -\infty$ by placing an *absorbing boundary* [25] at a finite position $x = a, a < 0$. The absorbing boundary is merely a trap which captures (absorbs) the particle when it hits $x = a$ for the first time. In Fig. 1, the boundary is at $x = -10$. The weight of absorbed trajectories increases with time and eventually tends to one.

The regularization is convenient for a numerical solution of (23) (see Appendix A), and is natural in Monte Carlo simulations. As long as $a \ll -(3k_{\rm B}T/k)^{1/3}$ is satisfied, this cutoff will not affect the properties of the slow stochastic motion on the plateau of the potential (1). Consequently, we

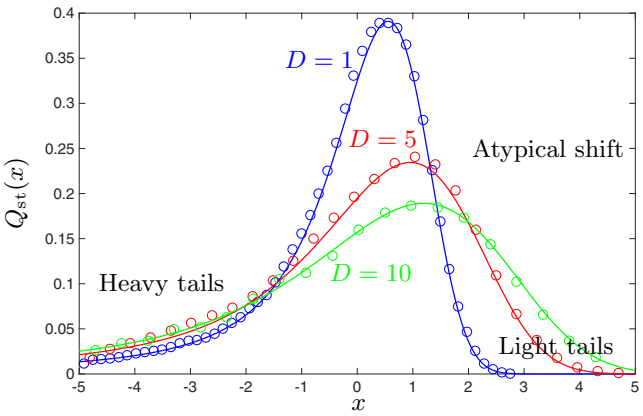

FIG. 7. Broadening of the quasistationary PDF (22) with increasing temperature. Solid lines depict numerical solutions of the eigenvalue problem (23) by the method explained in Appendix A. Circles stand for the outcomes of Monte Carlo simulations using 3×10^5 trajectories. In the simulations, the particle starts from the inflection point and evolves (if not absorbed) for $t = 7$ with the time step $\Delta t = 0.002$. The stiffness k of the cubic potential is set to one. Interesting effects due to the instability observed in the transient dynamics have their analogs reflected in the shape of the quasistationary PDF. The quasistationary PDF therefore can be used to describe unstable systems when averages diverge and transients are fast.

can require $\psi_0(x)$ to satisfy the absorbing boundary condition $\psi_0(a) = 0$ and the natural boundary condition at $x = \infty$.

Finally, notice that $P(x,t) \sim Q_{\rm st}(x)e^{-\lambda_0 t}$ determines just the main asymptotics of $P(x,t)$, i.e., the only significant term in the eigenvector expansion when $t \to \infty$. A time-dependent correction which describes relaxation towards the quasistationary distribution $Q_{\rm st}(x)$ decays exponentially fast, as $e^{(\lambda_0-\lambda_1)t}$. This is why in simulations $Q_{\rm st}(x)$ is readily observable for relatively short times. For counterexamples, where $Q(x,t)$ does not converge to a time-independent limit, we refer, e.g., to Refs. [59,60].

B. $Q_{\rm st}(x)$ as a steady-state distribution and Maxwell's demon

Usually, the term "steady state" is related to a stationary long-time system state with time-independent currents [61,62]. In particular, the Gibbs canonical equilibrium is an example of an isothermal steady state where all currents vanish. In more general nonequilibrium steady states, the currents (in our case a probability current) converge to nonzero values which are closely related to the local properties of the steady-state PDF. At first glance, the quasistationary distribution $Q_{\rm st}(x)$ is not related to such a scenario, because there is no nontrivial long-time state in the unstable cubic potential (the particle, once released, reaches $x = -\infty$ in a relatively short time). The quasistationary PDF results from the limit of the ratio (19) of two vanishing terms and not as the result of the balance of probability currents.

The direct meaning of $Q_{\rm st}(x)$, according to its definition (19), is that $Q_{\rm st}(x)$ stands for the PDF of a particle which survives (or, equivalently, stays on the potential plateau) for a long time. However, it is rather the following steady-state

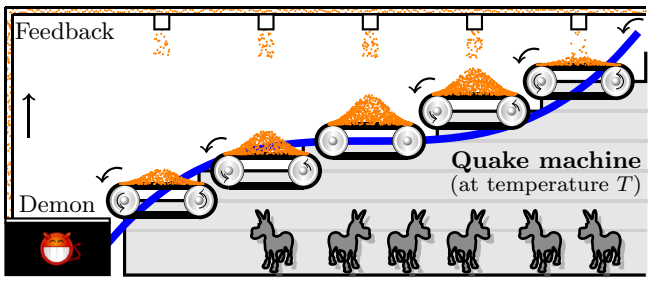

FIG. 8. Sketch of the steady-state factory producing $Q_{\rm st}(x)$ in an unstable cubic potential, where a standard stationary (equilibrium) distribution does not exist [64]. Instead of tracking a single-particle trajectory as in previous figures, here we turn to the following experiment with many particles (sand). The demon (the measurement-feedback mechanism) collects the sand which leaves the system at its left boundary and returns it back according to Eq. (24), such that the long-time distribution of sand on the belts is given by $Q_{\rm st}(x)$. A detailed description of the machine stemming from Eq. (24) is presented in Sec. V B.

interpretation which deepens our intuitive understanding of the model behavior and brings us straight to the results for the maximum and curvature of $Q_{\rm st}(x)$. It can also inspire an experimental method capable of reaching a quasistationary PDF using an external control of the Brownian motion. To obtain the steady-state interpretation of the quasistationary distribution we first notice that the Fokker-Planck equation for $Q(x,t)$ reads

$$\frac{\partial}{\partial t}Q(x,t) = \mathcal{L}Q(x,t) - J_Q(a,t)Q(x,t). \tag{24}$$

Equation (24) follows from the Fokker-Planck equation (20) after inserting $P(x,t) = Q(x,t)S(t)$ into Eq. (20) and dividing the resulting equation by $S(t)$ (see Appendix B for more details).

Above, $-J_Q(a,t)$ is the conditional probability current [63] flowing into the absorbing boundary,

$$J_Q(x,t) = -\left(D\frac{\partial}{\partial x} + \frac{k}{\gamma}x^2\right)Q(x,t). \tag{25}$$

The probability current $J_Q(a,t)$ is negative due to the sign convention (the current is positive when probability flows to the right), hence the second term on the right-hand side of Eq. (24) represents the positive source of the probability. It ensures that the normalization of $Q(x,t)$ remains constant in time, in contrast to the Fokker-Planck equation (20) for the generic PDF $P(x,t)$, where such a source term is missing and hence $P(x,t)$ is not normalized. The integral of this second term is exactly equal to the probability flow to the absorbing boundary.

The physical interpretation of Eq. (24) requires one to describe a complex measurement and feedback mechanism restoring the normalization of $Q(x,t)$. The mechanism uses an ensemble of particles, rather than just a single particle, which we explain in the following. It is depicted using a cartoon style in Fig. 8. In the cartoon, the diffusing particles are represented by orange sand grains. The three basic ingredients which drive the particles according to Eq. (24) and thus also the sand in the cartoon are as follows. (i) The cubic potential approximated by five conveyor belts: The velocities of the belts are proportional to the gradient of the cubic potential at their positions (arrows on the rotating wheels). The belts outside the plateau of the potential systematically transport the sand from right to left, and the belt at the plateau just collects the sand. (ii) The thermal noise represented by donkeys who randomly shake the conveyor holding the structure (the quake machine) as they stomp on its floor: At $T = 0$, the donkeys are unflappable—they do not stomp and the shaking (the thermal motion) stops. Nonzero temperature corresponds to nervous donkeys—they stomp vigorously on the floor and the whole structure vibrates. The noise (vibrations) thus affects globally the sand dynamics, but leaves intact the demon and feedback mechanism. Shaking causes sand grains to jump randomly from one belt to another, both to the left and to the right.

Formally, the two ingredients (i) and (ii) are included in the Fokker-Planck operator $\mathcal{L}$ (21). The last part (iii) of the dynamics described by Eq. (24), i.e., the absorbing boundary and the source term $-J_Q(a,t)Q(x,t)$, are depicted by a black box with a Maxwell demon on the left from the conveyor belts. The demon acts both as a sink and as a source of the sand, namely, it continuously monitors the number of sand grains on individual belts, accepts the sand which falls into the absorbing boundary from the leftmost conveyor belt, and instantaneously redistributes the accepted sand back to the belts. For the redistribution, the demon utilizes measured information about the instantaneous distribution of sand on all the belts. The demon is therefore continuously watching the whole factory. The portions of sand which are delivered to individual belts are determined proportionally to the amount of sand presented on the belts at the time of redistribution. For example, the belt containing 10% of all sand at the time of redistribution is refilled by 10% of the redistributed sand at that time. This rule is a direct interpretation of the source term $-J_Q(a,t)Q(x,t)$ in Eq. (24).

The total amount of sand in the system is fixed similarly as the norm of the PDF $Q(x,t)$ governed by Eq. (24). After a relatively short time [determined by the inverse gap $1/(\lambda_0 - \lambda_1)$, between the two largest eigenvalues of the Fokker-Planck operator (21)], the time-independent steady-state distribution of sand on the belts is established by balancing the sand (probability) currents caused by the three agents (i)–(iii) described above. The sand distribution then corresponds to the quasistationary PDF $Q_{\rm st}(x)$, for which the left-hand side of Eq. (24) vanishes.

Comparing the resulting stationary Fokker-Planck equation with Eq. (23), we get a noteworthy interpretation of the eigenvalue $-\lambda_0$. This inverse relaxation time is just the stationary conditional probability current flowing into the absorbing boundary,

$$\lambda_0 = -J_{Q_{\rm st}}(a), \tag{26}$$

where $J_{Q_{\rm st}}(a) = \lim_{t\to\infty} J_Q(a,t)$. In other words, λ_0 measures the amount of sand per unit time which falls from the leftmost belt into the box (in the steady state).

Last, but not least, note that the above interpretation of Eq. (24) closely resembles stochastic processes with resetting, where particles are instantaneously returned to a certain position or region in space following a given protocol [65–76]. This suggests that results found for systems with resetting can be readily used both in our model and in all similar scenar-

ios, where one considers a probability density of surviving particles. Here, we will evaluate the entropy flux extracted from the system by the Maxwell demon in order to sustain the quasistationary PDF $Q_{\rm st}(x)$.

We define the entropy of a surviving particle at time t as $\mathcal{S}(t) = -k_{\rm B}\int_{-\infty}^{\infty} dx\, Q(x,t)\log Q(x,t)$. Taking the derivative with respect to time gives the entropy production $\dot{\mathcal{S}}(t) = -k_{\rm B}\int_{-\infty}^{\infty} dx\, \partial Q(x,t)/\partial t \log Q(x,t)$. Substituting for $\partial Q(x,t)/\partial t$ from Eq. (24) into the last formula leads to the expression

$$\dot{\mathcal{S}}(t) = \dot{\mathcal{S}}_{\rm diff}(t) - \dot{\mathcal{S}}_{\rm Md}(t), \tag{27}$$

where $\dot{\mathcal{S}}_{\rm diff}(t) = -k_{\rm B}\int_{-\infty}^{\infty} dx[\mathcal{L}Q(x,t)]\log Q(x,t)$, and $\dot{\mathcal{S}}_{\rm Md}(t) = -J_Q(a,t)\mathcal{S}(t)$. The term $\dot{\mathcal{S}}_{\rm diff}(t)$ amounts for an entropy increase due to diffusion in the cubic potential. The term $\dot{\mathcal{S}}_{\rm Md}(t)$ is the entropy flux out of the system due to the demon pushing the system towards the quasistationary PDF. After the system relaxes to the quasistationary state, i.e., for $Q(x,t) = Q_{\rm st}(x)$, the left-hand side of Eq. (27) vanishes and thus the balance between the two entropy productions holds, $\dot{\mathcal{S}}_{\rm diff} = \dot{\mathcal{S}}_{\rm Md}$. The amount of entropy the demon takes out of the system per unit time in order to sustain the nonequilibrium quasistationary state is thus proportional to the stationary entropy of the system and the stationary probability flux out of the system,

$$\dot{\mathcal{S}}_{\rm Md} = -J_{Q_{\rm st}}(a)\mathcal{S}_{\rm st} = \lambda_0\mathcal{S}_{\rm st}, \tag{28}$$

where $\mathcal{S}_{\rm st} = -k_{\rm B}\int_{-\infty}^{\infty} dx\, Q_{\rm st}(x)\log Q_{\rm st}(x)$. Equation (28) illustrates another important role of the relaxation rate λ_0.

VI. QUASISTATIONARY VALUES OF MAXIMUM AND CURVATURE

The maximum of $Q_{\rm st}(x)$ and that of the generic PDF $P(x,t)$ (see Fig. 1) coincide after a relatively short time. Its exact position $x_{\rm max}$, however, depends on the potential and temperature in a nontrivial way. On the other hand, for the curvature at the maximum, $1/\sigma^2_{\rm max} = |Q''_{\rm st}(x_{\rm max})|/Q_{\rm st}(x_{\rm max})$, we obtain from the stationary version of the Fokker-Planck equation (24),

$$\frac{1}{\sigma^2_{\rm max}} = \frac{V''(x_{\rm max})}{k_{\rm B}T} + \frac{\lambda_0}{D}. \tag{29}$$

Namely, we obtain Eq. (29) from Eq. (24) after setting $\partial Q_{\rm st}/\partial t = 0$, $Q'_{\rm st}(x_{\rm max}) = 0$, and using Eq. (26) in the second term on the right-hand side.

The above equation provides us with an indirect and independent way of determining the local width of the generic PDF $P(x,t)$. It is enough to find the position of the maximum $x_{\rm max}$ and measure the decay rate λ_0. The latter measurement would be analogous to our recent experiments [35], since it is enough to determine the decay rate of the survival probability $S(t) \approx s_0 e^{-\lambda_0 t}$. Moreover, from the results of Ref. [35] it follows that the survival probability is easily measurable in highly unstable potentials. Such an independent measurement is needed because the direct determination of the local width is sensitive to the procedure used for fitting the PDF from experimental data.

The result (29) is notable also for its physical content. Interestingly, the more unstable the system (large λ_0), the narrower is the PDF around the maximum. Instability of the system can be controlled both by the strength of the thermal noise D and by the amplitude k of the cubic potential. Strong cubic potentials (larger k for a given D) are more unstable and the plateau region bounded approximately to the interval $[-(3k_{\rm B}T/k)^{1/3},(3k_{\rm B}T/k)^{1/3}]$ is small in this case. The local width of the PDF for more unstable potentials decreases.

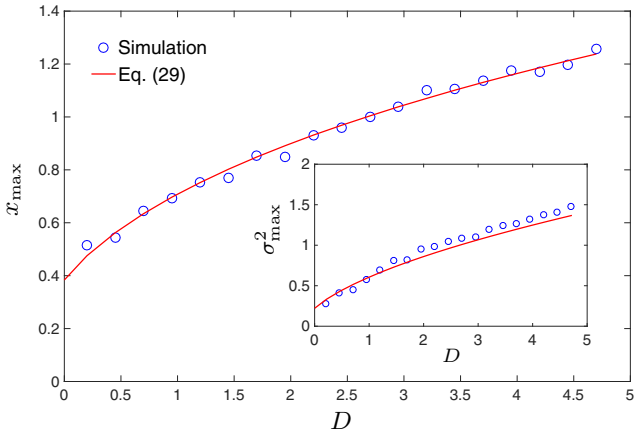

FIG. 9. The maximum and the inverse curvature (inset) of $Q_{\rm st}(x)$ as functions of temperature. Both quantities follow exactly the scaling (30). Solid lines depict numerical solutions of the eigenvalue problem (23) (cf. Appendix A). Circles represent simulated data using 3×10^5 trajectories. In simulations, the particle starts from the inflection point and evolves (if not absorbed) for $t = 7$ with the time step $\Delta t = 0.002$. The stiffness k of the cubic potential is set to one.

The temperature dependence of the quasistationary PDF can be understood from scaling arguments [22,34]. When the absorbing boundary is far from the origin, $a \ll -(3k_{\rm B}T/k)^{1/3}$, there remain only two length scales in the problem: the width of the plateau and the thermal length dictated by D. The quasistationary PDF should depend on their ratio, and hence any length in the problem scales as $(k_{\rm B}T/k)^{1/3}$. This is exactly what we observe for the maximum. A similar relation also holds for the local width of the PDF,

$$x_{\rm max} \sim D^{1/3}, \quad \sigma^2_{\rm max} \sim D^{2/3}. \tag{30}$$

The maximum of the quasistationary PDF climbs up to higher values of the potential for higher temperatures and the local width at the maximum increases. Both dependencies are demonstrated in Fig. 9. The scaling implies that the SNR (3) remains temperature independent.

VII. CONCLUDING REMARKS AND EXPERIMENTAL PERSPECTIVES

Unstable systems are important for their potential applications. However, their description and characterization are challenging even in the simplest cases. In the present paper, we have developed a statistical description of the position of a Brownian particle diffusing in a cubic potential. The task was complicated due to the high instability and nonlinearity of the model. As a consequence, the PDF of the particle position develops a heavy tail and its moments cease to exist. In this paper, we have proposed an appropriate, experimentally

accessible description focusing on the most probable position of the particle (position of the maximum of the PDF) and on a local curvature of the PDF at the maximum (instead of the variance). In contrast to the standard approach, which uses the moments, the two quantities are well defined even though the lifetime of any initial state is very short. We have described both the short-time (Sec. IV) and the long-time (Sec. V) properties of the two quantities, both from analytical and numerical perspectives, with an emphasis on their time and temperature dependencies. Our results are general for unstable potentials with an inflection point and should be easily observable directly using position detectors in experiments similar to that reported in Ref. [35].

In particular, the most probable position shows a peculiar behavior. The maximum of PDF can move opposite to the acting force both as the function of time and temperature (Figs. 4, 6, and 9). The curvature of the PDF around the maximum is related to the stability of the system. For highly unstable systems the position PDFs become broader, as we see from Eq. (7). This equation can be exploited in two ways: Either it can be used to get the local curvature at maximum $\sigma^2_{\max}$ from the knowledge of the relaxation rate λ_0, or it yields the relaxation rate from measurement of $\sigma^2_{\max}$ of an experimentally obtained PDF. The local curvature is therefore both measurable and an operational characteristic of the system. A recent experiment [35] already demonstrated Brownian motion in the cubic potential focusing on the first-passage properties of the particle [34]. Hence the methodology presented here is ready for an experimental test.

Similar unstable systems should be further analyzed in an underdamped limit, where inertia starts to play an important role, leading, e.g., to nonlinear oscillations near the plateau. Such an extension is essential since experiments on the cooling of nanoparticles in high vacuum have already reached the underdamped regime [1,4,77,78]. Thus, there already exists an experimental platform for probing the fundamentals of nonlinear stochastic dynamics in the limit of weak friction.

In recent years, the aforementioned progress in the cooling of nanoparticles in optical traps has brought us close to a quantum regime [79,80], where quantum superposition states can be induced by cubic nonlinear dynamics [9,81,82]. Quantum nonlinear effects in an unstable cubic potential are not only interesting for a fundamental comparison to their stochastic analogs, but they also open doors to quantum simulations and computation with continuous systems [7,8,83].

ACKNOWLEDGMENTS

R.F. and L.O. gratefully acknowledge financial support from the Czech Science Foundation (Project No. GB14-36681G). A.R. and V.H. gratefully acknowledge financial support of Project No. 17-06716S by the Czech Science Foundation. V.H. in addition gratefully acknowledges the support by the Alexander von Humboldt Foundation. L.O. acknowledges the support of Project No. IGA-PrF-2017-008 by the Palacký University.

APPENDIX A: NUMERICAL CALCULATION OF $Q_{\rm st}(x)$

The quasistationary distribution can be computed as the normalized eigenfunction corresponding to the largest eigenvalue of the Fokker-Planck operator $\mathcal{L}$, subject to the absorbing boundary condition at $x = a$ [cf. Eq. (23)]. We have calculated this eigenfunction using the discrete approximation of the generator similar to that used in recent work [84] for the steady state of a two-dimensional Brownian ratchet.

The main idea is to approximate the exact stochastic process in a semi-infinite continuous state space (a,∞) by a suitable process on a finite discrete lattice. This is possible because of the strength of the cubic potential for large $|x|$, which allows us to limit the state space to the interval (a,b), with $b \gg (3k_{\rm B}T/k)^{1/3}$ and $Q_{\rm st}(b) \ll 1$. This is equivalent to keeping the state space (a,∞) and redefining the cubic potential $V(x)$ as

$$\tilde{V}(x) = \theta(b-x)V(x) + \theta(x-b)\infty. \tag{A1}$$

Let us now discretize the interval $[a,b]$ on $N+1$ slices of length $\Delta = (b-a)/N$ and to identify the individual slices with the individual sites of the discrete lattice. We assume that the ith site corresponds to the slice next to the point,

$$x(i) = a + \Delta(i-1), \quad i = 1,\ldots,N+1. \tag{A2}$$

The vector $\mathbf{p}(t) = [p_1(t), p_2(t), \ldots, p_{N+1}(t)]$ of probabilities that the discrete system dwells at time t at site i fulfills the master equation

$$\frac{d}{dt}\mathbf{p}(t) = L\mathbf{p}(t), \tag{A3}$$

with the transition rate matrix L, whose off-diagonal elements are given by

$$l_{ij} = \frac{D}{\Delta^2}\exp\left[-D\frac{\tilde{V}(x(j)) - \tilde{V}(x(i))}{2}\right] \tag{A4}$$

and the diagonal elements

$$l_{ii} = -(l_{ii-1} + l_{ii+1}). \tag{A5}$$

Note that for $i = 1$ we get $r_{11} = -(l_{10} + l_{12})$, but l_{10} is not present elsewhere in the matrix L. This is how the absorbing boundary is implemented in the approximate discrete model. Due to this condition, the rate matrix no longer fulfills the condition $\sum_{j=1}^{N+1} l_{ij} = 0$ and thus the probability in the master equation (A3) is not conserved, similarly as for the Fokker-Planck equation (20).

The distribution $P(x,t)$ can be approximately calculated using the formula $P(x(i),t) = p_i(t)/\Delta$ and the approximation becomes exact in the limit $\Delta \to 0$. Having approximated the generator $\mathcal{L}$ by the rate matrix L, the approximate numerical calculation of the quasistationary distribution $Q_{\rm st}(x)$ is a matter of one line of computer code.

Let us note that the approximation of $Q_{\rm st}(x)$ using this discretization can be very accurate because the matrix L is sparse and thus it is possible to choose very large N (very small Δ). For example, performing the calculation in MATLAB on a standard quad-core PC with 16 Gb ram using the command "sparse" for constructing the matrix L and the command "eigs" for determining the eigenfunction corresponding to the largest eigenvalue of L, it is no problem to choose N of the order 10^6.

APPENDIX B: DERIVATION OF EQ. (24)

To derive dynamical equation (24) for the conditioned PDF $Q(x,t)$, we first insert $P(x,t) = Q(x,t)S(t)$ into the Fokker-Planck equation (20) for the unconditioned PDF $P(x,t)$. After dividing the resulting equation by $S(t)$, we obtain

$$\frac{\partial}{\partial t}Q(x,t) + \frac{Q(x,t)}{S(t)}\frac{dS}{dt} = \mathcal{L}Q(x,t). \tag{B1}$$

Equation (B1) formally differs from Eq. (20) by the second term on the left-hand side. To justify Eq. (24) we need to identify the conditional probability current (25) in this second term, i.e., we need to show that

$$\frac{1}{S(t)}\frac{dS}{dt} = J_Q(a,t). \tag{B2}$$

This is done in two steps. First, we relate the time derivative of the survival probability to the (unconditional) probability current into the absorbing boundary, $dS/dt = J(a,t)$. Here,

$$J(x,t) = -\left(D\frac{\partial}{\partial x} + \frac{k}{\gamma}x^2\right)P(x,t) \tag{B3}$$

is the probability current appearing in the generic Fokker-Planck equation (20), when it is written as the continuity equation [63], $\partial P/\partial t = -\partial J/\partial x$. Space integration of the continuity equation over the interval (a,∞) indeed yields $dS/dt = J(a,t)$. Second, we divide the relation $dS/dt = J(a,t)$ by the survival probability $S(t)$ and identify $Q(x,t) = P(x,t)/S(t)$ in the expression $J(a,t)/S(t)$, which then is equal to the conditional probability current (25), $J(a,t)/S(t) = J_Q(a,t)$. This completes the derivation of Eq. (B2) and thus of the sought equation (24).

[1] J. Gieseler, L. Novotny, and R. Quidant, Nat. Phys. **9**, 806 (2013).
[2] J. Gieseler, M. Spasenović, L. Novotny, and R. Quidant, Phys. Rev. Lett. **112**, 103603 (2014).
[3] J. Gieseler, L. Novotny, C. Moritz, and C. Dellago, New J. Phys. **17**, 045011 (2015).
[4] F. Ricci, R. Rica, M. Spasenović, J. Gieseler, L. Rondin, L. Novotny, and R. Quidant, Nat. Commun. **8**, 15141 (2017).
[5] G. I. Harris, U. L. Andersen, J. Knittel, and W. P. Bowen, Phys. Rev. A **85**, 061802 (2012).
[6] C. Schäfermeier, H. Kerdoncuff, U. B. Hoff, H. Fu, A. Huck, J. Bilek, G. I. Harris, W. P. Bowen, T. Gehring, and U. L. Andersen, Nat. Commun. **7**, 13628 (2016).
[7] S. Lloyd and S. L. Braunstein, Phys. Rev. Lett. **82**, 1784 (1999).
[8] D. Gottesman, A. Kitaev, and J. Preskill, Phys. Rev. A **64**, 012310 (2001).
[9] K. Miyata, H. Ogawa, P. Marek, R. Filip, H. Yonezawa, J.-i. Yoshikawa, and A. Furusawa, Phys. Rev. A **93**, 022301 (2016).
[10] M. Gavrilov and J. Bechhoefer, Phys. Rev. Lett. **117**, 200601 (2016).
[11] D. Gelbwaser-Klimovsky, A. Bylinskii, D. Gangloff, R. Islam, A. Aspuru-Guzik, and V. Vuletic, arXiv:1705.11180.
[12] B. Lindner, A. Longtin, and A. Bulsara, Neural Comput. **15**, 1761 (2003).
[13] N. Brunel and P. E. Latham, Neural Comput. **15**, 2281 (2003).
[14] P. Colet, M. San Miguel, J. Casademunt, and J. M. Sancho, Phys. Rev. A **39**, 149 (1989).
[15] L. Ramírez-Piscina and J. M. Sancho, Phys. Rev. A **43**, 663 (1991).
[16] F. T. Arecchi and V. Degiorgio, Phys. Rev. A **3**, 1108 (1971).
[17] D. Sigeti and W. Horsthemke, J. Stat. Phys. **54**, 1217 (1989).
[18] J. E. Hirsch, B. A. Huberman, and D. J. Scalapino, Phys. Rev. A **25**, 519 (1982).
[19] P. Reimann and C. Van den Broeck, Physica D **75**, 509 (1994).
[20] P. Reimann, C. Van den Broeck, H. Linke, P. Hänggi, J. M. Rubi, and A. Pérez-Madrid, Phys. Rev. Lett. **87**, 010602 (2001).
[21] P. Reimann, C. Van den Broeck, H. Linke, P. Hänggi, J. M. Rubi, and A. Pérez-Madrid, Phys. Rev. E **65**, 031104 (2002).
[22] T. Guérin and D. S. Dean, Phys. Rev. E **95**, 012109 (2017).
[23] O. A. Tretiakov, T. Gramespacher, and K. A. Matveev, Phys. Rev. B **67**, 073303 (2003).
[24] B. Spagnolo, C. Guarcello, L. Magazzù, A. Carollo, D. Persano Adorno, and D. Valenti, Entropy **19**, 20 (2017).
[25] S. Redner, *A Guide to First-Passage Processes*, 1st ed. (Cambridge University Press, Cambridge, U.K., 2007).
[26] P. Hänggi, P. Talkner, and M. Borkovec, Rev. Mod. Phys. **62**, 251 (1990).
[27] F. T. Arecchi, A. Politi, and L. Ulivi, Nuovo Cimento B **71**, 119 (1982).
[28] M. R. Young and S. Singh, Phys. Rev. A **31**, 888 (1985).
[29] M. O. Cáceres, C. E. Budde, and G. J. Sibona, J. Phys. A **28**, 3877 (1995).
[30] R. N. Mantegna and B. Spagnolo, Phys. Rev. Lett. **76**, 563 (1996).
[31] N. V. Agudov, Phys. Rev. E **57**, 2618 (1998).
[32] A. Fiasconaro, B. Spagnolo, and S. Boccaletti, Phys. Rev. E **72**, 061110 (2005).
[33] M. O. Cáceres, J. Stat. Phys. **132**, 487 (2008).
[34] A. Ryabov, P. Zemánek, and R. Filip, Phys. Rev. E **94**, 042108 (2016).
[35] M. Šiler, P. Jákl, O. Brzobohat, A. Ryabov, R. Filip, and P. Zemánek, Sci. Rep. **7**, 1697 (2017).
[36] N. V. Agudov and A. N. Malakhov, Phys. Rev. E **60**, 6333 (1999).
[37] A. A. Dubkov, N. V. Agudov, and B. Spagnolo, Phys. Rev. E **69**, 061103 (2004).
[38] M. Suzuki, Prog. Theor. Phys. **56**, 77 (1976).
[39] M. Suzuki, Prog. Theor. Phys. **56**, 477 (1976).
[40] M. Suzuki, Prog. Theor. Phys. **57**, 380 (1977).
[41] F. Haake, Phys. Rev. Lett. **41**, 1685 (1978).
[42] F. de Pasquale and P. Tombesi, Phys. Lett. A **72**, 7 (1979).
[43] H. Dekker, Physica A **103**, 80 (1980).
[44] F. de Pasquale, P. Tartaglia, and P. Tombesi, Phys. Rev. A **25**, 466 (1982).
[45] U. Weiss, Phys. Rev. A **25**, 2444 (1982).
[46] H. Dekker, Phys. Lett. A **88**, 279 (1982).
[47] P. K. Pollett, Quasi-stationary distributions: A bibliography (2015), https://people.smp.uq.edu.au/PhilipPollett/papers/qsds/qsds.pdf.
[48] P. Collet, S. Martínez, and J. San Martín, *Quasi-Stationary Distributions: Markov Chains, Diffusions and Dynamical Systems*, 1st ed. (Springer, Berlin, 2013).

[49] A. M. Yaglom, Dokl. Acad. Nauk SSSR **56**, 795 (1947).
[50] A. Hastings, Trends Ecol. Evol. **19**, 39 (2004).
[51] I. Nåsell, Adv. Appl. Probab. **28**, 895 (1995).
[52] D. Steinsaltz and S. N. Evans, Theor. Popul. Biol. **65**, 319 (2004).
[53] *Maxwell's Demon 2: Entropy, Classical and Quantum Information, Computing*, edited by H. S. Leff and A. F. Rex, 1st ed. (Taylor & Francis, London, 2002).
[54] J. M. R. Parrondo, J. M. Horowitz, and T. Sagawa, Nat. Phys. **11**, 131 (2015).
[55] R. Filip and P. Zemánek, J. Opt. **18**, 065401 (2016).
[56] R. Filip, Phys. Rev. A **88**, 063837 (2013).
[57] M. Cramer and J. Eisert, New J. Phys. **12**, 055020 (2010).
[58] C. Gardiner, *Handbook of Stochastic Methods for Physics, Chemistry, and the Natural Sciences*, 3rd ed. (Springer, Berlin, 2004).
[59] A. Ryabov and P. Chvosta, Phys. Rev. E **89**, 022132 (2014).
[60] A. Ryabov, E. Berestneva, and V. Holubec, J. Chem. Phys. **143**, 114117 (2015).
[61] R. A. Blythe and M. R. Evans, J. Phys. A **40**, R333 (2007).
[62] J. Tailleur, J. Kurchan, and V. Lecomte, J. Phys. A **41**, 505001 (2008).
[63] H. Risken, *The Fokker-Planck Equation: Methods of Solutions and Applications*, 2nd ed., Springer Series in Synergetics (Springer, Berlin, 1996).
[64] Donkeys were drawn using the code presented at http://tex.stackexchange.com/questions/312199/i-need-a-tex-donkey, and the devil face was taken from the open clip art gallery https://openclipart.org/detail/30289/tango-face-devil.
[65] S. C. Manrubia and D. H. Zanette, Phys. Rev. E **59**, 4945 (1999).
[66] M. R. Evans and S. N. Majumdar, Phys. Rev. Lett. **106**, 160601 (2011).
[67] L. Kusmierz, S. N. Majumdar, S. Sabhapandit, and G. Schehr, Phys. Rev. Lett. **113**, 220602 (2014).
[68] S. Gupta, S. N. Majumdar, and G. Schehr, Phys. Rev. Lett. **112**, 220601 (2014).
[69] A. Murugan, D. A. Huse, and S. Leibler, Phys. Rev. X **4**, 021016 (2014).
[70] J. M. Meylahn, S. Sabhapandit, and H. Touchette, Phys. Rev. E **92**, 062148 (2015).
[71] D. Hartich, A. C. Barato, and U. Seifert, New J. Phys. **17**, 055026 (2015).
[72] S. Eule and J. J. Metzger, New J. Phys. **18**, 033006 (2016).
[73] A. Pal, A. Kundu, and M. R. Evans, J. Phys. A **49**, 225001 (2016).
[74] J. Fuchs, S. Goldt, and U. Seifert, Europhys. Lett. **113**, 60009 (2016).
[75] A. Pal and S. Reuveni, Phys. Rev. Lett. **118**, 030603 (2017).
[76] M. Montero, A. Masó-Puigdellosas, and J. Villarroel, Eur. Phys. J. B **90**, 176 (2017).
[77] T. Li, S. Kheifets, and M. G. Raizen, Nat. Phys. **7**, 527 (2011).
[78] V. Jain, J. Gieseler, C. Moritz, C. Dellago, R. Quidant, and L. Novotny, Phys. Rev. Lett. **116**, 243601 (2016).
[79] N. Kiesel, F. Blaser, U. Delić, D. Grass, R. Kaltenbaek, and M. Aspelmeyer, Proc. Natl. Acad. Sci. USA **110**, 14180 (2013).
[80] M. Frimmer, J. Gieseler, and L. Novotny, Phys. Rev. Lett. **117**, 163601 (2016).
[81] P. Marek, R. Filip, and A. Furusawa, Phys. Rev. A **84**, 053802 (2011).
[82] M. Yukawa, K. Miyata, H. Yonezawa, P. Marek, R. Filip, and A. Furusawa, Phys. Rev. A **88**, 053816 (2013).
[83] S. D. Bartlett and B. C. Sanders, Phys. Rev. A **65**, 042304 (2002).
[84] A. Ryabov, V. Holubec, M. H. Yaghoubi, M. Varga, M. E. Foulaadvand, and P. Chvosta, J. Stat. Mech. (2016) 093202.

Diffusing up the Hill: Dynamics and Equipartition in Highly Unstable Systems

Martin Šiler,[1,*] Luca Ornigotti,[2] Oto Brzobohatý,[1] Petr Jákl,[1] Artem Ryabov,[3,†] Viktor Holubec,[3,4] Pavel Zemánek,[1] and Radim Filip[2,‡]

[1]*Institute of Scientific Instruments of the Czech Academy of Sciences, Královopolská 147, 612 64 Brno, Czech Republic*
[2]*Department of Optics, Palacký University, 17. listopadu 1192/12, 771 46 Olomouc, Czech Republic*
[3]*Charles University, Faculty of Mathematics and Physics, Department of Macromolecular Physics, V Holešovičkách 2, 180 00 Praha 8, Czech Republic*
[4]*Universität Leipzig, Institut für Theoretische Physik, Postfach 100 920, D-04009 Leipzig, Germany*

(Received 19 March 2018; revised manuscript received 20 August 2018; published 3 December 2018)

Stochastic motion of particles in a highly unstable potential generates a number of diverging trajectories leading to undefined statistical moments of the particle position. This makes experiments challenging and breaks down a standard statistical analysis of unstable mechanical processes and their applications. A newly proposed approach takes advantage of the local characteristics of the most probable particle motion instead of the divergent averages. We experimentally verify its theoretical predictions for a Brownian particle moving near an inflection in a highly unstable cubic optical potential. The most likely position of the particle atypically shifts against the force, despite the trajectories diverging in the opposite direction. The local uncertainty around the most likely position saturates even for strong diffusion and enables well-resolved position detection. Remarkably, the measured particle distribution quickly converges to a quasistationary one with the same atypical shift for different initial particle positions. The demonstrated experimental confirmation of the theoretical predictions approves the utility of local characteristics for highly unstable systems which can be exploited in thermodynamic processes to uncover energetics of unstable systems.

DOI: 10.1103/PhysRevLett.121.230601

Introduction.—Unstable stochastic dynamics of mechanical objects is a common ingredient of processes inside mechanical machines. They use explosive fuel to move a piston or its microscopic equivalent, adenosine triphosphate, to perform individual strokes [1–4]. However, instability generates rapidly diverging trajectories which complicate the description of motion, its experimental observation, and applications. Such trajectories can make all statistical averages increase very fast or even diverge. The standard deviation of position can diverge faster than its mean; hence, the observed average motion quickly becomes uncertain. Moreover, the probability density of the position can develop a heavy tail and, therefore, all its moments will diverge [5,6]. All this limits the statistical description of transient effects in unstable potentials and makes experimental observations challenging. The detrimental effects appear even in a strongly overdamped regime, where a system intensively dissipates energy to the environment. The simplest example is an overdamped Brownian particle diffusing in the highly unstable cubic potential $V(x) = \mu x^3/3$. The Langevin equation for the particle position reads

$$\gamma \frac{dx}{dt} = -V'[x(t)] + \sqrt{2\gamma k_B T}\xi(t), \tag{1}$$

where γ is the friction coefficient, T is the ambient temperature, k_B the Boltzmann constant, and $\xi(t)$ stands for the delta-correlated Gaussian white noise, $\langle \xi(t) \rangle = 0$, $\langle \xi(t)\xi(t') \rangle = \delta(t - t')$.

Equation (1) with the cubic potential $V(x) = \mu x^3/3$ models dynamics at the saddle-node bifurcation [7,8], which arises in several nonlinear stochastic models of physics, biology, and chemistry. Examples include optical bistability in lasers [9–11], firing of neurons [12,13], Brownian ratchets [14–17], and nonlinear maps [18]. Even though we primarily focus on the cubic nonlinearity with the inflection point, the described methodology is broadly applicable to any highly unstable potential. This we demonstrate in the Supplemental Material [19] on prominent examples: the unstable potential with no stationary point and the unstable potential with a local minimum. The latter is frequently used to study decays from metastable states in condensed matter models [26,27].

The instability in the cubic potential has been theoretically analyzed by means of statistical moments for times shorter than the appearance of any diverging trajectory [5] and using first passage times for distances far away from the instability [7,9,10,12,13,18,28–36]. In both cases, dynamical effects have been found to be stimulated by the initial temperature of the particle and the temperature of the surroundings. Recently, both described regimes have been observed experimentally for a micron-sized particle trapped in optical tweezers [37]. However, the transient regime beyond short-time approximation remained without

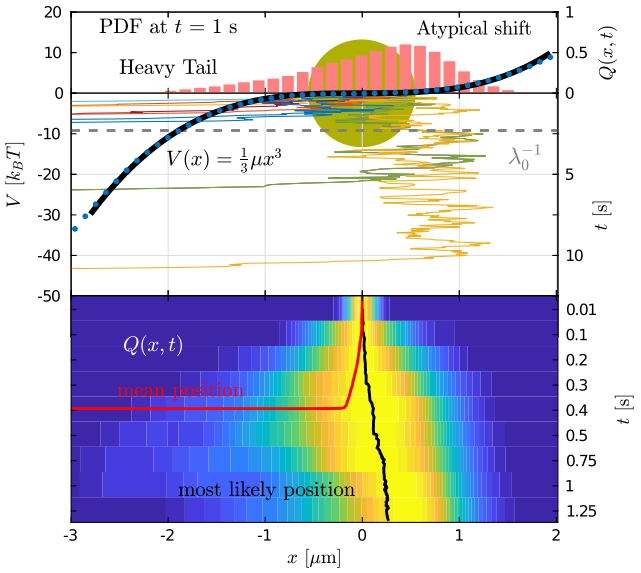

FIG. 1. The most likely motion of a particle in the highly unstable cubic potential. Upper-left axis: The potential $V(x)$ recovered from the experimental trajectories (blue points) fitted by the cubic dependence (black solid line). Upper-right axis: The normalized measured PDF for $x(t)$ at $t = 1$ s (histogram). Central-right axis: A typical set of nine measured trajectories starting at $x = 0$. The yellow sphere illustrates the size of the used colloidal particles (diameter ≈ 1 μm). Lower panel: Individual stripes show a measured PDF at different times (the lower-right axis). The mean particle position (the red curve) diverges around $t = 0.3$ s. In fact, all measured moments diverge at the same time. Contrary to this, the black curve demonstrates the regular evolution of the most probable particle position (the position of the PDF maximum) shifting to the right from $x = 0$ against the direction of acting force.

any description and physical understanding. The lack of description and understanding undermines applications of unstable stochastic dynamics in nanotechnology and in quantum technology.

Recently, a new methodology focused on the most likely position of the particle in unstable potential has been developed [6]. It uses directly measurable local features of the probability density of position instead of global diverging statistical moments. During the transient dynamics, this methodology evaluates a shift of the probability density maximum instead of the mean value and local curvature around the maximum instead of the standard deviation. Moreover, a transient decay of the probability density function (PDF) of particle position at late times follows $P(x,t) \sim Q_{\rm st}(x)e^{-\lambda_0 t}$, where $Q_{\rm st}(x)$ is a time-independent normalized PDF independent of initial conditions, and λ_0 is a positive decay rate. The PDF $Q_{\rm st}(x)$ is the so-called quasistationary distribution [38–44], and it predicts both the shift and local curvature of position PDF in the long-time limit.

In this Letter, we experimentally demonstrate the applicability of this local description focused on the most likely particle position in the unstable cubic potential illustrated in Fig. 1. The experimental data agree well with theory even for a small sample of measured trajectories, showing that the theory is robust and applicable even under severe experimental imperfections. We unambiguously distinguish the atypical shift of the most likely position for transients longer than the short-time limit and experimentally verify a fast convergence of the position PDF to the quasistationary state. Finally, we derive and experimentally verify the quasistationary generalization of the equipartition theorem showing that the quasistationary state has high energetic content which can be utilized in a postselection process removing divergent trajectories.

The experiments verify that the methodology proposed in Ref. [6] removes existing limitations in description and understanding of transients in highly unstable potentials. Experiments with other typical unstable potentials are included in the Supplemental Material [19]. They demonstrate wide applicability of the approach beyond the cases discussed in Ref. [6]. Direct applications of such most likely motion in unstable systems are expected in Brownian motors. The methodology can be translated to the recently achieved underdamped regime [45–47] and developing experiments approaching the quantum regime [48–50].

Experiments.—The quasi-one-dimensional cubic potential profile $V(x) = \mu x^3/3$, $\mu = (4.07 \pm 0.03)\ k_BT\,\mu{\rm m}^{-3}$ was created by two pairs of counterpropagating Gaussian laser beams in the configuration that ensures a conservative optical force [51,52]. We tracked the particle position with a CCD camera at 2000 fps. The frame rate is fast enough to analyze the transient unstable stochastic dynamics. Technical details of the setup and data processing are described in the Supplemental Material [19].

Strong instability of the cubic potential limits the duration of the experiments. As Fig. 1 illustrates, the number of nondiverging trajectories decreases rapidly with time. Thus, also the size of the ensemble of measured particle positions rapidly decreases because the divergent trajectories are excluded from the statistics. For example, at $t = 1$ s we processed into PDFs of roughly 55% of the total number of recorder trajectories (starting at $x_0 = 0$). At longer times, the number of nondiverging trajectories decays exponentially $\sim e^{-\lambda_0 t}$. Therefore, due to the strength of instability, a sufficient statistics of particle position is practically unreachable at longer times. This behavior is generic for highly unstable potentials (see other examples in the Supplemental Material [19]).

Furthermore, for such an unstable potential, the total number of trajectories recorded with a specific particle was rather limited. Typically, we performed ≈ 100 measurement cycles under the same experimental conditions. After that, a fine readjustment of the experimental system was needed to compensate for systematic changes like intrinsic mechanical drifts. Consequently, the profile of the optical potential slightly varied from the previous one, and, thus, the new set

of trajectories could not be mixed with the previous one into a larger statistical ensemble of measured trajectories.

Most likely position and its atypical shift.—A Brownian particle in the optical cubic potential and the results of a typical measurement are illustrated in Fig. 1. The histogram in the figure illustrates the measured PDF at time $t = 1$ s. The unstable cubic potential induces three crucial effects in the position PDF: (i) a heavy tail for $x \ll -(3k_BT/\mu)^{1/3}$, (ii) a light tail for $x \gg (3k_BT/\mu)^{1/3}$, and (iii) a shift of the PDF maximum away from $x = 0$. Moreover, owing to the thermal noise, the PDF after a short time loses all information about the initial particle position and attains a time-independent (quasistationary) spatial shape.

The weight of the heavy tail quickly increases with time because of a growing number of diverging trajectories (shown in the middle panel of Fig. 1). Several of them diverge in a short time; consequently, the averages $\langle x(t)\rangle$ (cf. red curve in the lower panels) and $\langle x^2(t)\rangle$ computed over all measured trajectories quickly grow above all bounds. These average global characteristics are strongly influenced by the divergence and, hence, bare no meaning for the description of the particle position [37]. The heavy tail negatively influences all quantities based on averaging over all trajectories.

Instead, as proposed in a recent theoretical work [6], it is beneficial to focus on the local characteristics. The first of them is the most likely particle position $x_{\max}(t)$ given by the maximum of the PDF $Q(x,t)$; see the black curve in the lower panel of Fig. 1. The second one quantifies a local uncertainty around the most probable position. It is defined as the (inverse) normalized curvature at the PDF maximum,

$$\sigma^2(t) = \frac{Q[x_{\max}(t),t]}{|\partial_{xx}^2 Q[x_{\max}(t),t]|}. \tag{2}$$

Different from the diverging mean and variance, the local quantities $x_{\max}(t)$ and $\sigma(t)$ remain finite and attain finite constant values at long times (see Fig. 3 and the discussion below). The ratio $x_{\max}(t)/\sigma(t)$ specifies a local visibility of the most likely particle position.

The measured time evolution of the local quantities is shown in Fig. 3 for different initial positions x_0, $x_0 = -1$, -0.75, -0.5, -0.25, and 0 μm. For large negative x_0, the maximum $x_{\max}(t)$ drifts first in the direction of the acting force, $-\mu x^2$. Later, it passes through its minimal value and starts to shift back *against* the force. Eventually, $x_{\max}$ becomes positive and independent of time and of the initial position. This is accompanied by non monotonic dynamics of the local standard deviation $\sigma(t)$. For large negative x_0, it passes through a pronounced maximum and later decreases [which corresponds to a sharper peak of $Q(x,t)$].

Quasistationary state in the unstable potential.—A remarkable fact demonstrated in Fig. 3 is that the two local characteristics quickly converge to constant values independent of initial conditions. The limiting values

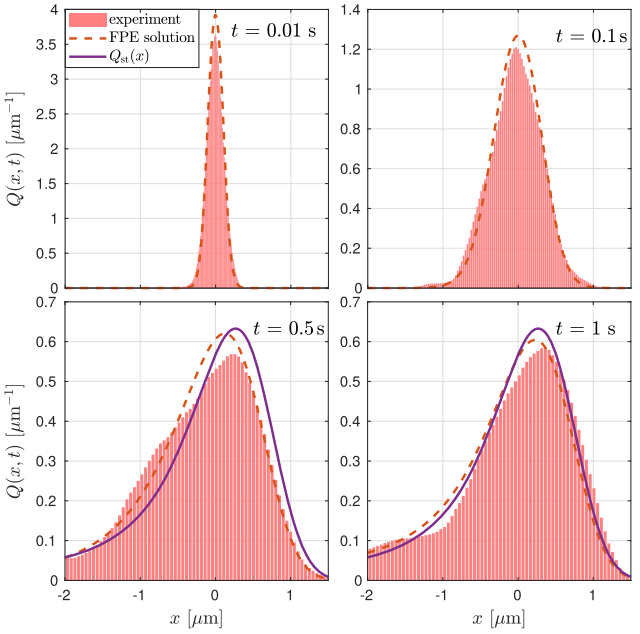

FIG. 2. Convergence of the position PDF $Q(x,t)$ towards the quasistationary state $Q_{\rm st}(x)$. The experimentally measured PDFs (histograms) are in a reasonable agreement with the numerical solutions of the corresponding Fokker-Planck equation (dashed lines). Solid lines in the lower panels depict the quasistationary PDF $Q_{\rm st}(x)$ calculated from Eq. (3). The atypical shift of $x_{\max}(t)$ right from $x = 0$ is clearly observable.

correspond to local properties of the quasistationary distribution, $Q_{\rm st}(x)$. The PDF $Q_{\rm st}(x)$ naturally arises in our experiment and is inherent in all highly unstable systems.

The quasistationary distribution is defined as the long-time limit of the normalized position PDF: $Q_{\rm st}(x) = \lim_{t\to\infty} P(x,t)/S(t)$, where $P(x,t)$ satisfies the Fokker-Planck equation for the discussed model, and $S(t) = \int_{-\infty}^{+\infty} dx' P(x',t)$ is the survival probability [53], which gives the probability that the trajectory has not diverged by the time t. Because of the high instability of the potential, the number of nondiverging trajectories decreases exponentially $S(t) \sim e^{-\lambda_0 t}$, $P(x,t) \sim Q_{\rm st}(x)e^{-\lambda_0 t}$, and the normalized PDF $Q(x,t) = P(x,t)/S(t)$ converges exponentially fast to $Q_{\rm st}(x)$. Introducing the normalized PDF $Q(x,t)$ into the Fokker-Planck equation corresponding to the Langevin equation (1) yields that $Q_{\rm st}(x)$ is given by the normalized eigenvector for the smallest λ_0 of the Fokker-Planck operator in question [6]:

$$\frac{1}{\gamma}[k_BT\partial_{xx}^2 + \partial_x V'(x)]Q_{\rm st}(x) = -\lambda_0 Q_{\rm st}(x). \tag{3}$$

Equation (3) is proven in the mathematical literature on quasistationary distributions [39] and explained on physical grounds in the Supplemental Material [19]. Figure 2 demonstrates fast convergence of the measured PDF in the highly unstable cubic potential $V(x) = \mu x^3/3$

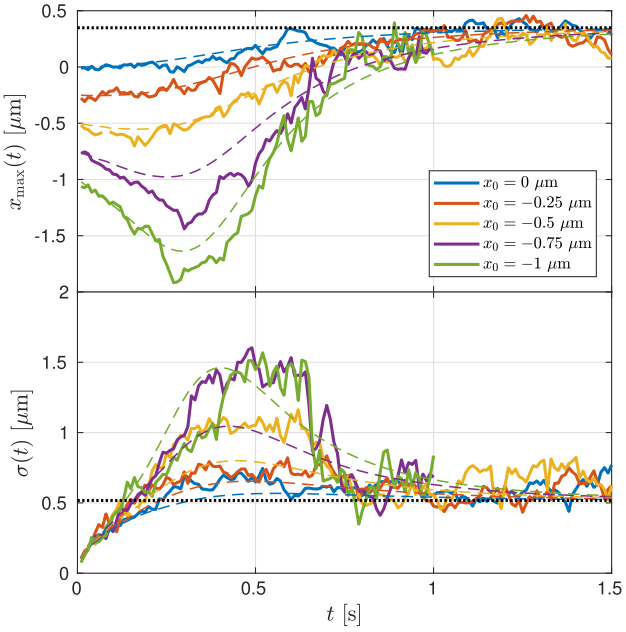

FIG. 3. Atypical shift of the PDF maximum against the acting force. Upper panel: The position of the PDF maximum $x_{\max}(t)$ for different initial positions x_0 evaluated from the experimental data (solid lines) and simulations (dashed lines). When $x_0 < -0.5$, all trajectories diverge extremely fast due to strong instability. The green and the purple curves stop at time $t = 1$ s because there are not enough data points to reconstruct the PDFs for $t > 1$ s. The lower panel shows $\sigma(t)$ evaluated for the same data. The transient dynamics quickly converges to the quasistationary state [constant dotted lines calculated from $Q_{\rm st}(x)$ defined by Eq. (3)].

towards $Q_{\rm st}(x)$ calculated from Eq. (3) (with natural boundary conditions). The histogram of measured positions is well approximated by $Q_{\rm st}(x)$ already for short times, $t > 1$ s.

Figures 2 and 3 show that the quasistationary limit of $x_{\max}(t)$, $x_{\max} \equiv \lim_{t\to\infty} x_{\max}(t)$ is shifted right from the origin against the direction of the acting force. This reflects the tendency of long nondiverging trajectories (the trajectories that have not diverged by the long time t, $t \to \infty$) to diffuse right from $x = 0$ for most of the time. Such long-surviving trajectories tend to avoid negative values of x, because an excursion to negative x, where the strong force may cause their divergence, would almost surely be fatal for them. Thus, the long-surviving trajectories are most probably found on the plateau region slightly right from $x = 0$.

In order to distinguish this quasistationary atypical shift in experimental data, the quasistationary value of $\sigma(t)$, $\sigma \equiv \lim_{t\to\infty}\sigma(t)$ should be reasonably small compared to $x_{\max}$. Large σ corresponds to a broad distribution around the maximum, where it may be hard to measure $x_{\max}$ with sufficient precision. The experimental results demonstrate saturation of the "shift-to-noise" ratio $x_{\max}/\sigma = (0.5 \pm 0.2)$. The solution of Eq. (3) predicts that $x_{\max}/\sigma \approx 0.67$. These values are sufficiently large to clearly observe the atypical shift of $x_{\max}$ from the origin. The atypical shift is a robust effect which can be observed even without cooling and for a strong nonlinearity.

Rate of divergence.—The magnitude of the eigenvalue λ_0 gives a quantitative measure of stability of the studied system. It is equal to the slowest decay rate in the given potential [54], or in our case, the rate at which the trajectories diverge. Evaluating Eq. (3) at $x = x_{\max}$ and identifying the quasistationary inverse local curvature σ^2 according to its definition (2), we obtain the relation

$$\lambda_0 = \frac{1}{\gamma}\left(\frac{k_B T}{\sigma^2} - V''(x_{\max})\right), \tag{4}$$

which allows us to determine λ_0 directly from stationary local quantities $x_{\max}$ and σ. Using $\mu = (4.07 \pm 0.03)\ k_B T\,\mu\text{m}^{-3}$ estimated from the experimental data, we calculate numerically $Q_{\rm st}(x)$, $x_{\max}$, and σ from Eq. (3), which yields $\lambda_0 = (0.44 \pm 0.01)\ \text{s}^{-1}$. The reciprocal magnitude $1/\lambda_0$ of the eigenvalue is the characteristic (longest) decay time. For our experiment, we get $1/\lambda_0 = (2.27 \pm 0.05)$ s. The decay time describes the asymptotic exponential decrease of the average number of nondivergent trajectories. Its magnitude of $\approx$2.3 s ensures that on average there are still enough trajectories around the time 1.5 s, where the quasistationary state emerges; see Figs. 2 and 3 to compare the timescales.

Quasistationary equipartition theorem.—The counterintuitive shift of $x_{\max}$ from zero suggests an interesting quasistationary energetics of the unstable system. As a first step towards the development of such a theory, we have derived a generalized equipartition theorem for the quasistationary state. The basic idea behind the theorem is to keep only nondiverging trajectories by a proper post-selection process (other trajectories are discarded). For odd unstable potentials $V(x) \sim x^n$, $n = 3, 5, \ldots$, the result reduces to the simple formula for the mean potential energy of the Brownian particle,

$$\langle V(x)\rangle_{\rm st,+} = \frac{k_B T}{n} + \frac{\lambda_0 \gamma}{2n}\langle x^2\rangle_{\rm st,+}. \tag{5}$$

Here, the averages are taken over a sufficiently stable section of the system based on the positive half line $x > 0$. That is, over the conditional PDF $Q_{\rm st,+}(x) = \theta(x) Q_{\rm st}(x)/\int_0^\infty dx' Q_{\rm st}(x')$, which describes the quasistationary statistics of the stable region, where the most likely particle position is located. The result (5) is obtained directly from the quasistationary Fokker-Planck equation (3) after multiplication of the equation by x^2 and integration over $x \in (0, +\infty)$. Its general form is derived in the Supplemental Material [19].

The average potential energy $\langle V(x)\rangle_{\rm st,+}$ is always higher than that obtained from the corresponding equilibrium

equipartition theorem $\langle V(x)\rangle_{\mathrm{eq}} = k_B T/n$ for the Gibbs state with the same support: $\mathcal{Q}_{\mathrm{eq}}(x) = \theta(x)\exp[-V(x)/k_B T]/Z$, where an infinite potential barrier restricts the particle to $x > 0$ to protect it against divergence. The excess energy in the quasistationary state is given by the second term on the right-hand side of Eq. (5). This term is always positive. Its experimentally measured value $(\lambda_0\gamma/6)\langle x^2\rangle_{\mathrm{st},+} = (0.05 \pm 0.02)k_B T$ agrees with the theoretical prediction $(0.051 \pm 0.001)k_B T$ computed using Eq. (3) for the measured μ.

In the conditional ensemble, we discard all diverging trajectories with low potential energies located at $x < 0$. The excess energy arises due to the heat accepted from the surroundings by nondiverging trajectories. The heat $\mathcal{Q}(t)$ accepted during $(0, t)$ is $\mathcal{Q}(t) = V[x(t)] - V[x(0)]$ because $V(x)$ is time independent [55]. Remarkably, the quasistationary conditional strategy can perform better in harnessing potential energy compared to the equilibrium one. This opens possibilities for further thermodynamic investigation of work and heat extractable from quasistationary states and calls for extension of our method to time-dependent potentials $V(x, t)$, where $\mathcal{Q}(t)$ will no longer be the simple difference of potential energies [55].

Summary and perspectives.—Our experimental tests successfully verified (i) utility of the approach based on the most likely motion of the unstable process, (ii) fast appearance of the quasistationary distribution for room-temperature overdamped dynamics, and (iii) the generalization of the equipartition theorem (5) for a regular part of the quasistationary PDF. All experimental results are in good agreement with the theory, even for a small number of trajectories. We showed that the naturally arising quasistationary state has higher energetic content than the equilibrium one. After further themodynamic investigation, this finding may stimulate development of new approaches to exploit this advantage and design new thermal machines based on unstable dynamics. From a general perspective, our results suggest a high potential of unstable systems for future applications in microscopic machines. The next experimental challenge is an unstable underdamped regime [45–47], where novel phenomena connected to the most likely dynamics are expected owing to the fact that the underdamped-overdamped correspondence is frequently broken even for stable dynamics [56–58]. Advantageously, the approach can be directly translated to almost unitary unstable dynamics in the quantum regime, where the experiments are currently entering [48–50].

The authors acknowledge support from the Czech Science Foundation: M. Š., L. O., O. B., P. J., P. Z., and R. F. were supported by Project No. GB14-36681G; A. R. and V. H. were supported by Project No. 17-06716S. V. H. is grateful for the support of the Alexander von Humboldt Foundation. L. O. is supported by Palacky University (Grant No. IGA-PrF-2017-008). L. O. and R. F. have received national funding from the MEYS of the Czech Republic (Project No. 8C18003) under Grant Agreement No. 731473 within the QUANTERA ERA-NET cofund in quantum technologies implemented within the European Unions Horizon 2020 Programme (Project TheBlinQC). The research infrastructure was supported by MEYS of the Czech Republic, the Czech Academy of Sciences, and the European Commission (Grants No. LO1212, No. RVO:68081731, and No. CZ.1.05/2.1.00/01.0017).

*siler@isibrno.cz
†rjabov.a@gmail.com
‡filip@optics.upol.cz

[1] R. D. Vale and R. A. Milligan, Science **288**, 88 (2000).
[2] M. Schliwa and G. Woehlke, Nature (London) **422**, 759 (2003).
[3] R. D. Astumian, Faraday Discuss. **195**, 583 (2016).
[4] S. Erbas-Cakmak, D. A. Leigh, C. T. McTernan, and A. L. Nussbaumer, Chem. Rev. **115**, 10081 (2015).
[5] R. Filip and P. Zemánek, J. Opt. **18**, 065401 (2016).
[6] L. Ornigotti, A. Ryabov, V. Holubec, and R. Filip, Phys. Rev. E **97**, 032127 (2018).
[7] D. Sigeti and W. Horsthemke, J. Stat. Phys. **54**, 1217 (1989).
[8] P. Reimann and C. Van den Broeck, Physica (Amsterdam) **75D**, 509 (1994).
[9] P. Colet, M. San Miguel, J. Casademunt, and J. M. Sancho, Phys. Rev. A **39**, 149 (1989).
[10] L. Ramírez-Piscina and J. M. Sancho, Phys. Rev. A **43**, 663 (1991).
[11] F. T. Arecchi and V. Degiorgio, Phys. Rev. A **3**, 1108 (1971).
[12] B. Lindner, A. Longtin, and A. Bulsara, Neural Comput. **15**, 1761 (2003).
[13] N. Brunel and P. E. Latham, Neural Comput. **15**, 2281 (2003).
[14] P. Reimann, C. Van den Broeck, H. Linke, P. Hänggi, J. M. Rubi, and A. Pérez-Madrid, Phys. Rev. Lett. **87**, 010602 (2001).
[15] P. Reimann, C. Van den Broeck, H. Linke, P. Hänggi, J. M. Rubi, and A. Pérez-Madrid, Phys. Rev. E **65**, 031104 (2002).
[16] T. Guérin and D. S. Dean, Phys. Rev. E **95**, 012109 (2017).
[17] A. V. Arzola, M. Villasante-Barahona, K. Volke-Sepúlveda, P. Jákl, and P. Zemánek, Phys. Rev. Lett. **118**, 138002 (2017).
[18] J. E. Hirsch, B. A. Huberman, and D. J. Scalapino, Phys. Rev. A **25**, 519 (1982).
[19] See Supplemental Material http://link.aps.org/supplemental/10.1103/PhysRevLett.121.230601 for details of the experiment, experimental results for other unstable potentials, and derivations of Eqs. (3) and (5), including Refs. [20–25].
[20] D. Lamouroux and K. Lehnertz, Phys. Lett. A **373**, 3507 (2009).
[21] A. O'Hagan and T. Leonard, Biometrika **63**, 201 (1976).
[22] R. C. Tolman, *The Principles of Statistical Mechanics* (Clarendon Press, Oxford, 1938).
[23] R. C. Tolman, Phys. Rev. **11**, 261 (1918).

[24] K. Huang, *Statistical Mechanics*, 2nd ed. (Wiley, New York, 1987).
[25] K. Sekimoto, *Stochastic Energetics* (Springer-Verlag, Berlin, 2010).
[26] O. A. Tretiakov, T. Gramespacher, and K. A. Matveev, Phys. Rev. B **67**, 073303 (2003).
[27] B. Spagnolo, C. Guarcello, L. Magazz, A. Carollo, D. Persano Adorno, and D. Valenti, Entropy **19**, 20 (2017).
[28] F. T. Arecchi, A. Politi, and L. Ulivi, Nuovo Cimento Soc. Ital. Fis. **71B**, 119 (1982).
[29] M. R. Young and S. Singh, Phys. Rev. A **31**, 888 (1985).
[30] M. O. Cáceres, C. E. Budde, and G. J. Sibona, J. Phys. A **28**, 3877 (1995).
[31] R. N. Mantegna and B. Spagnolo, Phys. Rev. Lett. **76**, 563 (1996).
[32] N. V. Agudov, Phys. Rev. E **57**, 2618 (1998).
[33] A. Fiasconaro, B. Spagnolo, and S. Boccaletti, Phys. Rev. E **72**, 061110 (2005).
[34] M. O. Cáceres, J. Stat. Phys. **132**, 487 (2008).
[35] A. Ryabov, P. Zemánek, and R. Filip, Phys. Rev. E **94**, 042108 (2016).
[36] P. Hänggi, P. Talkner, and M. Borkovec, Rev. Mod. Phys. **62**, 251 (1990).
[37] M. Šiler, P. Jákl, O. Brzobohatý, A. Ryabov, R. Filip, and P. Zemánek, Sci. Rep. **7**, 1697 (2017).
[38] A. M. Yaglom, Dokl. Acad. Nauk SSSR (in Russian) **56**, 795 (1947).
[39] P. Collet, S. Martínez, and J. San Martín, *Quasi-Stationary Distributions: Markov Chains, Diffusions and Dynamical Systems* (Springer-Verlag, Berlin, 2013).
[40] P. K. Pollett, *Quasi-Stationary Distributions: A Bibliography* (2015), https://people.smp.uq.edu.au/PhilipPollett/papers/qsds/qsds.pdf.
[41] I. Nåsell, Adv. Appl. Probab. **28**, 895 (1996).
[42] A. Hastings, Trends Ecol. Evol. **19**, 39 (2004).
[43] D. Steinsaltz and S. N. Evans, Theor. Popul. Biol. **65**, 319 (2004).
[44] A. Ryabov and P. Chvosta, Phys. Rev. E **89**, 022132 (2014).
[45] P. Z. G. Fonseca, E. B. Aranas, J. Millen, T. S. Monteiro, and P. F. Barker, Phys. Rev. Lett. **117**, 173602 (2016).
[46] F. Ricci, R. Rica, M. Spasenović, J. Gieseler, L. Rondin, L. Novotny, and R. Quidant, Nat. Commun. **8**, 15141 (2017).
[47] L. Rondin, J. Gieseler, F. Ricci, R. Quidant, C. Dellago, and L. Novotny, Nat. Nanotechnol. **12**, 1130 (2017).
[48] V. Jain, J. Gieseler, C. Moritz, C. Dellago, R. Quidant, and L. Novotny, Phys. Rev. Lett. **116**, 243601 (2016).
[49] T. M. Hoang, Y. Ma, J. Ahn, J. Bang, F. Robicheaux, Z.-Q. Yin, and T. Li, Phys. Rev. Lett. **117**, 123604 (2016).
[50] A. T. M. A. Rahman and P. F. Barker, Nat. Photonics **11**, 634 (2017).
[51] T. Čižmár, O. Brzobohatý, K. Dholakia, and P. Zemánek, Laser Phys. Lett. **8**, 50 (2011).
[52] P. Zemánek, M. Šiler, O. Brzobohatý, P. Jákl, and R. Filip, J. Opt. **18**, 065402 (2016).
[53] S. Redner, *A Guide to First-Passage Processes* (Cambridge University Press, Cambridge, England, 2001).
[54] H. Risken, *The Fokker-Planck Equation: Methods of Solutions and Applications*, Springer Series in Synergetics, 2nd ed. (Springer, New York, 1996).
[55] U. Seifert, Rep. Prog. Phys. **75**, 126001 (2012).
[56] I. A. Martínez, E. Roldán, L. Dinis, D. Petrov, and R. A. Rica, Phys. Rev. Lett. **114**, 120601 (2015).
[57] A. S. Bodrova, A. V. Chechkin, A. G. Cherstvy, H. Safdari, I. M. Sokolov, and R. Metzler, Sci. Rep. **6**, 30520 (2016).
[58] D. Arold, A. Dechant, and E. Lutz, Phys. Rev. E **97**, 022131 (2018).

The following manuscript "*Noise induced instantaneous speed and acceleration of a levitated particle*" is currently under review process for publication in Scientific Reports, and thus the excerpt that follows comprises of the submitted version of the manuscript.

Noise-induced instantaneous speed and acceleration of a levitated particle

Luca Ornigotti[1,*] **and Radim Filip**[1,†]

[1]Department of Optics, Department of Optics, Palacký University, 17. listopadu 1192/12, 771 46, Olomouc, Czech Republic
[*]luca.ornigotti@gmail.com
[†]filip@optics.upol.cz

ABSTRACT

Levitating nanoparticles trapped in optical potentials at low pressure open the experimental investigation of nonlinear ballistic phenomena. With engineered non-linear potentials and fast optical detection, the observation of autonomous transient mechanical effects, such as instantaneous speed and acceleration stimulated purely by initial position noise, are now achievable. By using parameters of current low pressure experiments, we simulate and analyse such noise-induced particle ballistics in a cubic optical potential demonstrating their evolution, faster than their standard deviations, justifying the feasibility of the experimental verification. We predict, the maxima of instantaneous speed and acceleration distributions shift alongside the potential force, while the maximum of position distribution moves opposite to it. We report that cryogenic cooling is not necessary in order to observe the transient effects, while a low noise in initial particle speed is required, via cooling or post-selection, to not mask the effects. These results stimulate the discussion for both attractive stochastic thermodynamics, and extension of recently explored quantum regime.

Introduction

Stochastic levitating optomechanics in vacuum is a dynamically expanding experimental platform with a unique potential to test and exploit strong nonlinear motional effects without any friction, and bring them close to the quantum domain. This uniqueness arises from the possibility to combine manipulation of the optical trapping potential by a spatial light modulator, inducing new unexplored nonlinearities, and fast optical measurement to verify rapid transient effects using modern optical detectors. At low pressure, it allows direct observation of stochastic underdamped mechanical phenomena[1–7], which allow access to the instantaneous particle speed not measurable in the overdamped motion[8,9]. In the transient ballistic regime, the surrounding environment does not modify the statistics of the instantaneous velocity[8,10,11]. Moreover, the initial noise of the levitating particle can be controlled, by postselection[12], feedback cooling[13–16] and ultimately, by coherent scattering to the mechanical ground states[17–19]. All these key ingredients encourage broader investigation of the fundamental aspects of statistical mechanics[20,21] and accelerate development of applications in mechanical sensing[5,22–24] and thermodynamical engines[25,26]. Recently, the highly unstable motion of a levitating particle in the cubic potential has been analysed[27,28] and experimentally verified[29,30] in the overdamped regime. It was demonstrated that the mean particle position, induced by the initial position uncertainty, increases faster than that uncertainty. Atypically, the position distribution maximum shifts in the opposite direction to the mean. These investigations have already been stimulating experimentally verifiable thermodynamical consequences[27].

In the low pressure limit the particle is deep in the underdamped regime so that the instantaneous particle speed and acceleration become new transient quantities to be first explored and later exploited for applications. In this paper we simulate and analyse nonlinear ballistic effects for instantaneous velocity and acceleration induced by the initial position noise, and predict the experimental regime where such phenomena are visible using parameters for current setups in laboratories[12,31–33]. We observe that the only requirement for a reliable experimental observation is a reduction of initial velocity noise. Importantly, we indicate that both the velocity and acceleration distributions' maxima, stimulated by initial position noise, shifts *normally* in the same direction as the velocity and acceleration mean. It is a crucial step to further accumulate such noise-induced phenomena, and later use them in the aforementioned applications.

Results

Underdamped, overdamped and deterministic nonlinear dynamics in cubic potential

To understand the low-pressure nonlinear effects, we must distinguish them from the already measured high-pressure over-damped limit[27,30], and aim to achieve them close to the zero-damping deterministic limit. First, we describe the properties of the stochastic motion of an underdamped Brownian particle in the unstable cubic potential. Second, we explore the high pressure limit in comparison to the over-damped approximation[27,30], and low pressure limit with comparison to the zero-damping deterministic approximation. The dynamics of the damped Brownian particle in the cubic potential $V(x) = Kx^3/3$ is described by the following Langevin equation

$$\ddot{x} + \gamma\dot{x} + \kappa x^2 = \sqrt{2\frac{k_B T\gamma}{m}}\xi(t), \qquad \langle\xi(t)\rangle = 0, \langle\xi(t)\xi(t')\rangle = \delta(t-t') \tag{1}$$

where $\kappa = K/m$ is the normalised cubic potential stiffness, $\gamma = \Gamma/m$ is the medium damping with Γ the drag coefficient of the medium (e.g. air at low pressure), T is the absolute temperature, k_B is the Boltzmann constant, and $F^{fluct} = \sqrt{2k_BT\Gamma}\xi(t)$ is the broadband Markov Langevin force, uncorrelated in time with zero mean and variance given by the fluctuation-dissipation theorem $\langle F^{fluct}\rangle = 0$, $\langle F^{fluct}(t)F^{fluct}(t')\rangle = \sqrt{2k_BT\gamma}\delta(t-t')$. We use Eq. (1) for all stochastic simulations, and also to present all the figures. The details of the simulation, comprising the re-scaling of Eq. (1) to allow usage of real experimental numbers, are described in the Methods. In the high pressure limit, the instantaneous velocity and acceleration require very fast measurement to be observed in the ballistic regime[11], therefore we use the *averaged* velocity $\bar{v} = \Delta x/\Delta t$, and *averaged* acceleration $\bar{a} = \Delta\bar{v}/\Delta t$ routinely measured in high pressure experiments. The time Δt has been adjusted to be tenfold the time-step dt to allow the computation of the averaged quantities. The details of the time scales, and convergence are presented in the Methods. Considering that $\bar{v}$ and $\bar{a}$ are still stochastic quantities, we further characterise their average motion by analysing their means, $\langle\bar{v}\rangle$, and $\langle\bar{a}\rangle$, and standard deviations, $\sigma_{\bar{v}}$, and $\sigma_{\bar{a}}$.

In the high pressure limit, Eq. (1) can be approximated by the over-damped equation of motion[28],

$$\dot{x} = -\frac{K}{\Gamma}x^2 + \sqrt{2\frac{k_BT}{\Gamma}}\xi(t), \tag{2}$$

comprising a change of mean position $\langle x(t)\rangle \approx -(K\sigma_{x_0}^2 t + 2Kk_BTt^2\Gamma^{-1})/\Gamma$, for initial Gaussian position distribution with $\langle x_0\rangle = 0$, evolving with standard deviation $\sigma_x(t) \approx \sqrt{\sigma_{x_0}^2 + 8(K/\Gamma)^2\sigma_{x_0}^4 t^2 + 2k_BTt/\Gamma}$, and generating a $SNR_x \approx (K^2\sigma_{x_0}^2 t^2 + K^2k_BTt^3\Gamma^{-1})/\Gamma$ [28]. At the time scale of this experiment $t = 0.1$ ms, 3 orders of magnitude shorter than the previous overdamped experiments $t = 1$s[29,30], the mean $\langle x(t)\rangle \approx 0$ and standard deviation $\sigma_x(t) \approx \sigma_{x_0}$ of position do not change in time, resulting in a negligible SNR_x as can be observed in Fig.1 for the high pressure regime (a). However, the average velocity $\langle\bar{v}\rangle$ already feels the initial noise evolving linearly with the latter as shown in Fig.1 (c) by the green line. The statistics of the average velocity $\bar{v}$, for short time Δt and Gaussian position and velocity distributions with $\langle x_0\rangle = 0$ and $\langle\bar{v}_0\rangle = 0$, approaches

$$\langle\bar{v}\rangle = \left\langle\frac{\Delta x}{\Delta t}\right\rangle \approx -\frac{K}{\Gamma}\sigma_{x_0}^2, \qquad \sigma_{\bar{v}} \approx \sqrt{2\left(\frac{K}{\Gamma}\right)^2\sigma_{x_0}^4 + \frac{2k_BT}{\Gamma}}, \qquad SNR_{\bar{v}} = \frac{|\langle\bar{v}\rangle|}{\sigma_{\bar{v}}} \approx \frac{1}{\sqrt{2\left(1 + k_BT\Gamma K^{-1}\sigma_{x_0}^{-2}\right)}}. \tag{3}$$

For small environmental temperature, $k_BT \ll K^2/\Gamma$, Eq. (3) generates a constant $SNR_{\bar{v}} \approx 1/\sqrt{2}$. On the other hand, in the experiments at room temperature and $\Gamma = 10$ Hz[29,30] the second term in the standard deviation of average velocity $\sigma_{\bar{v}}$ reduces the $SNR_{\bar{v}}$ to that of Eq. (3). The latter can be qualitatively observed in Fig.1 (c) by the non constant azure halo as a function of initial position noise. However, velocity uncertainty does not increase as quickly as in particle position, for the same short time scale. The statistics of the average acceleration $\bar{a}$, as shown in Fig.1(e), do not change neither for the mean $\langle\bar{a}\rangle$ (green), nor for the standard deviation $\sigma_{\bar{a}}$ (blue-green halo) for the short time dynamics and range of parameters we are interested in, and their approximate characterisation is therefore omitted. By numerically simulating Eq. (1) for values of $\Gamma \geq 10$ Hz, the position and average velocity statistics, obtained from Eq. (2) for the over-damped approximation, can be retrieved fully. A quantitative comparison is shown in Fig. 2 (a,c, green dots).

The aim of the low-pressure regime is to (i) reach the statistics of *instantaneous* speed, as compared to average speed in Eq. (3), and (ii) obtain *instantaneous* acceleration statistics, both not achievable in the high pressure regime without very fast measurements. We consider such a short-time regime characterised by no change in initial particle position, as depicted in Fig.1. Such short transient regime when the particle does not move defines the time scale of such effect.

The goal in this regime is to reach the ideal classical limit of the zero-pressure regime, approaching deterministic dynamics for $\Gamma = 0$, where Eq. (1) becomes

$$\ddot{x} + \kappa x^2 = 0, \tag{4}$$

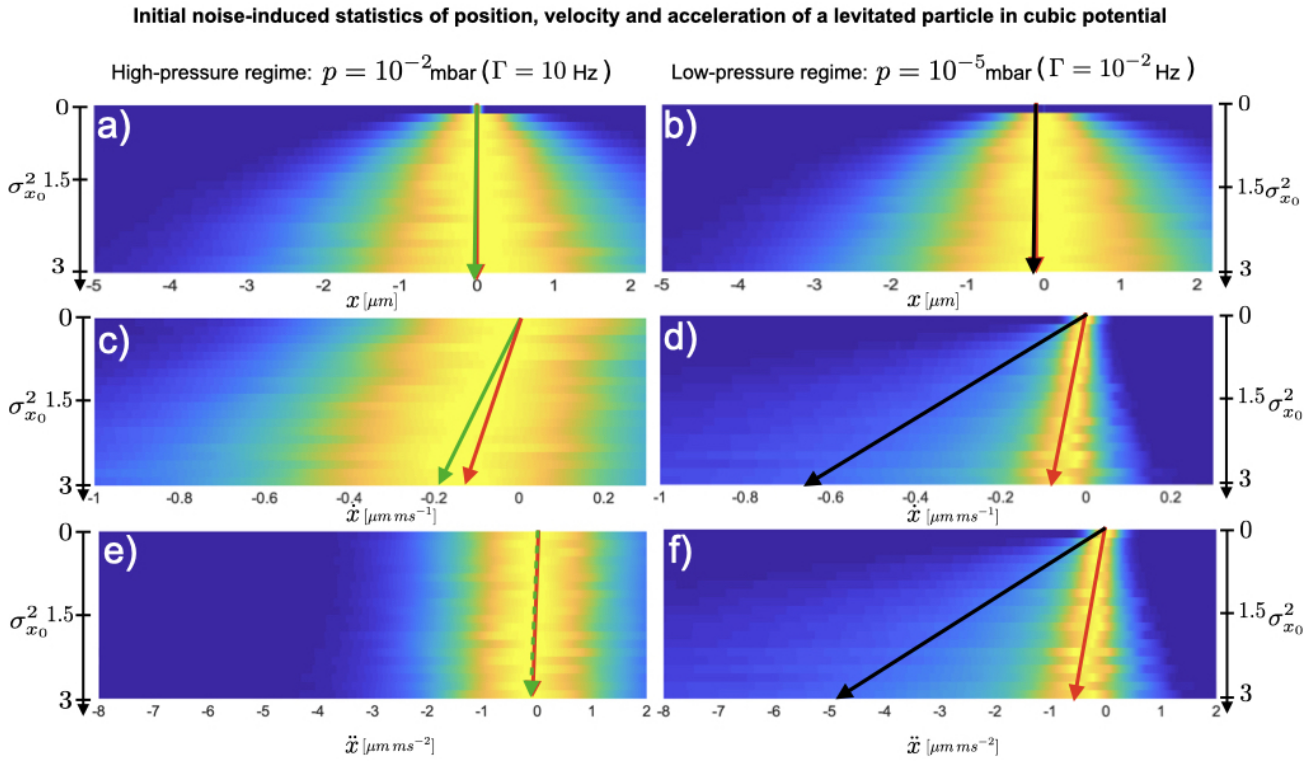

Figure 1. Noise-induced position, velocity and acceleration statistics of a levitated particle in cubic potential, for high pressure limit, corresponding to a pressure of $p = 10^{-2}$ mbar, (left column) and low pressure limit, corresponding to a pressure of $p = 10^{-5}$ mbar (right column). At initial time $t = 0$ ms, the Gaussian distributions of particle position has $\langle x_0 \rangle = 0$, while $\sigma^2_{x_0}$ triggers the nonlinear dynamics. In all cases, the Gaussian distribution of particle instantaneous speed has $\langle \dot{x}_0 \rangle = 0$ and $\sigma^2_{\dot{x}_0} = 0$. The initial position and speed are statistically independent. In the top panel, for both high pressure limit (a), and low pressure limit (b), the mean of particle position $\langle x \rangle$ (green, black) does not develop at short time scales, with increasing initial position noise σ_{x_0}, but its standard deviation σ_x increases with it (green-blue halo). The maximum of position distribution x_{max} (red) does not develop either with increasing initial position uncertainty. In the middle panel, for the high pressure limit (c), the shift of the maximum of average velocity $\bar{v} = \Delta x/\Delta t$ distribution (red) increases alongside the mean of average speed $\langle \bar{v} \rangle$ (green). While the maximum of instantaneous velocity $\dot{x} = dx/dt$ distribution, in the low pressure regime (d) does not increase compared to its high pressure counterpart, the mean of instantaneous speed $\langle \dot{x} \rangle$ (black), produces a larger noise-induced shift than in the high pressure regime (green). Simultaneously, the standard deviation $\sigma_{\dot{x}}$ (green-blue halo) and the uncertainty around the maximum $\sigma_{\dot{x}_{max}}$ are significantly reduced (yellow area). The bottom panel shows the evolution of particle's acceleration statistics in both high pressure (e) and low pressure (f) limits. For the high pressure limit (e) neither the maximum of average acceleration $\bar{a} = \Delta \dot{x}/\Delta t$ distribution (red), nor the mean of averaged acceleration (green), $\langle \bar{a} \rangle$, display any noise-induced shift. On the other hand, in the low pressure limit (f), the statistics exhibits a substantial noise-induced shift in the maximum of instantaneous acceleration $\ddot{x} = d\dot{x}/dt$ distribution (red) alongside the mean of instantaneous acceleration $\langle \ddot{x} \rangle$ (black).
To generate all the density plots, Eq. (1) has been simulated using $\kappa = 6k_B T \mu m^{-3} Kg^{-1}$, $T = 300$ K, $t = 0.1$ ms, $dt = 2 \times 10^{-5}$ ms. $N_t = 10^4$ trajectories where generated with 5000 samples each. To calculate the instantaneous quantities, $\dot{x} = dx/dt$, $\ddot{x} = d\dot{x}/dt$, the time interval used is given by the time-step $dt = 2 \times 10^{-5}$ ms, whereas for the average quantities $\bar{v} = \Delta x/\Delta t$, $\bar{a} = \Delta v/\Delta t$, the time interval, multiple of the time-step, has been used $\Delta t = 10 \times dt$.

yielding deterministic trajectories from initial position and velocity statistics. In this nonlinear ballistic regime, the Gaussian initial distribution of particle speed has $\langle \dot{x}_0 \rangle = 0$ and $\sigma^2_{\dot{x}_0} = 0$. The initial position and speed are statistically independent. In such regime, the initial position statistics is the only thermal energy resource that can be used in the nonlinear ballistics. For short time dynamics, from $\langle x_0 \rangle = 0$, the quantitative description of the zero-damping approximation for instantaneous acceleration gives

$$\langle \ddot{x} \rangle \approx -\kappa \sigma^2_{x_0}, \qquad \sigma_{\ddot{x}} \approx \sqrt{2}\kappa \sigma^2_{x_0}, \qquad SNR_{\ddot{x}} = \frac{|\langle \ddot{x} \rangle|}{\sigma_{\ddot{x}}} \approx \frac{1}{\sqrt{2}}. \tag{5}$$

Notice that both mean and standard deviation are advantageously independent of initial speed statistics. This helps to distinguish the nonlinear ballistics in the experiment. The evolution of mean instantaneous acceleration $\langle \ddot{x} \rangle$, and its standard deviation $\sigma_{\ddot{x}}$,

grow comparably with σ_{x_0} keeping a constant $SNR_{\ddot{x}} \approx 1/\sqrt{2}$. In Fig.2 (e,f), Eq. (1) has been simulated (black dots), for damping $\Gamma = 10^{-2}$ Hz, to generate $\langle \ddot{x} \rangle$, and $SNR_{\ddot{x}}$. At such small pressure, the dominant dynamics observed can be already described by the zero-damping approximation introduced in Eq. (4), resulting in a linear evolution of $\langle \ddot{x} \rangle$ with $\sigma^2_{x_0}$ as showed in Eq. (5) (black line). Simultaneously, the $SNR_{\ddot{x}}$ (black dots) generated with Eq. (1), converges quickly to the zero-damping approximation depicted in Eq. (4), resulting in a constant $SNR_{\ddot{x}}$ as obtained in Eq. (5). By formally integrating Eq. (4) $\dot{x}(t) \approx \dot{x}_0 - \kappa \int_0^t x_0^2(t')dt'$ with $\langle x_0 \rangle = 0$, the short-time evolution of instantaneous velocity unfolds as

$$\langle \dot{x}(t) \rangle \approx -\kappa \sigma^2_{x_0} t, \qquad \sigma_{\dot{x}}(t) \approx \sqrt{2}\kappa \sigma^2_{x_0} t, \qquad SNR_{\dot{x}}(t) = \frac{|\langle \dot{x}(t) \rangle|}{\sigma_{\dot{x}}(t)} \approx \frac{1}{\sqrt{2}}. \tag{6}$$

considering the initial conditions $\langle \dot{x}_0 \rangle = \sigma^2_{\dot{x}_0} = 0$. The mean $\langle \dot{x}(t) \rangle$ of instantaneous velocity evolves linearly with initial position variance $\sigma^2_{x_0}$, growing comparably with its standard deviation $\sigma_{\dot{x}}(t)$, ultimately leading to the constant $SNR_{\dot{x}} \approx 1/\sqrt{2}$ shown in Eq. (6). Simultaneously, by second time formally integrating Eq. (4) with $\langle x_0 \rangle = 0$, the position approaches $x(t) \approx x_0 + \int_0^t \dot{x}_0(t')dt' - \int_0^t \int_0^{t'} \kappa x_0^2(t'')dt''dt'$, while its statistics for short time dynamics evolves as

$$\langle x(t) \rangle \approx -\frac{1}{2}\kappa \sigma^2_{x_0} t^2, \qquad \sigma_x(t) \approx \sqrt{\sigma^2_{x_0} + \frac{1}{2}\kappa^2 t^4 \sigma^4_{x_0}}, \qquad SNR_x(t) = \frac{|\langle x \rangle|}{\sigma_x} \approx \frac{1}{\sqrt{2\left(1 + 2k^{-2}\sigma_{x_0}^{-2} t^{-4}\right)}}. \tag{7}$$

For the large time scale, starting at $t = 0.9$ ms, the mean position evolves as in Eq. (7), while the standard deviation is dominated by the second term, ultimately leading to a constant $SNR_x \approx 1/\sqrt{2}$. At this scale, the dynamics already makes the particle moving farther by initial position noise. At the short time scale, $t = 0.1$ ms however, the position at average does not move, while its standard deviation remains equal to σ_{x_0}. The resulting noise-induced dynamics produces a $SNR_x \approx 0$. At such a short time scale, the result is similar to the over-damped regime described by (2). This behavior can be observed in Fig.1 (b) by the black arrow for the mean position, and with the azure halo for the standard deviation. The behavior of the SNR_x can be observed in Fig.2 (b, black line), holding true for small pressure (black dots), as well as for high pressure (green dots).

Robustness of the noise-induced instantaneous speed and acceleration

Role of environmental temperature T

The instantaneous speed and acceleration stimulated by the initial position noise, can be affected by room temperature of external environment. Generalising the above results for non-zero damping γ, and environmental temperature T, assuming initial Gaussian distribution both in x and $\dot{x}$ with $\langle x_0 \rangle = \langle \dot{x}_0 \rangle = 0$, and vanishing variance $\sigma^2_{x_0} = 0$, the role of environmental noise can be discussed using the approximate formulae obtained from Eq. (1)

$$\langle x(t) \rangle \approx -\frac{1}{2}\kappa \sigma^2_{x_0} t^2, \quad \sigma_x(t) \approx \sqrt{\sigma^2_{x_0} + \frac{2k_B T\gamma}{3m} t^3 + \frac{1}{2}\kappa^2 \sigma^4_{x_0} t^4}, \quad SNR_x(t) = \frac{|\langle x \rangle|}{\sigma_x} \approx \frac{1}{\sqrt{2\left(1 + \frac{2k_B T\gamma}{3m\kappa^2 \sigma^4_{x_0} t} + \frac{2}{\kappa^2 \sigma^2_{x_0} t^4}\right)}} \tag{8}$$

$$\langle \dot{x}(t) \rangle \approx -\kappa \sigma^2_{x_0} t, \qquad \sigma_{\dot{x}}(t) \approx \sqrt{2\kappa^2 \sigma^4_{x_0} t^2 + 2\frac{k_B T\gamma}{m}} t, \qquad SNR_{\dot{x}}(t) = \frac{|\langle \dot{x} \rangle|}{\sigma_{\dot{x}}} \approx \frac{1}{\sqrt{2\left(1 + \frac{k_B T\gamma}{m\kappa^2 \sigma^4_{x_0} t}\right)}}, \tag{9}$$

$$\langle \ddot{x}(t) \rangle \approx -\kappa \sigma^2_{x_0}, \qquad \sigma_{\ddot{x}}(t) \approx \sqrt{2\kappa^2 \sigma^4_{x_0} + 2\frac{k_B T\gamma}{m}}, \qquad SNR_{\ddot{x}}(t) = \frac{|\langle \ddot{x} \rangle|}{\sigma_{\ddot{x}}} \approx \frac{1}{\sqrt{2\left(1 + \frac{k_B T\gamma}{m\kappa^2 \sigma^4_{x_0}}\right)}}. \tag{10}$$

The main significant difference, noticeable from Eqs. (8) to (10), is the time scale at which the environmental temperature T becomes relevant. Notice how advantageously the $SNR_{\ddot{x}}$ of Eq. (10) is time independent, compared to Eqs. (8), and (9). In Eq. (8) for position statistics, T plays a negligible role for short time scales (up to $t = 0.1$ ms), as the $SNR_x \approx 0$ is independent of the chosen T, as visible from Fig.2 (b) for the range of Γ from overdamped to zero-damping limit. For longer time scales (from $t = 0.3$ ms) the environmental temperature competes against the noise-induced effect when $T \geq 3m\kappa^2 t \sigma^4_{x_0}/(4k_B\gamma)$ ($T \approx 800\sigma^4_{x_0}$ K, for $\Gamma = 10^{-2}$ Hz), realising a growing SNR_x slowly converging to $SNR_x = 1/\sqrt{2}$ for the higher environmental temperature T. Given the high temperature requirement, such regime is not visible for the parameters of the experimental set-up we used[12]. In Eq. (9), the standard deviation of instantaneous velocity $\sigma_{\dot{x}}(t)$ is not affected by ambient temperature $T = 300$ K at low pressure, as the required condition to reduce the $SNR_{\dot{x}}(t)$ is $T \geq m\kappa^2 \sigma^4_{x_0} t/k_B\gamma$ ($T \approx 125 \times 10^2 \sigma^4_{x_0}$ for $\Gamma = 10^{-2}$ Hz (black

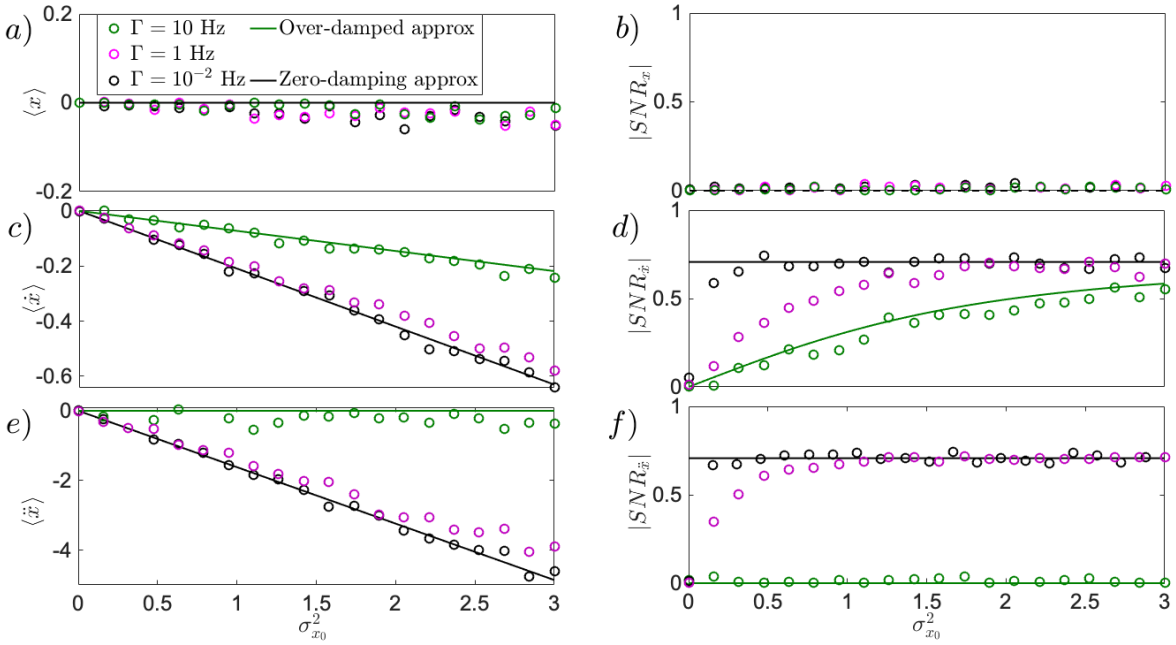

Figure 2. Noise-induced effect for initially steady particle in position x (a,b), instantaneous velocity $\dot{x}$ (c,d), and acceleration $\ddot{x}$ (e,f), driven by variance $\sigma^2_{x_0}$ of initial position. All simulations (dots) have been performed based on Eq. (1). In the top panel, for a short time scale up to $t = 0.1$ ms, the position statistics is trivial for all damping values, as the mean $\langle x \rangle$ (a) does not develop with increasing initial noise of position. Similarly, the SNR_x (b), is dominated by the noise spread and therefore vanishes. In the middle panel, (c), the evolution of the mean of instantaneous velocity is displayed for different values of damping. At low damping, $\Gamma = 10^{-2}$ Hz (black dots), the deterministic limit (black line), as derived in Eq. (6), can be reached. On the other hand, for higher damping, namely $\Gamma = 10$ Hz (green dots), the over-damped limit (green line), described by the mean of average velocity $\langle \bar{v} \rangle \approx -(K/\Gamma)\sigma^2_{x_0}$ is approached. The middle case of $\Gamma = 1$ Hz (purple dots), shows the sensitivity of mean of instantaneous velocity, $\langle \dot{x} \rangle$, to the damping coefficient γ. Simultaneously, in (d) the evolution of the $SNR_{\dot{x}}$ depicts the role of the environmental temperature T for different pressures, showing a regime dominated by the latter (purple dots) denoted by a linear increase of the $SNR_{\dot{x}}$ as discussed in Eq. (9). In the bottom panel, (e), the mean of instantaneous acceleration is depicted for different pressures. While for small damping $\Gamma = 10^{-2}$ Hz (black dots), the shift of mean instantaneous acceleration, $\langle \ddot{x} \rangle$, is visible and close to the deterministic limit (black line), given in Eq. (5). It vanishes for larger damping $\Gamma = 10$ Hz (green dots), where no instantaneous acceleration exists. (f) depicts, by contrast, the role of the environmental temperature T recognisable in the $SNR_{\ddot{x}}$ by the linear dependency in $\sigma^2_{x_0}$ of initial position, to be less present even at damping $\Gamma = 1$ Hz, in comparison to the case for velocity, as shown in Eq. (10).
Eq. (1) has been simulated using $\kappa = 6k_BT\mu m^{-3}Kg^{-1}$, $T = 300$ K (ambient temperature), $\langle x_0 \rangle = 0$, $\langle \dot{x}_0 \rangle = 0$, $\sigma_{\dot{x}_0} = 0$, $t = 0.1$ ms, $dt = 2 \times 10^{-5}$ ms. 10^4 trajectories where generated with 5000 samples each. To compute the average quantities, $\bar{v}$, $\bar{a}$, the multiple time-step has been used, $\delta t = 10 \times dt$.

dots). Differently is the case at higher pressures, $\Gamma = 1$ Hz (Fig.2,d, purple dots), where the condition softens to $T \approx 140\sigma^4_{x_0}$, reducing the $SNR_{\dot{x}}(t)$ at small initial noise $\sigma^2_{x_0}$. The condition, for environmental temperature T, in the standard deviation of instantaneous acceleration in Eq. (10) $\sigma_{\ddot{x}}$, is much harder to fulfill. As can be glimpsed from Fig.2 (f), for the low pressure limit (black dots) the environmental noise is negligible even at ambient temperature $T = 300$ K, leaving the $SNR_{\ddot{x}}(t) \approx 1/\sqrt{2}$ unmodified. To be able to witness the effect of the environmental noise at such low pressures $\Gamma = 10^{-2}$ Hz, Eq. (10) provides a condition $T \geq m\kappa^2\sigma^4_{x_0}/k_B\gamma$ ($T \approx 150 \times 10^2\sigma^4_{x_0}$K, for $\Gamma = 10^{-2}$ Hz) showing the high temperature requirement, index of high robustness against environmental noise. For higher pressures, $\Gamma = 1$ Hz (purple dots), the condition softens to $T \approx 144 \times 10^2\sigma^4_{x_0}$ K, allowing, for small $\sigma^2_{x_0}$ to witness a reduction of the $SNR_{\ddot{x}}(t)$ (purple dots).

Role of initial particle velocity

Thus far we have considered the case of an initially steady particle with $\langle x_0 \rangle = 0$. Assuming we have infinitely precise control over the choice of initial speed, $\sigma^2_{\dot{x}_0} = 0$, one can observe the noise-induced effect for moving particles, rendering the experimental test broad. Generalising Eq. (7) for non-zero $\langle \dot{x}_0 \rangle$, and introducing $\Delta x = x(t) - \dot{x}_0 t$, to exclude deterministic

position change, one obtains

$$\langle \Delta x \rangle \approx -\frac{\kappa \sigma_{x_0}^2 t^2}{2}, \qquad \sigma_{\Delta x} \approx \sqrt{\sigma_{x_0}^2 + \frac{k^2 t^4 \sigma_{x_0}^4}{2}}, \qquad SNR_{\Delta x} = \frac{|\Delta x|}{\sigma_{\Delta x}} \approx \frac{1}{\sqrt{2\left(1 + 2k^{-2}\sigma_{x_0}^{-2} t^{-4}\right)}}. \tag{11}$$

As visible from Fig.3(a,b), Eq. (11) holds true for particles moving at different initial speed (blue, green and red dots), showing that even quickly moving particles at the considered short time scale $t = 0.1$ms do not move on average.
For moving particles, the equation for instantaneous velocity reads $\dot{x}(t) = \dot{x}_0 - k x_0^2 t$. From the latter, the velocity difference $\Delta\dot{x} = \dot{x}(t) - \dot{x}_0$ is introduced, and its statistical evaluation comes as follows

$$\langle \Delta \dot{x} \rangle \approx -\kappa \sigma_{x_0}^2 t, \qquad \sigma_{\Delta \dot{x}} \approx \sqrt{2}\kappa \sigma_{x_0}^2 t, \qquad SNR_{\Delta \dot{x}} = \frac{|\langle \Delta \dot{x} \rangle|}{\sigma_{\Delta \dot{x}}} \approx \frac{1}{\sqrt{2}}. \tag{12}$$

As noticeable from Fig.3 (c,d), the mean instantaneous velocity of Eq. (12) holds true only for values of initial velocities $\langle \dot{x}_0 \rangle = \pm 0.5$ (blue dots). However, for particles initially moving at higher speed (green and red dots), the approximation in Eq. (12) fails to describe the motion now modified by higher order nonlinear terms, as the particle obtains more negative mean instantaneous velocity for smaller $\sigma_{x_0}^2$. This high order nonlinear effects can only be investigated by numerical stochastic simulations. The $SNR_{\dot{x}}$ (middle panel, right column), although affected by the change in initial velocity (green and red dots), for larger $\sigma_{x_0}^2$ converges to its constant value $SNR_{\dot{x}} = 1/\sqrt{2}$ of Eq. (12).
To visualise the effect of initial velocity $\dot{x}_0$ on instantaneous acceleration $\ddot{x}$, one needs to explore the second order approximation to Eq. (4). We rewrite Eq. (4) to a set of dynamical equations for the position x and speed $\dot{x}$. Substituting a short-time solution $x \approx x_0 + \dot{x}_0 t$ of the equation for the position x, to the right side of the equation for the speed $\dot{x}$, we obtain a solution for the acceleration $\ddot{x}(t) \approx -\kappa(x_0^2 + 2x_0\dot{x}_0 t + \dot{x}_0^2 t^2)$. Introducing the quantity $\Delta\ddot{x} = \ddot{x}(t) + \kappa \dot{x}_0^2 t^2$, a pure effect of $\sigma_{x_0}^2$ on acceleration can be described, for $\langle x_0 \rangle = 0$, non vanishing $\langle \dot{x}_0 \rangle$, and $\sigma_{\dot{x}_0}^2 = 0$ as follows

$$\langle \Delta \ddot{x} \rangle \approx -\kappa \sigma_{x_0}^2, \qquad \sigma_{\Delta \ddot{x}} \approx \sqrt{2}\kappa \sigma_{x_0}^2, \qquad SNR_{\Delta \ddot{x}} = \frac{|\langle \Delta \ddot{x} \rangle|}{\sigma_{\Delta \ddot{x}}} \approx \frac{1}{\sqrt{2}}. \tag{13}$$

Evidently, in Fig.3 (e,f), for a particle with small non-zero initial speed $\dot{x}_0$, the acceleration does not deviate from the approximation introduced in Eq. (13), but when $\dot{x}_0$ increases, the mean acceleration gets closer to zero and $SNR_{\Delta\ddot{x}}$ approaches $1/\sqrt{2}$ much slower for larger $\sigma_{x_0}^2$, as visible in Fig.3 (e,f, green). For even larger initial speed (red dots), the particle obtains less negative average acceleration for smaller $\sigma_{x_0}^2$, producing an initially decreasing $SNR_{\Delta\ddot{x}}$. Decreasing the time scale tenfold $t = 0.01$ ms brings the red dots closer to the zero-damping approximation (black line), indicating that the shift is generated by higher order nonlinear terms beyond the approximate result introduced in Eq. (13). The larger $\sigma_{x_0}^2$, the more the particle accelerates, resulting in an increase of the $SNR_{\Delta\ddot{x}}$, slowly approaching $1/\sqrt{2}$.
Fig.3 demonstrates that the noise-induced shift of particle position (a,b), instantaneous velocity (c,d) and instantaneous acceleration (e,f) can be observed also for slowly and deterministically moving particles (black, and blue, and green dots). Moreover, for $\langle \dot{x}_0 \rangle > 0$ stochastic breaking induced by initial noise can be witnessed where the particle breaks at average $\langle \dot{x} \rangle = 0$ for sufficiently large initial position noise $\sigma_{x_0}^2$. Similarly for $\langle \dot{x}_0 \rangle < 0$ stochastic speeding is observed, where the particle gains velocity for sufficiently large initial position noise $\sigma_{x_0}^2$. The latter can be observed even during the short time period, and it is noticeable by the sign flip of mean instantaneous velocity $\langle \Delta \dot{x}_0 \rangle = -|\dot{x}_0|$ (Fig.3 c,d, dashed blue line).

Sensitivity to velocity noise

Complementary to the previous section, here we investigate how sensitive the noise induced effect is to an increase of initial velocity noise $\sigma_{\dot{x}_0}^2$, for strictly zero initial velocity $\langle \dot{x}_0 \rangle = 0$, and $\langle x_0 \rangle = 0$. Assuming negligible γ, as witnessed already in Fig.2 for the short time dynamics, Eq. (1) can be studied to describe the effect of initial statistics of velocity. Due to non-zero initial

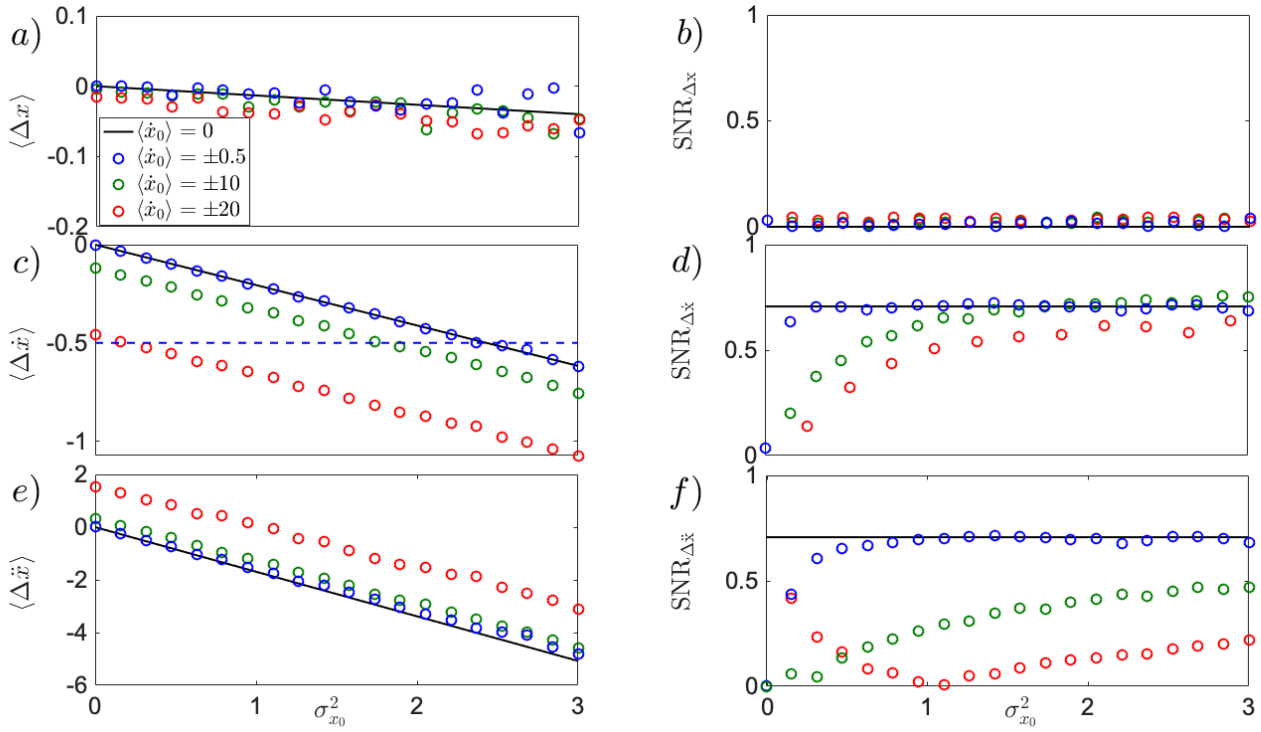

Figure 3. Noise-induced effects for initially moving particle in position statistics (a,b), instantaneous velocity statistics (c,d), and instantaneous acceleration statistics (e,f). All simulations (dots) have been performed based on Eq. (1) using $\sigma^2_{\dot{x}_0} = 0$. For mean particle position (a) the dynamics remains unchanged from that of Eq. (11) (black line) independent of the chosen initial velocity $\langle \dot{x}_0 \rangle$, while the $SNR_{\Delta x}$ (b, dots) remains small (close to zero), as the standard deviation increases faster than the mean. For mean instantaneous velocity (c,d), the approximation introduced in Eq. (12) (black line) holds true for values of initial velocity up to $\langle \dot{x}_0 \rangle = \pm 5$. Within this frame, stochastic speeding (for $\langle \dot{x}_0 \rangle > 0$) and stochastic breaking (for $\langle \dot{x}_0 \rangle < 0$) are witnessed when $\langle \Delta \dot{x} \rangle = -|\langle \dot{x}_0 \rangle|$. Specifically, for $\langle \dot{x}_0 \rangle = \pm 0.5$ (blue dots), the initial position noise induced stochastic speeding/breaking is met at values of $\langle \Delta \dot{x} \rangle = -0.5$ (blue dashed line). For values $|\langle \dot{x}_0 \rangle| > 5$ (green, and red dots) the dynamics can no longer be described by Eq. (12), as higher order nonlinear terms become relevant. As a result, the slope remains similar to that of the black line, but the curve is shifted to a non-zero value at $\sigma^2_{\dot{x}_0} = 0$. The resulting $SNR_{\Delta \dot{x}}$ display a slower convergence to the black line as the initial velocity becomes larger in magnitude. Particle acceleration (e,f) displays a solid robustness against the initial velocity $\langle \dot{x}_0 \rangle < 20$ in both mean (e), and $SNR_{\Delta \ddot{x}}$ (f). However, for values of $\langle \dot{x}_0 \rangle \geq 20$ (red dots), the evolution of mean instantaneous acceleration $\langle \Delta \ddot{x} \rangle$ deviates from the approximation of Eq. (13) (black line). In this regime, the $SNR_{\Delta \ddot{x}}$ presents an initial decrease, index of highly unstable dynamics, followed by a slow convergence towards the black line. Eq. (1) has been simulated using $\kappa = 6 k_B T \mu m^{-3} K g^{-1}$, $T = 300$ K, $\Gamma = 10^{-2}$ Hz, $t = 0.1$ ms, $dt = 2 \times 10^{-5}$ ms. 10^4 trajectories where generated with 5000 samples each.

velocity noise, Eqs. (5)- (7) modify to

$$\langle x(t) \rangle \approx -\frac{\kappa \sigma^2_{x_0} t^2}{2}, \qquad \sigma_x \approx \sqrt{\sigma^2_{x_0} + \sigma^2_{\dot{x}_0} + \frac{1}{2}\kappa^2 \sigma^4_{x_0} t^4}, \qquad SNR_x \approx \frac{1}{\sqrt{2}\sqrt{\frac{2\sigma^2_{x_0} + 2\sigma^2_{\dot{x}_0} t^2}{\kappa^2 \sigma^4_{x_0} t^4} + 1}} \tag{14}$$

$$\langle \dot{x}(t) \rangle \approx -\kappa \sigma^2_{x_0} t, \qquad \sigma_{\dot{x}} \approx \sqrt{\sigma^2_{\dot{x}_0} + 2\kappa^2 t^2 \sigma^4_{x_0}}, \qquad SNR_{\dot{x}} \approx \frac{1}{\sqrt{2}\sqrt{\frac{\sigma^2_{\dot{x}_0}}{2\kappa^2 \sigma^4_{x_0} t^2} + 1}} \tag{15}$$

$$\langle \ddot{x}(t) \rangle \approx -\kappa(\sigma^2_{x_0} + \sigma^2_{\dot{x}_0} t^2), \qquad \sigma_{\ddot{x}} \approx \sqrt{2\kappa^2(\sigma^4_{x_0} + \sigma^4_{\dot{x}_0} t^4)}, \qquad SNR_{\ddot{x}} \approx \frac{\left(\frac{\sigma^2_{x_0}}{\sigma^2_{\dot{x}_0}} + t^2\right)}{\sqrt{2}\sqrt{\frac{\sigma^4_{x_0}}{\sigma^4_{\dot{x}_0}} + t^4}}. \tag{16}$$

At short time scale, the mean position $\langle x(t) \rangle$ does not move, resulting in a vanishing SNR_x independent of the value of the initial velocity noise, as visible in Fig.4 (a,b). For time larger than $t = 0.3$ ms, when the nonlinear terms in Eq. (14) are prominent and SNR_x approaches $1/\sqrt{2}$, the initial velocity noise can modify the statistics of position if $\sigma^2_{\dot{x}_0} \gg \kappa \sigma^2_{x_0} t^2/\sqrt{2}$

($\sigma^2_{\dot{x}} \approx 10^{-2}\sigma^2_{\dot{x}_0}$, at $t = 0.3$ ms, $\Gamma = 10^{-2}$ Hz). The statistics of instantaneous velocity, as described in Eq. (15) are more affected by increasing initial velocity noise at short time scales. For values of $\sigma^2_{\dot{x}_0} \gg 2\kappa^2 t^2 \sigma^2_{x_0} \approx 4 \times 10^{-2}\sigma^2_{x_0}$ (at $t = 0.1$ ms, $\Gamma = 10^{-2}$ Hz), the statistics of $SNR_{\dot{x}}$ slowly approaches the constant $1/\sqrt{2}$ value, and rather approaches that of Eq. (15) as shown in Fig.4 (d, purple dashed line). As can be seen directly from Eq. (16), instantaneous acceleration bears the ability to be driven both by initial, velocity noise $\sigma_{\dot{x}_0^2}$, dominating in the long time scale, and initial position noise $\sigma_{x_0^2}$, dominating in the short time scale. As can be seen in Fig.4 (e) at timescales of $t = 0.1$ ms the term $\sigma_{x_0^2}$ dominates over the dynamics (black and purple dots), retrieving the zero-damping approximation results (black dashed line). At larger values of $\sigma_{\dot{x}_0^2}$ (orange dots) the enhancing effects of initial velocity noise becomes visible as the mean instantaneous acceleration becomes more negative than the zero-damping approximation (black dashed line). Simultaneously the $SNR_{\ddot{x}}$ (e) quickly converges to $1/\sqrt{2}$ independent of the choice of initial velocity noise.

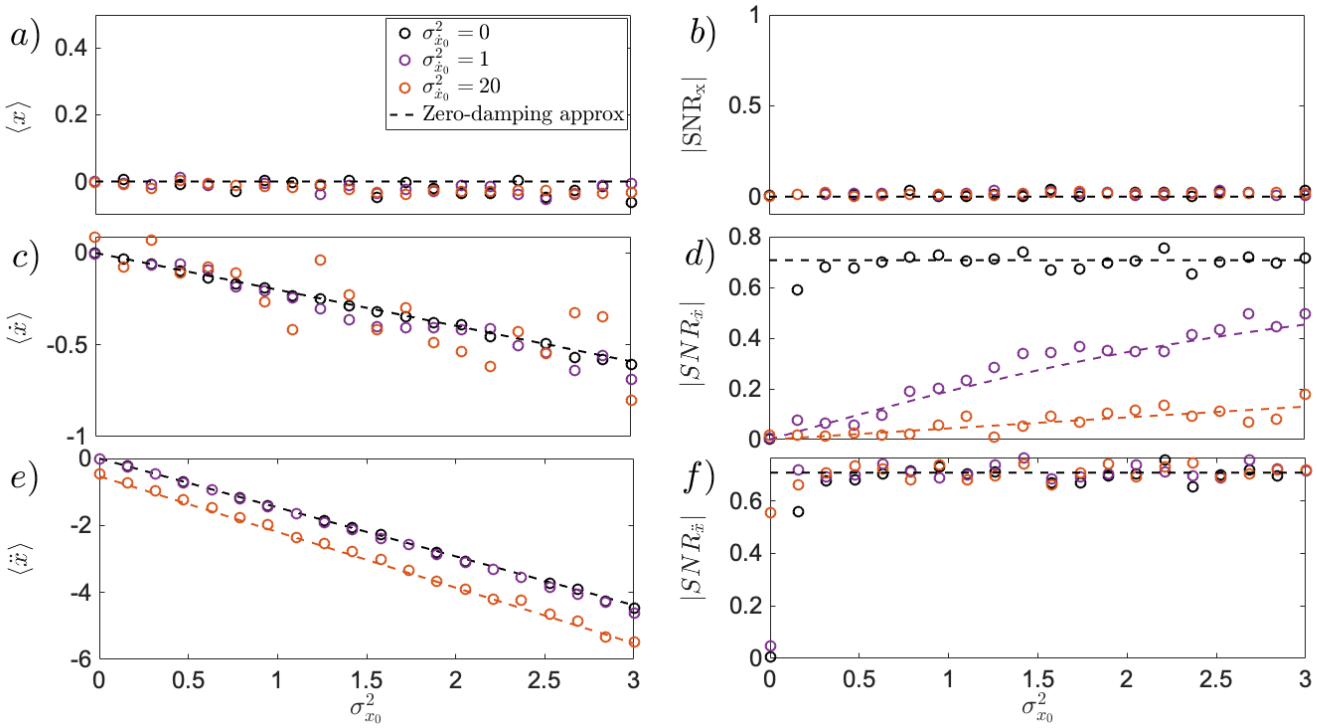

Figure 4. Robustness of initial noise-induced effect to initial velocity noise $\sigma^2_{\dot{x}_0}$ for position statistics (a,b), instantaneous velocity statistics (c,d), and instantaneous acceleration (e,f). All simulations (dots) have been performed based on Eq. (1) using $\langle x_0 \rangle = \langle \dot{x}_0 \rangle = 0$. In the top panel, for particle position, the increasing initial velocity noise $\sigma^2_{\dot{x}_0}$ does not modify the statistics of both mean position (a), and SNR_x (b). In the middle panel, for instantaneous velocity, the noise-induced feature is still observable for increasing initial velocity noise $\sigma^2_{\dot{x}_0}$, at the cost of high ensemble size requirements for mean instantaneous velocity computation (c). The $SNR_{\dot{x}}$ (d) still shows the noise induced effect, increasing with initial position noise, but its statistics gets modified, according to Eq. (15) (purple and orange dots), to a linearly increased $SNR_{\dot{x}}$ The bottom panel, (e,f) for instantaneous acceleration, displays a small sensitivity to initial velocity noise $\sigma^2_{\dot{x}_0}$. As obtained from Eq. (16), the condition the initial position uncertainty must fulfill to overthrow the initial velocity noise, $\sigma^2_{x_0} \gg \gamma\sigma_{\dot{x}_0}/\sqrt{2}\kappa \approx 5 \times 10^{-3}\sigma_{\dot{x}_0}$, is quite trivial, rendering the impact of $\sigma^2_{\dot{x}_0}$ negligible upon the statistics of instantaneous acceleration, never reaching, for the parameters of the experiment used, the regime introduced in Eq. (16) for $SNR_{\ddot{x}}$. The case of large initial velocity noise $\sigma^2_{\dot{x}_0} = 20$ (orange dots) introduces enhancement of mean instantaneous acceleration (e), that can be described by $\langle \ddot{x} \rangle \approx -\kappa(\sigma^2_{x_0} + \sigma^2_{\dot{x}_0} t^2)$ as introduced in Eq. (16). Eq. (1) has been simulated using $\kappa = 6k_B T \mu m^{-3} Kg^{-1}$, $T = 300$ K, $\Gamma = 10^{-2}$ Hz, $t = 0.1$ ms, $dt = 2 \times 10^{-5}$ ms. $N_t = 10^4$ trajectories where generated with $N = 5000$ samples each.

Coherent motion of maximum of distribution

To complete the analysis, the dynamics of a levitated particle in cubic potential needs to be characterised also by means of the most-likely position, speed and acceleration. The maxima of the respective distribution are not only a directly measurable characteristic of unstable motion, but they also open a new local use of Maxwell's deamon in stochastic thermodynamics [27]. Both mean and maximum of instantaneous quantities, stimulated by initial noise, should ideally increase coherently

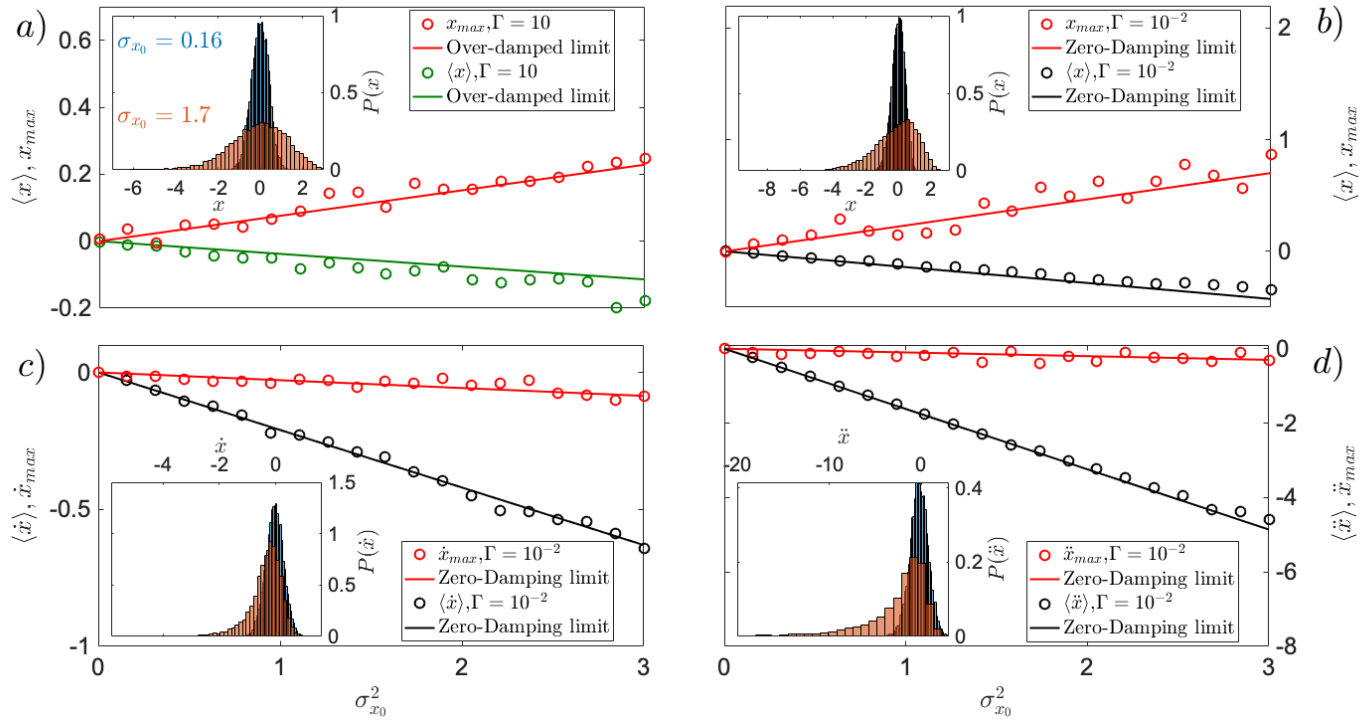

Figure 5. Initial noise-induced shift of maximum of position x_{max}, for high (a) and low (b) pressure limit, maximum of instantaneous velocity $\dot{x}_{max}$ (c), and acceleration $\ddot{x}_{max}$ (d). All simulations (dots) have been performed based on Eq. (1) using $\langle x_0 \rangle = \langle \dot{x}_0 \rangle = 0$, and $\sigma^2_{\dot{x}_0} = 1$. The top panel highlights the atypical evolution of maximum of particle position x_{max} (a, red dots) retrieved in [27,30] for over-damped dynamics (a, red line), and witnessed again in the low pressure limit (b, red). To make the shift in maximum more visible, Eq. (1) has been simulated with $t = 0.3$ ms. The maximum of instantaneous velocity $\dot{x}_{max}$, in the low pressure limit (c), introduces a new effect comprising of a coherent shift of $\dot{x}_{max}$ (red) alongside the potential force (black) The inset, showing snapshots of the $P(\dot{x}$ at different $\sigma^2_{x_0}$, highlights the instability (heavy tails on the left), with a clear shift of the maximum alongside. Similarly, the maximum of instantaneous acceleration $\ddot{x}_{max}$ (d, red), shifts coherently with its mean $\langle \ddot{x} \rangle$ (black), corroborated by the inset picture, showing the left shift of $\ddot{x}_{max}$ for different values of $\sigma^2_{\dot{x}_0}$. By comparing the shift of $\dot{x}_{max}$, and $\ddot{x}_{max}$, we notice that the latter is comprised of a larger shift induced by initial position noise $\sigma^2_{x_0}$. Moreover, comparing the $P(\dot{x})$, and $P(\ddot{x})$ (inset a,b), with the $P(x)$ (inset c,d), we notice the absence of light tail in the former, that is visible in position [27]. To produce the figure on the bottom panel, Eq. (1) has been simulated with $t = 0.1$ ms. The other parameters used to produce this graph from Eq. (1) are $\kappa = 6k_BT\mu m^{-3}Kg^{-1}, T = 300K, dt = 2 \times 10^{-5}$ ms. $N_t = 10^4$ trajectories where generated with $N = 5000$ samples each.

(typical motion in the same direction) with a constant signal-to-noise ratio. Fig.5 shows the dynamics of maximum of position distribution(a,b, red dots), in both high friction regime (a), as well as in low friction regime (b). The latter shifts more pronouncedly, while maintaining its atypical feature observed in [27,30] for over-damped dynamics. A new feature arises for the-most-likely speed, where both in high and low friction regime, the maximum of average and instantaneous velocity distribution shifts alongside the potential force as seen by the red arrow in Fig.1 (c,d). A more quantitative dynamics of the latter is shown in Fig.5 (c) showing that the deterministic limit (red line) is reached at damping of $\Gamma = 10^{-2}$ Hz. Contrarily to the mean instantaneous velocity, shown in Fig.4, the maximum of velocity distribution does not succumb to increasing initial velocity noise. The curvature on the other hand is responsible for the reduction of the $SNR_{\dot{x}_{max}}$, as it becomes larger with increasing initial velocity noise $\sigma^2_{\dot{x}_0}$, slowing down the convergence of the $SNR_{\dot{x}_{max}}$ as shown in Fig.6 (d).

The shift of the most-likely acceleration is alongside the potential force, as shown in Fig.1 (f, red arrow). It becomes evident only at low pressures, and disappears towards the high friction limit. The sharp shape of the acceleration distribution, displayed in the inset of Fig.5 (e) shows a large shift of mean of instantaneous acceleration, but a small shift of its maximum, although larger compared to the shift of the maximum of velocity distribution. Despite the negligible role that the uncertainty of the initial velocity state displays in the evolution of the maximum of acceleration distribution, as shown in Fig.6 (e,f), it is of notice the convergence of the $SNR_{\ddot{x}}$ to the $1/\sqrt{2}$, denoted by the dashed black line in Fig.6 (f).

The minimal requirement to observe a shift of the maximum in the acceleration distribution, is a non-zero noise in the initial velocity state, which mediates from the sharp tail on the right of the distribution, making its maximum hard to identify. Moreover

we report that the most-likely acceleration, when the dynamics starts at different initial position $\langle x_0 \rangle \neq 0$, shifts atypically for small values of initial position uncertainty. This is due by a pure deterministic drift in a regime dominated by inertia when the trajectory explore region away from the plateau. Moreover, their distribution shows no visible light tails, contrary to the position distribution in the over-damped regime[27], where the fast and unstable dynamics of x drags all the trajectories quickly to the divergence.

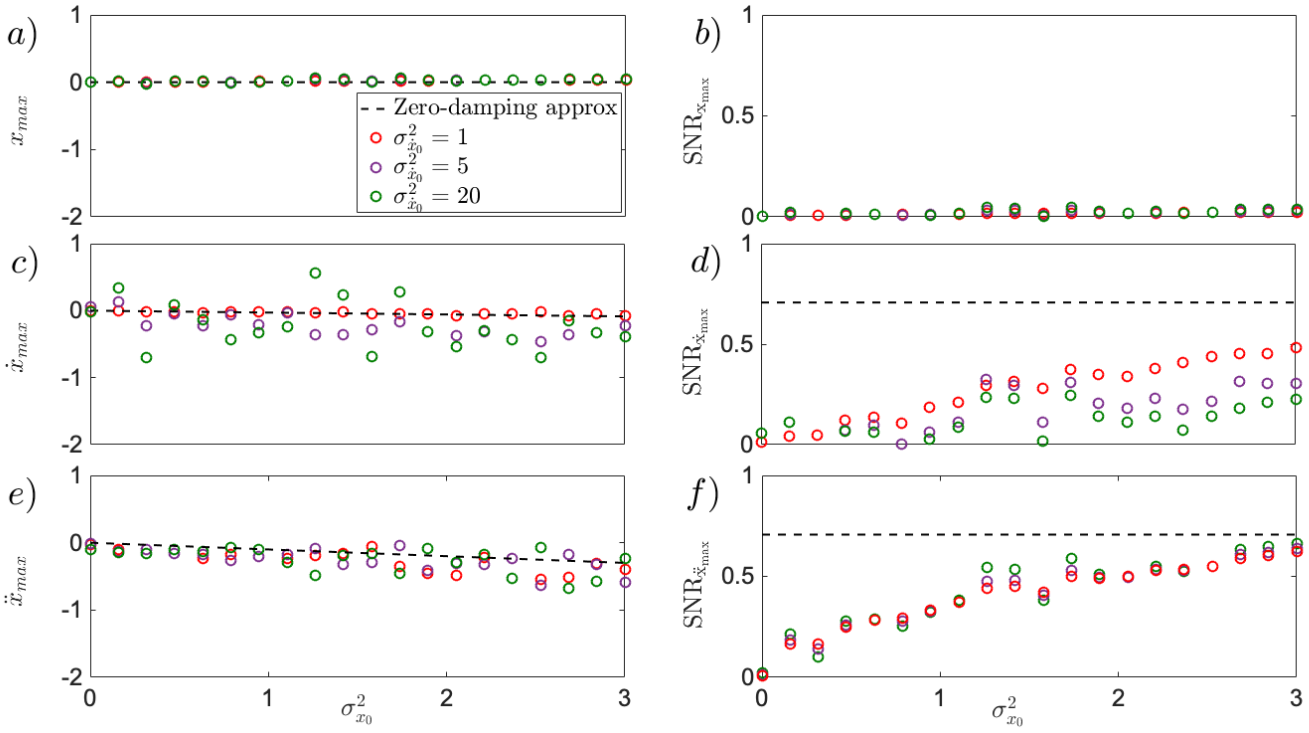

Figure 6. The noise-induced effect in the maxima of distribution for position, instantaneous velocity and acceleration to the uncertainty of the initial velocity state, $\sigma^2_{\dot{x}_0}$. (a,b), the evolution of the maximum of position distribution is not modified by increasing initial uncertainty of the velocity state, $\sigma^2_{\dot{x}_0}$, similar to its global counterpart $\langle x \rangle$. (c,d), the evolution of maximum of velocity distribution is investigated, showing on (c), almost no sensitivity to small changes in initial velocity noise, but increase requirement of ensemble size. Simultaneously , the $SNR_{\dot{x}}$ on (d) slowly converges to the $SNR_{\dot{x}} = 1/\sqrt{2}$ (black dashed line) value but its convergence is reduced with increasing initial velocity noise $\sigma^2_{\dot{x}_0}$. (e,f), the local characteristics of instantaneous acceleration, $\ddot{x}_{max}$ (e), displays little to no sensitivity to increasing initial velocity noise, while its $SNR_{\ddot{x}}$ requires a high ensemble size to be simulated ($N_t = 10^6$). The convergence of the $SNR_{\ddot{x}}$ (f) is not modified by increasing initial velocity noise $\sigma^2_{\dot{x}_0}$. The black dashed line correspond to the evolution of maxima of distribution for the zero-damping-limit, shown in Fig.5. Eq. (1) has been simulated using $\kappa = 6k_BT\mu m^{-3}Kg^{-1}, T = 300K, \langle x_0 \rangle = 0, \langle \dot{x}_0 \rangle = 0, t = 0.1ms, dt = 2 \times 10^{-6}$ ms. $N_t = 10^6$ trajectories where generated with $N = 5000$ samples each.

Conclusion for experimental tests

We have demonstrated the noise-induced instantaneous speed and acceleration of a levitated particle in the highly unstable cubic potential. Moreover, all the simulations have been performed using parameters of current underdamped experiments[12], together with the parameters of cubic optical potential[29,30] directly motivating our predictions to be experimentally tested to witness these new nonlinear mechanical phenomena. However, the analysis of the presented regime is also applicable to other underdamped experiments[31–33]. The first point worth experimentally verifying, shown in Fig.1 and Fig.2, is how the noise-induced effect turns to instantaneous velocity and acceleration, reaching the zero-damping approximation described in Eqs. (5) to (7) at pressures of $p = 10^{-5}$ mbar, and room temperature. Then, the experiment can proceed to investigate how robust the previous result was when the particle, instead of being initially steady at the plateau, possessed nonzero initial velocity $\langle \dot{x}_0 \rangle$ as showed in Fig.3. The latter unveiled an interesting feature, observable in the cubic potential, consisting of stochastic breaking and speeding induced by initial position noise $\sigma^2_{x_0}$. Moreover, remarkably the noise-induced effect can be observed even for slowly moving particles (see blue and green dots in Fig.3). A parameter that needs to be kept under control is the initial velocity noise, which although can drive the shift of instantaneous acceleration (Fig.4 orange dots), is disruptive for

the measurement of instantaneous velocity (purple and orange dots Fig.4). Last, but not least, we showed that the maxima of the instantaneous speed, and acceleration distributions shift normally, alongside their respective mean in contrast to the position maximum which maintains its atypical shift as previously observed in the over-damped regime[27,30] (Fig.5). The sensitivity of maxima towards increasing initial velocity noise, as shown in Fig.6, displays a worsening of the accuracy which in turns demands increasing ensemble size. All these experimental tests verify new underdamped transient effects of a particle living at the edge of instability, paving the way to explore highly nonlinear stochastic phenomena. Future targets comprise of quantum mechanical analysis of deeply underdamped and highly cooled particles in the unstable cubic potential, initially close to the mechanical ground state.

Methods

Numerical simulation with experimental numbers

To numerically simulate the Langevin dynamics described in Eq. (1) using real experimental values, one has to re-scale the equation of motion. Usually, for linear dynamics, the equation is re-scaled using the mechanical Q-factor. With nonlinear systems this is not valid anymore, and a different route must be followed. In the case of Eq. (1), it is useful to re-scale position and time as follows

$$q = \frac{x}{l}, \qquad \bar{t} = \frac{t}{\tau}, \tag{17}$$

with q being the dimensionless position, l the position re-scaler, $\bar{t}$ the dimensionless time, and τ the time re-scaler. It naturally follows from Eq. (17) that $\dot{q} = \tau\dot{x}/l$, and $\ddot{q} = \tau^2\ddot{x}/l$. In order to determine the values of the re-scaler, one can use, for the position $\bar{l} = 5\times10^{-6}$ which is the length of the potential used in experiment[30], and then focus attention on the positive part of the potential, of length $\bar{l}/2$. Subsequently choose a point, P belonging to it, with coordinate (xp, yp). With this point one can build a straight line passing through the origin and the chosen point, and notice that it forms a triangle containing the piece of potential up to point P chosen. The angle between the origin and the hypotenuse is then given by the stiffness k of the potential. Subsequently, the position re-scaler can be calculated as $l = 2\sqrt{A/k}$, where A denotes the area of the triangle previously built, and the factor 2 comes from the fact that we extend the calculation to the whole domain of the cubic potential. The re-scaler l calculated, now has a clear dependence on the stiffness of the potential $K \approx k_B T \mu m^{-3}$, and subsequently on the chosen temperature T, and it varies between $10^{-3}\mu m < l < 10^{-2}\mu m$. The time re-scaler, τ is calculated by numerically computing the first passage time for the selected parameters.
Following the re-scaling procedure explained before, the Langevin equation can be transformed into

$$\ddot{q} = -\gamma\tau\dot{q} - \bar{k}\tau^2 l q^2 + \frac{\tau^2}{l}\sqrt{\frac{2D}{\tau}}\bar{\xi}(t), \tag{18}$$

where $\bar{k} = \kappa/l^3$, and the mass m has been absorbed by $\kappa = K/m$, $\gamma = \Gamma/m$, $D = k_B T\gamma/m$, and $\bar{\xi}(t) = \sqrt{\tau^{-1}}\xi(t)$. The term $\bar{k} = \kappa/l^3$ comes from the re-normalisation of the potential stiffness, done to render the dimensions of the new stiffness, $\bar{k} = [1/(ms^2)]$, such that the potential term, $\bar{k}\tau^2 l q^2$ becomes a-dimensional in the re-scaling. As a crosscheck for the dynamics, the Pearson correlation coefficient is calculated, and simulated (Fig.7. As per its definition, the Pearson correlation is calculated as $\rho_{xy} = cov(xy)/\sigma_x\sigma_y$, where $cov(xy) = \langle xy\rangle - \langle x\rangle\langle y\rangle$ is the covariance matrix of the pair. The simulated pairs presents the following Pearson correlations, assuming negligible γ, as it does not seem to disrupt the dynamics much (bottom panel, centre column)

$$\rho_{\dot{x}\ddot{x}} = \frac{1}{\sqrt{\frac{\sigma^2_{\dot{x}_0}}{2\kappa^2\sigma^4_{x_0}t^2}+1}}, \quad \rho_{\dot{x}\Delta x} = \frac{\sigma^2_{\dot{x}_0}t + \kappa^2\sigma^4_{x_0}t^3}{\sqrt{\sigma^4_{\dot{x}_0}t^2 + \frac{5}{2}\kappa^2\sigma^2_{\dot{x}_0}\sigma^4_{x_0}t^3 + \kappa^4\sigma^8_{x_0}t^6}}, \quad \rho_{\Delta x\ddot{x}} = \frac{\kappa^2\sigma^4_{x_0}t^2}{\sqrt{2}\kappa(\sigma^2_{x_0}+\sigma^2_{\dot{x}_0}t^2)\sqrt{\sigma^2_{\dot{x}_0}t^2 + \frac{1}{2}\kappa^2\sigma^4_{x_0}t^4}}. \tag{19}$$

Noise-induced effects for non vanishing initial position

Throughout the paper we have always assumed to have a particle initially positioned at the inflection point $\langle x_0\rangle = 0$. It becomes natural to ask how different $\langle x_0\rangle$ affect the noise-induced effect described. As evidenced in Fig.8, for small nonzero $\langle x_0\rangle = 1$ (blue dots), Eqs. (14)- (16) still describe the dynamics for position (a,b), velocity (c,d), and acceleration (e,f), where their *SNR* (b,d,f) show no deviation from $1/\sqrt{2}$. A different case is the large non zero $\langle x_0\rangle$ (green dots) for which Eqs. (14)- (16) no longer holds. In this case, the particle already feels strong nonlinear terms, which require more terms in the time expansion from (4). While the respective *SNR* undergo an initial decrease (for velocity and acceleration), they all converge to $1/\sqrt{2}$ for increasing initial position noise $\sigma^2_{x_0}$. To preserve the short time dynamics at such nonlinear positions, a decrease of the time scale seems necessary (a tenth of $t = 0.1$ms is sufficient for the parameters used in Fig.8 to produce the green dots).

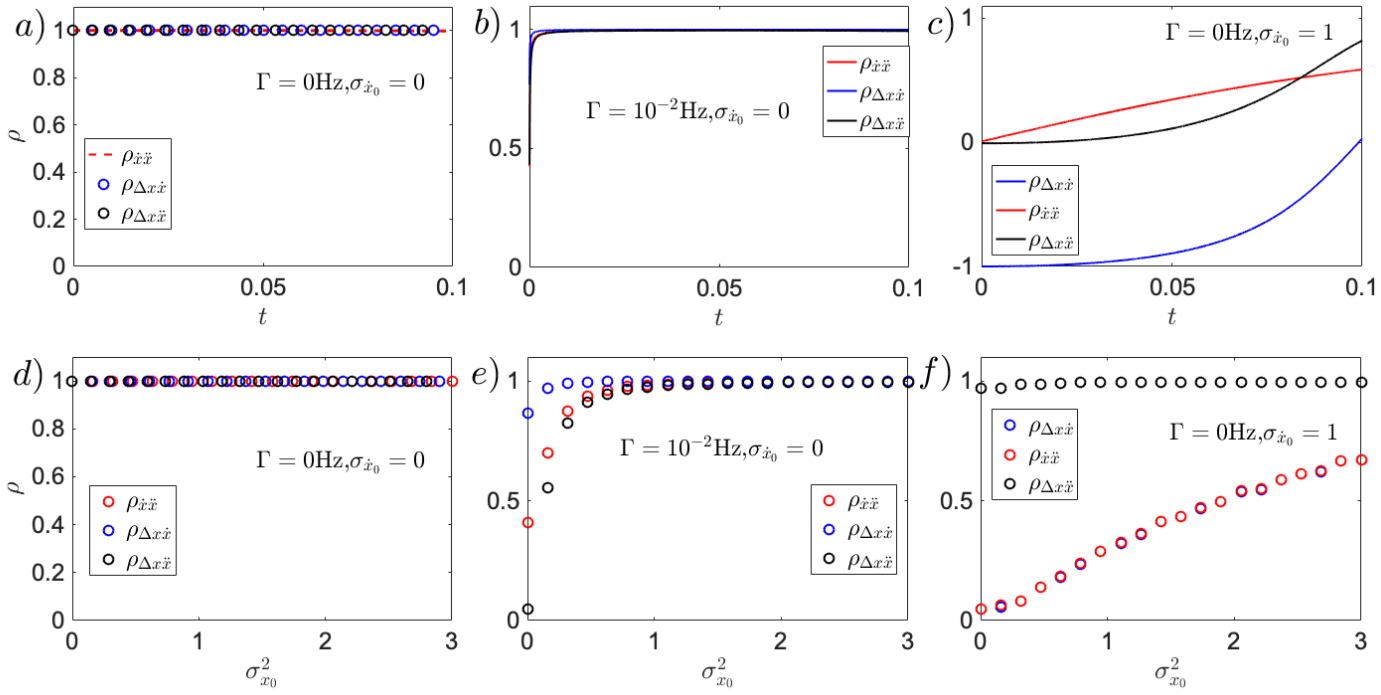

Figure 7. Pearson correlation coefficients, in time (a,b,c), and initial position noise (d,e,f) for the pairs $\rho_{\dot{x}\ddot{x}}, \rho_{\dot{x}\Delta x}, \rho_{\Delta x\ddot{x}}$. From left to right the pure deterministic dynamics for $\langle \dot{x}_0 \rangle = \langle x_0 \rangle = 0$, and noiseless initial velocity, followed by the small pressure regime (b,e), and finally the noisy initial velocity (c,f). (a,d) shows that in the pure deterministic scenario, $\Gamma = 0$, for $\sigma^2_{\dot{x}_0} = 0$, all the pairs are fully correlated with each other. A change in the damping, $\Gamma = 10^{-2}$ (b,e), shows little to no modification, as the elements of the pairs quickly become correlated. A change in initial velocity noise (c,f), shows all the pairs to be uncorrelated at $t = 0$, increasing with t to ultimately converge to full correlation $\rho = 1$. On the other hand, the pair $\rho_{\Delta x\ddot{x}}$ remains fully correlated as the initial position noise increases, whereas the two remaining pairs grow at the same rate, converging slowly to $\rho = 1$. Eq. (1) has been simulated using $\kappa = 6k_B T \mu m^{-3} K g^{-1}, T = 300K, \langle x_0 \rangle = 0, \langle \dot{x}_0 \rangle = 0, dt = 2 \times 10^{-5}$ ms. 10^4 trajectories were generated with 5000 samples each.

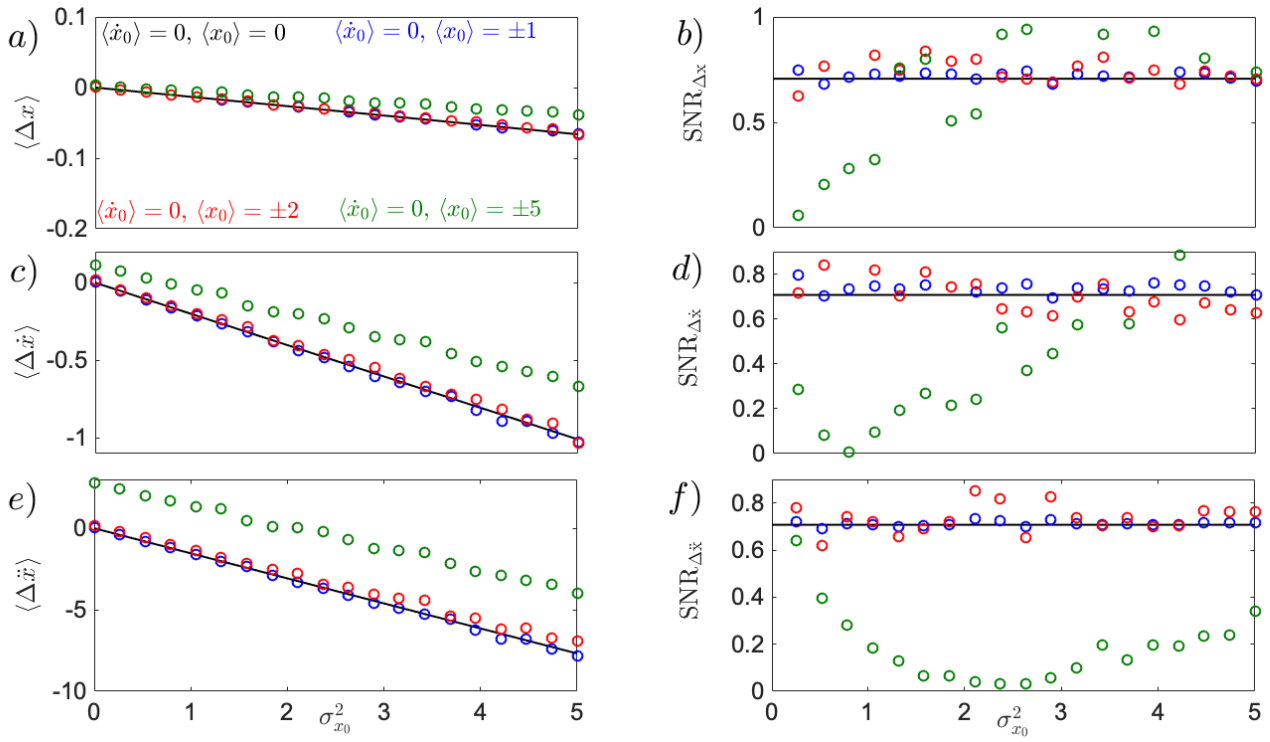

Figure 8. Noise-induced effects for non vanishing initial position $\langle x_0 \rangle$ for position statistics (a,b), instantaneous velocity statistics (c,d), and instantaneous acceleration statistics (e,f). All simulations (dots) have been performed based on Eq. (1) using $\sigma^2_{\dot{x}_0} = 0$, and $\langle \dot{x}_0 \rangle = 0$. Positioning the particle in different parts of the plateau region (blue dots), reveals no introduction of higher order term of the time series for neither position, velocity, nor acceleration. Their dynamics is well described by Eqs. (14)- (16). Similarly, by positioning the particle away from the plateau, where the nonlinearity starts to become relevant (red dots), Eqs. (14)- (16) still hold to describe dynamics of position, velocity, and acceleration. A different case is when the particle is positioned in a highly nonlinear region of the potential (green dots), i.e., down the slope of the cubic potential (negative values), or on the cubic wall (positive values). Such positions highly affect the dynamics, introducing new terms of the time series, where Eqs. (14)- (16) are no longer valid. As a result, the position still displays the noise-induced feature, witnessed by the increasing $SNR_{\Delta x}$ (b) that converges to the constant value $1/\sqrt{2}$. Velocity (d) and acceleration (f) display a *SNR* initially decreasing to zero, after which the noise-induced feature becomes visible once again, converging with different speed of growth to the constant value $1/\sqrt{2}$ for larger values of initial position noise. Eq. (1) has been simulated using $\kappa = 6 k_B T \mu m^{-3} K g^{-1}, T = 300K, \sigma^2_{\dot{x}_0} = 0, \langle \dot{x}_0 \rangle = 0, dt = 2 \times 10^{-5}$ ms. 10^4 trajectories where generated with 5000 samples each.

References

1. Rondin, L. *et al.* Direct measurement of kramers turnover with a levitated nanoparticle. *Nat. Nanotechnol.* **12**, 1130–1133, DOI: 10.1038/nnano.2017.198 (2017).
2. Ricci, F. *et al.* Optically levitated nanoparticle as a model system for stochastic bistable dynamics. *Nat. Commun.* **8**, 15141, DOI: 10.1038/ncomms15141 (2017).
3. Li, T., Kheifets, S. & Raizen, M. G. Millikelvin cooling of an optically trapped microsphere in vacuum. *Nat. Phys.* **7**, 527–530, DOI: 10.1038/nphys1952 (2011).
4. Jain, V. *et al.* Direct measurement of photon recoil from a levitated nanoparticle. *Phys. Rev. Lett.* **116**, 243601, DOI: 10.1103/PhysRevLett.116.243601 (2016).
5. Gieseler, J., Novotny, L. & Quidant, R. Thermal nonlinearities in a nanomechanical oscillator. *Nat. Phys.* **9**, 806–810, DOI: 10.1038/nphys2798 (2013).
6. Fonseca, P. Z. G., Aranas, E. B., Millen, J., Monteiro, T. S. & Barker, P. F. Nonlinear dynamics and strong cavity cooling of levitated nanoparticles. *Phys. Rev. Lett.* **117**, 173602, DOI: 10.1103/PhysRevLett.117.173602 (2016).
7. Ma, J. *et al.* Observation of nonlinear dynamics in an optical levitation system. *Commun. Phys.* **3**, 197, DOI: 10.1038/s42005-020-00467-2 (2020).
8. Kheifets, S., Simha, A., Melin, K., Li, T. & Raizen, M. G. Observation of brownian motion in liquids at short times: Instantaneous velocity and memory loss. *Science* **343**, 1493–1496, DOI: 10.1126/science.1248091 (2014). https://science.sciencemag.org/content/343/6178/1493.full.pdf.
9. Li, T. & Raizen, M. G. Brownian motion at short time scales. *Annalen der Physik* **525**, 281–295, DOI: 10.1002/andp.201200232 (2013). https://onlinelibrary.wiley.com/doi/pdf/10.1002/andp.201200232.
10. Li, T., Kheifets, S., Medellin, D. & Raizen, M. G. Measurement of the instantaneous velocity of a brownian particle. *Science* **328**, 1673–1675, DOI: 10.1126/science.1189403 (2010). https://science.sciencemag.org/content/328/5986/1673.full.pdf.
11. Huang, R. *et al.* Direct observation of the full transition from ballistic to diffusive brownian motion in a liquid. *Nat. Phys.* **7**, 576–580, DOI: 10.1038/nphys1953 (2011).
12. Flajšmanová, J. *et al.* Using the transient trajectories of an optically levitated nanoparticle to characterize a stochastic duffing oscillator. *Sci. Reports* **10**, 14436, DOI: 10.1038/s41598-020-70908-z (2020).
13. Gieseler, J., Deutsch, B., Quidant, R. & Novotny, L. Subkelvin parametric feedback cooling of a laser-trapped nanoparticle. *Phys. Rev. Lett.* **109**, 103603–, DOI: 10.1103/PhysRevLett.109.103603 (2012).
14. Asenbaum, P., Kuhn, S., Nimmrichter, S., Sezer, U. & Arndt, M. Cavity cooling of free silicon nanoparticles in high vacuum. *Nat. Commun.* **4**, 2743, DOI: 10.1038/ncomms3743 (2013).
15. Tebbenjohanns, F., Frimmer, M., Militaru, A., Jain, V. & Novotny, L. Cold damping of an optically levitated nanoparticle to microkelvin temperatures. *Phys. Rev. Lett.* **122**, 223601–, DOI: 10.1103/PhysRevLett.122.223601 (2019).
16. Conangla, G. P. *et al.* Optimal feedback cooling of a charged levitated nanoparticle with adaptive control. *Phys. Rev. Lett.* **122**, 223602–, DOI: 10.1103/PhysRevLett.122.223602 (2019).
17. Delić, U. *et al.* Cooling of a levitated nanoparticle to the motional quantum ground state. *Science* **367**, 892, DOI: 10.1126/science.aba3993 (2020).
18. Delić, U. c. v. *et al.* Cavity cooling of a levitated nanosphere by coherent scattering. *Phys. Rev. Lett.* **122**, 123602, DOI: 10.1103/PhysRevLett.122.123602 (2019).
19. Frimmer, M., Gieseler, J. & Novotny, L. Cooling mechanical oscillators by coherent control. *Phys. Rev. Lett.* **117**, 163601–, DOI: 10.1103/PhysRevLett.117.163601 (2016).
20. Seifert, U. Stochastic thermodynamics, fluctuation theorems and molecular machines. *Reports on Prog. Phys.* **75**, 126001, DOI: 10.1088/0034-4885/75/12/126001 (2012).
21. Ryabov, A., Holubec, V. & Berestneva, E. Living on the edge of instability. *IOPScience* **2019**, 084014, DOI: 10.1088/1742-5468/ab333f (2019).
22. Rodenburg, B., Neukirch, L. P., Vamivakas, A. N. & Bhattacharya, M. Quantum model of cooling and force sensing with an optically trapped nanoparticle. *Optica* **3**, 318, DOI: 10.1364/OPTICA.3.000318 (2016).
23. Timberlake, C., Gasbarri, G., Vinante, A., Setter, A. & Ulbricht, H. Acceleration sensing with magnetically levitated oscillators above a superconductor. *Appl. Phys. Lett.* **115**, 224101, DOI: 10.1063/1.5129145 (2019).

24. Lecamwasam, R. *et al.* Dynamics and stability of an optically levitated mirror. *Phys. Rev. A* **101**, 053857–, DOI: 10.1103/PhysRevA.101.053857 (2020).

25. Erbas-Cakmak, S., Leigh, D. A., McTernan, C. T. & Nussbaumer, A. L. Artificial molecular machines. *Chem. Rev.* **115**, 10081–10206, DOI: 10.1021/acs.chemrev.5b00146 (2015).

26. Blickle, V. & Bechinger, C. Realization of a micrometre-sized stochastic heat engine. *Nat. Phys.* **8**, 143–146, DOI: 10.1038/nphys2163 (2012).

27. Ornigotti, L., Ryabov, A., Holubec, V. & Filip, R. Brownian motion surviving in the unstable cubic potential and the role of maxwell's demon. *Phys. Rev. E* **97**, 032127 (2018).

28. Filip, R. & Zemánek, P. Noise-to-signal transition of a brownian particle in the cubic potential: I. general theory. *J. Opt.* **18**, 065401, DOI: 10.1088/2040-8978/18/6/065401 (2016).

29. Šiler, M. *et al.* Thermally induced micro-motion by inflection in optical potential. *Sci. Reports* **7**, 1697, DOI: 10.1038/s41598-017-01848-4 (2017).

30. Šiler, M. *et al.* Diffusing up the hill: Dynamics and equipartition in highly unstable systems. *Phys. review letters* **121**, 230601 (2018).

31. Setter, A., Vovrosh, J. & Ulbricht, H. Characterization of non-linearities through mechanical squeezing in levitated optomechanics. *Appl. Phys. Lett.* **115**, 153106, DOI: 10.1063/1.5116121 (2019).

32. Ahn, J. *et al.* Optically levitated nanodumbbell torsion balance and ghz nanomechanical rotor. *Phys. Rev. Lett.* **121**, 033603–, DOI: 10.1103/PhysRevLett.121.033603 (2018).

33. Delić, U. *et al.* Levitated cavity optomechanics in high vacuum. *IOPScience* **5**, 025006, DOI: 10.1088/2058-9565/ab7989 (2020).

Acknowledgements

We acknowledge the project 19-17765S of the Czech Science Foundation and and MEYS CR together with European Union's Horizon 2020 (2014–2020) research and innovation framework programme under Grant Agreement No. 731473 (project 8C18003 TheBlinQC). Project TheBlinQC has received funding from the QuantERA ERA-NET Cofund in Quantum Technologies implemented within the European Union's Horizon 2020 Programme.
We acknowledge Pavel Zemánek for fruitful discussions.

Author contributions statement

L.O. and R.F. developed theory. L.O. performed numerical simulations. R.F. supervised the project. All authors analysed data and prepared the manuscript.

Additional information

The authors declare no competing financial interests.

Katedra Optiky
Přírodovědecká fakulta
Univerzita Palackého v Olomouci

Dissertation report

Stochastic Non-Linear Dynamics of Optically Trapped Particles

by

M.Sc. Luca Ornigotti

Supervisor: **Prof. Mgr. Radim Filip, Ph.D.**
Co-Supervisor: **RNDr. Artem Ryabov, Ph.D.**

May 2021

Title:	**Stochastic Non-Linear Dynamics of Optically Trapped Particles**
Author:	M.Sc. Luca Ornigotti
Advisor:	Prof. Mgr. Radim Filip, Ph.D
Consultant:	RNDr. Artem Ryabov, Ph.D
PhD. Programme:	Optics and Optoelectronics
Institution:	Katedra Optiky Přírodovědecká fakulta Univerzita Palackého v Olomouci
Year:	2021
External Examiners:	Ass.-Prof. Dr. Thomas Nikolai Kiesel Mgr. Alexandr Jonáš, Ph.D.

This thesis is an original work, composed by its author, under the guidance of prof. Mgr. Radim Filip, Ph.D. and RNDr. Artem Ryabov, Ph.D. The thesis is based on the results of the scientific work, published in collaboration with other co-authors. This thesis may be freely distributed in an unchanged form. Palacký University has the rights to archive, publish and distribute the thesis according to its internal regulations and Czech law.

The thesis is available for reading at the study department of the Faculty of Science, Palacký University, 17. listopadu 12, Olomouc. It is also available online at stag.upol.cz under Browse and Theses.

Abstract

The fast pace that optically levitated platforms have experienced over the past decade has opened new ways to investigate a plethora of nonlinear stochastic mechanical effects. Amongst them, noise-to-signal transitions, peculiar and interesting processes in physics, are the focus of this thesis. They allow to transform the environmental noise to useful mechanical effects.

This thesis investigates the paradigm of stochastic highly nonlinear dynamics of a levitated nanosphere in the classical, overdamped and underdamped regime. With main focus on the dynamical noise-to-signal transitions in the optical cubic potential $V(x) = kx^3/3$, where its inherent instabilities were positively exploited as a thermally driven source to autonomously transform noise into useful coherent mechanical displacement.

Such transformation can be performed because the nonlinearity, one

of the essential ingredients together with instabilities, brings the mechanical system out of its thermal equilibrium, thus allowing energy from the fluctuating environment to be used as a source of coherent mechanical displacement and oscillations.

Keywords— Nonlinear Dynamics, Optical Trapping and Manipulation, Brownian Motion, Transient Stochastic Effects, Non-equilibrium Statistical Mechanics

Contents

Introduction

This report contains a brief summary of the main results presented in the thesis *Stochastic Non-Linear Dynamics of Optically Trapped Particles*. Chapter 1 discusses the results presented in [1, 2], comprising of a new methodology based on the maximum of position distribution, to characterise the otherwise divergent dynamics of highly nonlinear systems. Chapter 2, based on a manuscript under review process for publication in Scientific Reports, illustrates the dynamics of a particle trapped in the optical cubic potential in the low pressure regime; introducing new unexplored nonlinear ballistic effects appearing in the instantaneous speed and acceleration, obtained for parameters of current underdamped experiments. Furthermore, Chapter 3 briefly discusses the numerical methodology required to numerically simulate dynamics of highly nonlinear systems beyond their characteristic times.

Lastly, Chapter 3 summarises the main results of the research.

Chapter 1

Overdamped Stochastic Dynamics in Cubic Potential

We investigate the noise-to-signal transitions in the optical cubic potential $V(x) = kx^3/3$ by positively exploiting its inherent instabilities as a thermally driven source to autonomously transform noise into useful coherent motion.

The governing equation of motion for the overdamped regime can be well

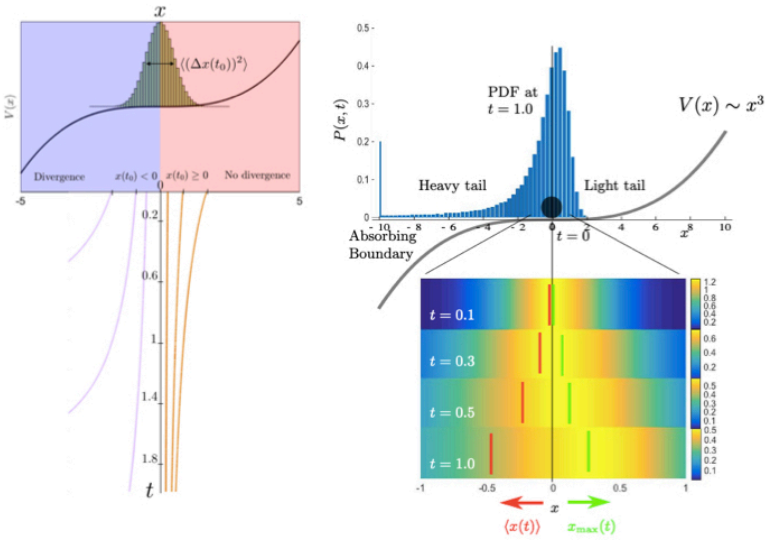

Figure 1.1: Noise-to-signal transitions, different point of view. *On the left panel, the illustration shows how the uncertainty of the initial state enhances the instability of the cubic potential, showing first hand the non-linear effect of the noise-induced displacement effect, as described in Eq.(1.3). On the right panel, the illustration shows how the unstable dynamics of a Brownian particle in cubic potential leads to the generation of heavy tails on the PDF, generated by diverging trajectories, which shows the limitation of the description by global statistical moments. Simultaneously it can be noticed the atypical dynamics of the local characteristics, evolving against the potential force, it too driven by the initial thermal noise, Eq.(1.9), and environmental noise [1].*

approximated by the following Langevin equation

$$\dot{x} = -\kappa x^2 + \sqrt{2D}\xi(t), \tag{1.1}$$

where $\kappa = k/\gamma$ is the normalised cubic potential stiffness, and $D = k_B T/\gamma$ is the diffusion parameter. Solution of the deterministic motion of Eq.(1.1) shows diverging trajectories for negative initial position $x(t_0)$ [3]

$$x(t) = \frac{x(t_0)}{1_k x(t_0)(t - t_0)}, \tag{1.2}$$

as $\lim_{t\to\infty} x(t)|_{x_0<0} = -\infty$, limiting the dynamics with a characteristic time $\tau^0_\infty = 1/(k|x(t_0)|)$ [3]. As shown in Fig.1.1(left), by drawing initial conditions from a Gaussian centered at $\langle x_0\rangle = 0$, but with nonzero variance σ_0, the value of the initial position in the cubic potential is a random value either positive, or negative. The uncertainty of the initial state introduces a noise-induced displacement effect, observed in the moments of particle position [3]

$$\langle x(t)\rangle = -k\langle x(t_0)^2\rangle(t - t_0) - kD(t - t_0)^2, \tag{1.3}$$

$$\langle(\Delta x(t))^2\rangle = \langle(\Delta x(t_0))^2\rangle + 2D(t - t_0) + 8k^2(t - t_0)^2\langle(\Delta x(t_0))^2\rangle^2, \tag{1.4}$$

at the second order approximation in time.

In the absence of the diffusion term D, the initial noise is enough to produce drift on the particle motion with unchanged variance, showing a noise-induced displacement driving the mean particle position. For negligible initial thermal noise, the mean displacement evolves with a quadratic term in time transforming environmental noise to displacement, while the variance evolves with free diffusion fashion. At larger time scales the cu-

bic nonlinearity starts to affect the evolution of the variance, as the PDF grows heavy tails [1, 3], visible in Fig.1.1(right).

The witness of the noise-to-signal transition embedded in Eq.(1.3),(1.4) can be quantified by the signal to noise ratio (SNR $= |\langle x(t)\rangle|/\sigma_x(t)$) [3, 4], defined as a ratio between the useful signal in the motion $\langle x\rangle$, and its uncertainty σ_x.

The SNR quantifies the quality of the noise-to-signal process, and if it grows the coherent displacement increases faster than the noise, viceversa, the SNR starts to decrease, regardless of the increasing mean value [3].

In the limit of small diffusion, the SNR evolve as [3]

$$\mathrm{SNR}(t) \propto k\sqrt{\langle(\Delta x(t))^2\rangle}(t-t_0), \tag{1.5}$$

evolving linearly in time, and powered by initial thermal noise, as showed in Fig.1.2(left panel), quantifying the noise supplying the transitions. Similarly, in the strong diffusion regime, the SNR reaches [3]

$$\mathrm{SNR}(t) \propto \frac{\sqrt{2}}{2}k\sqrt{D}(t-t_0)^{3/2}, \tag{1.6}$$

which increases faster in time than its small diffusion counterpart in Eq.(1.5), as the system is continuously supplied with energy due to the Brownian noise, as shown in Fig.1.2 (right). While the SNR increases in time for both regimes, the characteristic time of divergence bounds

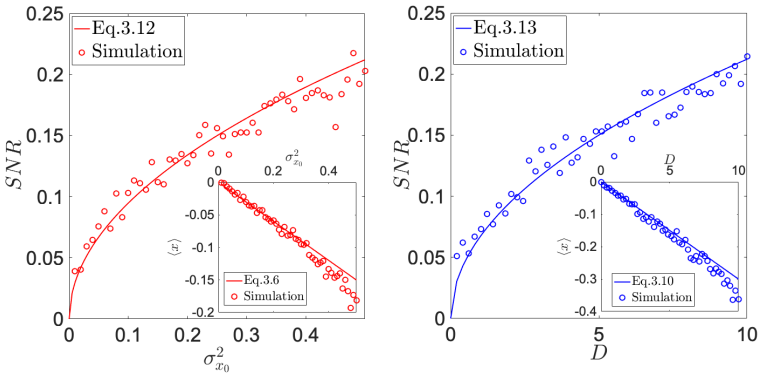

Figure 1.2: Noise-to-signal transitions powered by initial noise (left), and environmental noise (right) of a particle in cubic potential in terms of mean displacement and SNR***.***
The simulation are compared with analytical results presented in Eq.(1.3) *for the mean displacement* $\langle x(t) \rangle$ *(red and blue line in inset), and Eqs.*(1.5),(1.6) *for the* SNR*, respectively in red and blue on the figure. For this figure, Eq.*(1.1) *has been simulated, using, for the left picture,* $t = 0.1, D = 0, dt = 10^{-5}, k = 3$*, and for the right one,* $\sigma_0 = 0.0, t = 0.1, dt = 10^{-5}, k = 3$*. 5000 trajectories were generated. The figure has been taken from the thesis*

the dynamics, after which the divergence dominates. Such limitation is clearly marked by the prominent drop of the SNR (see Fig.1.3, red) and it renders the description of the dynamics, by global statistical moments, useless beyond it.

While the generation of heavy tails towards the divergence dominates the flow of $\langle x \rangle$, and σ_x dynamics, culprit of the drop of SNR, the maximum of position distribution (Fig.1.1, right), exhibits a shift against the poten-

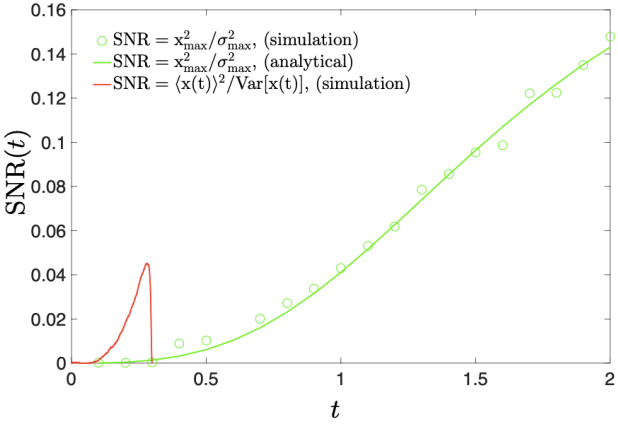

Figure 1.3: Fast divergence of the global description using averages is demonstrated by a swift drop of the SNR ***(red line).***
The local description using the maximum of the PDF, and the curvature around it, maintains its information value for all times (green line). $D = 0.1$, $k = 1$, $dt = 2 \cdot 10^{-3}$, $x_0 = 0$, and $4 \cdot 10^5$ trajectories where used.

tial force. In [1, 2] we discuss the characterisation of the most probable particle position described by the maximum of the particle distribution $P(x,t)$ to substitute the mean displacement, and the uncertainty around it characterised by the curvature around the maximum [6]. The investigation is focused on the dynamics at the plateau of those trajectory that survives the divergence, bearing little to no information about it [6].

The dynamics is still quantified by the Signal to Noise Ratio, written now for local characteristics, $\mathrm{SNR}(t) = x^2_{max}(t)/\sigma^2_{max}(t)$, where the maximum x_{max} is calculated by looking at the zero point of the derivative of the

PDF, $\partial_x P(x,t) = 0$, leading for deterministic dynamics, to [11]

$$x_{max}(t) = \frac{1}{kt} + \frac{1 + x_0 kt - \sqrt{(1+x_0 kt)^2 + 8\sigma_0^2 (kt)^2}}{4\sigma_0^2 (kt)^3}, \tag{1.7}$$

and the curvature is defined according to its definition [11]

$$\sigma^2_{max}(t) = \frac{P(x_{max}(t),t)}{|\partial_x^2 P(x_{max}(t),t)|}. \tag{1.8}$$

To better understand the origin of the local characteristics, one can imagine a trajectory starting from x_0 that follows the deterministic dynamics $x(t) = x_0/[1 + x_0 kt]$. A trajectory initially starting on the right of the inflection point, converges to the origin as $x(t) \approx 1/kt$ [11], while a trajectory starting on the left diverges. The trade-off between the two evolution leads to a plethora of behavior of local characteristics that strongly depends on the initial distribution [11].For non-vanishing x_0, at short times, the evolution of maximum and curvature of particle position can be approximated by [11]

$$x_{max}(t) \approx x_0 + (2\sigma_0^2 - x_0^2)kt, \tag{1.9}$$

$$\sigma^2_{max}(t) \approx \sigma_0^2 - 4\sigma_0^2 x_0 kt - 10k^2\sigma_0^4 t^2. \tag{1.10}$$

The sufficient condition to observe the atypical shift in Eq.(1.9), against the potential force $-\partial_x V(x)$ is given by the inequality $0 < x_0/\sqrt{2} < \sigma_0$, while the narrowing of the curvature in Eq.(1.10) requires only $x_0 > 0$ [11].

The noise to signal transition for the maximum of particle position is shown in Fig.1.4 showing the atypical shift powered by noise in the limit of negligible environmental noise, and weak diffusion. The SNR for local characteristics, is a parameter that determines how well the most likely position can be observed experimentally [1]. In turns it is required to have a non-negligible SNR to be able to detect the shift of the maximum of particle position. In contrast to the SNR for global characteristics, it does not show a drop as time grows, remaining nonzero for any t, as both maximum and curvature converge to a positive value [1]. As shown in Fig.1.3, while the drop of the ratio for averages shows that the signal in the position is neg-

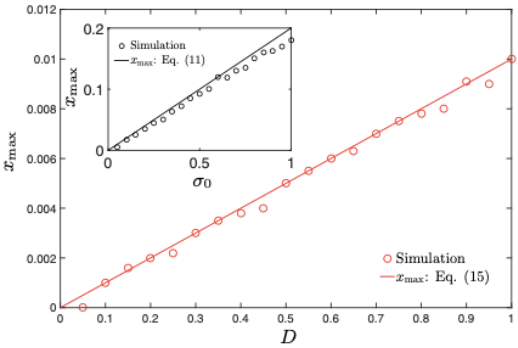

Figure 1.4: Atypical shift of maximum powered by initial thermal noise (inset, black), and environmental noise(red) [7]
The figure demonstrates the noise-to-signal transition for the most likely trajectory, with the atypical shift against the potential force.
The solid lines represent the analytical solutions, while the dots are the numerical simulation obtained via Eq.(1.1), and using $\gamma = 1, \langle x_0 \rangle = 0, dt = 2 \times 10^-3, \sigma^2_{x_0} = 0$ *($D = 0$ for the inset), and* $nt = 3 \times 10^5$ *trajectories where generated.*

ligible compared to the noise, the SNR for local characteristics exhibits the maximum of particle position maintaining its information values for all times.

From the equation of motion Eq.(1.1), the mean average velocity $\langle \bar{v} \rangle = \Delta x/\Delta t$ can be calcualted, for the short time dynamics, as

$$\langle \bar{v} \rangle = \left\langle \frac{\Delta x}{\Delta t} \right\rangle \approx -\kappa \sigma_{x_0}^2, \tag{1.11}$$

$$\sigma_{\bar{v}} \approx \sqrt{2\kappa^2 \sigma_{x_0}^4 + 2D}, \tag{1.12}$$

$$\mathrm{SNR}_{\bar{v}} = \frac{|\langle \bar{v} \rangle|}{\sigma_{\bar{v}}} \approx \frac{1}{\sqrt{2\left(1 + D\kappa^{-1}\sigma_{x_0}^{-2}\right)}}. \tag{1.13}$$

The knowledge of average velocity paves the way towards the underdamped regime, where the instantaneous velocity and acceleration become the principal quantities to be driven by the initial thermal noise, as shown in Fig.1.5.

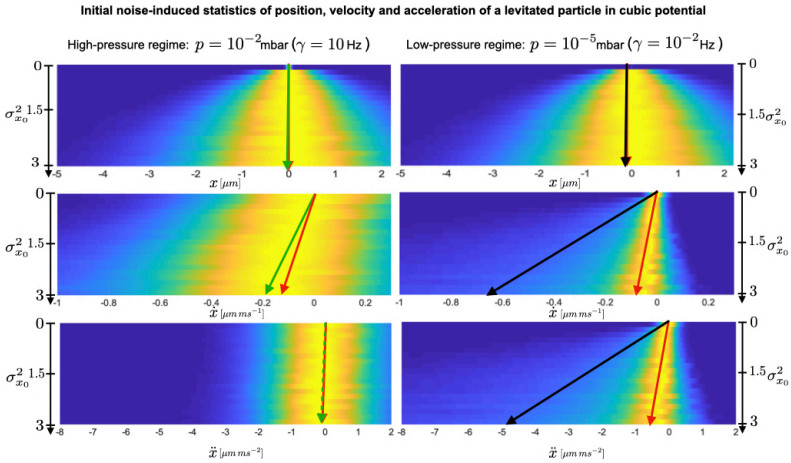

Figure 1.5: Noise-induced position, velocity and acceleration statistics of a levitated particle in cubic potential for the high pressure limit (left column) and for the low pressure limit (right column).

The initial Gaussian distribution comprises of $\langle x_0 \rangle = 0$, $\langle \dot{x}_0 \rangle = 0$ *and* $\sigma^2_{\dot{x}_0} = 0$, *while* $\sigma^2_{x_0}$ *triggers the nonlinear dynamics. Top panel: the mean (green, black) and maximum (red) of position distribution do not develop at such short time scale, while their standard deviations (green-blue, yellow halo) increase as initial noise increases. Middle panel: comparing the mean average velocity (left column, green) to the mean instantaneous velocity (right column, black), the former produces a smaller noise-induced shift. Their standard deviation (green blue halo) is significantly reduced in the low pressure regime. The maxima of velocity distributions (red) increase alongside the potential force with a significant reduction in the curvature for the low pressure regime (right column, yellow halo). Bottom panel: comparing the mean average acceleration (green) with the mean instantaneous acceleration (black), the former does not display a noise-induced effect, while it is substantial in the low pressure regime. Similarly, their standard deviation (green-blue halo) increases with noise only in the low pressure regime. The maxima of acceleration distribution (red) increases, alongside the potential force with a significant reduction in the curvature only in the low pressure regime (right). In the high pressure regime (left), the maximum does not develop, and it is surrounded by a large curvature (yellow halo). To generate all the density plots, Eq. (2.1) has been simulated using* $\kappa = 6k_B T \mu m^{-3} Kg^{-1}$,$T = 300$ *K,* $t = 0.1$ *ms,* $dt = 2\times10^{-5}$ *ms.* $nt = 10^4$ *trajectories where generated with* 5000 *samples each. To calculate the instantaneous quantities,* $\dot{x} = dx/dt$, $\ddot{x} = d\dot{x}/dt$, *the time interval used is given by the time-step* $dt = 2 \times 10^{-5}$ *ms, whereas for the average quantities* $\bar{v} = \Delta x/\Delta t$, $\bar{a} = \Delta v/\Delta t$, *the time interval, multiple of the time-step, has been used* $\Delta t = 10 \times dt$.

Chapter 2

Underdamped Stochastic Dynamics in Cubic Potential

We investigate the dynamics of a particle trapped in an optical cubic potential in the low pressure regime, discussing new unexplored nonlinear ballistic effects appearing in the instantaneous speed and acceleration. The equation of motion governing the dynamics can be well approximated

by the following Langevin equation

$$\ddot{x} = -\kappa x^2 - \gamma\dot{x} + \sqrt{\frac{2k_BT\gamma}{m}}\xi(t), \tag{2.1}$$

where $\kappa = k/m$ is the normalised cubic potential stiffness, $\gamma = \Gamma/m$ is the medium damping with drag coefficient Γ of the medium (i.e. air at low pressure), T is the absolute temperature, and k_B is the Boltzmann constant.

In the limit of low friction, the dynamics is that of Eq.(2.1), where the characterisation of the statistics of instantaneous speed $\dot{x}$ and acceleration $\ddot{x}$ unfold without changing initial position x_0. While these quantities are well defined in the underdamped regime, they exist only on average in the high friction limit $\bar{v} = \Delta x/\Delta t$ (Eqs.(1.11)-(1.13)), and $\bar{a} = \Delta\bar{v}/\Delta t$.

If we consider the dynamics to be deterministic, i.e. $\gamma = 0$, and characterised by a Gaussian initial distribution with $\langle\dot{x}_0\rangle = \sigma_{\dot{x}_0} = 0$, the nonlinear ballistic dynamics is using only initial position uncertainty as a thermal energy resource. This translates into the following quantitative description of the moments of instantaneous acceleration and velocity

$$\langle\ddot{x}\rangle \approx -\kappa\sigma_{x_0}^2, \qquad \langle\dot{x}(t)\rangle \approx -\kappa\sigma_{x_0}^2 t, \tag{2.2}$$

$$\sigma_{\ddot{x}} \approx \sqrt{2}\kappa\sigma_{x_0}^2, \qquad \sigma_{\dot{x}}(t) \approx \sqrt{2}\kappa\sigma_{x_0}^2 t, \tag{2.3}$$

$$\mathrm{SNR}_{\ddot{x}} \approx \frac{1}{\sqrt{2}}, \qquad \mathrm{SNR}_{\dot{x}}(t) \approx \frac{1}{\sqrt{2}}. \tag{2.4}$$

The first experimental verification to distinguish the nonlinear ballistic dynamics comprises of the shift of instantaneous acceleration $\langle \ddot{x}(t) \rangle$ powered by initial position noise, as demonstrated in Fig.1.5 (comparison left and right column of the bottom panel).

The second main feature of the nonlinear ballistic dynamics is characterised by a prominent noise-induced shift of mean instantaneous velocity $\langle \dot{x}(t) \rangle$, with reduced uncertainty Fig.1.5 (comparison left and right column of the middle panel).

Notice how both mean instantaneous acceleration, and velocity Eq.(2.2), and their respective standard deviation Eq.(2.3) are equally powered by $\sigma_{x_0}^2$ to produce a constant SNR as shown in Fig.2.1 (bottom and middle panel).

The short time scale of the transient regime is defined by a particle which on average does not move $\langle x(t) \rangle \approx 0$. The evolution of moments of position unveils as follows

$$\langle x(t) \rangle \approx -\frac{1}{2}\kappa\sigma_{x_0}^2 t^2, \tag{2.5}$$

$$\sigma_x(t) \approx \sqrt{\sigma_{x_0}^2 + \frac{1}{2}\kappa^2 t^4 \sigma_{x_0}^4}, \tag{2.6}$$

$$\mathrm{SNR}_x(t) = \frac{|\langle x \rangle|}{\sigma_x} \approx \frac{1}{\sqrt{2\left(1 + 2k^{-2}\sigma_{x_0}^{-2} t^{-4}\right)}}. \tag{2.7}$$

For the long time transient dynamics, but before the divergence, the mean position of Eq.(2.5) evolves quadratically in time. Simultaneously, the

standard deviation depends on two terms, the first of which becomes negligible at long time scales, $t > 0.9$ ms (for the parameters used to produce Fig.2-1), leaving a standard deviation that grows comparably to mean position and realising a constant $\mathrm{SNR}_x \approx 1/\sqrt{2}$.

For short time scale ($t \leq 0.1$ for the parameters used to produce Fig.2-1) the position does not move on average, while the standard deviation of Eq.(2-6) is dominated by the first term $\sigma_x^2(t) \approx \sigma_{x_0}^2$. The resulting dynamics produces a vanishing SNR_x.

This quick overview of the deterministic motion proves that the noise-induced effect is prominently visible in the moments of instantaneous quantities $\ddot{x}, \dot{x}$ Eqs.(2-2), and vanishes for position x as can be seen in Fig.2-1 for the short time dynamics. The curves in Fig.2-1, have been simulated using real experimental parameters of the current setups [7], showing that at values of $\Gamma = 10^{-2}$Hz (black dots) the zero-damping approximation of Eqs.(2-2)to(2-7) (black line) is reached. Moreover, it shows that at larger damping values $\Gamma = 10$Hz (green dots), the results from the high friction limit (green line) are obtained for position (top panel) and average velocity (middle panel), and the vanishing of acceleration is observed (bottom panel). In principle, both mean and maximum of the instantaneous quantities should increase coherently with a constant signal-to-noise ratio, and as the noise-induced evolution is unveiled (Fig.2-2), we recall the result of the over-damped regime for maximum of position (Fig.1-4, inset, and Fig.2-2 top panel, left column) moving atyp-

ically against the potential force (Fig.2.2, top panel, right column).

The new feature of coherent motion of maximum velocity and acceleration appears at low frictions, where the latter shift alongside the potential force (qualitatively visible in Fig.1.5 middle and bottom panel, right column, red arrow). A quantitative analysis of the shift of the most-likely velocity and acceleration can be based on the results shown in Fig.2.2, where the sharp shape of the acceleration distribution (bottom panel, right column, inset) leaves room for a visible shift of its maximum, which is larger compared to the shift of the maximum of velocity distribution (bottom, panel, left column).

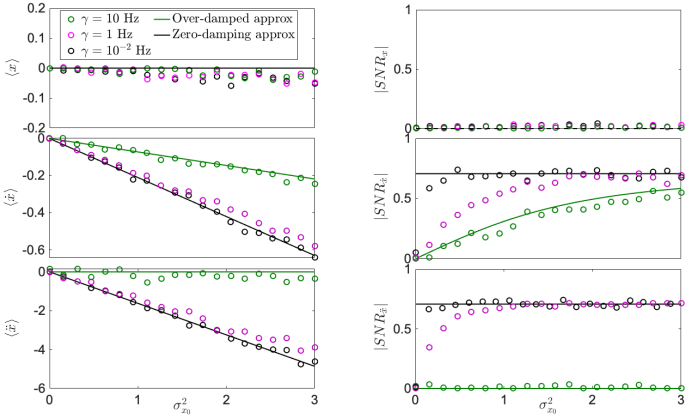

Figure 2.1: Noise-induced effect for initially steady particle in position x (top), instantaneous velocity $\dot{x}$ (middle), and acceleration $\ddot{x}$ (bottom), driven by variance $\sigma^2_{x_0}$ of initial position.
Top panel: the mean position $\langle x \rangle$ (left) does not develop with increasing initial noise $\sigma^2_{x_0}$ at the short time scale in neither of the damping values explored, spacing from low pressure regime (black) to high pressure regime (green). Because of the vanishing mean position, and the large noise spread dominating the position dynamics, the SNR_x (right) vanishes too. Middle panel: the mean instantaneous velocity $\langle \dot{x} \rangle$ (left) displays a noise-induced shift that reaches the deterministic limit (black line) for both $\Gamma = 10^{-2}$ (black dots), and $\Gamma = 1$ (purple dots), while it retrieves the overdamped approximation of Eq.(1.11) for $\Gamma = 10$ (purple dots). The respective $SNR_{\dot{x}}$ (right) shows how sensitive is the standard deviation of velocity to environmental temperature T, at different pressures, keeping the low pressure closer to deterministic approximation (black), while leading to a converging $SNR_{\dot{x}}$ for the higher pressure regime (green), retrieving once again the results from the overdamped regime, namely Eq.(1.13). Bottom panel: the mean of instantaneous acceleration $\langle \ddot{x} \rangle$ (left) clearly shows the main difference between the two limits (low pressure, black line, and high pressure green line), demonstrating the noise-induced feature for instantaneous acceleration close to the deterministic approximation (black) for $\Gamma = 10^{-2}$ (black) and $\Gamma = 1$ (purple), while vanishing for larger damping (green). The role of environmental temperature can be observed for $SNR_{\ddot{x}}$ (left) where an increase in pressure (purple) leads to a larger standard deviation and to a converging $SNR_{\ddot{x}}$. Eq. (2.1) has been simulated using $\kappa = 6k_BT\mu m^{-3}Kg^{-1}$,$T = 300$ K (ambient temperature), $\langle x_0 \rangle = 0$, $\langle \dot{x}_0 \rangle = 0$, $\sigma_{\dot{x}_0} = 0$, $t = 0.1$ ms, $dt = 2 \times 10^{-5}$ ms. 10^4 trajectories where generated with 5000 samples each. To compute the average quantities, $\bar{v}$, $\bar{a}$, the multiple time-step has been used, $\delta t = 10 \times dt$.

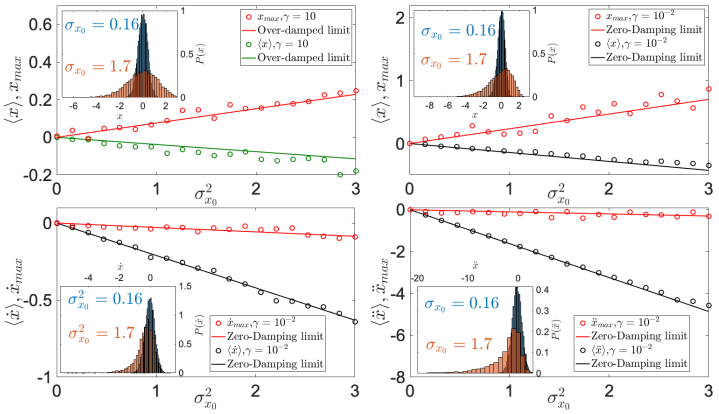

Figure 2.2: Initial noise-induced shift of maximum of position x_{max} (top), for high (left) and low (right) pressure limit, maximum of instantaneous velocity $\dot{x}_{max}$ (bottom left), and acceleration $\ddot{x}_{max}$ (bottom right).

All simulations (dots) have been performed based on Eq. (2.1) using $\langle x_0 \rangle = \langle \dot{x}_0 \rangle = 0$, and $\sigma^2_{\dot{x}_0} = 1$. Top panel: The atypical motion of maxima of position is highlighted (red), following in the high friction limit (left) the results obtained in the overdamped regime [1, 2]. The same atypical evolution is yet encountered at low pressures (right, red), where the red line indicates the zero damping limit evolution of the maxima. To make the shift in maximum more visible, Eq. (2.1) has been simulated with $t = 0.3$ ms. Bottom panel: The maximum of instantaneous velocity at the low pressure limit (left) comprises of a coherent shift (red) alongside the mean instantaneous velocity (black). A similar behavior is noticeable for statistics of acceleration (right) with its maxima (red) shifting faster at higher initial noise than that of velocity. All the insets show a snapshot of the probability distribution at different $\sigma^2_{x_0}$ highlighting the instability (heavy tails on the left), and showing once again a clear shift of the maximum alongside the potential force. To produce the figure on the bottom panel, Eq. (2.1) has been simulated with $t = 0.1$ ms. The other parameters used to produce this graph from Eq. (2.1) are $\kappa = 6k_BT\mu m^{-3}Kg^{-1}, T = 300K, dt = 2 \times 10^{-5}$ ms. $nt = 10^4$ trajectories where generated with $N = 5000$ samples each.

Methods 3

Stochastic Simulation in Unstable Cubic Potential

Simulating a nonlinear system, as a Brownian particle evolving in the unstable cubic potential, bares certain intrinsic difficulties that require innovative method to tackle. The first lies in the discretisation of time, by dividing it into N small finite steps of length dt, such that

$$t_n = \tau n, \qquad n = 1, 2, ..., N. \tag{3.1}$$

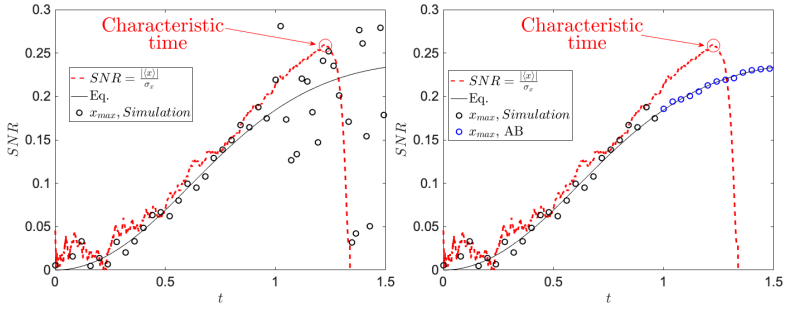

Figure 3.1: *Computation of x_{max} compared to characteristic time(top). The graph can be split into two main parts; the first is for time smaller than the characteristic time, defined in this graph as the maximum of the* SNR *calculated from global dynamics, where the x_{max} can be computed accurately by mere increase of ensemble size. Secondly approaching the characteristic time, the error performed on the computation of x_{max} increases, resulting in a poor accurate computation for time larger than the the turning point of* SNR.
Computation of x_{max} compared to characteristic time, extension with rejection scheme (bottom). The blue dots show the improvement upon the calculation of x_{max} for time approaching the characteristic time, and beyond. The accuracy obtained by applying the rejection scheme is much higher than in the computation of x_{max} in the figure on the top panel, for the same ensemble size. For this figure Eq.(1.1) has been simulated, using $k = 1, D = 0.1, \sigma_0 = 0.0, dt = 10^{-5}$. An ensemble size of 3×10^5 has been used to generate this graph.

Failure to use the correct time-step will result in a wrong computation of the stochastic process $\int_0^t g(x,t)dW_t$,, approximated in numerical simulation as $\sum_{n=0}^{N} g(x,t_n)(W_{t_n+1} - W_{t_n})$ in the limit of $dt \to 0$ [8].

Different algorithms can be adopted to solve a stochastic equation of the form of Eq.(1.1), but the Euler-Maruyama scheme is the one used in

this thesis work. With the choice of the algorithm comes the conditions upon the convergence, requiring the function to be four time continuously differentiable with bounded derivatives, and not quickly growing with parameters [9]. Such convergence schemes need carefulness when dealing with unbounded and unstable potentials as, given certain regions of parameters, they lead to quickly diverging functions [1, 3]. Nonetheless, in short time dynamics (shorter than the divergence time), one can safely operate the Euler-Maruyama scheme within the boundary imposed by the convergence, worrying only about the size of the statistical ensemble required to generate data with high accuracy.

Accuracy can be thought of as a measure of closeness between the simulated value and the real one [9], defined as the Mean Absolute Error

$$MAE = \sum_{i=1}^{n} \frac{|y_i - x_i|}{n}, \tag{3.2}$$

where y_i is the prediction, and x_i is the true value. For time shorter than the characteristic time, a mere increasing of the ensemble size is enough to obtain accurate results, while for time larger than the divergence time, this is not true anymore, as shown in Fig.3.1(left). To simulate beyond the divergence time, and achieve high accuracy in the computation of the local characteristics, one needs to implement a rejection scheme upon the evolving trajectory, following the rule "*Whenever the trajectory hits the absorbing boundary for the first time, reject the entire trajectory*" [6],

which bias the evolution to only those trajectories surviving the divergence. The latter is achieved by applying an absorbing boundary to the evolving trajectory, following the condition $a < -(3k_BT/k)^{\frac{1}{3}}$ to avoid affecting any properties on the plateau [1]. The resulting estimation of x_{max}, showed in Fig.3.1 (right) presents an improvement upon the estimation of the local characteristic without the rejection scheme, for the same ensemble size.

In the underdamped regime, the numerical challenge lies in the computation of the average and instantaneous quantities. For instance, given a position trajectory evolving in time $x(t)$, one can compute the average velocity simply as the ratio between the distance travelled and the elapsed time $\bar{v} = \Delta x/\Delta t$. By taking its limit as the elapsed time Δt approaches zero $\dot{x} = \lim_{\Delta t \to 0} \Delta x/\Delta t = dx/dt$ allows to calculate the instantaneous velocity, telling us how fast the particle is moving anywhere along its path. In the underdamped regime, the instantaneous velocity $\dot{x}$ is naturally introduced in the equation of motion and in the low friction limit, where the damping time is long, the computation always outputs the instantaneous quantity with accuracy varying with the sample size (see Fig. 3.2 top panel). As the friction increases the damping time shortens, resulting in a time evolution of velocity comprising both ballistic ($t \ll \Gamma$) and diffusive dynamics ($t \gg \Gamma$). The behavior can be observed in Fig. 3.2 (bottom panel, red dots), where for short time the velocity fits with the theoretical approximation of Eq.(2.2) (red dashed line), whereas for larger

time the simulated curve converges to the result of average velocity of Eq.(□.□))(solid black line). Tweaking the spacing between the position difference $\Delta x = x(n+m) - x(n)$ and time $\Delta t = mdt$, or simply running simulations for larger timesteps dt, allows to calculate more efficiently the average velocity $\bar{v} = \Delta x/\Delta t$. A similar logic applies for the computation of both instantaneous $\ddot{x} = d\dot{x}/dt$ and average $\bar{a} = \Delta\bar{v}/\Delta t$ acceleration.

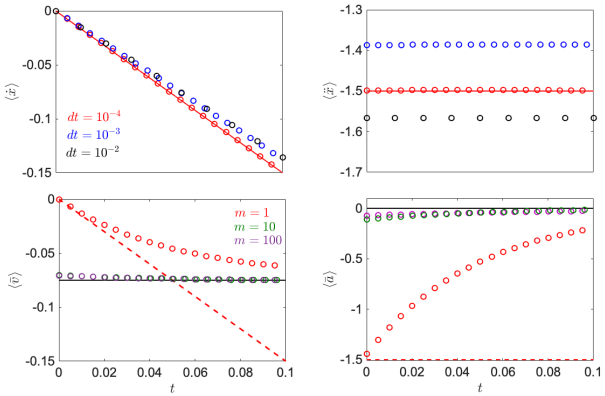

Figure 3.2: Computation of average and instantaneous velocity (left column) and acceleration (right column) for different timesteps dt***, for low pressure regime (top) and high pressure regime (bottom).***
To obtain the dots, Eq.(2.1) has been simulated. Top panel: The instantaneous velocity $\dot{x}$ *(left) is naturally introduced in the equation of motion Eq.(2.1), and its mean* $\langle \dot{x} \rangle$ *can be easily computed even at larger timesteps (black). Instantaneous acceleration* $\ddot{x}$ *(right) requires the numerical differentiation algorithm to be calculated, and hence its mean* $\langle \ddot{x} \rangle$ *is more prone to error for increasing timesteps (blue, black). Bottom panel: in the high friction limit, by accessing the velocity output from eq.(2.1), one registers both ballistics and diffusive timescales (red dots). By making use of the differentiation algorithm* $x(n+m) - x(n)/mdt$ *one can see a quick convergence of the average velocity (left) and acceleration (right) for small values of m (green) to the analytical results for overdamped dynamics (black). The Red lines correspond to analytical predictions at low pressure, whereas black lines correspond to analytical prediction at high pressure.*

Conclusions

In this work, we investigated noise-to-signal transitions for a Brownian particle evolving in the unstable cubic potential. We studied two essential regimes with high experimental relevance in the actual scientific scope, comprising of overdamped and underdamped regime.

The main result, at the heart of the unstable nonlinear systems, lies in the noise induced mechanical mean displacement $\langle x \rangle$ (in the high friction limit) Fig.1.3 (red line) [3]. A consequence of the unstable dynamics sees the PDF of the particle position developing heavy tail, while its moments cease to exist. Motivated by the limitation imposed by the rapid diverging trajectories, resulting in variance of position growing faster than its mean, we proposed and analyzed local directly measurable characteristics $x_{max}, \sigma_{x,max}$, overcoming such limitation [1]. A key result in this framework shows the peculiar behavior of the most probable position, which moves opposite to the acting force; both in time and temperature.

Those results have been experimentally observed [2, 10], showing the time evolution of both mean and maximum of position distribution in short and long times dynamics.

Motivated by the already reached underdamped regime for levitated experiments [11–14], which allow to probe the fundamentals of nonlinear stochastic dynamics in the limit of weak friction, we proposed and demonstrated the first nonlinear ballistic effect for levitated nanoparticles optically trapped in high vacuum, consisting of the noise-induced instantaneous speed and acceleration of in the highly unstable cubic potential. The key result, shown in Fig.1.5, demonstrates that the noise-induced effect turns to instantaneous velocity and acceleration. Moreover, we observed the coherent motion, alongside the potential force, of the mean and maxima of instantaneous speed and acceleration distributions, Fig.2.2.

In the last chapter, 3, we discussed the numerical methodologies to simulate the dynamics of a particle in unstable potentials. Although we focus on a particle in cubic potential, our methodologies are broadly applicable to any highly unstable potential.

The key result of this chapter is contained within the rejection scheme that not only allowed to compute the maximum of the distribution beyond the characteristic time, but it also proved useful to minimise the demanding ensemble size requirement for its computation.

Bibliography

[1] L. Ornigotti, A. Ryabov, V. Holubec, and R. Filip, "Brownian motion surviving in the unstable cubic potential and the role of maxwell's demon," *Physical Review E*, vol. 97, no. 3, p. 032127, 2018.

[2] M. Šiler, L. Ornigotti, O. Brzobohatỳ, P. Jákl, A. Ryabov, V. Holubec, P. Zemánek, and R. Filip, "Diffusing up the hill: Dynamics and equipartition in highly unstable systems," *Physical review letters*, vol. 121, no. 23, p. 230601, 2018.

[3] R. Filip and P. Zemánek, "Noise-to-signal transition of a brownian particle in the cubic potential: I. general theory," *Journal of Optics*, vol. 18, p. 065401, apr 2016.

[4] P. Zemánek, M. Šiler, O. Brzobohatý, P. Jákl, and R. Filip, "Noise-to-signal transition of a brownian particle in the cubic potential: Ii. optical trapping geometry," vol. 18, no. 6, p. 065402, 2016.

[5] R. Filip, "Distillation of quantum squeezing," *Physical Review A*, vol. 88, pp. 063837–, 12 2013.

[6] A. Ryabov, V. Holubec, and E. Berestneva, "Living on the edge of instability," vol. 2019, no. 8, p. 084014, 2019.

[7] J. Flajšmanová, M. Šiler, P. Jedlička, F. Hrubý, O. Brzobohatý, R. Filip, and P. Zemánek, "Using the transient trajectories of an optically levitated nanoparticle to characterize a stochastic duffing oscillator," *Scientific Reports*, vol. 10, no. 1, p. 14436, 2020.

[8] B. S. Daan Frenkel, *Understanding Molecular Simulation*. Academic Press, 2002.

[9] D. C. Rapaport, *The Art of Molecular Dynamics Simulation*. Cambridge University Press, 2004.

[10] M. Šiler, P. Jákl, O. Brzobohatý, A. Ryabov, R. Filip, and P. Zemánek, "Thermally induced micro-motion by inflection in optical potential," *Scientific Reports*, vol. 7, no. 1, p. 1697, 2017.

[11] J. Gieseler, L. Novotny, and R. Quidant, "Thermal nonlinearities in a nanomechanical oscillator," *Nature Physics*, vol. 9, no. 12, pp. 806–810, 2013.

[12] F. Ricci, R. A. Rica, M. Spasenović, J. Gieseler, L. Rondin, L. Novotny, and R. Quidant, "Optically levitated nanoparticle as

a model system for stochastic bistable dynamics," *Nature Communications*, vol. 8, no. 1, p. 15141, 2017.

[13] R. Huang, I. Chavez, K. M. Taute, B. Lukić, S. Jeney, M. G. Raizen, and E.-L. Florin, "Direct observation of the full transition from ballistic to diffusive brownian motion in a liquid," *Nature Physics*, vol. 7, no. 7, pp. 576–580, 2011.

[14] V. Jain, J. Gieseler, C. Moritz, C. Dellago, R. Quidant, and L. Novotny, "Direct measurement of photon recoil from a levitated nanoparticle," *Phys. Rev. Lett.*, vol. 116, p. 243601, Jun 2016.

Published articles

1. **Brownian motion surviving in the unstable cubic potential and the role of maxwells demon**

   L. Ornigotti, A. Ryabov, V. Holubec, and R. Filip

   Physical Review E, vol. 97, no. 3, p. 032127, 2018.

2. **Diffusing up the hill: Dynamics and equipartition in highly unstable systems**

   M. Šiler, L. Ornigotti, O. Brzobohatỳ, P. Jákl, A. Ryabov, V. Holubec, P. Zemánek, and R. Filip

   Physical review letters, vol. 121, no. 23, p. 230601, 2018.

3. **Noise induced instantaneous speed and acceleration of a levitated particle**

   L. Ornigotti, and R. Filip

   Under review process for publication in Scientific Reports.